



FR9701750

JET-P-94-29

Many Authors

JET Papers presented to the
21st EPS Conference on
Controlled Fusion and Plasma Physics
(Montpellier, France, 27 June–1 July 1994)

L

28-10

JOINT EUROPEAN TORUS

JET

This document is intended for publication in the open literature. It is made available on the understanding that it may not be further circulated and extracts or references may not be published prior to publication of the original, without the consent of the Publications Officer, JET Joint Undertaking, Abingdon, Oxon, OX14 3EA, UK.

Enquiries about Copyright and reproduction should be addressed to the Publications Officer, JET Joint Undertaking, Abingdon, Oxon, OX14 3EA, UK.

JET Papers presented to the
21st EPS Conference on
Controlled Fusion and Plasma Physics
(Montpellier, France, 27 June–1 July 1994)

Many Authors

JET Joint Undertaking, Abingdon, Oxon, OX14 3EA, UK.

Preprint of a paper to be submitted for publication in
Proceedings of 21st EPS Conference

July 1994

**JET Papers presented to the
21st EPS Conference on Controlled Fusion and Plasma Physics,
(Montpellier, France, 27 June - 1 July 1994).**

Title	Main Author	Page No:
1) Effects of Sawtooth Crashes on Beam Ions and Fusion Product Tritons in JET	F B Marcus	1
2) Beta Limits in H-Modes and VH-Modes in JET	P Smeulders	7
3) Impurity Induced Neutralization of MeV Energy Protons in JET Plasmas	A A Korotkov	13
4) Development of Thin Foil Faraday Collector as a lost Alpha Particle Diagnostic for High Yield D-T Tokamak Fusion Plasmas	F E Cecil	19
5) 15-MeV Proton Emission from ICRF-Heated Plasmas	O N Jarvis	25
6) Pulse compression radar reflectometry for density measurements on fusion plasmas	C Laviron	31
7) Gamma-Ray Emission Profile Measurements during JET ICRH discharges	P J A Howarth	37
8) The New JET Phased ICRH array. First Experiments and Modelling	M Bures	43
9) Simulation of Triton Burn-up in JET Plasmas	M J Loughlin	49
10) Parametric Dependencies of JET Electron Temperature Profiles	B Schunke	55
11) Detached Divertor Plasmas in JET	L D Horton	61
12) Excitation of Global Alfvén Eigenmodes by RF Heating in JET	W Kerner	67
13) The comparative analysis of the different mechanisms of toroidal rotation in tokamaks	R Sabot	73
14) Effect of Shear in the Radial Electric Field on Confinement in JET	D P O'Brien	79

Title	Main Author	Page No:
15) Plasma Transport Properties at the L-H Transition and High Performance Phase of JET Discharges	V Parail	85
16) A Numerical Study of Plasma Detachment Conditions in JET Divertor Plasmas	R Simonini	91
17) The SOL Width and the MHD Interchange Instability in Tokamaks	O Pogutse	97
18) Nonlinear Magnetic Reconnection in Low Collisionality Plasmas	M Ottaviani	103
19) Topology and Slowing Down of High Energy Ion Orbits	F Porcelli	109
20) Sawtooth Crashes at High Beta on JET	B Alper	115
21) Fusion Performances and Alpha Heating in Future JET D-T Plasmas	B Balet	121
22) A Stable Route to High- β_p Plasmas with Non-Monotonic q-Profiles	F X Soldner	127
23) A Theory for the Propagation of Changes to Confinement	J P Christiansen	133
24) Spatial distribution of γ emissivity and fast ions during (^3He)D ICRF heating experiments on JET	E Righi	139
25) The JET Multi-Camera Soft X-Ray Diagnostic	B Alper	145
26) Radiation Phenomena and Particle Fluxes in the X-event in JET	H J Jackel	151
27) Local measurement of transport parameters for laser injected trace impurities	R Giannella	157
28) Impurity transport of high performance discharges in JET	L Lauro Taroni	163

Title	Main Author	Page No:
29) Negative snakes in JET: Evidence for negative shear?	R D Gill	169
30) Prospects of real-time ion temperature and rotation profiles based on neural-network charge exchange analysis	R W T König	175
31) Ion Temperature Anisotropy in High Power Helium Neutral Beam Fuelling Experiments in JET	A C Maas	181
32) Impurity Line Emission due to Thermal Charge Exchange in JET Edge Plasmas	C F Maggi	187
33) The Control of Convection by Fuelling and Pumping in the JET Pumped Divertor	P J Harbour	193
34) VH Mode Accessibility and Global H-mode Properties in Previous and Present JET Configurations	T T C Jones	199
35) Ion Cyclotron Emission by Spontaneous Emission	O Da Costa	205
36) Analysis of JET LHCD/ICRH Synergy Experiments in Terms of Relativistic Current Drive Theory	D F H Start	211
37) Correlations between Locked Modes and Impurity Influxes	K D Lawson	217
38) An Analysis of JET Fast-Wave Heating and Current Drive Experiments Directly Related to ITER	V P Bhatnagar	223
39) The H-Mode Power Threshold in JET	D F H Start	229
40) The Density Limit in JET Diverted Plasmas	D J Campbell	235



FR9701751

Effects of Sawtooth Crashes on Beam Ions and Fusion Product Tritons in JET

F B Marcus, J M Adams¹, D S Bond¹, M A Hone,
P J A Howarth², O N Jarvis, M J Loughlin, G Sadler, N Watkins¹.

JET Joint Undertaking, Abingdon, Oxon, OX14 3EA.

¹ AEA Technology, Harwell Laboratory, Harwell, Oxfordshire, UK.

² University of Birmingham, Birmingham, UK.

ABSTRACT

The objective of this study is to examine the effect of a sawtooth crash on the radial distribution of the slowing down fusion product tritons and on beam ions. The JET neutron emission profile monitor (Fig. 1) was used to measure the 2.5 MeV and 14 MeV neutron emission line-integrals before and after sawtooth crashes in the Joint European Torus (JET). In deuterium discharges, the 14 MeV neutron production was wholly attributable to burnup of the 1 MeV fusion product tritons from d-d fusion. It has been known for many years that the global emission of 14 MeV neutrons is not affected by sawtooth crashes. Examination of the data obtained with the profile monitor shows that the local emissivity of 14 MeV neutrons, and hence of the profile of thermalizing tritons, is only weakly affected by crashes in the discharges studied. This is in contradiction with the apparent behaviour of injected beam ions as deduced from a study of the considerable changes in local emissivity of the 2.5 MeV neutrons. Nevertheless, the behaviour of the fusion product tritons is consistent with the scaling of the beam injected deuterium, as explained below. A complete discussion is given in Ref. 1.

NEUTRON EMISSIVITY PROFILES

To obtain good time resolution for studying the effect of a sawtooth crash on the 14 MeV neutron emissivity (from the 1.0 MeV triton burnup, we analyse discharges with the highest rates of d-d fusion, corresponding to the maximum production rates of 1.0 MeV tritons. To optimise counting statistics, the data from six similar high performance discharges were added together over equal time bins just before and just after a sawtooth crash during a period of high 14 MeV neutron emission. These discharges all achieved the hot ion H or VH mode, and were heated primarily by a total of about 15 MW of deuterium neutral beam injection at 80 and 140 keV, with two of them having an additional 4-7 MW of ICRF heating. The improved statistics from the summation allowed a channel by channel comparison of the count rate before and after a sawtooth crash. The resulting count rates are presented in Fig. 2 for time bin intervals of 100 ms for 14 MeV neutrons. Very little change has occurred due to the sawtooth crash.

Discharge No. 26087 produced the highest d-d fusion rate from JET. A sawtooth crash occurred at 13.469 s, just after the maximums in plasma pressure and 2.5 MeV neutron emissivity, while the plasma was in the hot-ion, H-mode condition. Soft X-Ray (SXR) data sampled at 200 kHz shows a collapse which lasted only 100 μ s, and extended across the entire plasma, as was observed in other high beta discharges in JET. The sawtooth crash occurred at a plasma beta of 0.8 times the Troyon limit. The electron density profile was relatively flat. The deuterium ion density before the crash was more peaked, and showed a fall of about 10% at 50 ms after, compared to 50 ms before, the sawtooth crash.

Fig. 3 shows the line-integrals of neutron emissivity from the central plasma regions, as measured by channels (No. 4-8) of the horizontal camera, plotted for discharge No. 26087

as histograms for time intervals of 100 ms each for the 14 MeV neutron data, and for 10 ms each for the 2.5 MeV neutron data. The line-integral data clearly show a large sawtooth crash in the 2.5 MeV neutron line integrals, but any crash in the 14 MeV neutron line integrals is smaller than the $\approx \pm 10\%$ level of statistical fluctuation in the data.

In Fig. 4, the 2-D emissivity profiles of the 14 MeV neutrons are plotted versus major radius R and height z , (a) for the time interval 13.36-13.46 s just before the sawtooth crash, and (b) for the interval 13.48-13.58 s just after the crash. A time-bin of 100 ms is required to obtain better than $\pm 10\%$ statistics for the 14 MeV data in Discharge No. 26087. The axial value of the 14 MeV emissivity fell by about 20%, and the global emission fell by 8%, attributable to the axial deuterium density decrease of about 10%. Therefore, not more than 10% of the high energy tritons at the axis were redistributed. The response of the 2.5 MeV neutrons to the sawtooth crash was much stronger.

EFFECTS OF BEAM-THERMAL FRACTION AND EMISSIVITY WIDTH

Beam ions and partially slowed down tritons at comparable energies should respond similarly to sawtooth crashes. Discharges with the highest fraction of beam thermal fusion give the nearest approximation to the neutron emissivity response to a sawtooth crash of the t - d emission, which is 100% beam-thermal. Several discharges has been analysed with TRANSP. These calculations determined the fractional contribution of beam thermal fusion to the total 2.5 MeV neutron emissivity on axis just before the sawtooth crash, defined as (F_{bt}). In discharge No. 26042, at a time long after the initial heating period and peak 2.5 MeV neutron yield, the ratio F_{bt} reaches 0.8 just before the sawtooth crash. There was no observable change in the global 2.5 MeV or 14 MeV neutron emission. There was an observable change in the axial emissivity of the 2.5 MeV neutrons, but not of the 14 MeV neutrons.

Sawtooth crashes were examined in several discharges in the time interval between 0.0 and 0.8 s after the start of high power beam heating. The ratio F_{bt} varies between 0.26 and 0.69 and tends to increase with heating time. During this period, there was a high 2.5 MeV neutron yield, of order 10^{16} n/s, which allowed the use of 10 ms integration times for neutron tomography analysis, just before and just after each sawtooth crash. Fig. 5 shows the response of beam-injected deuterium ions to a sawtooth crash. It illustrates that the ratio of the axial neutron emissivity due to d - d fusion after the crash (S_1) to that before the crash (S_0) increases approximately linearly, from 0.2 to 0.5, as the relative contribution of beam-plasma fusion to the total fusion rate rises from 0.2 to 0.8. For the case of d - t fusion from triton burnup, shown as $F_{bt}=1$ for discharge No. 26087, the ratio S_1/S_0 is 0.8 (i.e. only a 20% decrease at the crash.) Triton burnup is conceptually the equivalent to 100% beam-thermal reactions. On this basis, the observations from d - d fusion can be extrapolated to show that no large change in the 14 MeV emissivity is to be expected.

A similar scaling is also observed in the behaviour of the spatial width of the neutron emissivity profiles as shown in Fig. 6, when the full-widths at half-maximum (FWHM) of the neutron emissivity profiles are plotted versus beam-thermal fraction, before and after the sawtooth crashes. The width before the crash increases as the beam thermal fraction increases, but the width after the crash is independent of the initial width. The width of the 14 MeV neutron emissivity profile from d - t fusion is nearly unchanged due to the crash. Extrapolation of the 2.5 MeV neutron data to a 100% beam-thermal fraction indicates that the expected change in the 14 MeV neutron axial emissivity should be small and the initial emissivity width should be the same as the width after the crash, as observed.

SOFT X-RAY EMISSIVITY WIDTH AND INVERSION RADIUS COMPARISONS

The response of SXR emissivity profiles to a sawtooth crash have been analysed in the same way as the neutron emissivity profiles. The ranges of the FWHM's of the SXR (and 2.5 MeV neutron) emissivity profiles are 0.54-0.92 m (and 0.30-0.75 m) before the sawtooth crash, and 1.08-1.28 m (and 0.98-1.17 m) after the sawtooth crash. The full width in the midplane of the sawtooth crash inversion diameter, presumably corresponding to the approximate location of the $q=1$ surface, is 0.68-0.80 m (and 0.54-0.78 m) for these discharges. The SXR emissivity profile is peaked before the crash in these discharges, and the peak emissivity region moves off-axis and rotates before the crash occurs.

CONCLUSIONS

In many sawtooth crashes affecting 2.5 MeV neutron emission, a large crash in axial neutron emissivity is observed because of initially peaked beam ions and significant beam-beam or thermal fusion contributions. The minimal response to an MHD crash of the axial 14 MeV neutron emissivity from the fusion product tritons is due to: a) the 100% beam-thermal contribution; b) the observation that net particle redistribution is weak in the central region of a distribution with a neutron emissivity FWHM greater than the SXR emissivity profile inversion diameter. The implication is that beam ion and 3.5 MeV alpha particle profiles in JET or ITER may be relatively resilient to sawtooth crashes, when the spatial width of their density is sufficiently large.

REFERENCE

/1/ F.B. Marcus et al., "Effects of Sawtooth Crashes on Beam Ions and Fusion Product Tritons in JET," Preprint JET-P(93)97, accepted for publication in NUCLEAR FUSION.

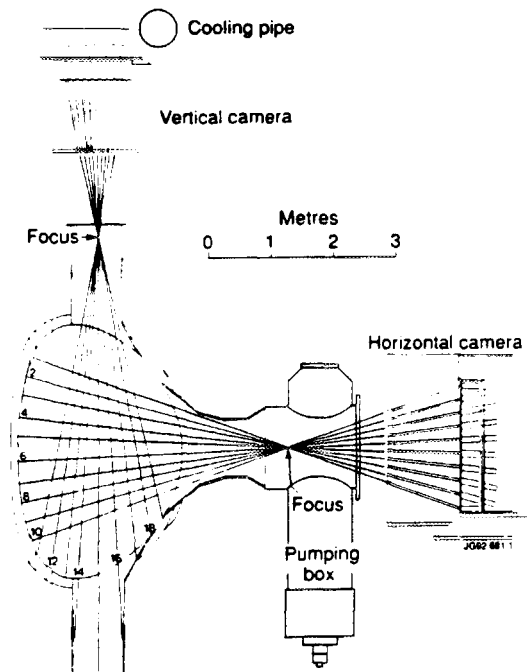


Fig. 1. The JET neutron emission profile monitor is drawn schematically, showing the lines-of-sight. It consists of two fan-shaped multi-collimator cameras using NE-213 scintillators for neutron detection..

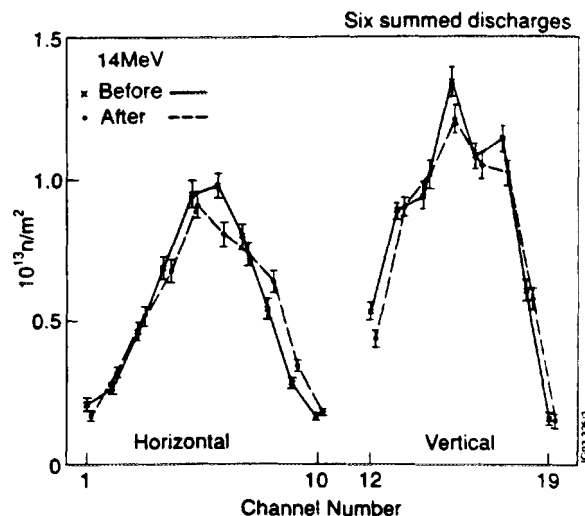


Fig. 2. 14 MeV neutron emission line integrals summed over six discharges for 100 ms before (x) and 100 ms after (•) a sawtooth crash in each discharge. (The points for the before and after data have been drawn with a slight horizontal displacement.)

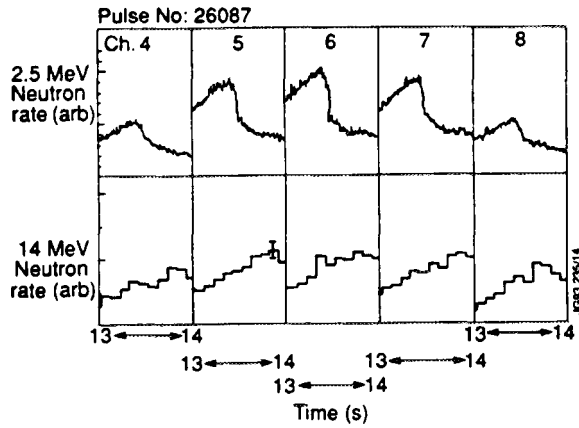


Fig. 3. The neutron emission line-integrals of channels 4-8 of the horizontally viewing camera are plotted for time intervals of 10 ms for the 2.5 MeV neutron data, and 100 ms for the 14 MeV neutron data, each frame spanning 13 s to 14 s which contained a sawtooth crash in discharge 26087 at 13.47 s.

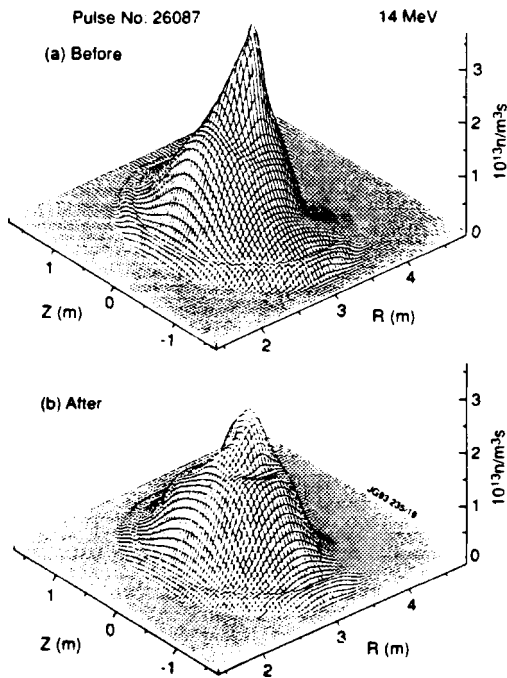


Fig. 4. The 2-D emissivity profiles of the 14 MeV neutrons are plotted versus major radius R and height z for (a) the time interval just before the sawtooth crash, and (b) the interval just after the crash in No. 26087.

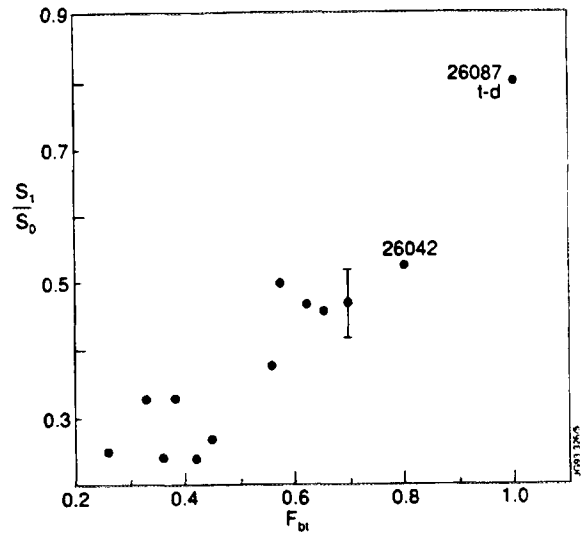


Fig. 5. The ratio of the axial neutron emissivity (S_1) just after the crash to (S_0) just before the crash, versus the fractional contribution of beam thermal fusion to the 2.5 MeV neutron emissivity on axis just before the sawtooth crash, defined as F_{bt} . The 2.5 MeV neutron data from discharge No. 26042, and the 14 MeV neutron data from discharge No. 26087 are shown for F_{bt} values of 0.8 and 1.0 respectively.

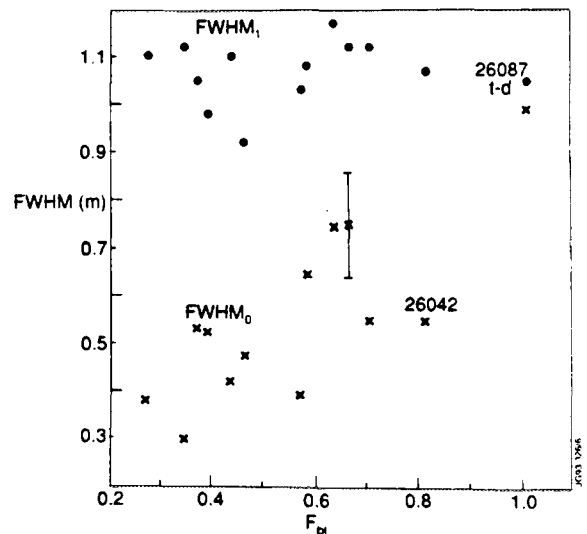


Fig. 6. The Full Width Half Maximum of the tomographically deduced neutron emissivity profile in the midplane ($FWHM_0$) just before (x), and ($FWHM_1$) just after the crash (\bullet), versus F_{bt} .



FR9701752

Beta Limits in H-Modes and VH-Modes in JET

P Smeulders, T C Hender, G Huysmans, F Marcus, S Ali-Arshad,
B Alper, B Balet, M Bures, N Deliyankis, H de Esch, G Fishpool,
O N Jarvis, T T C Jones, W Ketner, R König, K Lawson, P Lomas,
M F Nave¹, D O'Brien, G Sadler, D Stork, P Stubberfield, P Thomas,
K Thomen, J Wesson.

JET Joint Undertaking, Abingdon, Oxon, OX14 3EA.

¹ Associação EURATOM/IST, Instituto Superior Técnico, Lisbon, Portugal.

Abstract. In Hot-ion H- and VH-modes, the highest achieved beta was about 10% below the Troyon value in the best case of discharge 26087. The operational space of the high beta discharges obtained before March 1992 has been explored as function of the parameters $H_{ITER89P}$, β_n , q_{95} , I_p . Also, a limiting envelope on the fusion reactivity as a function of the average plasma pressure and beta has been observed with $R_{DD} \propto \beta_\phi^2 \cdot B_\phi^4$. MHD stability analysis shows that the JET VH modes at the edge are in the 2-nd region for ballooning mode stability. The dependence of ballooning stability and the $n=1$ external kink on the edge current density is analysed.

Confinement and Beta value. The quality of the confinement as measured by the H-multiplier of the measured diamagnetic energy confinement time against the ITER-89P scaling has been correlated to the normalised toroidal beta $\beta_n = \beta_\phi / (I_p(\text{MA})/a(\text{m})B_\phi(\text{T}))$. It should be noted that the β values are typically 10% lower for the discharges analysed by TRANSP (based on the kinetic plasma pressure) than those used in this paper, which are obtained by equilibrium code calculations based on magnetic measurements. The ratio of H/q [Perkins], shown in fig. 1, is not very sensitive on the beta value, demonstrating that there is no gradual

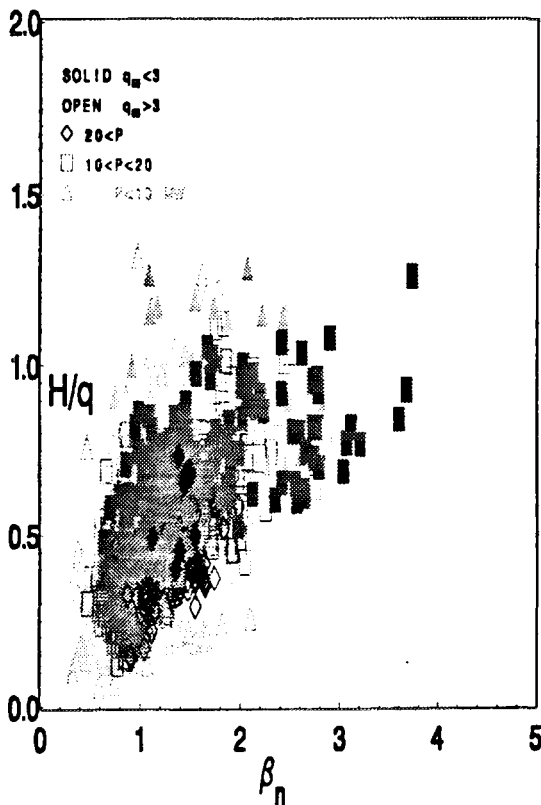


Fig. 1 H/q versus β_n for $P < 10$, $10 < P < 20$, and $P > 20$ MW.

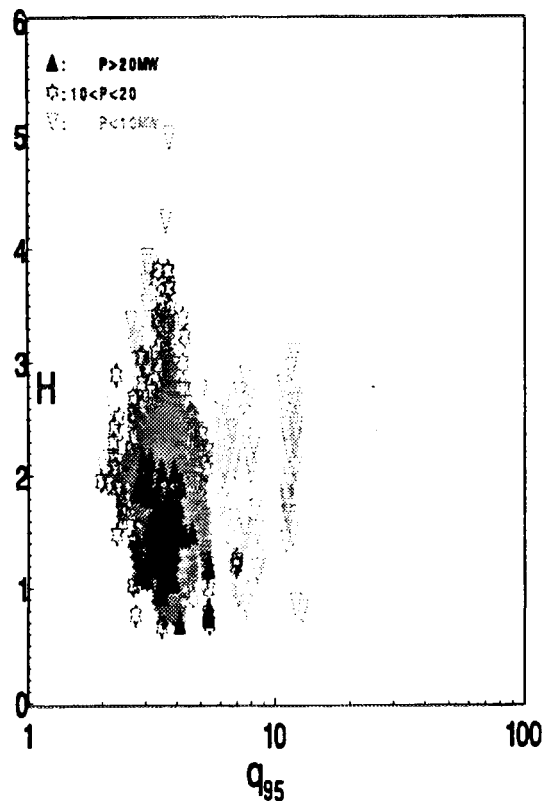


Fig. 2 The H-mode multiplier versus q_{95} on logarithmic scales for P .

deterioration of the confinement with beta. The ratio does not depend on q_{95} or on the heating scheme applied (NBI, ICRH or combined heating).

Confinement and edge safety value q . At low values of q_{95} the confinement multiplier H however is deteriorating rapidly (fig.2) with H/q remaining roughly constant, similar to what has been observed by DIII-D [Lazarus]. The best values of H of ≈ 4.5 have been obtained at $q_{95} \approx 4$, at low $q_{95} > 2$ the H -multiplier found is again close to 2 and at high q the best values are again close to 2. There appears also a power dependence: the highest H values have been obtained at powers less than 10 MW. At power levels up to 20 MW very similar values have been reached, however with powers between 20 and 30 MW the best H -multiplier values are ≈ 2.2 . The vast majority (75%) of these discharges are however limiter plasmas with only a small number of shots in an X-point configuration.

Fusion performance relation to beta values. The best fusion performance as measured by the DD-reaction rate has been obtained in high pressure or high beta discharges. This can be seen in fig. 3, which shows the square root of the DD-reaction rate R_{DD} ($2 \cdot R_n$, the DD neutron rate) as a function of the average measured plasma pressure from the equilibrium code calculations. The best performance can be described by the scaling:

$R_{DD} (10^{16} s^{-1}) \approx (1/60) \beta_{\phi}^2 B_{\phi}^4$. In the ion temperature range at JET the thermal DD-fusion rate is roughly proportional to $n_i^2 T_i^2$ and the (temperature dependent) beam-thermal reactivity is comparable to the thermal fusion rate.

Performance Limitation. The duration of the good confinement period of a discharge in JET has been measured with the diamagnetic loops and can be expressed by a quantity $\Delta t(80\%)$, which is the time span the plasma energy is over 80% of its peak value. Fig. 4 gives $\Delta t(80\%)$

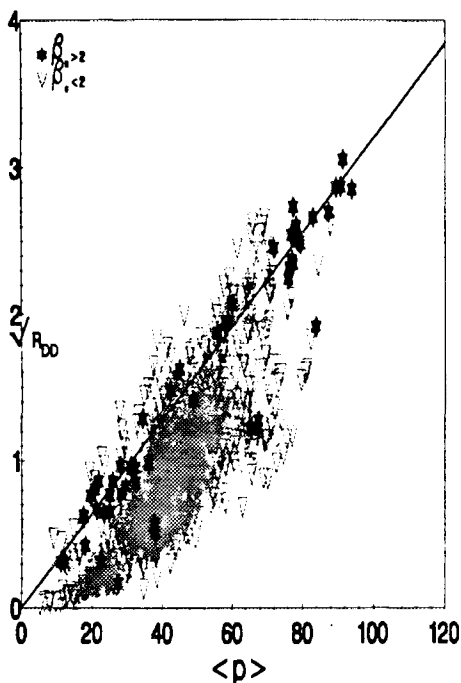


Fig. 3 $\sqrt{R_{DD}}$ ($10^{16} s^{-1}$) versus $\langle p \rangle$ for D plasmas with ICRH and D- NBI for $\beta_n > 1$.

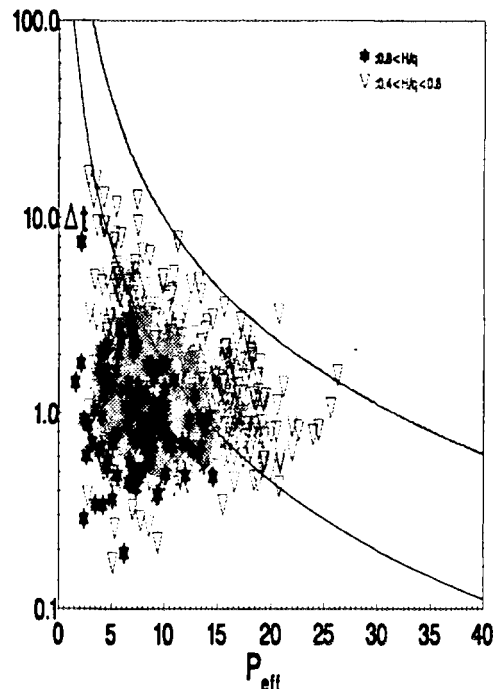


Fig. 4 $\Delta t(80\%)$ versus P_{eff} . The top curve corresponds to target plates T of 2500 °C. The lower curve, an upper bound for high confinement shots, corresponds to a T of 1100 °C.

as a function of $P_{\text{eff}}=P_{\text{in}}-dW/dt$. The limiting curve is given by $\Delta t(s) = 1000/P(\text{MW})^2$, corresponding to a temperature of the target tile area of around ≈ 2500 °C [Wesson], [Jäckel]. It can be seen from the figure that the high performance discharges with $H(\text{ITER89P})/q_{95} > 0.8$ have much reduced performance duration. The reduction of the period of good confinement is related to the X-event, which in a very short time increases the effective power loss from the plasma to the target plates [Jaekel].

MHD Stability of VH mode discharges. No global MHD stability limit (for ballooning and external kink modes) is reached in VH mode discharges. The β obtained in the VH modes, where $\beta_N \sim 2.6$, is well below the theoretical global limit set by ballooning modes (at $\beta_N \sim 3.5$). Local instabilities near the edge of the plasma driven by the large pressure gradient and the associated bootstrap current could however end the VH mode confinement. In this section we discuss the stability of ballooning modes, the second stability region and the stability of the external $n=1$ kink mode. The internal kink is discussed by [Alper]. For three different JET plasma shapes the access to second stability is calculated as a function of the edge current density; the shapes are that of the JET high performance discharge 26087

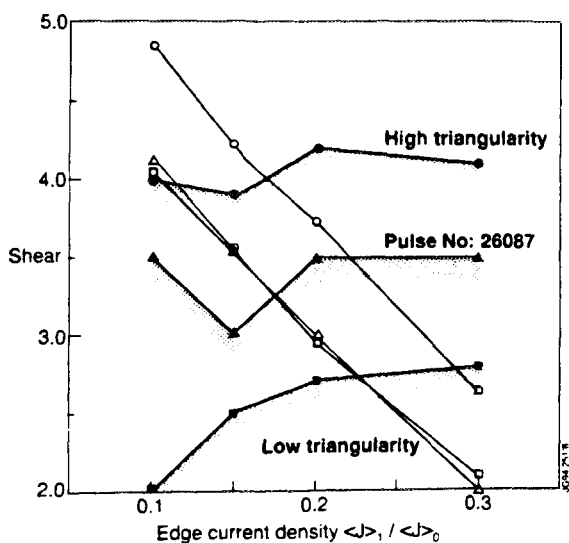


Fig. 5 The bold curves show the maximum shear below which the plasma is in the 2nd stability region (at $\psi=0.95$). The thin lines with the corresponding markers show the shear of the equilibria as a function of the edge current density (normalised to the central current density).

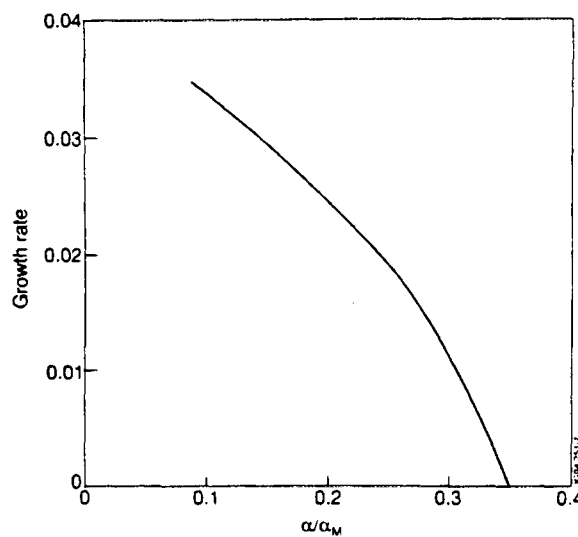


Fig. 6 The growth rate of the external kink as a function of the edge pressure gradient. The pressure gradient is normalised to the pressure gradient α_M which is marginally stable to ballooning modes (at the first stability limit with zero edge current density).

$\delta=0.33$), and for two other single X-point plasma configurations one with a small ($\delta=0.13$) and one with a large triangularity ($\delta=0.42$). The relevant plasma parameters match the values of the JET high performance discharge 26087. Fig.5 shows the result for the three cases. The relative edge current density $\langle J \rangle_1 / \langle J \rangle_0$ needed to get into second stability is about 0.17 for the old JET shape (nearly up/down symmetric) and high triangularity case. For the low triangularity in the new JET configuration a slightly higher relative edge current of 0.23 is required.

The stability of the external $n=1$ kink mode for these equilibria is calculated using the CASTOR code [Kerner]. The stability of the external $n=1$ kink mode is found to depend strongly on the edge pressure gradient. The growth rate of the $n=1$ kink mode as a function of the edge pressure gradient is shown in fig.6. The $n=1$ kink mode is stable for pressure gradients larger than 0.35 of the ballooning limit, the experimental value of α/α_M is typically around 1. Thus, the region of second stability can be reached without the $n=1$ kink mode becoming unstable but it does need the stabilising effect of the edge pressure gradient. This stabilising effect is due to the favourable average curvature in toroidal geometry.

Conclusions. High confinement regimes have been obtained at a variety of q values at various β_n . Confinement enhancement over ITER89-P seems to degrade with decreasing q while H/q remains roughly constant, an optimum is obtained at q values around 3.5 with an H factor of ≈ 4.5 . The fusion performance is roughly proportional to the plasma average pressure squared. This relationship favours for a given beta limit high toroidal field operation to getting high fusion performance. The good performance duration in the best cases, for moderate H/q values, seems to be set by simple tile heating to temperatures around 2500 °C, in the high performance this limitation is provoked earlier by the vast power load of the X-events. The MHD stability study of the high performance VH-modes has shown that the combination of high enough pressure gradient and current density at the plasma edge allows this region to become in the 2-nd stable ballooning region and be stable to the $n=1$ external kink.

References.

- [Alper] B. Alper et al, this conference.
- [Jaekel] H. Jaekel et al, 1993 EPS Conf. on Contr. Fusion and Plasma Physics, Lisboa.
- [Kerner] W. Kerner et al., Proc. EPS Berlin, (1991), part IV, p89-93.
- [Lazarus] E. Lazarus et al, 35th APS Annual Meeting, St. Louis, USA, 1993.
- [Perkins] F. Perkins, private communication, March 1994.
- [Wesson] J. Wesson, private communication, 25 March 1992.



FR9701753

Impurity Induced Neutralization of MeV Energy Protons in JET Plasmas

A A Korotkov¹, A Gondhalekar.

JET Joint Undertaking, Abingdon, Oxon, OX14 3EA.

¹ A F Ioffe Institute, St. Petersburg, Russia.



ABSTRACT

This paper presents a model elucidating the role of carbon and beryllium, the main impurities in JET plasmas, in neutralizing MeV energy protons. Such protons arise during ion cyclotron resonance frequency (ICRF) heating of deuterium plasmas in the hydrogen minority heating mode D(H), and from D-D fusion reactions. The model establishes charge transfer from hydrogen-like[H] impurity ions to protons as the main process for neutralization. Calculations for deducing the proton energy distribution function $f(E_p)$ from measured hydrogen flux are described. The validity of this model of Impurity Induced Neutralization(IIN) is tested by using it to describe the measured flux in different conditions of plasma heating and fueling. Using this model, and an experimental procedure in which a known change in the density of deuterium atoms at the plasma center is made by applying neutral beam injection(NBI), we have deduced the background thermal deuterium atom density at the plasma center, which is an important new diagnostic result. A full account of the subject of this paper is given in [1].

1. INTRODUCTION: One of the first observations made with the new NPA on JET to measure the distribution of ICRF driven MeV energy protons was that of unexpectedly efficient neutralization of such protons in the plasma center, without recourse to injection of donors for charge-exchange(CX) reactions. We called this "passive" flux. Flux arising when ICRF and NBI were applied together was called "active" flux. The experimental set-up and instrument details are given in [2]. Measurements of "passive" and "active" fluxes are shown in fig.1. Subsequent to [2] the NPA was recalibrated; the corrected data shown here supersedes that in [2]. Before neutralized ICRF driven protons were measured in JET plasma only radiative recombination of protons and electrons, and CX between protons and atoms were considered amongst processes that would cause this flux. The expectation, contrary to fig.1, was of a flux of MeV hydrogen to the NPA arising only upon application of atomic beams to the plasma in the form of NBI from octant 4. Fig.2 shows $\Gamma_H(E)$, energy distributions of the "passive" and "active" hydrogen fluxes.

2. IMPURITY IONS PLAY A KEY ROLE IN NEUTRALIZING MeV PROTONS: From these measurements, we need to account for (i) existence of the "passive" flux, (ii) the "active" flux showing a uniform and energy independent increase over the "passive" when NBI is applied, (iii) in other pulses with D(H) ICRF heating a similar flux, approximately equal to the "active" flux, measured when NBI was applied only at oct.8 on the opposite side of the torus from the NPA. Such observations indicate that the "active" flux is not entirely due to direct CX of protons with NBI atoms at oct.4, and that the main effect of NBI into the plasma is to amplify the process giving rise to the "passive" flux. We show that the flux is, in most part, due to CX between [H] impurity ions and protons. Two key circumstances determine that IIN plays a predominant role in JET plasmas. They are:

2.1. BIG CROSS-SECTIONS FOR CX BETWEEN PROTONS AND [H] IMPURITY IONS: Cross sections for CX between protons and [H] ions of He, Be and C have not been measured. Therefore we have compiled them from best available theoretical calculations. Only CX from ground state of the ions is important for our

considerations. The energy range of interest here, $0.3 \leq E_p(\text{MeV}) \leq 3$, is wide and extends into the high energy Born range ($v \gg Z$). In the vicinity of cross-section maximum ($v \approx Z/\sqrt{2}$) we use results of [3]. In the high energy range ($v > Z$) we employ calculations of [4,5,6]. Our analysis [1] of cross-sections shows that [H] ions of He, Be and C have larger cross-section for CX with protons in the energy range under consideration than background thermal deuterium atoms or beam atoms do. Also the estimated accuracy of cross-sections is enough to accurately determine $f(E_p)$ and the proton tail temperature T_p , for $T_p \leq 0.3$ MeV.

2.2. LARGE DENSITY OF IMPURITY DONOR IONS AT THE PLASMA CENTER: At the core of JET plasmas the densities of [H] ions of He, Be and C are comparable to that of beam atoms. We have developed a model for calculating the density of [H] and [He] donors of He, Be and C arising from presence in the plasma of beam (n_b), halo (n_h), background thermal deuterium (n_d) atoms and impurity nuclei (n_z). We compute impurity donor densities using a system of steady-state ion balance equations for bare, [H] and [He] impurity ions. Equation for density of impurity nuclei n_z and of [H] impurity ions n_{z-1} , which are much more abundant than [He] impurity ions, is:

$$I_{z-1} n_{z-1} n_e = n_z \cdot \left\{ 1/\tau_z + \alpha_z n_e + \beta_z n_d + (\langle \sigma v \rangle_{cx_z}^b n_b \gamma_b + \beta_z n_h \gamma_h)_{\text{oct.4}} + (\langle \sigma v \rangle_{cx_z}^b n_b \gamma_b + \beta_z n_h \gamma_h)_{\text{oct.8}} \right\} \quad \text{eq.1}$$

The rate coefficients are: I for ionization of ions by electrons, α for radiative recombination of ions, β for CX of ions with thermal deuterium atoms, $\langle \sigma v \rangle_{cx_z}^b$ for CX between impurity nuclei and beam atoms, and β_z for CX between impurity nuclei and halo atoms. γ_b and γ_h are factors describing coupling of ionization balance between oct.4 and oct.8 during NBI. Except for the unknown n_{z-1} , all parameters in eq.1 are usually well defined. n_z is measured using charge-exchange resonance spectroscopy [7], τ_z is measured variously [8] but here its effect is weak because of observed slow ion transport in the core of JET for most plasma modes. n_d is determined from a comparison of "active" and "passive" hydrogen fluxes. Fig.3 shows deduced densities of the different donors at the center of plasma for the pulse.

2.3. TOTAL PROTON NEUTRALIZATION PROBABILITY: P_ν , the total neutralization probability for the protons, is sum of different individual contributions.

$$P_\nu = \langle \sigma v \rangle_{cx_b} \cdot n_b + \langle \sigma v \rangle_{cx_d} \cdot n_d + \langle \sigma v \rangle_{cx_h} \cdot n_h + \sum_q \langle \sigma v \rangle_{cx_q} \cdot n_q + \langle \sigma v \rangle_r \cdot n_e \quad \text{eq.2}$$

$\langle \sigma v \rangle_{cx_{b,d,h,q}}$ are rate coefficients for CX between protons and beam atoms, thermal deuterium atoms, halo atoms, and impurity ions respectively, $\langle \sigma v \rangle_r$ is the radiative recombination rate coefficient. $n_{e,b,d,h,q}$ are densities of electrons, beam atoms, thermal deuterium atoms, halo atoms, and density of [H] and [He] ions of impurities involved, represented by n_q . Fig.4 shows contributions to total P_ν , due to different donors present in the plasma.

3. INFERENCE OF ENERGY DISTRIBUTION $f(E_p)$ OF ICRF DRIVEN PROTONS: Then, from the measured fluxes, $f(E_p)$ in the NPA solid angle is inferred thus

$$f(E_1) \cdot P_\nu(E_1) \cdot \gamma(E_1) \cdot S \cdot \Delta E_1 \cdot \mu(E_1) = \{ N(E_1) - N_b(E_1) \} \quad \text{eq.3}$$

Although here $f(E_p)$ is integrated along the line-of-sight the active region has an extent of only $\pm 0.3\text{m}$ about the center [1]. $i=1, \dots, 8$ is the NPA channel number, γ is plasma transparency for the neutralized protons, S is area viewed by the NPA in the observation volume at the plasma mid-plane, ΔE_1 is energy width of each channel, μ is channel detection efficiency, $N(E_1)$ is measured total count rate, and $N_b(E_1)$ is the background noise count rate. Two important applications of the methods discussed in the foregoing are:

3.1. DETERMINATION OF THERMAL DEUTERIUM ATOM DENSITY IN THE PLASMA CORE:

Fig.5 shows comparisons of minority proton energy distribution functions derived from "passive" and "active" fluxes at two close time points where $f(E_p)$ may be assumed constant. Iteration of the value of n_d is performed to obtain a best match of the two distribution functions and thereby the core thermal deuterium density is determined. Varying n_d changes the ratio of $f(E_p)$ derived from the "passive" and "active" fluxes without changing the shape of the distribution function. In fig.5 n_d is varied from $0.5 \times 10^{13} \text{m}^{-3}$ to $2.5 \times 10^{13} \text{m}^{-3}$, the best match is obtained for $n_d = 1.5 \times 10^{13} \text{m}^{-3}$.

3.2. ENERGY DISTRIBUTION AND TAIL TEMPERATURE IN HIGH POWER ICRF HEATING:

An early observation using the new NPA for study of high power ICRF heating was of saturation in energy distribution of measured hydrogen flux [9], and an implied saturation of tail temperature of the ICRF driven protons. Fig.6 shows the inferred ICRF driven $f(E_p)$ at different powers, determined from measured hydrogen flux, and the associated tail temperature T_p . Whereas $\Gamma_H(E)$ showed saturation for $P_{\text{ICRF}} \geq 6\text{MW}$, IIN modeling, using available measured time behaviour of n_2 , shows that this comes about due to reduction in impurity concentration during the measurement. In fig.6 $f(E_p)$ evolves as expected up to $P_{\text{ICRF}} = 10\text{MW}$. This emphasizes the importance of impurities and of IIN modeling developed here for interpretation of NPA data.

4. CONCLUSIONS:

1. Impurity Induced Neutralization(IIN) is the dominant neutralization process for MeV energy ICRF driven minority protons in JET plasmas. IIN modeling emphasizes the importance, for interpretation of the high energy NPA flux data, of properly taking into account impurity charge donor densities and the cross-sections for CX with protons.
2. IIN modeling allows inference of effective temperature T_p associated with the proton energy distribution function with good accuracy for $T_p \leq 0.3 \text{ MeV}$. Minority proton density is inferred with $\approx 50\%$ accuracy.
3. A method for determining thermal deuterium density in the core of JET plasmas is developed, based on comparison of "passive" and "active" fluxes. $n_d \approx 10^{13} \text{m}^{-3}$ can be determined with estimated accuracy of $\approx 40\%$.
4. Modeling of ITER plasma predicts that IIN will be a dominant process for neutralization of protons of $E_p \leq 1\text{MeV}$. Using a NPA similar to that used on JET "passive" measurement of ICRF driven protons in ITER will be feasible, without recourse to injection of atomic donors.

5. REFERENCES:

- [1]. A.A.Korotkov and A.Gondhalekar, JET Report, 1994, to be published.
- [2]. M.P.Petrov, et. al., Europhysics Conf. Abstracts, 16C(1992)II-1031.
- [3]. T.G.Winter, Physical Review A35(1987)3799.
- [4]. S.Mukherjee and N.C.Sil, Journal of Physics B13(1980)3421.
- [5]. K.Taulbjerg, R.O.Barrachina and J.H.Macek, Phys. Review A41(1990)207.
- [6]. T.G.Winter and S.G.Alston, Physical Review A45(1992)1562.
- [7]. A.Boileau, et.al., Nuclear Fusion 29(1989)1449.
- [8]. R.Giannella, et.al., Plasma Phys. and Controlled Fusion 34(1992)687.
- [9]. A.A.Khudoleev, et.al., Europhysics Conf. Abstracts, 16E(1992)117.

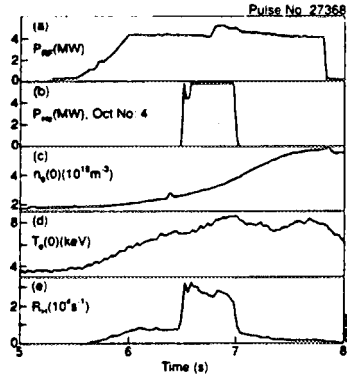


Figure 1

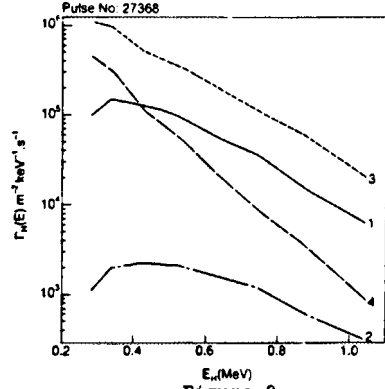


Figure 2

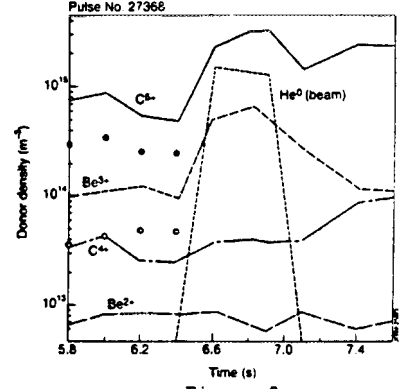


Figure 3

Figure 1-Observation of "passive" and "active" H flux in experiment in which a deuterium plasma with $I_p=3.5$ MA and $B_0=2.9$ T was heated with ≈ 6 MW of NBI power with 120 kV 4 He atoms from oct.4 and ≈ 5 MW ICRF power for D(H) heating. Traces show evolution of $n_e(0)$, $T_e(0)$, heating powers, and count rate R_H for 0.42 MeV H^0 flux received into the NPA. The "passive" flux arose with application of ICRF power, and independently of NBI. The "active" flux arose only when NBI and ICRF powers were applied together.

Figure 2-Energy distribution of hydrogen flux, $\Gamma_H(E)$, showing spectrum of: (1) measured "passive" flux at 6.4s, (2) "passive" flux if radiative recombination were its source, (3) measured "active" flux at 6.6s, (4) "active" flux if direct CX with beam atoms were its source. In [1] we deduce that neither CX with beam atoms, nor recombination with plasma or 'cold' beam electrons, are sufficient to give the observed large flux or its energy dependence.

Figure 3-Comparison of density of donors at the plasma center at oct.4. These consist of He^0 atoms from 5.8 MW of 120 kV beams, [H] and [He] ions of C and Be deduced using measured impurity nuclear densities and the ion balance model developed here. Impurity nuclear densities at $t=6.6$ s, measured using charge-exchange resonance spectroscopy[7], were: $n_{C,Be,He} (m^{-3}) = 10^{18}, 9 \times 10^{17},$ and 2×10^{18} .

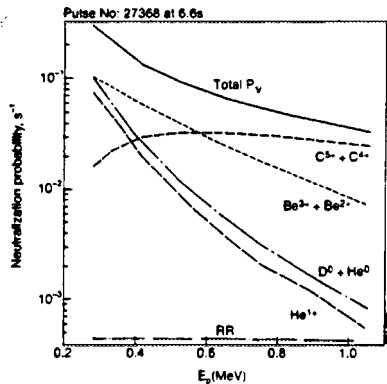


Figure 4

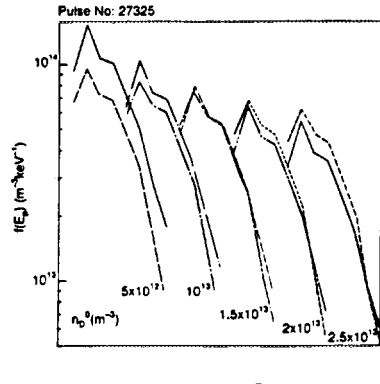


Figure 5

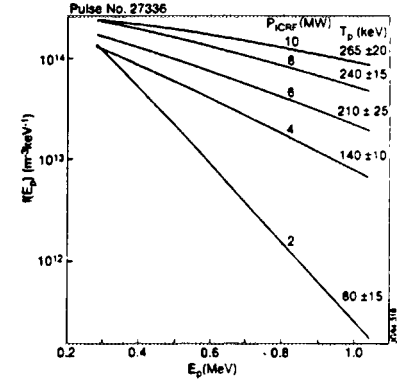


Figure 6

Figure 4- Total neutralization probability for protons is the sum over all donors, $P_v = \sum \langle \sigma v \rangle_{CX} \cdot n_{DO}$, showing contributions due to (1) C^{5+} and C^{4+} , (2) Be^{3+} and Be^{2+} , (3) He^{1+} , and (4) beam of atoms of He^0 from oct.4 and background thermal deuterium atoms D^0 , and (5) radiative recombination of electrons and protons(RR).

Figure 5- Proton energy distribution function inferred from "passive" and "active" fluxes at two close time points where $f(E_p)$ may be assumed constant. n_d was iterated to obtain agreement between $f(E_p)$ derived from the two fluxes. Five iterations of n_d are shown, the best match was obtained for $n_d = 1.5 \times 10^{23} m^{-3}$. Constant $\tau_z = 2.5$ s was used in the calculations. However, τ_z does not have much effect on the resulting best value of n_d , for $\tau_z \geq 0.5$ s.

Figure 6- Best fitting Stix-like energy distribution function for minority protons driven by ICRF, showing variation of $f(E_p)$ and associated tail temperature T_p with applied power. The experimental proton distribution function was inferred from hydrogen flux measurements described in [9].



FR9701754

Development of Thin Foil Faraday Collector as a Lost Alpha Particle Diagnostic for High Yield D-T Tokamak Fusion Plasmas

F E Cecil¹, P van Belle, O N Jarvis, G J Sadler.

JET Joint Undertaking, Abingdon, Oxon, OX14 3EA.

¹ Permanent address: Colorado School of Mines, Golden, USA.



Introduction

Alpha particle confinement is necessary for ignition of a D-T tokamak fusion plasma and for first wall protection. Due to high radiation backgrounds and temperatures, scintillators and semiconductor detectors may not be used to study alpha particles which are lost to the first wall during the D-T programs on JET and ITER. We are developing an alternative method of charged particle spectrometry capable of operation in these harsh environments

Description of proposed detector

The proposed lost alpha particle diagnostic consists of thin foils of electrically isolated conductors with the flux of alpha particles determined by the positive current flowing from the foils. By measuring the current from a stack of separated foils, the energy of the particles can be measured with a resolution limited by the range and range straggling of the particles in the foils. An example of one such device with three foils is pictured in Fig. 1.

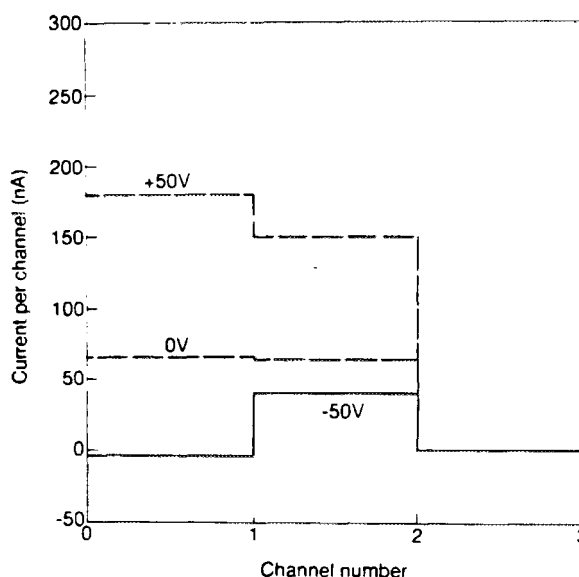
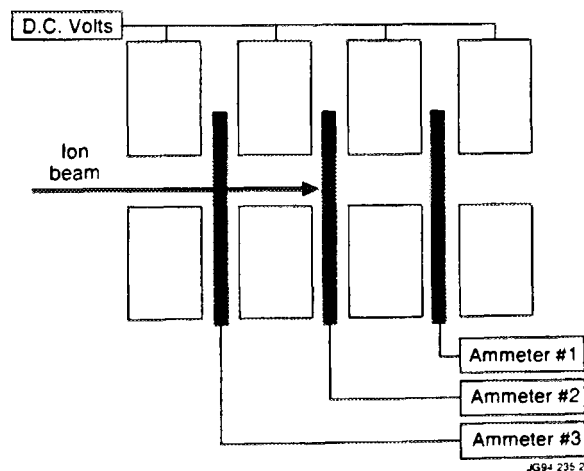


Figure 1. Three foil device with thick intermediate plates for the suppression of the secondary electrons

Figure 2. Currents from three foil device exposed to 50 nA of 1.2 MeV proton beam for -50V, 0V and +50V on the intermediate plates. The foil diameters and separations are 12 mm.

If each of the foils in this device were 10μ in thickness, then normally incident alpha particles with energies between 0 and 2.8 MeV, between 2.8 and 4.7 MeV, and between 4.7 and 6.2 MeV will stop in the first, second and third foils respectively with range straggling varying between 0.2 to 0.4μ . The device will serve as a multi-channel spectrometer if the secondary electrons emitted by the ions as they pass through or stop in the foils are suppressed by the intermediate plates. This suppression was demonstrated by bombarding the device with collimated beams of protons from the Univ. of Birmingham (U.K.) dynamitron accelerator. The beam was centred on, and perpendicular to the plane of, the foil. The results with the 1.2 MeV protons, in which the beam stops in the second foil, are indicated in Fig. 2. As expected, for a small negative bias ($\approx 50V$) the secondary electrons are successfully suppressed while for positive bias the current of secondary electrons from the foils are measured. Consequently, the larger currents measured with a positive bias, together with a large area foil, may allow the device to be used under circumstances such as the near term JET program, where the flux of particles is considerably less than in the case of the D-T plasmas on JET. The behaviour of the device in the presence of strong magnetic fields was modelled and we found that the secondary electrons are effectively suppressed in an external magnetic field of magnitude 3T. The time resolution of the device will be limited by the RC time constant of the equivalent circuit consisting (primarily) of the capacitance of the foils and cable and of the input resistance of the digitiser. The dominant capacitance will be in the long signal cables where a capacitance of $10^{-8}F$ might be encountered. Coupled to a digitiser with an input impedance of $10 K\Omega$ we would thus expect a time resolution of about $100 \mu s$.

Expected signal

We have estimated the alpha particle currents at the first wall for D-T operation on JET. We have chosen a baseline case of a D-T fusion plasma producing 10^{19} D-T reactions per second. Using the particle following code ORBIT, we have modelled the behaviour of 3.6 MeV alpha particles randomly launched from the plasma. We have found that, for particles launched at minor radii in excess of about 40 cm., there is a significant probability of the particle striking the JET first wall during the course of their first classical banana orbit. By folding these probabilities with the measured neutron profiles of the JET preliminary tritium experiment [1], we estimate that about 3% of the total yield of alpha particles will strike, and be distributed evenly over, the lower half of the outer portion of the JET first wall. corresponding to an alpha particle flux of $6 \times 10^{11} \text{ cm}^{-2}\text{-s}^{-1}$, or a measured current of about $200 \text{ nA}\text{-cm}^2$. Anomalous loss mechanisms such as stochastic ripple losses, TAE modes etc. will increase the signal above the ambient levels. For an ITER D-T plasma generating a first wall flux of about $2 \times 10^{14} \text{ 14 MeV neutrons cm}^{-2} \text{ s}^{-1}$, we would estimate a flux of lost alpha particles of about $6 \times 10^{12} \text{ cm}^{-2} \text{ s}^{-1}$ or $2 \mu\text{A}\text{-cm}^{-2}$ if we assume the same loss fraction of 3% as was predicted for JET. The currents from such a device with an active area of a few cm^2

will thus be comparable to or larger than the current signals from many tokamak diagnostic devices and hence should be easily measurable as long as the radiation induced background signals are small compared to the current from the alpha particle fluxes.

Background

For the proposed device located at the JET first wall, the flux of 14 MeV neutrons and energetic gamma rays (up to about 10 MeV) during the baseline example shot assumed above will each be about $5 \times 10^{12} \text{ cm}^{-2}\text{-s}^{-1}$. The only significant sources of current from a foil will be the negative current resulting from (n,p) and (n, α) reactions (for the neutrons) in the foil in which the positively charged reaction products leave the foil, the positive current from the same reaction products in the walls of the cavity which stop in the foil and the corresponding currents (of opposite signs) from the Compton scattering of the gamma rays in the foils and walls. For $10\mu\text{ Al}$ foil, the yields for these reactions correspond to a total current of $-0.015 \text{ nA}\text{-cm}^2$ for the neutron induced reactions and $+0.005 \text{ nA}\text{-cm}^2$ for the gamma ray induced reactions in the foil. The foil currents due to the reactions in the walls will be comparable in magnitude and opposite in sign from the currents due reaction products from the foil. As noted above, the neutron fluxes at the ITER first wall will be about $10^{14} \text{ neutron}\text{-cm}^{-2}\text{-s}^{-1}$ and hence the backgrounds calculated above will be on the order of $1 \text{ nA}\text{-cm}^{-2}$; again well below the minimum estimated alpha particle current of $2 \mu\text{A}\text{-cm}^{-2}$.

On JET under conditions comparable to those used in estimating the alpha particle flux at the first wall, we would expect a of flux of roughly $10^{14} \text{ X-rays cm}^{-2}\text{-s}^{-1}$ at an average energy of about 5 keV. If the thin foils in the proposed device were directly exposed to this flux of X-rays, then the photoelectric reactions in the foil would result in a positive current from the foil of about $30 \text{ nA}\text{-cm}^{-2}$. However, the induced current from the X-ray flux can be greatly reduced by mounting the device in an open ended box oriented to admit tangential escaping alpha particles while shielding the device from the direct flux of X-rays.

The main heat load on the foils in the proposed device will be the heat deposited by the alpha particle flux. We have modelled this heat transport problem assuming the edges of the foil are clamped to the JET first wall temperature of 600°K and found that for a $1 \text{ cm} \times 1 \text{ cm} \times 10\mu\text{ Al}$ foil, exposed to a $1 \mu\text{Amp}\text{-cm}^{-2}$ flux of 3.5 MeV alpha particles, the foil comes to an equilibrium temperature of about 720°K in about 300 msec.

The currents from the foils due to the alpha particles must be measured in a potentially noisy electrical environment. The graphite probes which were installed near the edge of the plasma on Tore Supre successfully measured fast-ion losses at the 10 - 100 nA levels [2]. We have installed prototypes devices consisting of single Al foils of area 20 cm^2 and thickness 6μ in partially enclosed, grounded, conducting containers near (about 4 m) the vacuum vessels on TFTR (see Fig. 3) and JET. We found in both cases the noise from the foil corresponded to a few nA, much less than the signal if the foil were exposed to a current of $100 \text{ nA}\text{-cm}^{-2}$.

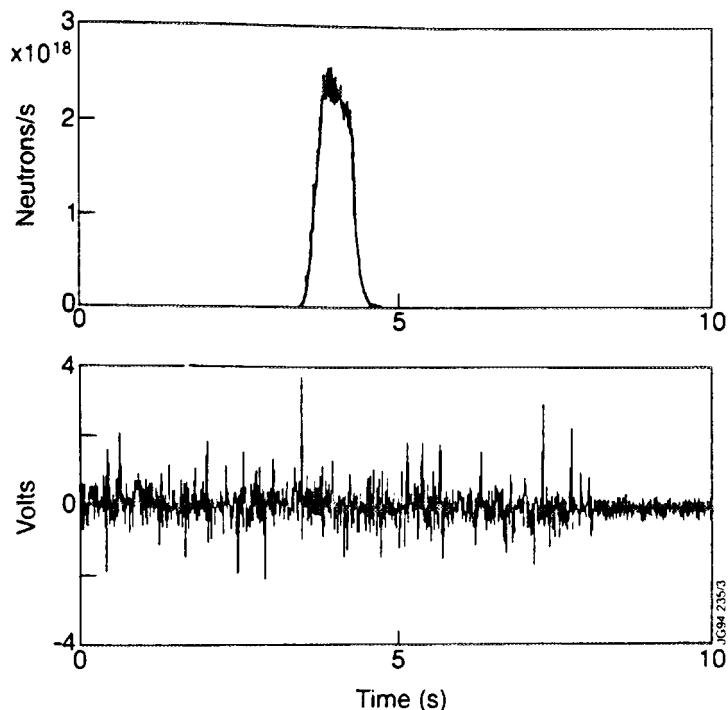


Figure 3. Comparison of digitised current from test foil outside TFTR during and after a recent high yield D-T shot (lower trace) with the neutron source strength (upper trace). If the foil had been exposed to a current of 100 nA/cm^2 , the digitised signal would be about 2 V

Conclusions

The proposed device offers the possibility of measuring the flux of escaping alpha particles from JET during its D-T phase and ITER in its technology phase. Use of a large area version with *positive* bias on the intermediate electron suppression plates offers the possibility of measuring escaping fast ions on JET in the near term program in which reaction rates in the range $10^{16} - 10^{17} \text{ sec}^{-1}$ are expected. We are continuing evaluation of this concept in an effort to determine the optimum design and operating parameters. We expect to install one or more of these devices during the JET opening presently scheduled for mid 1995.

We would like to thank Richard Gill for several useful discussions and Lindsay Earwacker and the Univ. of Birmingham radiation centre operating staff, and Sid Medley, Lane Roquemore and Stewart Zweben at PPPL. This work was supported in part by the U.S. Department of Energy.

References

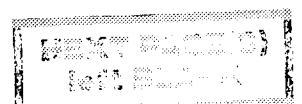
1. F.B. Marcus et al., "Neutron profile measurements during first tritium experiments on JET", Nucl. Fusion **33** (1993) 1325.
2. V. Basiuk, A. Becoulet, T. Hutter, G. Martin and B. Saoutic, "Energy measurements of fast ions trapped in the toroidal field ripple of Tore Supra" in "IAEA Technical Committee Meeting on alpha particles in fusion research" Trieste, Italy. May 10-14, 1993 (1993) 89.



15-MeV Proton Emission from ICRF-Heated Plasmas

O N Jarvis, S W Conroy, M Hone, G J Sadler, P van Belle.

JET Joint Undertaking, Abingdon, Oxon, OX14 3EA.



ABSTRACT

^3He -d fusion reaction protons emitted from ICRF-heated discharges were recorded with a silicon diode detector installed in the Joint European Torus (JET). The detection rates demonstrated that sawtooth crashes eject fast particles from the inner region of the plasma. The energy spectra of the fusion product protons using H minority provided evidence for the second harmonic acceleration of deuterons at sub-MW levels of RF power and those with ^3He minority did not possess the expected twin-lobed shape predicted by kinematics calculations.

INTRODUCTION

A study of 15 MeV proton emission from ^3He -d reactions was carried out in order to obtain information on the performance of ICRF heating using ^3He and H minority ions. A wall-mounted silicon diode detector (2 mm thick) was used to record the prompt loss charged fusion product protons. The following production routes must be distinguished: ^3He - d thermal reactions; burn-up reactions in which the 0.8 MeV $^3\text{He}'$ fusion product ions from $\text{d} + \text{d} \rightarrow ^3\text{He}'(0.82\text{MeV}) + \text{n}(2.45\text{MeV})$ reactions suffer $^3\text{He}' + \text{d} \rightarrow ^4\text{He}(3.71\text{MeV}) + \text{p}(14.64\text{MeV})$ reactions whilst slowing down in the plasma; and non-thermal reactions between fast ^3He ions generated by ICRF heating and bulk deuterium ions (and *vice versa*).

THE PROTON DETECTORS

A probe containing a water-cooled detector was installed in an upper port of the JET vacuum vessel with its lower end above the outermost closed flux surface. The prototype probe (KP1) was commissioned in April 1985 but survived only two months due to irradiation damage. An improved probe (KP2), commissioned in September 1987, survived until March 1988. Many of the observations made with KP1 were puzzling, with only the main result - the expulsion of fast particles from the central region of the plasma by the action of the sawtooth crash - being unequivocal [1,2]. The outstanding problems were resolved with KP2.

IDEAL PROTON ENERGY SPECTRA

The relativistic, two-particle, kinematics code FPS [3] was used to compute proton energy spectra for specified ion energy and pitch-angle distributions for both of the reacting particles. The proton energy spectra in fig. 1 were computed for the following situations:

- (i) thermal $\text{d}-^3\text{He}$ reactions for $T_i = T_e = 5$ keV.
- (ii) burnup of the isotropic 0.8 MeV $^3\text{He}'$ ions in $^3\text{He}' + \text{d} \rightarrow ^4\text{He} + \text{p}$ reactions.

- (iii) fusion reactions initiated by RF-heated ^3He ions. For RF-heating simulations, an approximation to the formulation of Stix [4] was used, with the fast ion tail temperature determining v_{\perp} and the background temperature determining v_{\parallel} .

The two-lobed energy spectrum corresponding to calculation (iii) was not observed, although it had been by Heidbrink [5] on PLT. The inability of the calculations to reproduce the JET results is believed to lie in the adoption of the 1-D Maxwellian to represent the fast ion energy tail. Stix [4] provided solutions for two extreme cases, the fast ion distribution being a simple function of either v (isotropic) or v_{\perp} (anisotropic). For the latter case, usually adopted for RF heating, the distribution function possesses an exponent with two factors, F_1 and F_2 , the first of which is simply $-E/T_{tail}$, with $T_{tail} = T_e(1 + 3\xi/2)$, where ξ is determined by the local value of the RF power density. It is customary to set $F_2 = 1$. This underestimates the strength of the population at low energies. Moreover, the lower energy ion distributions will become isotropic as a result of pitch-angle scattering. Stix quotes the energy above which electron drag is more important than pitch-angle scattering as $E_{crit} = 14.8 \cdot T_e \cdot \{2 \cdot A^{1/2} \cdot Z_{eff}\}^{2/3}$. As a rough guide, we assume that E_{crit} divides the complete distribution into two parts: the higher energy part being strongly anisotropic, and the lower energy part fully isotropic. The shape of the fusion product proton energy spectrum now depends on T_{tail} and E_{crit} .

The contribution from the isotropic part of the fast ion distribution is readily calculated. The example presented in fig. 2 is for fundamental frequency heating of ^3He ions in a deuterium plasma with $T_e = 4$ keV, $T_i = 3$ keV, $\xi = 30$ ($T_{tail} = 200$ keV), $Z_{eff} = 3.3$ and $E_{crit} = 330$ keV. 50% of the total reactivity lies below E_{crit} , falling to 20% when F_2 is set to unity.

PROTON DETECTION EFFICIENCY

All detected protons must pass through a collimator in front of the detector. An orbit following code was employed to calculate the flux recorded from the integral $Flux = \frac{1}{4\pi} \int_0^A dA \int_0^{4\pi} \cos\theta d\Omega \int_0^{\infty} S(l) dl$, where A gives the area of the detector, θ is the angle of incidence of the proton to the normal at the detector face, S is the proton source strength and l gives the orbit path length. The proton source strength was assumed to possess an isotropic birth distribution and to be constant over the volume defined by neighbouring flux surfaces. Fig. 3 shows that a 3.0 T/2.7 MA plasma imposes a sharp cut-off at about 3.50 m and an extreme sensitivity to proton energy that is unique to this particular set of conditions.

SUMMARY OF OBSERVATIONS

1. RF heating, tuned to hydrogen, is effective at accelerating deuterons even at the lowest power levels (see fig. 4). As a result, the anticipated signature of ^3He burnup reactions was never recorded during RF(H) heating because of the residual presence of ^3He in the plasmas.

2. RF-accelerated ions are ejected from the inner region of the plasma by the action of full sawtooth crashes, but not by partial crashes (see fig. 5). Due to the short slowing down time of these ions, bursts of prompt loss protons are recorded coincident with the crashes.
3. Once the energy dependence of the detection efficiency is taken into account, the proton energy spectra from RF heating of deuterons and of ^3He ions are well centred and nearly gaussian in shape, regardless of whether the detector views the plasma region within the $q=1$ radius or outside it (in which case the spectrum corresponds to the spikes following the sawtooth crashes, see fig. 6). The incorrect prediction (fig. 1) of the two-lobed form for the energy spectra obtained at JET is understood to be a result of using a fast ion distribution function that neglects pitch-angle scattering effects. The apparent contradiction between the present results and those obtained by Heidbrink [5] arises from the fact that the PLT discharges were run in relatively clean plasmas (Z_{eff} near unity) at low plasma temperature (typically $T_e \approx 1.5$ keV and $T_i \approx 1.0$ keV), leading to $E_{\text{crit}} \approx 80$ keV. With $\xi \approx 30$, and the particularly low ion temperature, less than 4% of the total reaction rate is contributed by that portion of the fast particle distribution for which pitch-angle scattering is important.

REFERENCES

1. G.Sadler, P.van Belle, M.Hone, et al., Europhys. Conf. Abs., Vol. 10C, Part I (1987)105.
2. G.Martin, O.N.Jarvis, J.Kallne, et al., Physica Scripta T16 (1987)171.
3. P.van Belle and G.Sadler, in EUR 10797 EN, Vol.III (1987) 767.
4. T.H.Stix, Nuclear Fusion 15 (1975) 737.
5. W.W.Heidbrink, Nuclear Fusion 24 (1984) 636.

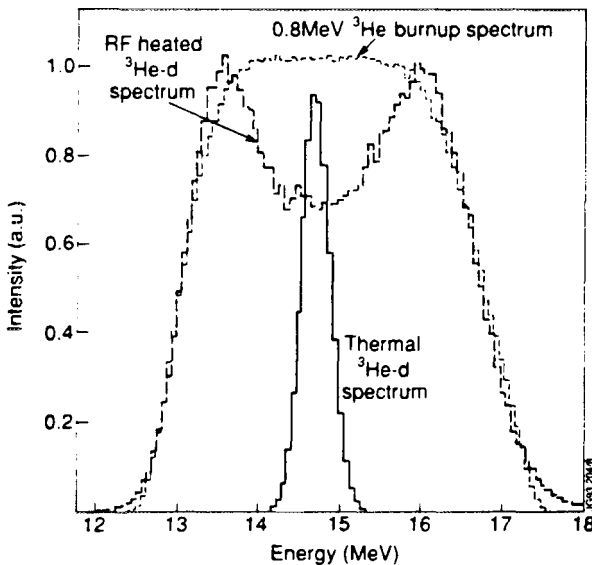


Fig. 1. Energy spectra corresponding to the three production routes discussed in the text.

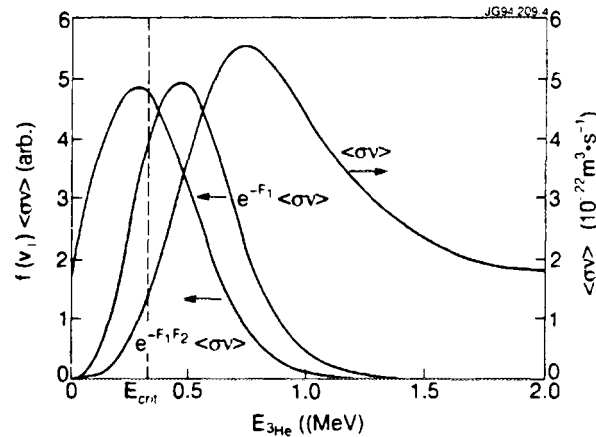


Fig. 2. Reactivity σv for fast ^3He particles in a deuterium plasma and reaction rates calculated using (i) the full Stix formula, (ii) as in (i) but with $F_2=1$.

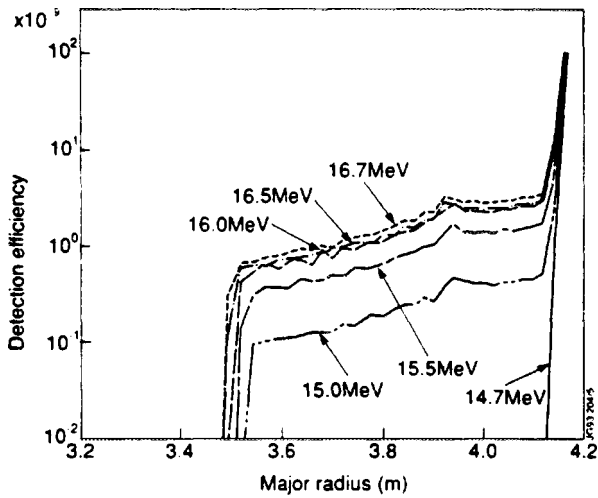


Fig. 3. Detection efficiency for protons as a function of minor radius (and energy). Discharge 5441; $B_T=3.0T$, $I_p=-2.7MA$.

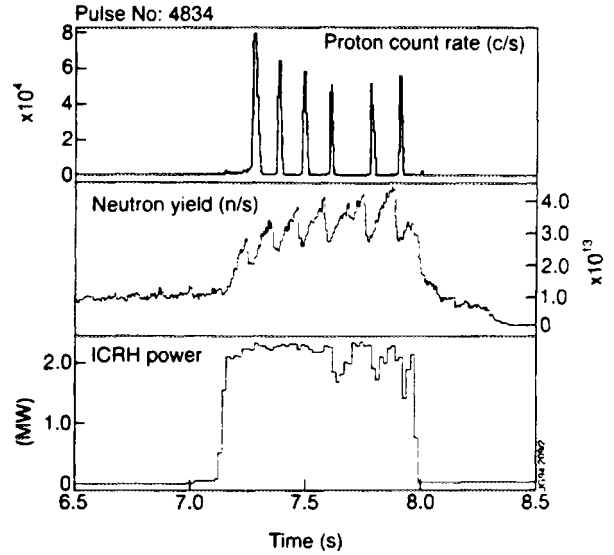


Fig. 5. Proton (upper), neutron (central) and ICRF power (lower) time-traces for RF(3He) heating. Pulse 4834; $B_T=3.4T$, $I_p=-2.8MA$.

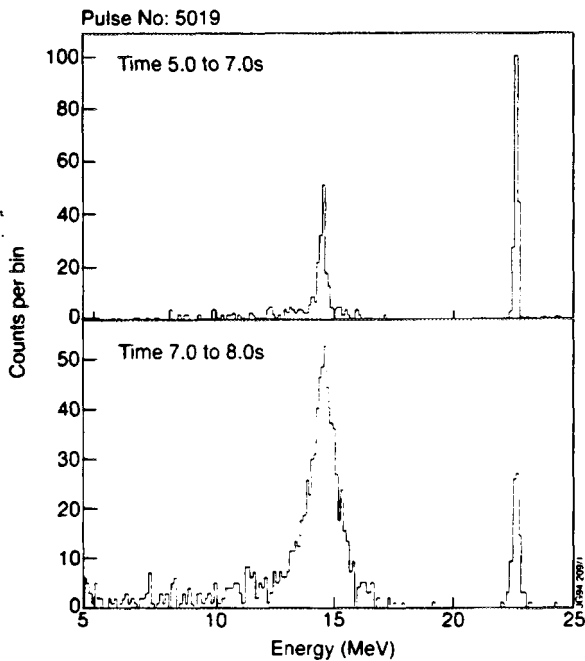


Fig. 4. Proton energy spectra. (Upper) Ohmic heating; thermal ^3He-d reactions only. (Lower) 0.5 MW ICRF(H) heating; the peak is too narrow for 0.8 MeV $^3He'$ burnup, and too broad for thermal reactions. RF-accelerated deuterons are clearly implicated. Discharge 5019; $B_T=2.0T$, $I_p=-2.2MA$

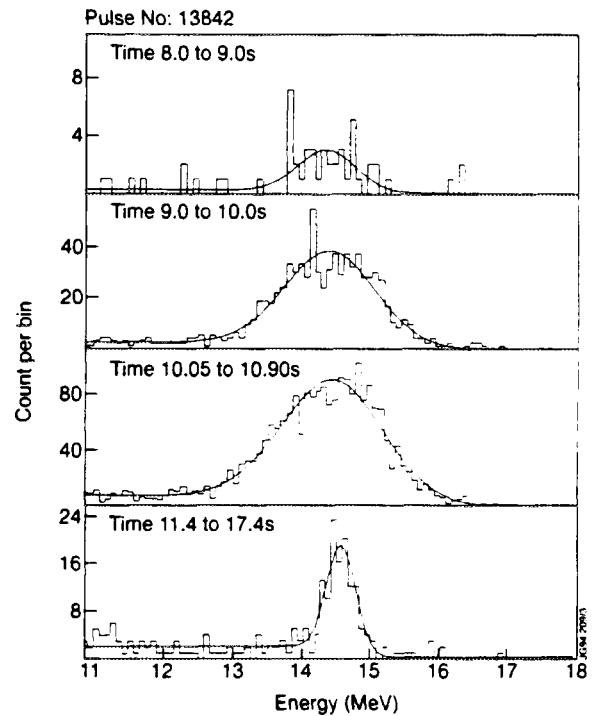


Fig. 6. Proton spectra corresponding to sawtooth spikes during RF(3He) heating with powers (top down) of 0.2, 0.6, 1.0 MW and ohmic only. The fitted curves are gaussians. Discharge 13842; $B_T=3.5T$, $I_p=-3.6MA$.



FR9701756

Pulse Compression Radar Reflectometry for Density Measurements on Fusion Plasmas

C Laviron¹, A Costley, P Millot², R Prentice.

JET Joint Undertaking, Abingdon, Oxon, OX14 3EA.

¹ Permanent address: C E Cadarache, DRFC/SPPF, St-Paul-lez-Durance, France.

² CERT/DERMO, Toulouse, France.



Introduction

On tokamaks and other toroidal machines devoted to fusion plasma experiments, reflectometry is a very rapidly developing technique for density profile measurements, particularly near the edge. Its principle relies on the total reflection of an electromagnetic wave at a cutoff layer, where the critical density is reached and the local refractive index goes to zero. The measurement of the phase difference between the incident and reflected waves give information about the position of the reflecting layer.

The different methods currently used for implementing the technique suffer serious limitations due mainly to three reasons:

- the characteristics of the the transmission waveguides vary with the frequency, the more so because the complexity of the line increases with length and number of bends.
- plasma fluctuations induce amplitude and phase variations over the duration of the measurement.
- the microwave sources currently used have non linearities and the frequency output is not perfectly reproducible.

With the new fast frequency synthesizers now available, a method based on pulse compression radar has been proposed for plasma reflectometry [1-2]. This method can, in principle, overcome the limitations stated above. The measurement can be made on a time-scale which is effectively very short relatively to the plasma fluctuations, and the very high reproducibility and stability of the source allows an absolute calibration of the waveguides to be made, which corrects for the effects of the parasitic reflections. It is a very powerful method when the transmission lines have to be long and/or complex (as for ITER) or when some plasma regions are difficult to access (as in the JET divertor).

Experimental setup

To study the efficiency of pulse compression radar, tests have been made at JET, on very long (55m) and complex (18 bends, mixing H- and E-plane) oversized (WG10 = S band) waveguides. To further degrade the configuration, only one antenna was used, the same waveguide line being used for transmission and reception, inducing many parasitic reflections over a total length of 110m with 36 bends. At the end of the waveguide, different configurations have been tested, from a simple open waveguide to a system made of taper and horn. The plasma was simulated by using a reflector facing the antenna at adjustable distances. Two extreme frequency bands relevant to reflectometry have been used in these tests: 26-40 and 75-110 GHz. The reflector gave

(*) Permanent address: CE Cadarache, DRFC/SPPF, 13108 Saint-Paul-lez-Durance, France

(**) CERT/DERMO, 2 avenue Edouard Belin, 31400 Toulouse, France

a signal typically 10 dB below those created by the numerous parasitic reflections. Therefore, with all these extreme characteristics, this setup would prevent the successful application of most other reflectometry methods.

important features of a given test included: type of reflector used, interface between the transmission line and the reflector (tapers and/or horns), frequency band and number of steps. Using a vector analyser (ABmm, model MVNA 8-350), measurements consisted of recording the amplitude and phase of the reflected signal for all the selected frequencies. For each configuration a set of measurements were made for the reflector placed in different positions and one with no reflector, this last measurement being used as the reference.

Two sets of measurements with the same parameters are necessary for the analysis: the reference without any reflector and one with the reflector at a given position. The first step consists of subtracting the two measurements (complex $Ae^{j\psi}$ for each frequency step) in order to remove the components due to the transmission line. Then, a Fourier transform calculation is applied to this complex signal to convert it to the time domain, using a window (Hamming or Kaiser-Bessel) and the zero padding technique to improve the accuracy.

Results

Figure 1 shows a typical example, for a mirror placed at 63.5cm from the horn aperture, in the band 33-34GHz, with 1MHz frequency steps. The horizontal axis is converted from the time delay to a distance by multiplication by the speed of light in vacuum. Fig.1(left) is the result obtained without calibration and fig.1(right) is after calibration. It can be seen that without calibration, the peak corresponding to the reflector (at about 110m) is 10dB below some parasitic reflections. This structure is exactly the same as the one which would be detected from a 1ns real pulse. After

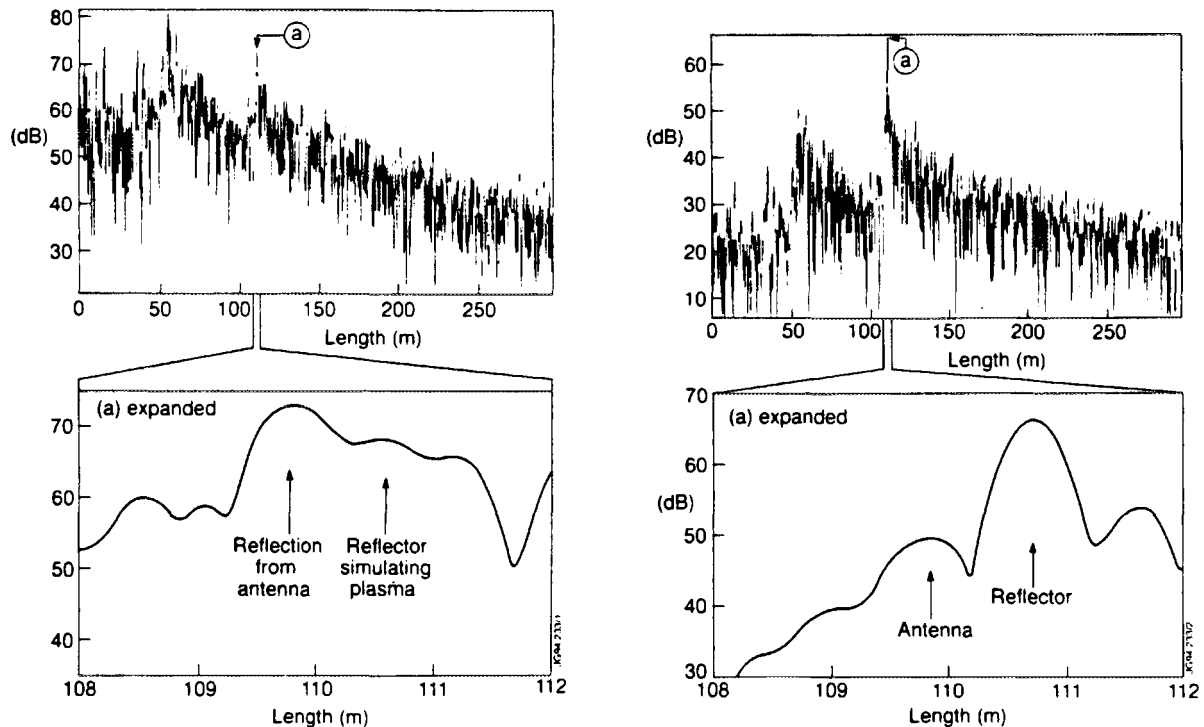


Fig.1 - Reconstructed echoes structure of a pulse, for a reflector at 63.5cm from antenna: not calibrated (left) and calibrated (right)

calibration, the reflector peak is 15dB above the parasitic reflections, and the position of the peak can be measured accurately: here 110.710m. Moving the reflector to 43.5cm moves the peak to 110.312m. The difference (40cm) corresponds exactly to the return path difference between the two positions. As described by the theory [1], the accuracy is much better than the resolution.

For this same configuration, the position of the measured position has been represented on fig.2 as a function of the position of the reflector on the bench using the calibration procedure (circles) and without calibration (triangles). Compared with the true relationship (solid line), it shows that the calibration is very important for such a poor transmission line.

A window has also been inserted between the waveguide end and the reflector. To degrade the configuration as much as possible, it has been positioned perpendicular to the beam. After calibration, the peak is still well above parasitic peaks, but is 32(±5)mm further away. This difference corresponds to the window path length $2t(n-1)$, t being the thickness of the window (=14mm) and n its refractive index.

On an actual plasma, speed of measurement is an important parameter and a smaller number of frequency steps will be necessary. In order to determine how small this number can be, we reanalysed the data, using only a subset. For a configuration, the standard deviation of the peak position as a function of the number of frequency steps is represented in figure 3 for a 3GHz bandwidth. It shows that with only 20 to 30 frequency steps, a standard deviation of 15mm is achieved.

The influence of the bandwidth on the precision of measurement has also been investigated. Figure 4 summarises the relation between accuracy and bandwidth for 30 and 150 frequency steps. The relation in Δf^{-1} corresponds exactly to the theory. This standard deviation corresponds to the measurement of one pulse. By averaging many of them, the final accuracy can be much better.

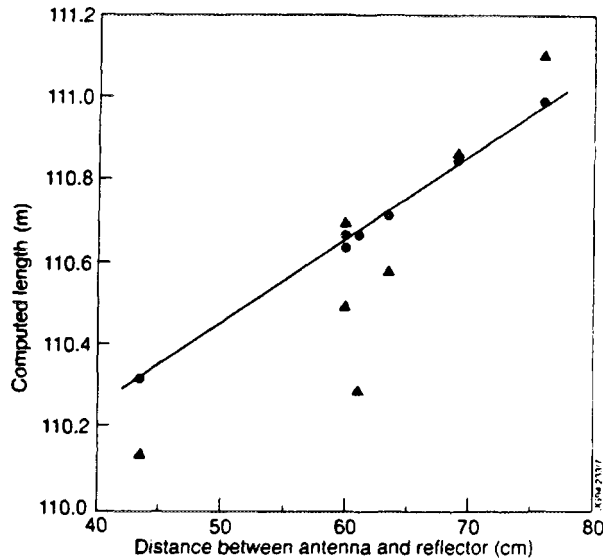


Fig.2 - Comparison between calibrated and uncalibrated measurements. The solid line represents the true position.

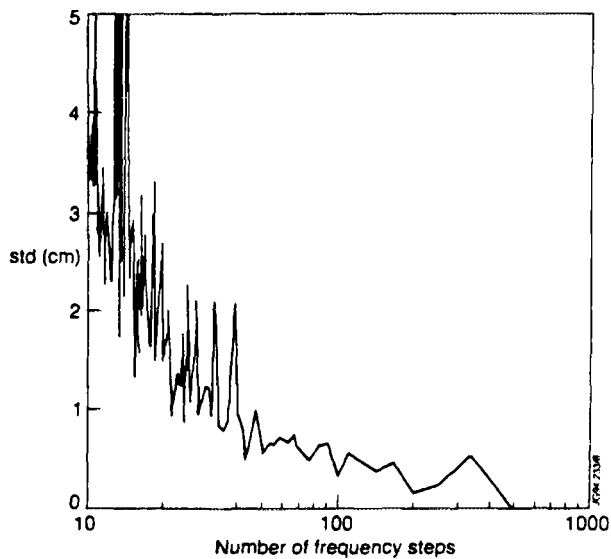


Fig.3 - Relationship between precision of measurement and number of frequency steps

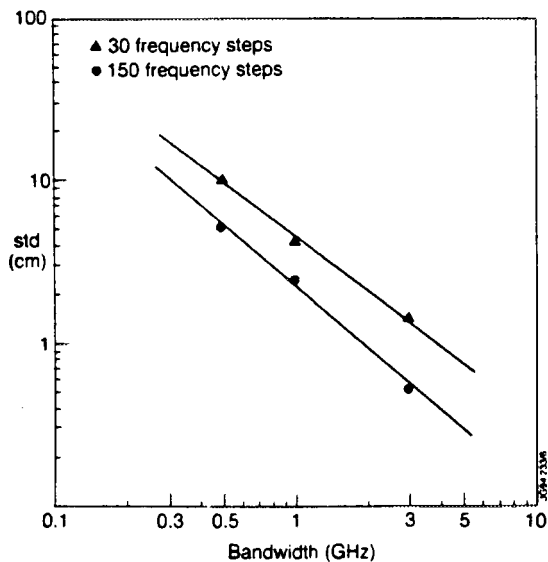


Fig.4 - Relationship between precision and bandwidth

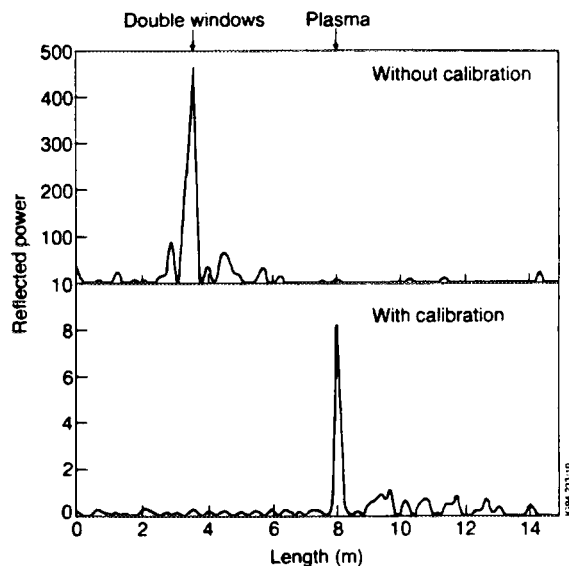


Fig.5 - Reconstructed echo from plasma, for measurement in band 31-33GHz

Tests with JET plasmas

Experiments have recently been performed on JET plasmas using a radar system based on two fast frequency synthesizers. Frequency steps were made every $4\mu\text{s}$ in the range 26-36GHz. Fig.5 shows a typical result using a long and single waveguide system (only one antenna) for a total path length of about 53m, after reflection from the plasma. In this example, 100 frequency steps of 20MHz provided a 2GHz bandwidth.

This result shows a reflection from the plasma with a high S/N ratio.

Conclusion

As extensive tests have been done, all results cannot be presented in detail here. To summarize, they show that with a standard taper and horn on the end of the waveguide, next to the reflector, a precision of typically 1cm can be obtained for the measured position of the reflector. With an open waveguide, which removes the parasitic reflections due to taper and horn, the precision improves to 1mm. From decimation analysis, we conclude that only 20 to 50 frequency steps are necessary to achieve a precision of 1 cm. With the frequency synthesizers currently available (100ns/step), the complete measurement can be made in 2 to 5 μs . In a plasma application, the fluctuations due to MHD and most of the microturbulence would be effectively frozen.

First analysis of recent tests on JET plasmas have demonstrated that compressed pulses with high S/N are obtained from the plasma.

The authors would like to thank Michel Paume and Jean-Marc Chareau (CE Cadarache) for the loan of the vector analyser and their valuable assistance in the measurements.

References

- [1] P. Millot, Proc. of IAEA Technical Committee Meeting on "Microwave Reflectometry for Fusion Plasma Diagnostics", Culham (1992), 204
- [2] P. Millot, H. Lé vêque, Proc. of 18th Int. Conf. on Infrared and Millimeter Waves, Colchester (1993), 240



FR9701757

Gamma-Ray Emission Profile Measurements during JET ICRH Discharges

P J A Howarth¹, J M Adams², D S Bond², O N Jarvis,
F B Marcus, G Sadler, P van Belle, N Watkins².

JET Joint Undertaking, Abingdon, Oxon, OX14 3EA.

¹ Birmingham University, Edgbaston, Birmingham, B15 2TT, UK.

² AEA Technology, Harwell, Oxfordshire, OX11 0RA, UK



Abstract.

Ion Cyclotron Resonant Heating (ICRH) that is tuned to minority fuel ions can induce an energy diffusion of the heated species and create high energy tail temperatures of ~ 1 MeV. The most energetic of these accelerated minority ions can undergo nuclear reactions with impurity Be and C that produces γ -ray emission from the decay of the excited product nuclei. This RF-induced γ -ray emission has been recorded using the JET neutron emission profile diagnostic which is capable of distinguishing neutrons and γ -rays. Appropriate data processing has enabled the RF-induced γ -ray emission signals to be isolated from the γ -ray emission signals associated with neutron interactions in the material surrounding the profile monitor.

The 2-d γ -ray emission profiles show that virtually all the radiation originates from the low field side of the RF resonance layer, as expected from RF-induced pitch angle diffusion. The emission profiles indicate the presence of a small population of resonant ^3He ions that possess orbits lying near the passing-trapped boundary.

Gamma-ray emission associated with RF Heating.

The ^3He - ^9Be fusion reactivity is sufficiently large that the observation of nuclear γ -rays is now routinely used at JET to diagnose the presence of fast ion energy tails from RF heating [1]. Figure 1 shows the γ -ray energy spectrum from ^3He - ^9Be plasma-impurity reactions from which it is deduced that the ^3He ions were accelerated by the RF to MeV energies. During a series of D- ^3He discharges, the detector sensitivities of the neutron profile monitor were optimised to detect the γ -ray emission from ^3He - ^9Be plasma-impurity reactions.

The JET neutron emission profile diagnostic and γ -ray measurements.

The diagnostic consists of a series of detectors housed in two high density concrete cameras that have collimated lines of sight arranged in a poloidal orientation around the vessel [2], figure 2. The width of the poloidal viewing area of each channel in the central region of the plasma is ~ 10 cm. Neutrons and γ -rays are detected with NE213 liquid scintillators and Pulse Shape Discrimination electronics are used to separate neutron and γ -ray events.

The scintillation detectors are sensitive to γ -ray radiation originating from neutron-induced nuclear reactions with the surrounding material as well as the γ -ray radiation from

RF- induced plasma-impurity nuclear reactions. To obtain profiles of the latter, the two γ -ray signals must be separated. Although, measurements of RF-induced γ -ray emission profiles were first reported by Sadler [3], the two γ -ray components were not isolated. The basis of a new technique to isolate the RF-induced γ -ray emission signal is described below.

The neutron-induced γ -ray emission is assumed to be devoid of profile structure because it originates from neutrons that have undergone scattering, and possibly thermalisation. Therefore, during discharge periods without RF heating, the γ -ray signal for each detector channel should scale linearly to the global neutron emission as measured by the fission chambers. Thus, it is reasonable to assume that during periods of RF heating the neutron-induced γ -ray component can be reconstructed from the global neutron emission such that the γ -ray signal from plasma-impurity nuclear reactions can be isolated.

Results.

An interesting series of D-³He discharges, #23450 to #23461, involved a radial scan in the location of the RF resonance layer. The ICRF was tuned to the first harmonic of ³He (~28.5 MHz) with a power range of 7 to 10 MW. A tomographic image reconstruction, using the NEUTOMO code [4], of the γ -ray emission profile for discharge #23450 is shown in figure 3. The radial profile shows that the peak γ -ray emitting region is displaced off axis and to the low field side of the resonance layer.

The location of the resonance layer was calculated using IDENTC and corrections were taken into account for diamagnetic and paramagnetic properties of the plasma [5]. The most significant uncertainty on the location of the resonance layer is from the IDENTC determination of the magnetic axis of the plasma, typically ± 10 cm. However, for the discharges of interest, the radial location of the magnetic axis as calculated using IDENTC agreed to ± 3 cm of the centroid of neutron emission during discharge periods that were dominated by D-D neutron emission.

As shown in figure 3, the γ -ray emission profile appears to peak to the low-field side of the resonance layer. Figure 4 shows that the inboard position at which the γ -ray emission is cut-off follows closely the radial location of the resonance layer, whereas the peaks of the γ -ray and neutron emission are located 20 cm outboard of the resonance layer. The off-axis displacement of the peak neutron emission is not unexpected because of ⁹Be(³He,n)¹¹C reactions when there was RF heating only.

The γ -ray and neutron emission profiles are displaced off-axis due to the ICRH preferentially accelerating the perpendicular velocity component of the resonant ions and so converting their orbits from passing to trapped. The ICRH continues to accelerate the minority ions such that they possess trapped-particle orbits with pitch angles of 90 degrees at the location of the resonance layer. Thus, the RF is responsible for inducing a radial drift of the

minority ions to the low field side of the resonance layer until the gyrocentres of the bounce points lie within the resonance layer.

Even though the ICRH is focused on the mid-plane, the exceptionally prominent peaking of the vertical γ -ray emission profile is difficult to predict from RF-induced energy and pitch angle diffusion. However, simulations of the 2-D profile with the aid of the ORBIT code have shown that the vertical profile peaks sharply on axis by including a small population of energetic counter-passing ions with orbits that have pitch angles of $\sim 100^\circ$. These ions lie near the passing-trapped boundary of the fast ion anisotropic velocity distribution. The very localised nature of these counter-passing orbits suggests that only a fraction of the fast ^3He ions require such orbits for them to dominate the γ -ray emission profile. Since the counter-passing ions are situated to the low-field side of the resonance layer, the γ -ray emission profile must peak radially somewhat further outboard of the resonance layer.

A numerical simulation of the γ -ray emission profile has been obtained by Righi [6], who calculated the velocity distribution for an ensemble of ^3He ions using a steady state bounce-averaged Fokker-Planck model that includes an RF diffusion operator. The resulting γ -ray emission profile data is consistent with the proposition that ions with orbits near the passing-trapped boundary are responsible for the prominent peaking of the profile. However, as a result of the geometrical approximations involved, the simulated profile is displaced radially by ~ 15 cm inboard relative to the measured profile.

Conclusions.

Gamma-ray emission from plasma-impurity reactions caused by minority ICRH accelerating fuel ions to MeV energies has been measured using the JET neutron profile monitor. A successful data analysis technique has been used to isolate the RF-induced γ -ray emission that was detected by the profile monitor enabling profiles of γ -ray emission to be obtained. The shape of the profiles can be understood from relatively straight forward theory on the effect of RF heating on the orbits of resonantly interacting minority ions. Theoretical modelling of the γ -ray emission profiles agree adequately with measured data.

References.

- [1] Sadler G, et al. Fusion Technology 18 (1990) 556.
- [2] Adams J M, et al. Nuclear Instruments and Methods. Vol 329 (1993) 277.
- [3] Sadler G. Alpha-Particles in Fusion Research, IAEA Vol 1 July (1991) 97-132
- [4] Granetz R S and Smeudlers P. Nuclear Fusion 28 (1988) 457.
- [5] Start D. Private Communication (1993).
- [6] Righi E. this conference.

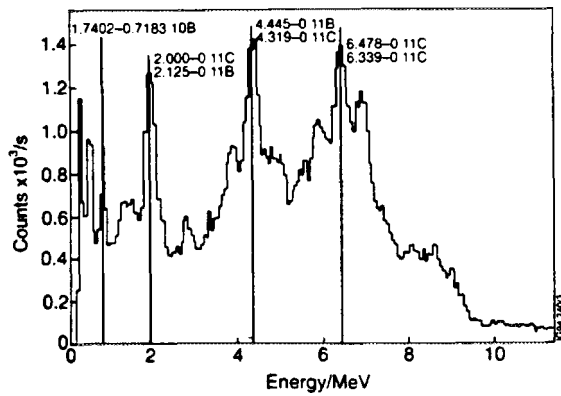


Figure 1. Gamma-ray energy spectrum for discharge 23450 at 49.0 seconds. Gamma decay lines from ${}^9\text{Be}({}^3\text{He},p){}^{11}\text{B}$, ${}^9\text{Be}({}^3\text{He},d){}^{10}\text{B}$ and ${}^9\text{Be}({}^3\text{He},n){}^{11}\text{C}$ are marked.

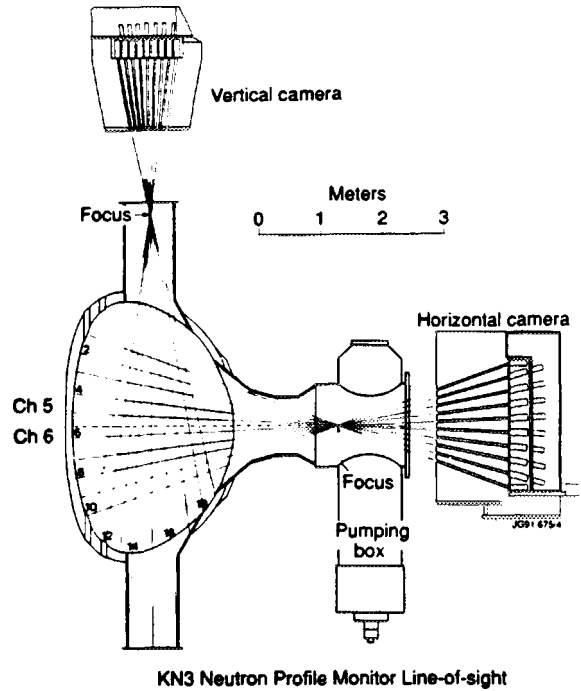


Figure 2. Schematic of the JET Neutron emission profile monitor showing the lines of sight for each detector channel.

Figure 3. Tomographic reconstruction of the γ -ray emissivity for #23450 between 48.5 and 49.5 seconds. The location of the resonance layer is shown by the dark line. The outline of the vacuum vessel is sketched on the diagram.

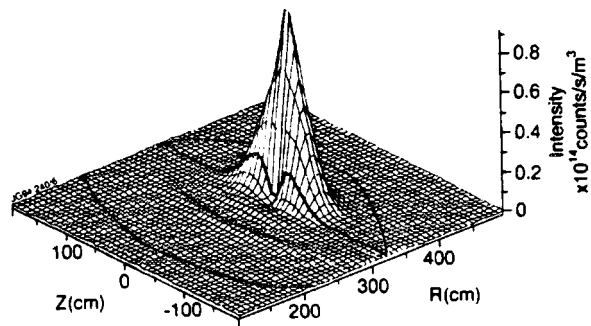
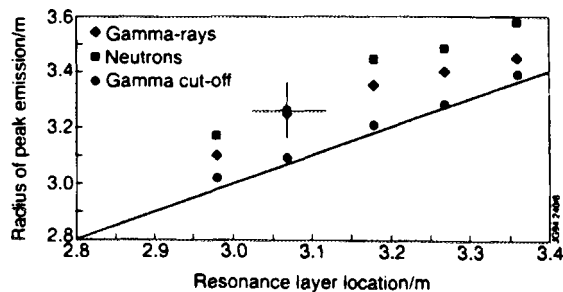


Figure 4. Radial location of peak of neutron and γ -ray emission as a function of resonance layer location.





FR9701758

The New JET Phased ICRH Array: First Experiments and Modelling

M Bures, V Bhatnagar, T Brown, B Fechner, C Gormezano,
R Goulding¹, A Kaye, P Lamalle², M Lennholm, F Nguyen³,
E Righi, F Rimini, A Sibley, D Start, T Wade.

JET Joint Undertaking, Abingdon, Oxon, OX14 3EA.

¹ Oak Ridge National Laboratory, Oak Ridge, Tennessee, USA.

² Plasma Physics Laboratory, ERM, Brussels, Belgium.

³ CEA, Centre d'Etudes de Cadarache, France.



Introduction. New ICRH antennas on JET were designed to couple to the new JET divertor plasma configurations and to improve the Fast Wave Current Drive (FWCD) capabilities. The A2 antenna consists of 4 straps whose currents can be phased at arbitrary angles. In total 4 antennas are installed with a 2MW amplifier per strap. The real time automatic tuning acts on frequency, line length (line phase shifters) and stub length. As in the past provision is made for the coupling resistance/plasma position feedback to accommodate the fast changes in antenna loading. In this paper we report on the first coupling, tuning and heating results in $0\pi0\pi$, 0000 and $00\pi\pi$ phasing. Also we describe a new antenna model which was developed to simulate the measured antenna loading in terms of plasma parameters and to provide a starting point for the real time automatic tuning.

Antenna conditioning. The high power ICRH requires conditioning of all antennas. This is due to: a) novel design where a ceramic cone separating the vessel vacuum from the antenna vacuum transmission line (VTL) was removed thus allowing the pressure rises, in the VTL, associated with vessel conditioning and gas pulses, b) getter pumps previously active on the VTL were moved to pump only the double feedthrough interspace separating the VTL and main transmission lines (MTL). Conditioning sequence was 1) low voltage, short pulse multipactor vacuum conditioning, 2) high voltage, short pulse vacuum conditioning and 3) high power, long pulse plasma conditioning. Approximately 10 plasma pulses were required. To protect the VTL and the feedthroughs the RF generators are tripped, in addition to reflected power trips, when the VTL pressure reaches 10^{-4} mbar.

ICRH plasma heating. During the initial JET operations, until the new set of diagnostic coils are fully commissioned, the magnetic equilibrium reconstruction depending on the old set of coils is not accurate. The present data have large error bars but some estimates and conclusions about the initial performance of ICRH system and heating efficiency can be made. 1) $P_{rf}=6$ MW was coupled into a 1.5MA/2.8T plasma in $0\pi0\pi$ phasing and D(H), 42 MHz for 4s and max.power reached ≈ 9 MW. 2) $P_{rf}\leq 4$ MW was coupled for 8s. 3) $T_e(0)^{max} = 7-8$ keV was achieved and sawteeth were stabilised for 1.4 s. 4) Heating in $0\pi0\pi$ is consistent with the L-mode scaling and $T_e(0)/n_e$ scales with RF power as observed previously. 5) Heating in 0000 phasing at low power ≤ 2 MW has very low efficiency. The final conclusion about these results requires a future comparison at high power. Possible reasons for the lack of heating are: i) all power in 0000 spectrum is contained in $k_{//} < 2.5\text{m}^{-1}$. The low $k_{//}$ waves tend to reflect from the resonance zone and do not suffer sufficient damping. At high power the increasing temperature broadens the minority cyclotron layer, the cyclotron damping is enhanced and the minority tail can form. Also the direct electron damping becomes more efficient. ii) H concentration is too high. At high

concentrations the distance of cut-off layer to the minority cyclotron layer increases and the waves are readily reflected. Support for this hypothesis follows from the lack of 5.5MeV gamma radiation resulting from the reactions between the high energy protons and deuterons. iii) Parasitic dissipation in RF sheaths. Previous experiments (ref.1) with the 2 strap A1 antennas on JET in 00 phasing and large angle between the edge magnetic field and Faraday screen (FS) elements have shown that a large fraction of RF power can be dissipated in the RF sheaths at the front surface of antenna. RF sheaths are driven by the radial oscillating magnetic flux passing through electrical circuits formed by magnetic field lines connecting material surfaces on FS and/or protection tiles/limiters. Large convective cells (ref.2) are formed in front of FS which cause a strong interaction with the SOL/plasma edge. Indeed strong interaction plasma edge/poloidal limiter was observed with A2 antennas (0000) resulting in enhanced radiation. The possible circuits driving the convective cells result from magnetic field lines connecting FS and the poloidal limiter and the lines connecting poloidal limiters on both sides of antenna.

Results on antenna/plasma RF coupling. The initial operational constraints on JET control parameters implied plasma configurations which were not optimised for RF coupling. In particular the misalignment of the plasma boundary/antenna FS in the poloidal plane affects the coupling of large fractions of antenna straps which lowers the effective antenna loading. The uncertainty about the magnetic configuration means that most of JET plasmas were significantly detached. The initial operational experience nevertheless shows that the RF coupling resistance, measured on the transmission lines $R_C = 2P_{rf}(Z_0/V_{max})^2$, depends on:

- antenna/plasma distance as shown in fig.1. d_{a-p} is the distance of the Last closed flux surface (LCFS) from a surface ≈ 3 cm in front of FS measured at the mid plane. The solid lines are calculated from the model discussed below.
- phasing. Coupling in 0000 is significantly higher than in $0\pi 0\pi$. Also $R_C^{00\pi\pi} \geq R_C^{0\pi 0\pi}$
- SOL density e-folding length λ_n which is substantiated by the high coupling observed at low plasma current 1 MA.
- density. Present data set shows a weak density dependence which we attribute to lack of accurate data. Regression analysis shows the strongest dependence of R_C on d_{a-p} .
- frequency, $R_C^{32MHz} \approx 0.5R_C^{42MHz}$. This can be explained by two effects. First the 32MHz operation was done at low magnetic field 2.1T which implies short λ_n , second the A2 antenna is resonating at rather high frequency 42 MHz.
- the observed dependencies are in satisfactory agreement with model predictions.

In addition the divertor sweeping modulates R_C by up to 20%. During Elmy H-modes the ELMs modulate the reflected generator power by a significant fraction.

Automatic matching. Tuning of the antenna/transmission line system requires a generator load equal to the characteristic impedance of line Z_0 . It is based on control of relative phase between the forward voltage on the MTL and the reflected voltage on the generator output line(OTL) e.g. $Re\{V_r^{OTL}/V_f^{MTL}\}=0$ as well as the amplitude of the OTL reflected voltage, $Im\{V_r^{OTL}/V_f^{MTL}\}=0$. The first condition is satisfied by feedback loop on frequency and MTL phase shifters and the second by feedback on stubs. Example of the automatic tuning is shown in fig.2. Voltages V_r^{OTL} on all four lines are very low. The frequency and stub error signals are zero when the match is achieved. Time response of tuning is determined by the speed of stubs. Fast changes of loading have to be accommodated by the feedback R_C /radial plasma position as in the past.

Antenna/plasma RF coupling model . The model antenna consists of 4 toroidal straps, each strap has 4 poloidal sections of which 2 are shorted. The loading impedance matrix Z_S is calculated using the 5-region model shown in fig.3. TE waves are excited in vacuum regions I and II, FW are excited in the exponential plasma density region III, linear k_{\perp}^2 region IV and constant plasma density region V. The antenna capacitance matrix C_S is calculated from TM waves as described in ref.4. Antenna currents and their phases are defined at the antenna strap shorts as current vector I_{vec} . The vacuum solutions assume $\omega/c \ll k_{//}$ and the FW dispersion in region III is derived (ref.2) for $k_0^2 S \gg k_{//}^2$. S is the cold dielectric tensor element in Stix's (ref.3) notation. The FW wave field solution can be found for the poloidal electric field $E_y(x)^{III}$ in form:

$$E_y^{III}(x) = A^{III} J_{\nu}(\xi) + B^{III} J_{-\nu}(\xi) \quad \text{where}$$

$$\xi = 2\lambda_n \alpha \exp(x/2\lambda_n) ; \alpha^2 = \mu_0 m_H (A\omega^2/B^2) n(0) ; \nu^2 = 4\lambda_n^2 k_{//}^2 (1 + \omega/\omega_{ci})$$

and $J_{\pm\nu}(\xi)$ are Bessel functions of fractional order ν .

In region IV the oscillating and evanescent FW fields are derived (ref.3) from the singular turning--point equations in terms of Bessel functions $J_{\pm 1/3}$ and $I_{\pm 1/3}$. In the constant plasma parameters region V we consider only the single pass fields. Poloidal variation of the fields is neglected, $k_y = 0$. The solutions of 5 regions are matched across their boundaries in standard fashion. Knowing Z_S and $Y_S = i\omega C_S$ we analyze wave propagation along the antenna in terms of TEM modes (ref.4):

- Calculate the matrices K, L, D, G and Z_c , the columns of K and L are voltage and current eigenvectors

$$D = K^{-1} Z_S Y_S K = L^{-1} Y_S Z_S L \quad G = \sqrt{D} = \text{diagonal}(\gamma_i), i=1-4$$

$$Z_c = G^{-1} K^{-1} Z_S L \quad Y_c = Z_c^{-1}$$

- Define matrix T and equivalent impedance Z_{eq} for the shorted strap sections of length l_1 and matrices C and S for the main strap sections of length l_2

$$T = \text{diagonal}[\text{th}(\gamma_i l_1)] \quad Z_{eq} = K T Z_c L^{-1} \quad C = \cosh(\gamma_i l_2) \quad S = \sinh(\gamma_i l_2)$$

- Define transfer matrices (ref.5) to calculate the input voltages and currents into strap sections l_2 from the current vector I_{vec} defined at the input of sections l_1

$$X_V = K [C K^{-1} Z_{eq} + Z_c S L^{-1}] \quad X_I = L [Y_c S K Z_{eq} + C L^{-1}]$$

- Define antenna impedance matrix Z_A and total input voltages and currents

$$Z_A = X_V (2X_I)^{-1} \quad I_{in} = 2X_I I_{vec} \quad V_{in} = Z_A I_{in}$$

- R_c is calculated on transmission lines from antenna input impedance V_{in}/I_{in} , where the division is performed on the corresponding components of the V_{in} and I_{in} vectors.

References.

- [1] M.Bureš et al, Nucl.Fus. 32, 7(1992)1139.
- [2] D.A.D'Ippolito et al., Phys.Fluids B5(10),1993 p.3603
- [3] T.H.Stix, Theory of Plasma Waves, McGraw-Hill, 1962.
- [4] P.V.Lamalle et al., IEEE Transactions on Plasma Science, Vol.PS-15, 1(1987)60
- [5] R.H.Goulding et al, Bull.Am.Phys.Soc., APS1993.

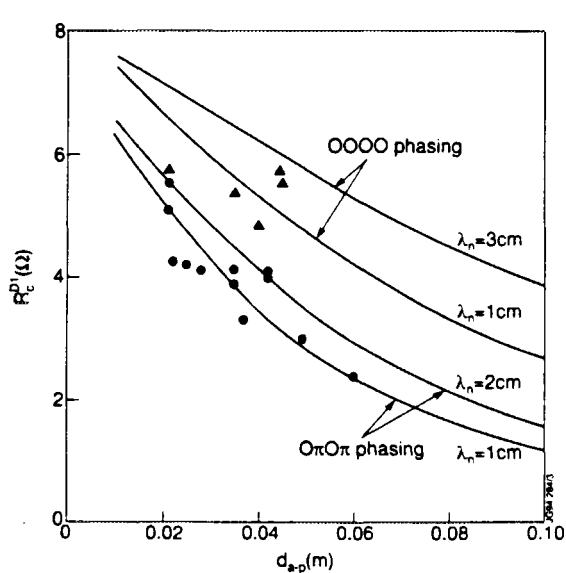


Fig.1 Coupling resistance R_c as a function of distance LCFS/FS + 3cm

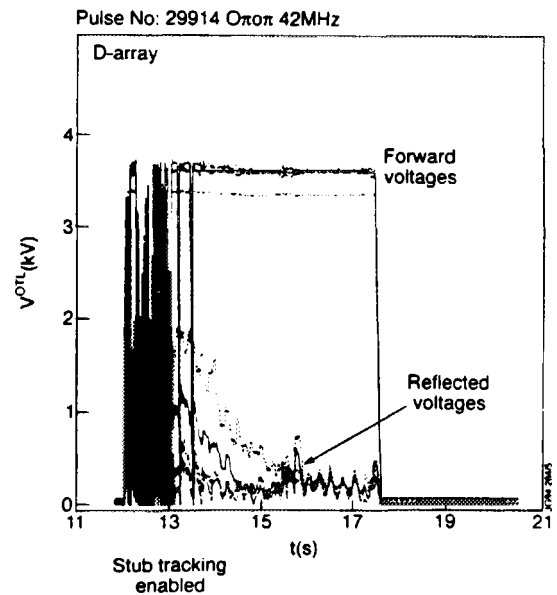


Fig.2 Forward and reflected voltages on OTL with automatic tuning enabled

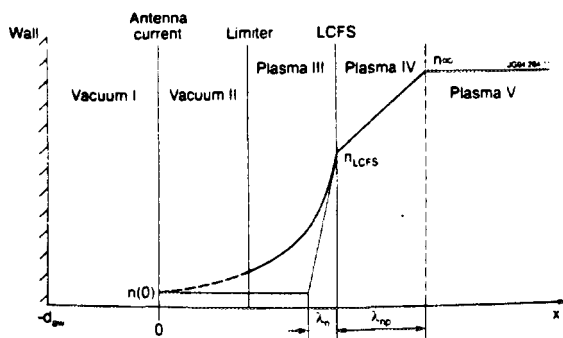


Fig.3 Schematic drawing of the 5-regions in the antenna/plasma RF coupling model

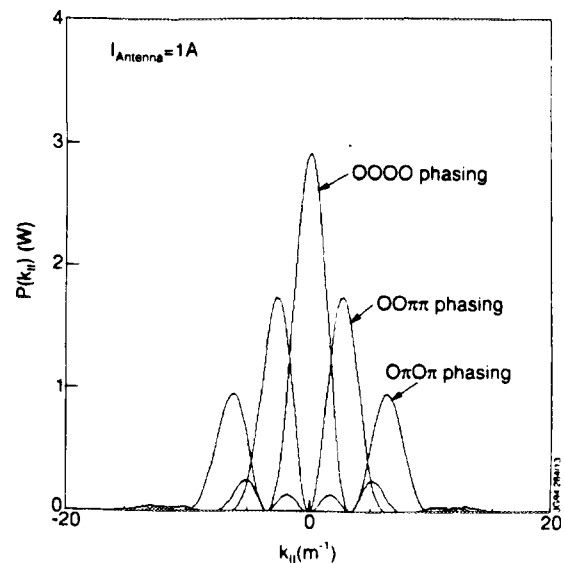


Fig.4 Antenna radiation power spectra for the phasings indicated in figure



FR9701759

Simulation of Triton Burn-Up in JET Plasmas

M J Loughlin, B Balet, O N Jarvis, P M Stubberfield.

JET Joint Undertaking, Abingdon, Oxon, OX14 3EA.



ABSTRACT

This paper presents the first triton burn-up calculations for JET plasmas using the transport code TRANSP. Four hot ion H-mode deuterium plasmas are studied. For these discharges, the 2.5MeV emission rises rapidly and then collapses abruptly. This phenomenon is not fully understood but in each case the collapse phase is associated with a large impurity influx known as the 'carbon bloom'. The peak 14MeV emission occurs at this time, somewhat later than that of the 2.5MeV neutron peak. The present results give a clear indication that there are no significant departures from classical slowing down and spatial diffusion for tritons in JET plasmas.

INTRODUCTION

The time behaviour of 14MeV emission (Y_{dt}) depends on the electron temperature and density, scales linearly with deuteron density (n_d) and is only weakly dependent on T_i . At sudden events such as the carbon bloom, the instantaneous Y_{dt} is affected only by changes in n_d . However, changes in the 2.5MeV emission (Y_{dd}) are due to a combination of reductions in both n_d and T_i . Simultaneous calculations of both the dd and dt neutron emission can provide information on n_d , which is notoriously difficult to determine.

CALCULATIONS

TRANSP [1]

TRANSP is a time dependent transport analysis code. Experimentally measured radial profiles of T_e , n_e , T_i and Z_{eff} are used as input. The plasma impurities are modelled as one impurity with an arbitrary charge, Z_{imp} , which does not necessarily have an integer value. In the TRANSP runs discussed here Z_{imp} was constant throughout the discharge. The triton burn-up is calculated using the Monte-Carlo technique. The triton birth-rates and profiles are calculated. Tritons are produced with an energy of 1.01MeV and slow down classically; first orbit and charge exchange losses, after taking re-ionisation into account, are included.

TRAP-T [2]

The major respect in which TRAP-T differs from TRANSP is that the experimentally determined 2.5MeV neutron emission is used directly as the triton source term. The triton

burn-up is calculated assuming the plasma parameters (e.g. T_e , n_e , Y_{dd}) to be constant around the magnetic flux surface. The tritons slow down classically but a triton confinement time of 2.0 seconds is applied throughout the discharge. The tritons are assumed to be confined to flux surfaces and no losses are taken into account. For the results presented here, the axial Z_{eff} used by TRANSP was used as input and the profile was assumed to be flat. All other input data are taken from the JET database.

MEASUREMENTS OF TRITON BURNUP

The time dependent 14MeV neutron emission is measured using a silicon diode. This detector is sensitive only to dt neutrons since it utilises (n,p) and (n, α) reactions which have thresholds well above the energy of neutrons produced in dd reactions. The efficiency of the diode is determined by comparison with determinations of the total 14MeV neutron yield derived from activation measurements using silicon, copper and iron [3].

RESULTS

The TRANSP calculation of the dd reaction rate is compared with the measured total neutron emission in figure 1 for discharge 26061. Excellent agreement was obtained for the discharges studied.

Triton Burn-up

A typical TRANSP calculation is presented in figure 2. The calculations agree to within 15-30% of the measured burn-up rates at the maximum. The largest discrepancy occurs at the time of the carbon bloom i.e. when the deuterium density is least well known. At other times the agreement is much better. The estimated accuracy of the calculations and measurements are 20% and 8%, respectively.

Good agreement was also obtained between calculations using TRAP-T and the measurement. TRAP-T has been used to calculate the triton burn-up in a greater variety of discharges and the results indicated that the tritons slow down classically [4-6]. The 2sec confinement time effectively accounts for the losses.

Deuterium Density

The volume integrals of the densities of deuterons, electrons and the impurity derived by TRANSP are shown in figure 3 for shot 26061. The timing of the abrupt change in the neutron emission is compared to that for the reduction of deuterium in table 1. In discharges 26023 and 26087 the deuterium reduction is initially slow then proceeds more quickly 0.7-1.0

seconds after the fall in the neutron emission. The large decrease in the dd reaction rate has been ascribed to the reductions in the ion temperature as reported in [7]. The agreement between the triton burn-up calculations and the measurements is poorer in these two discharges.

Shot	t_n	t_d	Z_{imp}
26000	15.7	15.8	6.0
26023	13.3	14.0	5.6
26061	13.4	13.4	6.0
26087	13.4	14.4	5.3

Table 1: Times of abrupt change in neutron emission (t_n) and deuteron reduction (t_d) and the charge of impurity (Z_{imp}).

DISCUSSION

To correctly model the neutron emission throughout the discharge the charge on the impurity was set to 5.6 and 5.3 in 26023 and 26087. This was to account for the presence of both Be and C in the plasma. These values correspond to C:Be ratios of 4.0 and 2.0. A constant C:Be ratio is clearly not adequate for these discharges. Work has begun to simulate these plasmas using time varying Z_{imp} to account for the increase in the C:Be ratio at the carbon bloom.

CONCLUSIONS

These results give a clear indication that there are no significant departures from classical slowing down and spatial diffusion of tritons in JET plasmas. The correct calculation of both the dd and dt reaction rates through the carbon bloom effectively determines the deuteron density and provides information on the impurity influx under conditions which are exceptionally problematic for the more conventional diagnostic techniques.

REFERENCES

- [1] R.J.Goldston *et al.*, J.Comput Phys **43** (1981) 61.
- [2] S.Conroy Ph.D Thesis (1990) Imperial College of Science and Technology, London, UK.
- [3] O.N.Jarvis *et al.*, Nucl Fusion **20** (1991) 265
- [4] S.Conroy *et al.*, Nucl. Fusion **28** (1988) 2127
- [5] S.Conroy *et al.*, Proc. 16th EPS Conf. on Cont. Fusion and Plasma Physics **1** (1989) 67
- [6] S.Conroy *et al.*, Proc. 17th EPS Conf. on Cont. Fusion and Plasma Physics **1** (1990) 98
- [7] B.Balet *et al.*, Nucl. Fusion **33** (1993) 1345

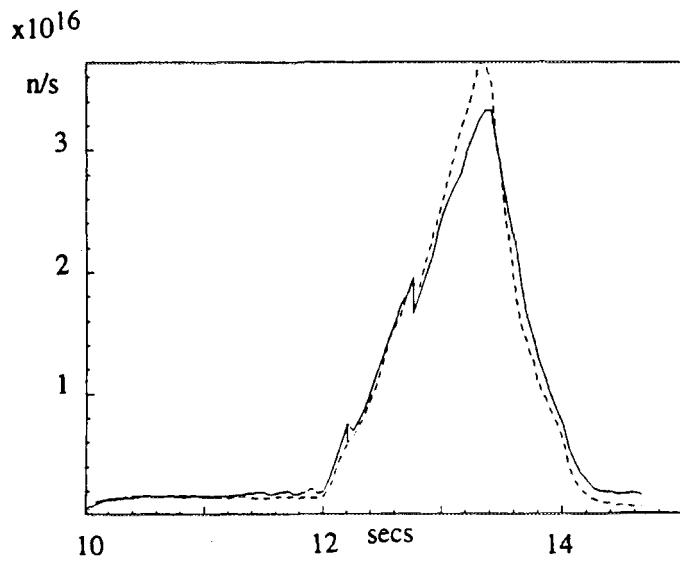


Figure 1: Measured (solid line) and calculated (dashed line) total 2.5MeV neutron emission for shot 26061.

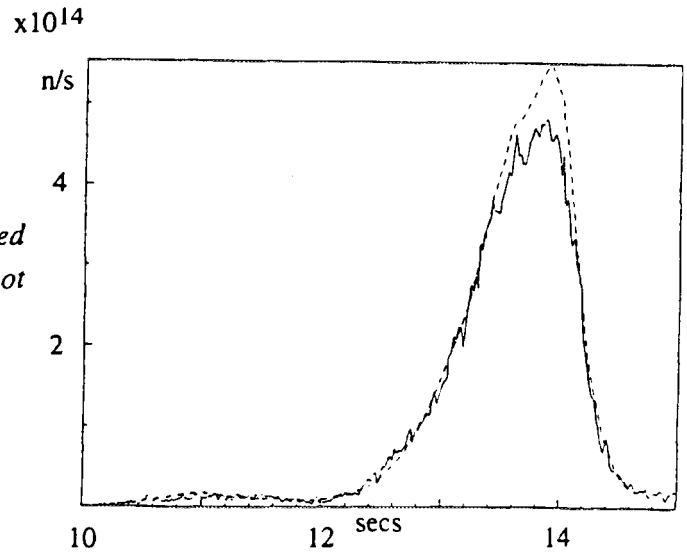


Figure 2: Measured (solid line) and calculated (dashed line) 14MeV neutron emission for shot 26061.

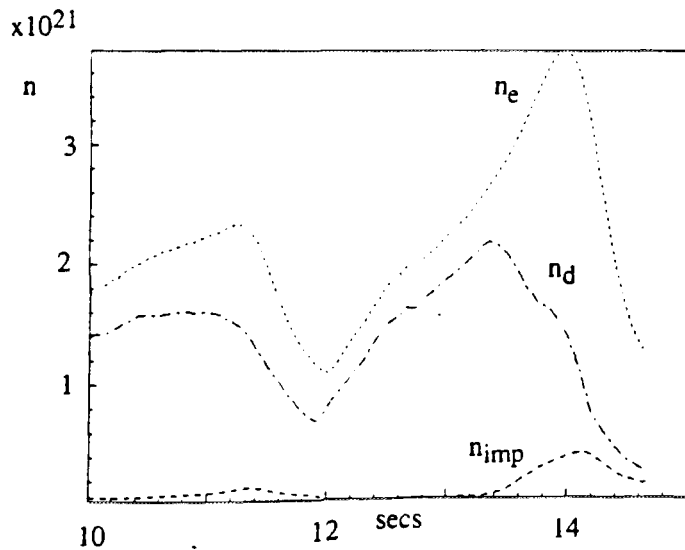


Figure 3: Volume integrals of TRANSP derived electron, deuterium and impurity densities for shot 26061.



FR9701760

Parametric Dependencies of JET Electron Temperature Profiles

B Schunke, K Imre¹, K Riedel¹.

JET Joint Undertaking, Abingdon, Oxon, OX14 3EA.

¹ New York University, New York, USA.



The JET Ohmic, L-Mode and H-Mode electron temperature profiles obtained from the LIDAR Thomson Scattering Diagnostic [1] are parameterised in terms of the normalised flux parameter ψ and a set of the engineering parameters like plasma current I_p , toroidal field B_T , line averaged electron density \bar{n} , ... We intend to use the same model to predict the profile shape for D-T discharges in JET and in ITER.

1. The log-additive temperature profile model

Assuming that the electron temperature profile in a tokamak depends only on the global parameters, we adopt a generalised log-additive model to describe the electron temperature profile [2]

$$\ln[\theta(\psi, \bar{u})] = f_0(\psi) + \sum_{i=1}^L f_i(\psi) h_i(\bar{u}) \quad \text{with} \quad h_i(\bar{u}) = (\ln[I_p], \ln[B_T], \ln[\bar{n}], \ln[\kappa], \dots),$$

where all variables are normalised to their mean values in the data set.

To estimate the unknown $f_i(\psi)$ we expand in B-splines: $f_i(\psi) = \sum_{k=1}^K \alpha_{ik} \beta_k(\psi)$ using cubic spline functions $\beta_k(\psi)$. All spline coefficients are estimated simultaneously with a penalised

least square regression by minimising
$$\sum_{i,j} \left(\frac{\ln[T_i(\psi'_j)] - \theta(\psi'_j, \bar{u}_i)}{\sigma_{i,j}} \right)^2 + \sum_1 \lambda_1 \int_0^1 |f_i(\psi)|^2 d\psi.$$

$T_i(\psi'_j)$ is the j th radial measurement of the i th measured temperature profile and $\sigma_{i,j}$ is the associated error. The second term is the smoothness penalty function, which damps down artificial oscillations in the estimated $f_i(\psi)$. We use the Rice criterion C_R to estimate the total predicted error, which consists of variance plus smoothing bias plus the model bias (the error arising from the use of an incorrect model):

$$C_R = \frac{\sum_{i,j} (y_{ij} - \theta_{ij})^2 / \sigma_{ij}}{(N - 2 \times \text{degrees of freedom})} \quad \text{where} \quad y_{i,j} = \ln[T_i(\psi)].$$

The Rice criterion differs from a least square fit by the denominator and enables us to compare models and optimise a given model with respect to the smoothing parameters, choosing λ_1 , adding one parameter at a time during a sequential selection procedure and minimising C_R .

2. Advantages of the log-additive model:

- Discharge specific phenomena are eliminated by fitting all profiles simultaneously.
- Physics insight into which global variables influence temperature profile.
- Compact representation for a class of discharges.
- The fitted profiles may easily be input into analysis codes.

- Extrapolation to new values of engineering parameters possible.
- Self consistent errors, including discharge variability, are estimated using repeated measurements.

3. JET electron temperature profile parameterisation

We have compiled and, using the fitting method described above, statistically analysed a 43-profile Ohmic data set, a 55-profile L-Mode data set and a 51-profile H-Mode data set. The data were taken from experimental campaigns from 89 to 92 (see Figure 1 for examples of the fit obtained). Our parameter range is: $I_p = 1\text{-}5$ MA, $B_T = 1.1\text{-}3.4$ T, $q_{95} = 2.8\text{-}17$. Each profile is measured at 50 locations along the mid-plane of the JET vessel. The raw profile data show much radial structure and vary slowly in parameter. We remove the outermost points near the inner wall, where the dumping of the laser light causes a spurious spike on the profile.

Ohmic temperature analysis: Table 1 visualises the selection procedure of the dominant covariants for the Ohmic data set. Fitting all candidates in a one variable fit, one finds that I_p minimises C_R . This parameter is then selected and paired with all other variables in a two variable fit. The variable that minimises C_R in combination with I_p is then selected as second parameter, and we continue to add another variable to minimise CR.

Table 1: Rice Table for Ohmic data set

Vars	1 Var	2 Var	3 Var	4 Var	5 Var
$\ln[\bar{n}]$	8.58	3.07	1.90	seed	seed
$\ln[q_{95}]$	5.70	3.23	2.42	1.50	seed
$\ln[I_p]$	3.49	seed	seed	seed	seed
$\ln[B_T]$	7.20	2.81	seed	seed	seed
$\ln[\kappa]$	7.92	3.49	2.76	1.86	1.49
a	8.48	3.44	2.79	1.88	1.46
V_{loop}	8.51	3.45	2.71	1.85	1.46
Z_{eff}	8.01	3.24	2.78	1.87	1.43
ℓ_j	7.79	2.91	2.61	1.77	1.47

The sequential selection procedure shows that I_p is the most important variable in determining the plasma temperature, followed by the toroidal field B_T , the line average density \bar{n} and q_{95} . Adding a fifth variable does not appreciably decrease C_R , so we choose the four variable model. The Rice table shows that the plasma inductance is not particularly influencing the temperature.

The resulting model for the JET Ohmic temperature profile is:

$$T(\psi) = \mu_o(\psi) I_p^{f_I(\psi)} B_T^{f_B(\psi)} \bar{n}^{-f_n(\psi)} q_{95}^{f_q(\psi)} \quad \text{with } \mu_o(\psi) = \exp(f_o(\psi)) \quad (1)$$

Because Eq(1) already contains B_T and I_p , q_{95} seems to account for changes in R, a and κ . Thus we can reparameterise (1) using $q_{95}I_p/B_T$ as the fourth variable. As seen in Figure 2 the electron temperature profile broadens and becomes slightly hollow with increasing current when the other parameters are held constant. The same effect is also seen with decreasing toroidal magnetic field for constant current. Since $f_I(\psi) = c - f_B(\psi)$ the profile shape depends primarily but not exclusively on the ratio I_p/B_T . Our best fit has an average error of 183 eV, which is 12.6 % of the typical line average temperature. The error bar for predicting new measurements is larger than the typical residual fit error. With $C_R \approx 1.5$ the error bar for

predictions is 22% larger than the typical measurement error.

A similar fit to the Ohmic density profiles shows that $n(\psi)$ depends only on \bar{n} and B_T and that a good approximation is $f_B(\psi) = c - f_n(\psi)$.

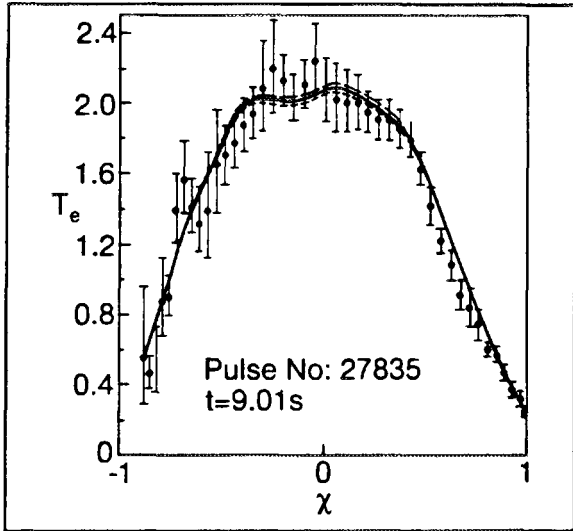


Figure 1: Example of predicted temperature profile from model with raw data

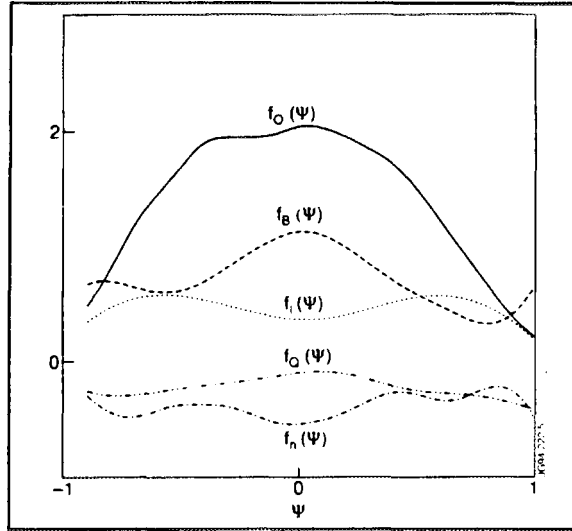


Figure 2: Spline functions for Ohmic electron temperature profile fits

L- Mode temperature fit: Repeating the analysis on the L-Mode data, we find the dependency on B_T to be stronger than in Ohmic discharges. T_e decreases and broadens with \bar{n} . The dependency on the current is weaker ($\sim I_p^{0.4}$) than in the Ohmic case. ICRH heated discharges are more peaked than NB heated discharges, therefore we introduce the parameter $\gamma = P_{RF}/P_{tot}$ into the set of covariants.

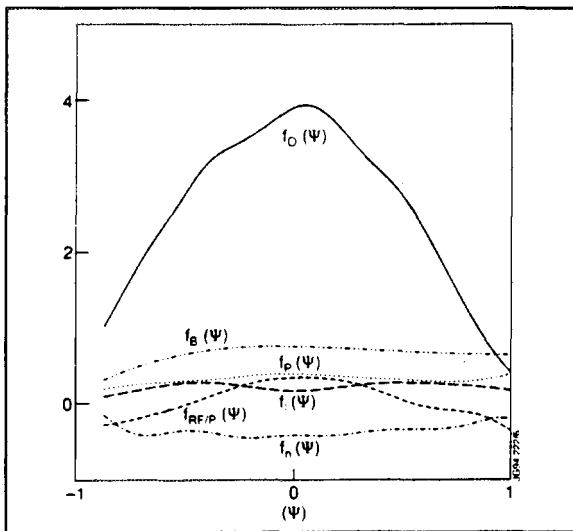


Figure 3: Spline functions for L-Mode temperature profile fits

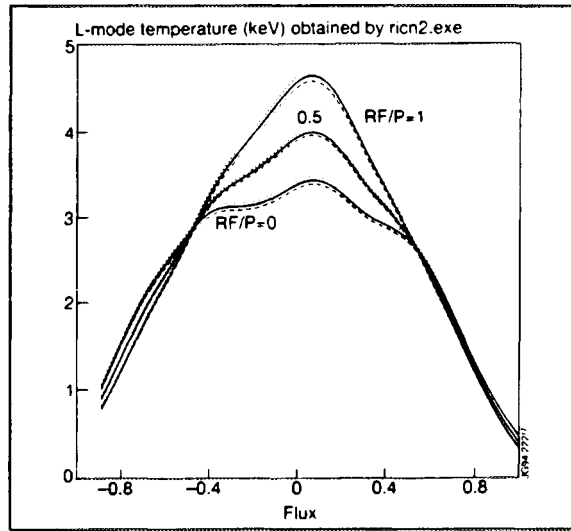
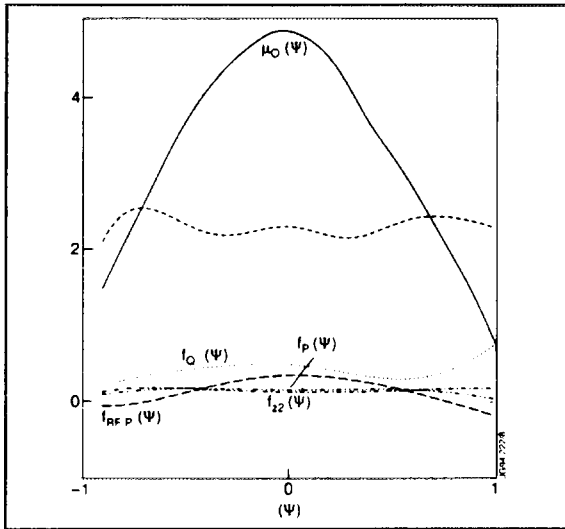


Figure 4: L-Mode temperature profiles varying γ

Best fit model: $T(\psi) = \mu_o(\psi) P_{tot}^{f(\psi)} \exp\{\gamma^{f(\psi)}\} \bar{n}^{f(\psi)} B_o^{f(\psi)} I_p^{f(\psi)}$ (Figure 3)

Figure 4 shows how the L-Mode temperature profiles change according to our model when varying γ . Regardless of the value of γ the profile shape stays the same outside 0.5χ , inside 0.5χ the application of radio frequency heating alone produces a more peaked temperature profile than the application of neutral beam heating.



H-Mode temperature fit: Our best fit parameterisation shows a strong dependency on the current ($\sim I_p^2$). We found that q_{95} has an influence on the electron temperature profile in the H-Mode case, but there is no significant dependency on the density as in the L-Mode data set. Again we find ICRH heated discharges to be more peaked than NB heated discharges, and the parameter $\gamma = P_{RF}/P_{tot}$ appears also in the parametric description of the H-Mode profile as a covariant. We also found that Z_{eff} strongly influences the H-Mode temperature.

Figure 5: Spline functions for H-Mode temperature profile fits

Best fit model: $T(\psi) = \mu_o(\psi) z_{eff}^{f(\psi)} P_{tot}^{f(\psi)} I_p^{f(\psi)} q_{95}^{f(\psi)} \exp\{\gamma^{f(\psi)}\}$ (Figure 5)

Conclusions

The statistical analysis of JET Ohmic, L- and H-Mode data sets shows that the electron temperature profiles fit a log-additive model well. The further analysis of JET L- and H-Mode discharges, e.g. the inclusion of parameters describing the sawtooth phase or the power deposition profile - if feasible, will clarify the parametric dependencies. The parameterisation and characterisation of the corresponding density profiles is nearly completed and will be reported later. A Multimachine database for extrapolation to ITER performance seems possible.

- [1] H.Salzmann, J.Bundgaard, A.Gadd, et al., Rev.Sci.Instrum.59, 1451(1988)
- [2] McCarthy, P.J., Riedel, K.S., Kardaun, O.J.W.F., Murmann, H., Lackner, K., Nuclear Fusion, 31, 1595 (1991)



FR9701761

Detached Divertor Plasmas in JET

L D Horton, K Borrass, G Corrigan, N Gottardi, J Lingertat,
A Loarte, R Simonini, M F Stamp, P C Stangeby¹, A Taroni.

JET Joint Undertaking, Abingdon, Oxon, OX14 3EA.

¹ Institute for Aerospace Studies, University of Toronto, Ontario, Canada.



During 1991/92 a series of experiments was performed in which the divertor density was raised to the point where a sudden reduction of the particle flux to the target plates occurred [1]. The radiation from these detached plasmas can be as high as 90% of the input power, thus making it possible to run discharges with input energies far above what would otherwise be the limit of the target tiles. The primary diagnostics for assessing the radiation from these plasmas are, of course, the bolometer arrays. During 1991/92 there were three such arrays, two spanning the entire plasma as viewed from a main horizontal port ($R = 5.8$ m, $Z = \pm 0.5$ m), and one vertical camera which viewed virtually the entire plasma except the divertor. In addition, there is data available from a CCD camera and from several discrete visible spectroscopy views. The geometry of the plasma and of these visible lines-of-sight are shown in Fig. 1. The divertor target tiles shown as boxes in Fig. 1 were made of beryllium while the rest of the divertor region was covered with graphite. This significantly complicates the analysis, since both surfaces quickly become a mixture of the two elements.

PLASMA MODELS

In order to estimate the power radiated from detached plasmas, some model of the background plasma is required. Ideally, one would construct a completely self-consistent model including the radiation losses from the various plasma species. In reality this is still not possible and compromises are necessary. Here two models of the background plasma are constructed and the resulting radiation patterns compared with experiment.

An analytic model for detached plasmas has been proposed whereby the plasma momentum along open field lines is reduced by neutral-ion charge exchange collisions [2,3]. In this model the SOL is divided into two regions, one dominated by ion-neutral collisions and the other by ionisation and electron heat conduction:

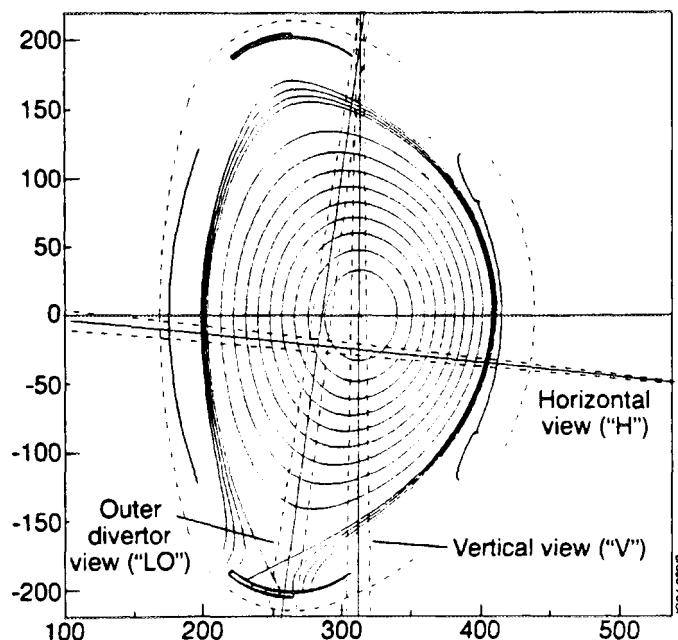
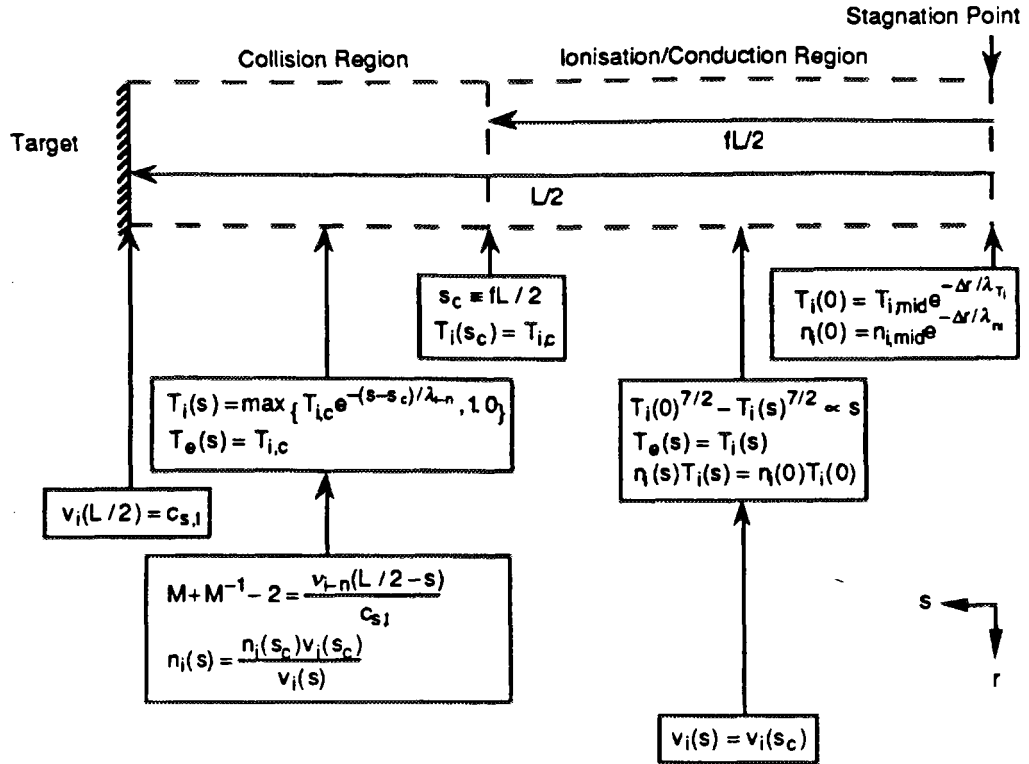


Figure 1: Viewing lines of the visible spectroscopy overlaid on the plasma magnetic geometry for JET pulse 26848.



There are seven inputs to this model: f , the position of the entrance of the collision region as a fraction of the SOL length (0.55 in the simulations shown below); $T_{i,mid}$, the ion temperature on the separatrix at the stagnation point (75 eV); $n_{i,mid}$, the ion density on the separatrix at the stagnation point ($4.3 \times 10^{19} \text{ m}^{-3}$); λ_{T_i} , the ion temperature scrape-off length at the outer midplane (2 cm); λ_{n_i} , the ion density scrape-off length at the outer midplane (2 cm); $T_{i,c}$, the ion temperature at the entrance to the collision region (2 eV); and λ_{i-n} , the ion-neutral elastic collision mean-free-path (50 cm). The advantage of this model is its flexibility in describing different lengths and therefore volumes of the collision region. This must be set against the fact that the plasma so derived is not self-consistent.

Recently, the two dimensional fluid code EDGE2D/U has been applied to the simulations of detached plasmas [4]. In some of these simulations, a first attempt at assessing the effects of impurity radiation was made using a radiation loss term first used to model carbon radiation from ASDEX plasmas [5]:

$$Q_{rad} = \alpha_{imp} n_e^2 \left(\frac{2 \cdot 10^{-18} \text{ erg-cm}^3 / \text{s}}{(T_e / 15 \text{ eV})^{1.5} + (T_e / 15 \text{ eV})^{-3}} \right)$$

In these simulations, the value of α_{imp} is spatially constant and is adjusted at each time step so as to give a prescribed total radiated power. When this total power is raised to a certain level the divertor plasma detaches, with a significant drop in the ion current to the target plates, as observed in experiment. For the background plasma used below it was assumed that 10 MW of the 15 MW input power enter the annular calculational grid, with the other

5 MW supposed lost due to radiation from the core. In addition, 6 MW of impurity radiation was assumed, roughly matching the measured total radiated power.

COMPARISON WITH EXPERIMENTAL RESULTS

In order to assess the radiation from different hydrogen and impurity species, the two background plasmas were used as input to the DIVIMP impurity transport code [6], which has been coupled to NIMBUS, the same neutral transport code used with EDGE2D/U. In each case, two DIVIMP runs were performed, one assuming the targets to be pure beryllium (run A/Be for the analytic plasma background and run E/Be for the EDGE2D/U background plasma) and the other pure carbon (runs A/C and E/C). Comparison of the code results with experiment is given in Table 1.

The most obvious discrepancy between model and experiment is in the radiated power. In addition, neither carbon simulation can reproduce the observed carbon emission even assuming that the beryllium tiles behave as though they were pure carbon. In contrast, there is generally good agreement between simulation and experiment for the beryllium signals. Thus, it is concluded that beryllium cannot be the main radiating species.

In contrast to the beryllium profiles, the deuterium radiation is not well modelled by the EDGE2D/U simulation. The ratio of measured to simulated D_α is 3 at the target, suggesting the source there is approximately correct, while the same ratio is 70 along the vertical chord. By varying the length of the collision region in the analytic model, it is possible to study the variation in deuterium leakage from the divertor and the accompanying affect on radiated power. The analytic background plasma shown in Table 1 was the most successful attempt at reproducing the deuterium signals. Such a match requires a cold plasma which extends far beyond the X-point into the SOL. Even in such an extreme example, the total deuterium radiation is less than 1 MW and does not account for the measured radiated power.

There are three possible reasons for the discrepancy between the predicted and measured carbon content of the plasma. Firstly, the plasma is not in steady state. These plasmas were ELMy throughout. Due to the limitations of the probes, the plasma we model is that which is seen between ELMs. Secondly, chemical sputtering from the targets and from the walls may play an important role in carbon release at these low temperatures. Thirdly, non-thermal distribution functions may be important. In cases where the bulk of the plasma is below the physical sputtering threshold, a small fraction of fast particles would dominate the impurity yield. With this in mind, it is tempting to scale the carbon content of the plasma to the influx measured at the outer target. This would result in a radiated power of 16 MW. It also, however, results in an order of magnitude overprediction of the carbon signals along the vertical and horizontal channels. The carbon radiation will, however, be dominated by such a large source at the target.

	Exp.	E/C	E/Be	A/Be	A/C
Total Radiated Power (MW)	11.5	0.41	0.54	0.96	0.86
Impurity Radiation (MW)	-	0.026	0.16	0.10	0.003
Hydrogen Radiation (MW)	-	0.38	0.38	0.86	0.86
Isat inner (A/cm ²)	1-2*	14	14	7.3	7.3
Isat outer (A/cm ²)	3-4	10	10	2.3	2.3
D _α (LO)	5 ²⁰	1.6 ²⁰	1.6 ²⁰	4.5 ²⁰	4.5 ²⁰
D _α (V)	9 ¹⁹	1.3 ¹⁸	1.3 ¹⁸	5.6 ¹⁹	5.6 ¹⁹
D _α (H)	1 ¹⁹	3.2 ¹⁷	3.2 ¹⁷	1.2 ¹⁸	1.2 ¹⁸
Be II 4361 (LO)	5 ¹⁷	-	2.5 ¹⁷	9.9 ¹⁶	-
Be II 5270 (V)	1 ¹⁶	-	7.5 ¹⁵	2.8 ¹⁵	-
Be II 5270 (H)	2 ¹⁵	-	3.0 ¹⁵	1.9 ¹⁵	-
C II 6578 (LO)	1.5 ¹⁸	2.5 ¹⁵	-	-	2.0 ¹⁴
C III 4647 (V)	1.5 ¹⁸	3.1 ¹⁶	-	-	1.0 ¹⁵
C III 4647 (H)	7.5 ¹⁷	2.0 ¹⁶	-	-	4.5 ¹⁵

Table 1: Comparison of experimental measurements with signals synthesized from the four different simulations described in the text. *The measured ion saturation current from the inner probe is known to be low due to shadowing by the target tile.

CONCLUSIONS

In simulations with high radiated power fractions, it is possible to produce the drop in ion current to the divertor targets typical of detached plasmas. Despite the fact that these experiments were performed on beryllium target tiles, radiation from deuterium and beryllium cannot account for the measured power losses. The neutral deuterium levels in the SOL in these plasmas are higher than the model predicts. This may be due to leakage from the divertor or to additional wall sources related to the non-steady nature of these plasmas. In contrast, a surprisingly high level of carbon is present in these discharges; higher even than would be predicted were the divertor target tiles pure carbon. This level may well be large enough to produce the measured radiation, but more detailed information on the source profile is required.

- [1] S. Clement, S.K. Erents, N. Gottardi, *et al.*, 19th EPS Conf. on Contr. Fusion and Plasma Phys., Innsbruck (1992) II-723.
- [2] K. Borrass and P.C. Stangeby, 20th EPS Conf. on Contr. Fusion and Plasma Phys., Lisboa (1993) II-763.
- [3] P.C. Stangeby, Nucl. Fusion **33** (1993) 1695.
- [4] A. Taroni, G. Corrigan, R. Simonini, J. Spence, and S. Weber, to be published in the proceedings of the 11th PSI Conference, Mito (1994).
- [5] R. Schneider, B. Brahms, D. Reiter, *et al.*, Contributions to Plasma Phys. **33** (1992) 450.
- [6] P.C. Stangeby and J.D. Elder, J. Nucl. Mater. **196-198** (1992) 258.



FR9701762

Excitation of Global Alfvén Eigenmodes by RF Heating in JET

W Kerner, D Borba, A Fasoli¹, C Gormezano, G Huysmans,
F Porcelli, S Sharapov², D Start.

JET Joint Undertaking, Abingdon, Oxon, OX14 3EA.

¹ CRPP, Lausanne, Switzerland.

² RRC Kurchatov Institute, Moscow, Russia.



INTRODUCTION

The alpha-particle confinement of future D-T experiments at JET can be severely degraded by Global Alfvén Eigenmodes (AE). Scenarios for the excitation of Alfvén eigenmodes in usual (e.g. D-D) plasmas are proposed, which provide a MHD diagnostic and allow the study of the transport of super-Alfvénic ions.

Active studies with separate control of TAE amplitude and energetic particle destabilisation, measuring the plasma response, give more information than passive studies, in particular concerning the damping mechanisms. The linear regime of the Alfvén physics can be exploited for a MHD diagnostic, where no significant perturbation of the plasma is required.

The TAE excitation can be achieved by means of the saddle coils, modelled in Ref. [1,2], and the ICRH antenna. In this paper the experimental method is introduced together with a theoretical model for RF excitation.

EXPERIMENTAL METHOD

Whereas the saddle coils constitute a direct drive of global Alfvén waves via oscillatory currents with a frequency range of 20 - 500kHz (covering BAE, TAE and EAE), the ICRH antenna operates at much higher frequencies. Direct excitation has, consequently, to be achieved by frequency/amplitude modulation or by the nonlinear interaction of two fast waves whose frequency differ by the AE frequency. The beat wave excitation, satisfying energy ($\omega_1 - \omega_2 = \omega_{\text{TAE}}$) and momentum ($\vec{k}_1 - \vec{k}_2 = \vec{k}_{\text{TAE}}$) balance, relies on the generation of a volume current, \vec{j}_{nl} , inside the plasma with a power transfer $\langle \vec{j}_{\text{nl}} \cdot \vec{E}_{\text{TAE}}^* \rangle$ into the TAE. The corresponding radial magnetic field amplitude can be large at marginal stability ($\gamma_{\text{TAE}} \rightarrow 0$), $\delta B_r / B_0 \approx \omega_{\text{TAE}} / \gamma_{\text{TAE}} \cdot v_{\text{osc}}^2 / v_A^2$. A second method is given by the generation of high-energy ions, which subsequently provide the drive for AE destabilisation. Due to the high power of the JET ICRH antennae, these methods could generate finite-amplitude AE, allowing a systematic study of the AE enhanced energetic particle transport.

In the active studies the frequency in the driver is swept, correspondingly the modulation amplitude/frequency or the difference between the two driving RF wave frequencies. When a global Alfvén eigenmode is encountered, a resonance appears in the plasma response. The corresponding width gives a measure for the damping.

Synchronous detectors, whose reference signal is taken directly from the saddle coil exciter or, in the beat wave case, from the frequency difference of the two fast waves, are used to diagnose the plasma response. In phase ('real') and quadrature ('imaginary') components are provided. Different signals (up to 48) are considered, namely the active saddle coils for the antenna impedance, the passive saddle coils for the perturbed \vec{B}_r (n-mode analysis), the magnetic probes for the perturbed \vec{B}_θ (n- and m-mode analysis) and other space-resolved, non-magnetic diagnostics, such as ECE and reflectometry, to resolve the spatial mode structure

The Data analysis fits the antenna-plasma-detectors transfer function with a rational fraction, with the discrete AE resonances being represented as poles in the complex plane, where the real part corresponds to the frequency and the imaginary part to the damping or drive. When Alfvénic fast particles ($v \sim v_{\text{Alfvén}}$) are produced in the plasma, e.g. by ICRH or NBI, an AE instability driving effect is produced and the imaginary part of these poles is modified.

WAVE-PARTICLE INTERACTION

Theoretical estimates for the RF drive of the TAE mode are based on a perturbative approach valid for a small drive. In the hybrid kinetic-MHD model a quadratic form is constructed, where the non-adiabatic, kinetic contribution $\delta W_{\text{hot}} = -\frac{1}{2} \int d^3x d^3v L^{(1)*} f^{(1)}$ is defined by the perturbed Lagrangian of the particle motion in the drift approximation and the perturbed distribution function $f^{(1)}$ Ref. [3]. The growth rate is proportional to its imaginary part, i.e. $\gamma \propto \text{Im}\{\delta W_{\text{hot}}\}$. Here $L^{(1)} = -(mv_{\parallel}^2 - \mu B) \vec{\xi} \cdot \vec{\kappa} + \mu B \nabla \cdot \vec{\xi} = -(mv_{\parallel}^2 + \mu B) \vec{\xi} \cdot \vec{\kappa}$, where $\vec{\kappa}$ denotes the curvature of the magnetic field and $\vec{\xi}$ the MHD perturbation. It holds that $\tilde{L}^{(1)} = \hat{L}^{(1)} \exp(-i n \phi^{(-)})$ is periodic in τ . Therefore, a Fourier expansion is possible $\tilde{L}^{(1)}(\tau) = \sum_{-\infty}^{\infty} Y_p(E, \mu, P_\phi; \sigma) \exp(-ip\omega_b\tau)$, where $\omega_b \equiv 2\pi/\tau_b$. The Fourier coefficients are defined as $Y_p(E, \mu, P_\phi; \sigma) = \oint \frac{d\tau}{\tau_b} \tilde{L}^{(1)} \exp(ip\omega_b\tau)$. Integration over the gyro angle and poloidal angle leads to

$$\delta W_{\text{hot}} = -\frac{2\pi^2 c}{Zem^2} \int \sum_{\sigma} dP_{\varphi} dE d\mu \tau_b (\omega - n^{\circ} \omega_*) \frac{\partial F}{\partial E} \sum_p \frac{|Y_p|^2}{\omega + n^{\circ} \langle \dot{\phi} \rangle + p\omega_b}. \quad (1)$$

Resonances appear for $\omega + n^{\circ} \langle \dot{\phi} \rangle + p\omega_b = 0$. The equilibrium distribution function $F = f^{(0)}$ is a function of the adiabatic invariants, i.e. $F = F(E, \mu, P_{\varphi})$.

In order to enable a fast analysis of JET discharges several approximations are introduced in form of a analytic, small-orbit approximation and a local treatment on a flux surface. The evaluation of δW_{hot} requires still the calculation of the bounce-average Fourier components, Y_p and the sum of the resonant contributions integrated over $\Lambda = \mu B_0 / E$.

In the case of passing particles good agreement with the results of Betti and Freidberg, [4], is found as shown in Fig. 1. For RF heated JET discharges the fast particle distribution is modelled by a slowing down distribution, Fig. 2, and by the Stix approximation $f_h^{(0)} = \exp\left(-\frac{E}{T_{\text{eff}}}\left(1 + H\left(\frac{E}{E_j}\right)\right)\right)$ [5], Fig. 3. The results for deeply trapped particles, i.e. $\Lambda = 1$, and for on-axis heated particles, i.e. $\Lambda = 1 - \epsilon$, are displayed in the figures.

CONCLUSIONS

RF Heating provides interesting schemes to: i) excite TAE directly by nonlinear wave-wave drive and ii) generate sufficiently many energetic ions to destabilise the TAE, i.e. wave-particle drive.

The stability analysis shows that it is possible to destabilise TAE modes in JET discharges via particle resonances for relatively low $\beta_{\text{hot}} \sim 10^{-4}$ in low density plasmas, $n_e \sim 10^{19} \text{ m}^{-3}$, if ions with very high energy ($\geq 1 \text{ MeV}$) are generated by RF heating. These results are in qualitative agreement with the reported observation of TAE activity in JET [6]. It is emphasised that improved high-frequency diagnostics will enable more detailed comparison between theory and experiments.

Utilising the high-accuracy detection installed for the saddle coils excitation, i.e. frequency sweeping, synchronous detection and measurement of the plasma response, allows for accurate, independent determination of the damping effects and the destabilisation.

REFERENCES

- [1] L. Villard, J. Vaclavik, S. Brunner, H. Lütgens and A. Bondeson, Proc. 20th Eur. Conf. on Controlled Fusion and Plasma Physics, ed. by J.A. Costa Cabral, M.E. Manso, F.M. Serra, F.C. Schuller, EPS Lisbon, (1993) IV, 1347.
- [2] G.T.A. Huysmans, H. Holties, W. Kerner, J.P. Goedbloed, D. Borba and F. Porcelli, *ibidem* I, 187.
- [3] F. Porcelli, R Stankiewicz, W. Kerner, H.L. Berk Phys. Plasmas 1, 470, 1994.
- [4] R. Betti and J.P. Freidberg Phys Fluids B4, 1465, 1992.
- [5] T.H. Stix, Nuclear Fusion 15, 737, 1975.
- [6] S. Ali-Arshad, D.J. Campbell, JET-P(94)12

STABILITY DIAGRAMS

Local stability analysis of TAE modes with $n=3$, $m=3,4$ localised at $q=7/6$, as a function of β_{hot} for the following plasma parameters: $T_e=T_i=10$ Kev, $E_{hot}= 1 \rightarrow 3$ Mev, $B_T=2.8$ T, $n_e=n_i=10^{19}m^{-3}$ at $V_\alpha/V_A=1$. Different values of V_α/V_A are scanned by changing the density n_e and keeping the magnetic field constant.

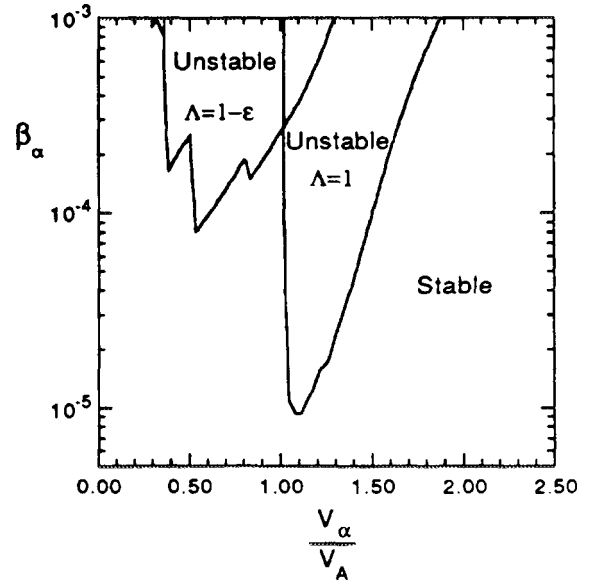
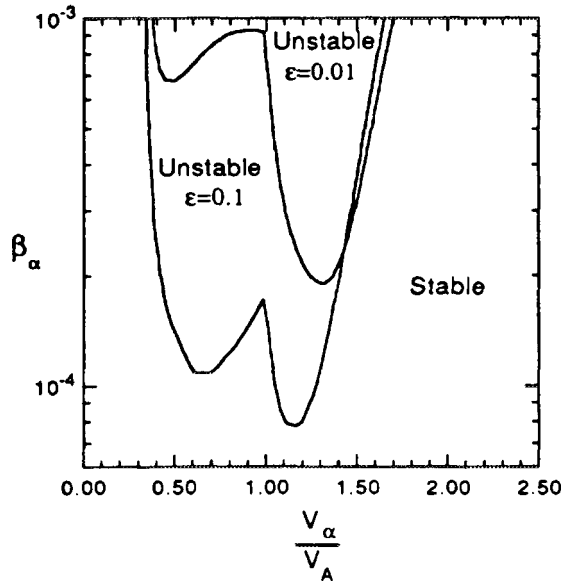


Figure 1 Isotropic slowing down distribution for particles with the birth energy of 3.5 MeV

Figure 2 Anisotropic slowing down distributions for different pitch angles

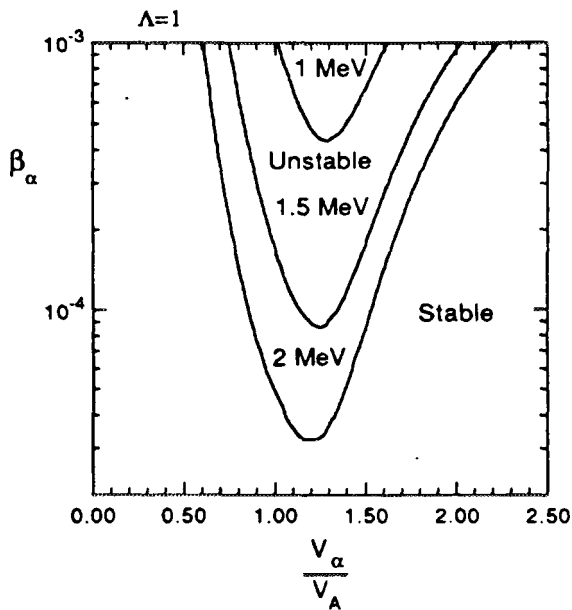


Figure 3a Stix distribution function for deeply trapped particles

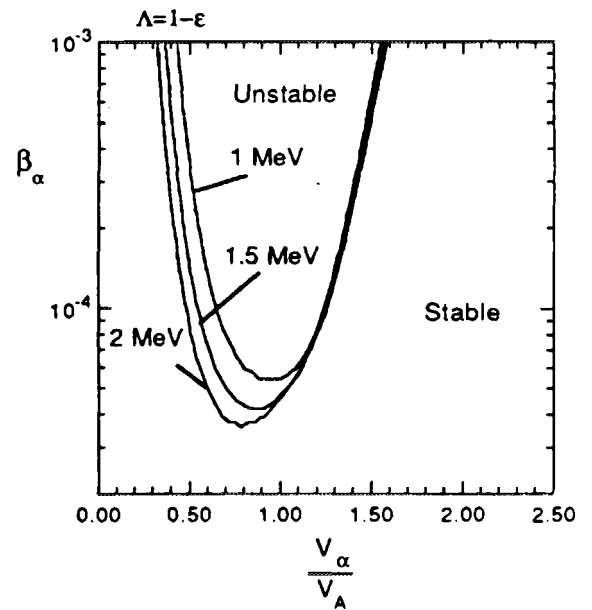


Figure 3b Stix distribution function for on-axis heated trapped particles



FR9701763

The Comparative Analysis of the Different Mechanisms of Toroidal Rotation in Tokamaks

R Sabot¹, V Parail².

JET Joint Undertaking, Abingdon, Oxon, OX14 3EA.

¹ Present address; Association Euratom-CEA, CE Cadarache,
St Paul-lez-Durance, France.

² Permanent address: Russian Research Centre
“Kurchatov Institute”, Moscow, Russia.



Recent results on the physics of L-H transition [1] emphasise the role of the toroidal plasma rotation as one of the possible mechanism for suppression of plasma turbulence. Several mechanisms are believed to contribute to the toroidal plasma rotation. We present the results of numerical analysis of the toroidal rotation on JET for which we include the effects of: the neoclassical viscosity due to banana and ripple trapped particles, the anomalous viscosity due to plasma turbulence, the momentum input by NBI and ion momentum loss near the separatrix due to prompt ion losses.

Though all the mechanisms under consideration have a kinetic nature, we used their fluid form, the momentum balance equation for the ions is thus:

$$n_i m_i \frac{d\mathbf{v}_i}{dt} = n_i e_i (\mathbf{E} + \mathbf{v}_i \times \mathbf{B}) - \nabla p_i - \nabla \cdot \bar{\pi}^{\text{neo}} - \nabla \cdot \bar{\pi}^{\text{rip}} - \nabla \cdot \bar{\pi}^{\text{ano}} + \mathbf{F}^{\text{NBI}} + \Gamma_r^{\text{edge}} \times \mathbf{B} \quad (1)$$

where p_i is the ion pressure, $\bar{\pi}^{\text{neo}}$ the neoclassical viscous stress tensor, $\bar{\pi}^{\text{rip}}$ the viscous tensor due to ripple trapped particles [2], $\bar{\pi}^{\text{ano}}$ the anomalous viscous tensor [3], \mathbf{F}^{NBI} the momentum source from Neutral Beam and Γ_r^{edge} the prompt ion losses current [4].

We consider only steady state and neglect inertia and variations of temperature or density on flux surfaces. The toroidal projection of (1) leads after averaging over flux surfaces to :

$$-\langle R^2 \nabla \varphi \cdot \nabla \cdot \bar{\pi}^{\text{rip}} \rangle - \langle R^2 \nabla \varphi \cdot \nabla \cdot \bar{\pi}^{\text{ano}} \rangle + \langle R^2 \nabla \varphi \cdot \mathbf{F}^{\text{NBI}} \rangle + n_i e_i \langle R^2 \nabla \varphi \cdot (\Gamma_r^{\text{Edge}} \times \mathbf{B}) \rangle = 0 \quad (2)$$

Using the circular magnetic field model $\mathbf{B} = B_0 / (1 + \epsilon \cos \theta) ((1 + \delta(r, \theta) \cos(N\varphi)) \mathbf{u}_\varphi + \Theta \mathbf{u}_\theta)$ with $\epsilon = r/R_0$, $\Theta = \epsilon/q$, δ the ripple value and N the number of coils, we estimated the ripple contribution in the ripple plateau regime [3], [5]:

$$\langle R^2 \nabla \varphi \cdot \nabla \cdot \bar{\pi}^{\text{rip}} \rangle = \frac{\sqrt{\pi} n_i T_i N \langle \delta^2 \rangle}{v_{\text{thi}}} \frac{\epsilon^3}{\epsilon^3 + (Nq\delta)^3} \bar{v}_\varphi \quad (3)$$

where v_{thi} is the ion thermal velocity and $\bar{v}_\varphi = \langle (B_0/B_\varphi) v_\varphi \rangle$ the flux average of the toroidal velocity times B_0/B_φ . The anomalous stress tensor is estimated from [3]. For simulation of JET shots we used for \mathbf{F}^{NBI} the

Neutral Beam momentum deposition profile computed by a multiple pencil beam code. This leads to the differential equation for \bar{v}_φ :

$$\frac{1}{r} \frac{\partial}{\partial r} \left(r \mu \frac{\partial \bar{v}_\varphi}{\partial r} \right) - \frac{\sqrt{\pi} n_i T_i q N \langle \delta^2 \rangle}{v_{\text{thi}} R_0} \frac{\epsilon^3}{\epsilon^3 + (Nq\delta)^3} \bar{v}_\varphi + \langle F_\varphi^{\text{NBI}} \rangle + n_i e_i \langle v_r^{\text{edge}} \rangle B_0 \Theta = 0 \quad (4)$$

where $\mu = n_i m_i \mu_0$ is the anomalous viscosity.

Non ambipolar losses of ions at the plasma edge can also contribute to plasma rotation. In spite of the fact that such losses are important only within one poloidal larmor radius inside the LCFS, they can be a significant source of momentum for the bulk plasma due to the anomalous viscosity which redistributes the toroidal momentum along minor radius. We take the losses value from [4]:

$$\text{div}(n_i < v_r^{\text{edge}} >) = - \frac{n_i v_i}{\sqrt{v_{*i} + (\rho_{\theta i} e_i E_r / T_i)^4}} \exp\left(-\sqrt{v_{*i} + (\rho_{\theta i} e_i E_r / T_i)^4}\right) \quad (5)$$

with $v_{*i} \equiv v_i R q / \epsilon^{3/2} v_{\text{thi}}$, $\rho_{\theta i}$ is the poloidal ion larmor radius and v_i the ion collision frequency. To obtain expression for the radial electric field we should use the poloidal and radial projection of (1). The poloidal projection comprises only two terms: the momentum produced by prompt ions losses and the neoclassical viscosity for which we obtain [3]:

$$\langle R^2 \mathbf{B}_\theta \cdot \nabla \cdot \bar{\pi}^{\text{neo}} \rangle = - (n_i \sqrt{\pi} m_i v_{\text{thi}} \epsilon R_0 B_0 / 6) (v_\theta - v_\theta^{\text{neo}}) \quad (6)$$

with $v_\theta^{\text{neo}} = -(1/2 e_i B_0) [dT_i / dr]$. Substituting the average poloidal velocity v_θ in the radial projection of (1) gives the radial electric field. The differential equation for the radial current together with (4) closes the differential system for the toroidal rotation:

$$\frac{1}{r} \left(\frac{\partial r n_i < v_r^{\text{edge}} >}{\partial r} \right) = - \frac{n_i v_i}{\sqrt{x}} \exp(-\sqrt{x}) \quad (7)$$

$$\text{with } x = v_{*i} + \left(\rho_{\theta i} \left(\frac{d \ln n_i}{dr} + \frac{3}{2} \frac{d \ln T_i}{dr} \right) + \frac{2 \bar{v}_\phi}{v_{\text{thi}}} - \frac{12 R_0 < v_r^{\text{edge}} >}{\sqrt{\pi} \rho_i \epsilon} \frac{1}{v_{\text{thi}}} \right)^4.$$

The system (4,7) was solved with the following boundary condition. Inside the SOL the only drag force is the anomalous viscosity, and it should compensate the momentum produced by losses of ions in the SOL. The integration over the SOL leads to:

$$-\mu \frac{d \bar{v}_\phi}{dr} \Big|_a 4 \pi^2 R_0 a = n_i \Delta 4 \pi^2 R_0 a \frac{C_s}{2 \pi R_0} m_i \bar{v}_\phi \quad (8)$$

where a is the minor radius, C_s the sound speed and the SOL width Δ is estimated by:

$$\frac{\Delta^2}{\mu_0} = \frac{L_{//}}{C_s} = \frac{2 \pi q R_0}{C_s} \quad (9)$$

This leads to the boundary condition:

$$\bar{v}_\phi(a) + \sqrt{\frac{2 \pi R_0 \mu_0}{q C_s}} \frac{d \bar{v}_\phi}{dr} \Big|_a = 0 \quad (10)$$

System (4,7) together with boundary condition (10) was solved for typical JET condition: $R_0=3$ m, $a=1$ m, $B_0=1.5-2.8$ T, $I_{\text{plasma}}=1.5-3$ MA, $P_{\text{NBI}}=3-8$ MW, $\delta(0) < 10^{-6}$, $\langle \delta(a) \rangle = 0.3\%$ with 32 coils, $\delta(0) = 10^{-3}$, $\langle \delta(a) \rangle = 3\%$ with 16 coils. The results of numerical analysis are shown on Fig 1-2.

Fig 1a and 1b show the modifications produced by different damping mechanisms of the plasma toroidal velocity profile induced respectively by NBI and prompt ion losses. With constant anomalous viscosity, the edge rotation induced by prompt ion losses is important and can dominate the rotation produced by NBI. But

if the anomalous viscosity increases toward the edge ($\mu_0 \propto q$ or q^2), the edge rotation is strongly reduced. A large ripple (16 coils in JET, $\langle \delta \rangle = 3\%$ at the edge) can almost stop the NBI toroidal rotation for $\rho > 0.5$, and damp the edge rotation induced by ion losses.

This ripple damping was studied on JET during the 1992 campaign when plasma rotation in similar shots with 16 and 32 coils was examined [7]. In fig 2a and 2b we present the rotation profile for 2 similar shots: 27147 with 32 coils, and 27125 with 16 coils. With 32 coils the rotation velocity, measured by charge exchange, is large in the centre and decreases toward the edge. We managed to simulate it with $\mu_0 = 1.5 \text{ m}^2/\text{s}$. With only 16 coils, the central rotation is small, and almost constant for $\rho > 0.5$. With the anomalous viscosity deduced from the 32 coils shot, and including the large ripple damping we can simulated quite well the velocity profile for 16 coils including the small central value and the flat profile for $\rho > 0.5$, but we cannot explain the counter rotation shift. This could be either due to a systematic measurement error or due to an acceleration produced by the ripple, but in any case it cannot be explain by localised losses of ions at the edge.

CONCLUSIONS

The comparative analysis of the different mechanisms of toroidal plasma rotation initiation and damping was done for characteristic JET plasma parameters.

The NBI appeared to be the principal source of toroidal plasma rotation although prompt ions losses can contribute to plasma rotation near the separatrix.

In all the results we present, we take an anomalous viscosity into consideration. Its presence is compulsory to link the toroidal rotation across the minor radius. The values used (of the order of $1 \text{ m}^2/\text{s}$) correspond roughly to the values of the anomalous ion thermal diffusivity for L-mode plasma.

The ripple viscosity, although much smaller than the momentum produced by prompt ion losses at the edge, can damp this edge rotation because it exists within a much larger volume (half minor radius against a poloidal larmor radius). This damping can in particular explain the small toroidal rotation observed in the 16 coils experiment in JET.

The authors gratefully acknowledge discussions with N. Hawkes and B. Tubbing.

- [1] K. H. Burrell, et al, Plasma Phys. and Contr. Fusion Research, 34, 1859 (1992).
- [2] P. N. Yushmanov, in: Reviews of Plasma Physics, Vol. 16, ed. by B. B. Kadomsev, Consultants Bureau, New York (1990) 117.
- [3] V. Rozhansky, M. Tendler, Physics of Fluids B, 4, 1877 (1992).
- [4] K. C. Shaing, et al, in: Proceedings of the 12th International Conference on Plasma Physics and Controlled Nuclear Fusion, Nice, 1988 (IAEA, Vienna, 1989), Vol. 2, 13.
- [5] M. Coronado, H. Wobig, Physics of Fluids, 29, 427 (1986).
- [6] JET Team, in: Proceedings of the 14th International Conference on Plasma Physics and Controlled Nuclear Fusion, Wurzburg, 1992 (IAEA, Vienna, 1993), Vol. 1, 429.

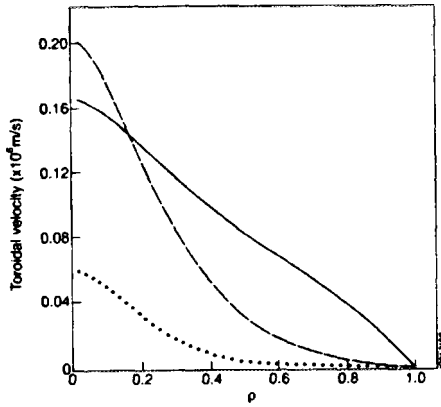


Fig 1a: Effect of ripple on the toroidal rotation generated by NBI with $\mu_0=0.5 \text{ m}^2/\text{s}$ (dotted) or $\mu_0=0.4q^2$ (dashed). Solid line- rotation without ripple losses with $\mu_0=0.5 \text{ m}^2/\text{s}$.

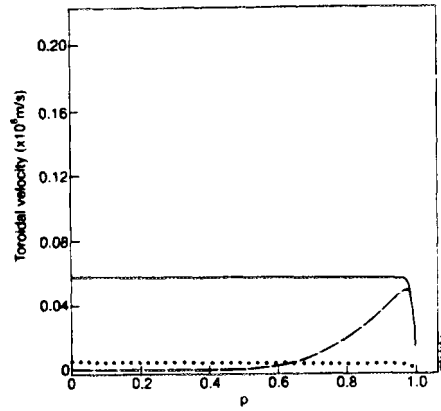


Fig 1b: Ripple (dashed) or viscous damping ($\mu_0=0.4q^2$ dotted, $\mu_0=0.5$ solid) of the toroidal rotation generated by prompt ion losses.

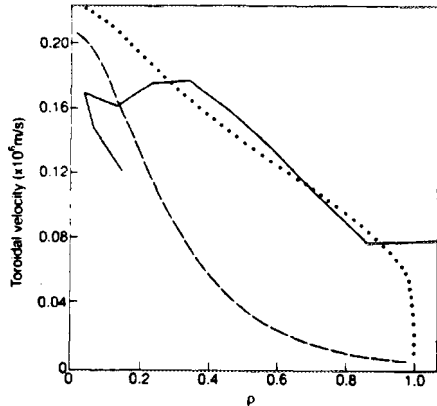


Fig 1c : Simulation of experimental rotation (solid line) including both NBI and ions losses with two different μ_0 profile: $\mu_0=0.5 \text{ m}^2/\text{s}$ (dotted) and $\mu_0=0.4q^2$ (dashed).

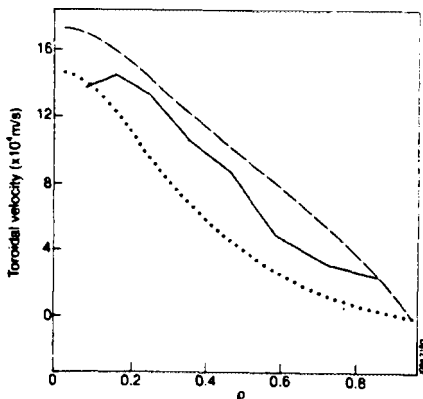


Fig 2a: The solid, dashed and dotted lines show the experimental and computed (with $\mu_0=1.5 \text{ m}^2/\text{s}$ or $1.5q^2$) toroidal rotation

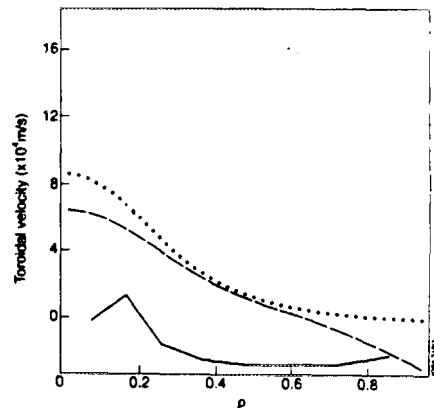


Fig 2b: The solid and dotted lines show the experimental and computed toroidal rotation with large ripple damping (16 coils), the dashed line includes edge ions losses.



FR9701764

Effect of Shear in the Radial Electric Field on Confinement in JET

D P O'Brien, B Balet, N Deliyannis,
J G Cordey, P M Stubberfield.

JET Joint Undertaking, Abingdon, Oxon, OX14 3EA.



INTRODUCTION

High confinement discharges at JET are characterised by a confinement time which rises to a factor of 3 above that of Goldston L-mode scaling. Although the transport characteristics often improve immediately following the L-H transition, the presence of ELMs can impede the development of the improved confinement. The subsequent disappearance of the ELMs has been associated with access to the second stable regime to ideal ballooning modes and is discussed in [1]. Another mechanism which has been put forward as a reason for the enhanced confinement is the stabilisation of turbulence by shear in the radial electric field [2]. In the present work the role of shear in the radial electric field during high performance beam heated and ICRH heated discharges at JET is examined.

THE ELECTRIC FIELD

The electric field is calculated from the zero order force balance equation, it contains contributions from the poloidal and toroidal rotation and the pressure gradients.

$$E_r = (Zen)^{-1} \nabla P - v_\theta B_\phi + v_\phi B_\theta$$

It has been shown that there is no significant contribution to the radial electric field from poloidal rotation [3]. We present results from two series of experiments a) beam dominated with the addition of a small amount of ICRH and b) ICRH dominated discharges, showing that for high performance ICRH heated discharges which obtain the high confinement regime there is evidence against the $\underline{E} \times \underline{B}$ flow stabilisation. For beam heated discharges we show that the main contribution to the radial electric field comes from the toroidal rotation achieved during the enhanced confinement phase, with this phase being marked by a "spin up" in the toroidal velocity in the plasma interior, giving some shear to the radial field profile. However in high performance beam heated discharges in which a small amount of ICRH heating was applied, the effect of the ICRH was to reduce the toroidal rotation and its shear substantially, and there was no deterioration in the confinement time. For the ICRH dominated discharges,

the confinement improves over a substantial region of the plasma, however the radial electric field shear is mainly in the edge region due to the large pressure gradients in this region.

NBI HEATED DISCHARGES

In JET, there is no direct evidence that shear suppression of turbulence is responsible for the improved confinement. However it is seen from Fig. 1 that in two similar discharges, one which obtains VH-mode and one which does not, there is drastically different behaviour in the toroidal rotation. In the discharge which obtains VH-mode (26087) the toroidal rotation and its shear increases continuously throughout the plasma cross-section. In the discharge which remains in H-mode, the toroidal rotation and its shear through most of the plasma cross-section drop continuously during the H-mode phase, following an initial rise after the L→H transition.

For beam heated discharges the main contribution to E_r comes from the toroidal rotation term. We see from Fig. 3 that during the enhanced confinement phase of the discharge there is an increase in the radial electric field and its shear over a substantial fraction of the plasma volume. CXRS measurements from which the rotation is determined have a radial resolution of 10 to 16 cm. There is no evidence of the change in rotation preceding change in confinement.

ICRH HEATED DISCHARGE COMPARED TO NBI HEATED DISCHARGE

For ICRH heated discharges the main contribution to E_r comes from the pressure gradients which exist close to the edge of the plasma during the enhanced confinement phase with both the toroidal and poloidal rotations being negligible. We see from Fig. 2 that the radial electric field is small except for a region close to the edge. Kinetic profiles near the edge were generated using the microwave reflectometer (for electron density) and heterodyne radiometer (for electron temperature).

COMBINED ICRH, NBI HEATING

In these types of pulses a small amount (~2MW) of ICRH was applied, there is some evidence against the $E \times B$ flow stabilisation. The effect of the ICRH was to reduce the toroidal rotation and the $E \times B$ flow.

Consider pulse 26038 a reference pulse with 15 MW of NBI and no ICRH compared with pulse 26043 in which additionally there is a small amount of ICRH injected, just after the L→H transition. We see from Fig. 3a and Fig. 3b there is quite a substantial drop in the

rotation and its shear when the ICRH is applied. The confinement time is actually larger in the pulse with ICRH Fig. 5. In pulse 26043 the ICRH was applied just after the L→H transition.

CONCLUSIONS

The role of the radial electric field during enhanced confinement of JET discharges has been studied. From an examination of NBI, ICRH and combined NBI, ICRH discharges which achieve enhanced confinement there appears to be some evidence against the $E \times B$ flow stabilisation in these discharges. Further experiments at JET are planned in order to study this problem in more detail.

REFERENCES

- [1] N. Deliyakis et al. The VH-mode at JET, JET-P(93)82.
- [2] Burrell et al. General Atomics Report GA-A 21308, 1993.
- [3] N. Hawkes, EPS, Lisbon, 1993.
- [4] C.M. Greenfield et al., Plasma Phys. Control. Fusion 35 (1993) B263-B276

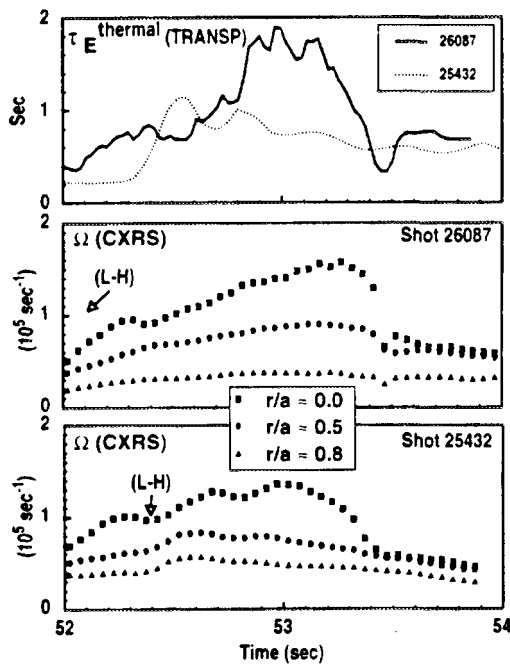


Fig. 1. Time development of two discharges: shot 26087 (SN, $I_p = 3.2$ MA, $B_T = 2.9$ T, $P_{NBI} = 14.6$ MW), which obtains VH-mode, and shot 25432 (DN, $I_p = 3.1$ MA, $B_T = 2.9$ T, $P_{NBI} = 15.6$ MW) which does not. The discharge which obtains VH-mode is characterised by toroidal rotation which is increasing everywhere in the plasma during the H and VH-mode phases. In contrast the discharge which remains in H-mode exhibits toroidal rotation which decreases everywhere along with the confinement time. The toroidal rotation is plotted at different major radii, as indicated.

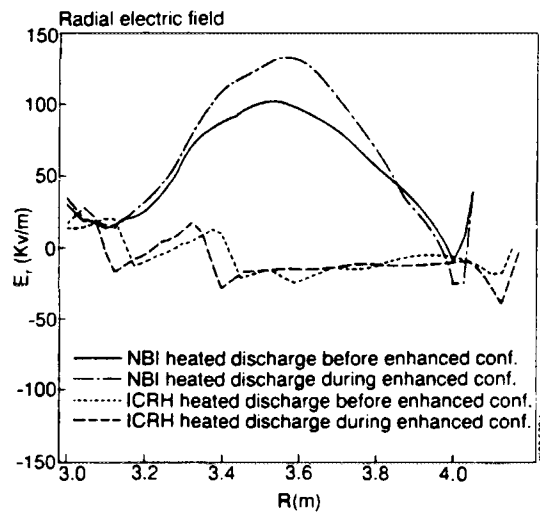


Fig. 2. The radial electric field profiles of two discharges during the H- and VH-mode phases of the discharge: shot 26087 (SN, $I_p = 3.2$ MA, $B_T = 2.9$ T, $P_{NBI} = 14.6$ MW) which is NBI heated and shot 25264 (DN, $I_p = 1.0$ MA, $B_T = 2.8$ T, $P_{ICRF} = 7$ MW) which is ICRF heated. The NBI heated discharge shows a significant steepening of the radial electric field which is mainly due to toroidal rotation. In comparison the ICRF heated discharge has little radial electric field except near the edge of the plasma where it is due to high density gradients.

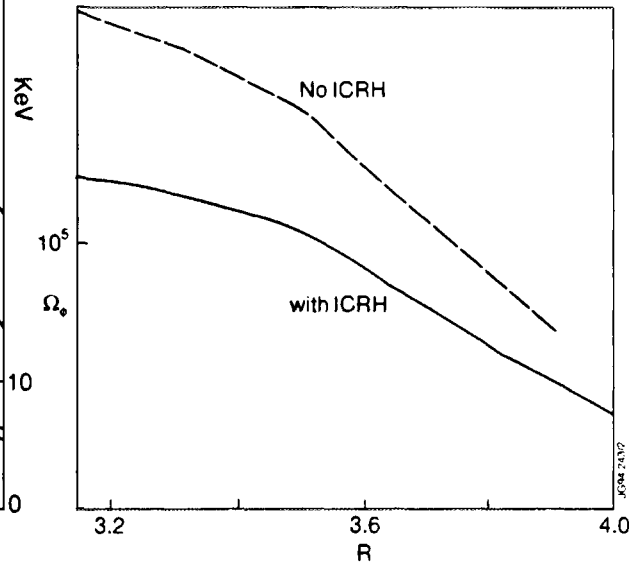
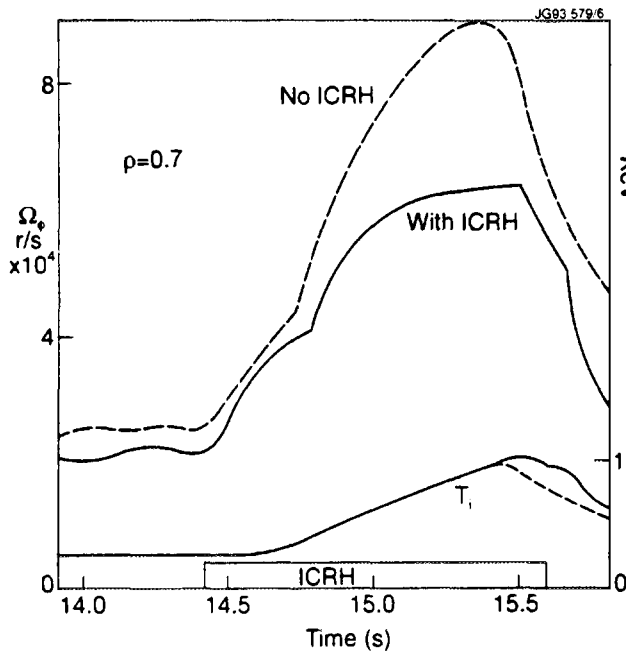


Fig. 3a. The time development of the plasma rotation of two discharges at a normalised radius of $\rho = 0.7$, comparing the reference discharge S26038 (DN, $I_p = 3.2$ MA, $B_T = 2.9$, $P_{NBI} = 15$ MW, $P_{ICRF} = 0$) which has no ICRF heating to the discharge S26043 (DN, $I_p = 3.2$ MA, $B_T = 2.9$, $P_{NBI} = 15$ MW, $P_{ICRF} = 1.8$ MW) which has in addition to the NBI heating, 1.8 MW of ICRF.

Fig. 3b. Comparison of the rotation profiles. We see that the shear in the toroidal rotation and hence E_r can be reduced by applying ICRH.

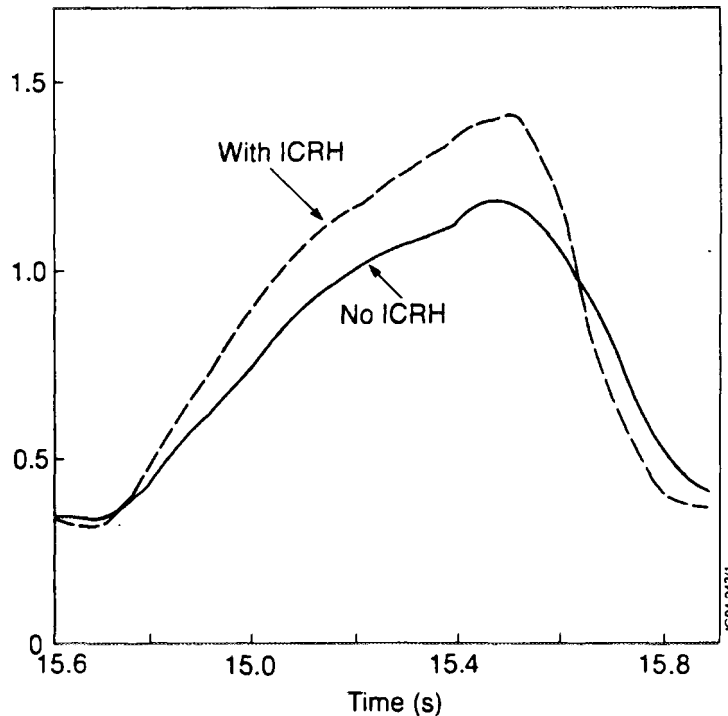


Fig. 4. The confinement time of the reference discharge 26038 compared with that of the discharge with some ICRH.



FR9701765

Plasma Transport Properties at the L–H Transition and High Performance Phase of JET Discharges

V V Parail¹, B Balet, J G Cordey, M Erba, T T C Jones,
P J Lomas, P Smeulders, E M Springmann, P M Stubberfield,
A Taroni, K Thomsen.

JET Joint Undertaking, Abingdon, Oxon, OX14 3EA.

¹ Permanent address: Russian Scientific Centre “Kurchatov Institute”,
Moscow, Russia.



INTRODUCTION

Recently [1] an analysis of a series of low density high power JET pulses has revealed that this type of discharge can not be correctly described by conventional picture of L-H transition in accordance with which the transition is caused by an abrupt reduction of transport coefficients only in a narrow region near the separatrix. In particular it has been deduced from the fast response of the electron temperature at the transition [2] that the electron transport must change over a very wide region extending from the edge to a position approximately half way in less than a few msec time ($\Delta t \leq 4\text{msec}$) after L-H transition. TRANSP analysis shows [3] that not only χ_e , but also the ion thermal diffusivity χ_i , the effective particle diffusivity and toroidal anomalous viscosity also drop abruptly at the transition over a wide radial region outside $q = 1$ surface (fig. 1). The analysis shows also (see fig. 2) that the global energy confinement time increases more than three times in comparison with L-mode phase in the best hot ion shots, and this change also occurs in less than a few msec after L-H transition. This figure shows that there is no separate H-VH transition in these low density hot ion JET pulses, however it appears that the extent of energy confinement time increase after L-H transition depends on the intensity of plasma wall interaction.

NUMERICAL ANALYSIS

All these facts support the idea that the plasma turbulence is linked in the radial direction by the toroidicity. If the plasma turbulence does form such an extended structure with the characteristic radial correlation length Δr of the order $\sim a$, then the suppression of plasma turbulence in one place (e.g. near the separatrix) should lead to the formation of a very wide transport barrier. We will refer to this model of the L-H transition as the global one. In the conventional local model of L-H transition the characteristic speed of the modification of plasma parameters (e.g. T_e) is determined by the velocity of heat pulse propagation, whilst in the global model this speed corresponds to the group velocity of plasma turbulence. It was shown in [2] by predictive modelling that global model can easily explain experimentally observed dynamics of fast electron temperature modification after L-H transition. On the contrary, conventional local model of L-H transition, in which χ_e is reduced near plasma edge only, fails to reproduce the experimental picture if we do not use

strong nonlinear dependences of χ_e on ∇T_e or on T_e . In order to check what kind of nonlinearity is required to fit the experiment, we conducted a predictive modelling of T_e evolution after L-H transition assuming that χ_e depends on ∇T_e and T_e as follows:

$$\chi_e = \chi_0 \frac{(\nabla T_e)^{m+1}}{T_e^m}. \quad (1)$$

Analysis shows (fig. 3) that only the very extreme, unrealistically non-linear forms for χ_e ($m \gg 10$) can account for the fast response of the electron temperature in the plasma mid region. Therefore we can conclude that during L-H transition all of the plasma transport coefficients experience a very fast and large reduction over a wide radial region outside $q = 1$ surface. It is quite possible that such a strong modification of plasma turbulence can result not only in change of the value of the confinement time but also in modification of its dependence on plasma parameters (for example τ_E can change from Bohm to gyroBohm type). To investigate this problem we study the further evolution of plasma parameters beyond L-H transition. We chose hot ion H-modes ($I_p = 3\text{MA}$) pulses (#26087 and 26095) and a high β_θ H-mode pulse with $I_p \sim 1\text{MA}$ (#25264) as reference pulses and carry out a numerical analysis of these pulses with predictive transport code JETTO. The evolution of plasma density was taken from the experiment, equations for T_e and T_i were solved with the following boundary conditions:

$$-\left[\chi_{e,i} n \nabla T_{e,i} + \frac{3}{2} T_{e,i} D \nabla n_{e,i} \right]_{r=a} = \alpha_{e,i} T_{e,i} \Gamma_{\parallel r=a} \quad (2)$$

where Γ_{\parallel} is the parallel particle flow in the SOL. Numerical analysis shows that such boundary conditions allow us to reproduce the formation of a transport barriers after L-H transition when both χ_e and χ_i are significantly reduced as compared with the L-mode. We used the following expressions for χ_e and χ_i .

$$\chi_i = \chi_i^{\text{neo}} + \alpha_2^i \frac{c \nabla n T_e}{eB n} a q^2, \quad \chi_e = \alpha_1 \frac{c^2}{\omega_{pe}^2} \frac{V_{Te}}{qR} \frac{r}{R} + \alpha_2^e \frac{c \nabla n T_e}{eB n} a q^2 \quad (3)$$

Where χ_i^{neo} is the neoclassical ion thermal diffusivity, α_1, α_2^i numerical coefficients. The first term in right hand side of (2) leads to Alcator scaling, second term in (2) and (3) gives Bohm-type transport. Model (2-3) was used to simulate L-mode JET discharges with $\alpha_2^i = 3\alpha_2^e = 10^{-3}$ and $\alpha_1 = 0.71$.

The calculated temporal evolution of the electron and ion energy content for the H-mode phase of shot II 26095 is shown in fig. 4 together with experimental behaviour. The radial profiles of T_e and T_i are shown in Fig. 5 at $t = 53.3\text{s}$. Analysis of the reference

discharges show that the best agreement can be achieved if one assumes that $\alpha_2^i = 3\alpha_2^e = 10^{-4}$ in ELM free H-mode discharges. It corresponds to more than one order of magnitude reduction in ion thermal diffusivity near plasma edge. This reduction is so big that ion transport becomes of the order of neoclassical in the inner half of plasma column. This is most easily seen for the 1MA discharge, where when $\chi_i^{\text{neo}} \sim q^2$ becomes so large that even the very moderate assumption $\chi_i \simeq 3\chi_i^{\text{neo}}$ leads to underestimation of ion temperature and energy content.

CONCLUSIONS

Both electron and ion thermal diffusivities are reduced by one order of magnitude everywhere, not only in a narrow region near separatrix during the L-H transition. There is no separate H-VH transition on JET, this "transition" corresponds to (coincides with) the cessation of ELMs. In the ELM free phase ion transport in the core is close to its neoclassical value, but probably rises towards plasma edge (however still remaining much less than it was in L-mode). The best agreement with experiment is obtained with the model which simultaneously takes into account both the global reduction of Bohm type anomalous transport in plasma core (which probably changes confinement from Bohm to gyroBohm) and formation of temperature pedestal near plasma edge.

REFERENCES

- [1]. Neudatchin, S.V., Cordey, J.G., and Muir, D.G. 20th EPS Conf. on Contr. Fus. and Plasma Phys., Lisboa, 1993 part II, p. 83.
- [2]. Parail, V.V., Cordey, J.G. Springmann, E. and Taroni, A., JET-P(93)87, submitted to Nuclear Fusion.
- [3]. Cordey, J.G. Muir, D.G., Neudatchin, S.V. Parail, V.V. et al., Workshop on H-mode Confinement, Japan 1993, will be published in Plasma Physics and Contr. Fusion, 1994.
- [4]. Conner, J.W., Hastie, R.J., and Taylor, J.B., Proc. Roy. Soc. London Ser. A 365, 1 (1979).
- [5]. Romanelli, F., and Zonca, F., 20 EPS Conf. on Contr. Fusion and Plasma Phys. Lisboa, 1993, part IV, p. 1383.
- [6]. Le Brum, M.J. et al., Phys. Fluids B, 5 (1993) 752.

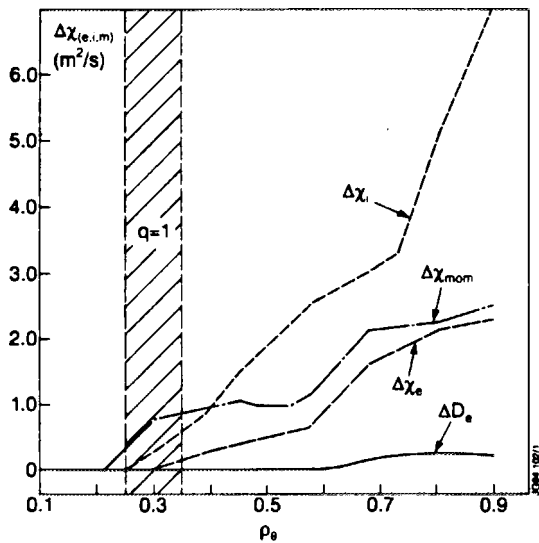


Fig. 1 . Modification of plasmas transport coefficients after L-H transition

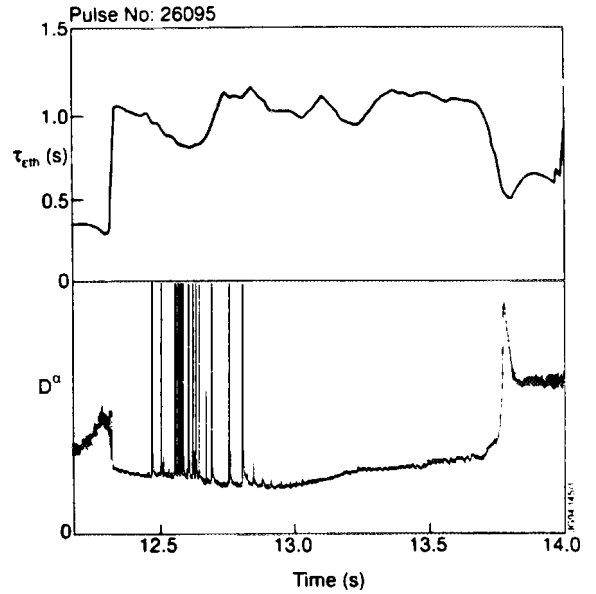


Fig. 2. Temporal evolution of τ_{eth} and D_{α} signal in hot-ion shot

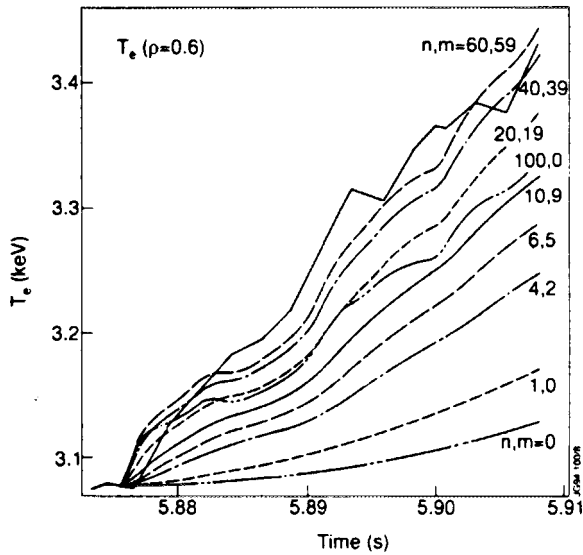


Fig. 3. Evolution of calculated T_e ($\rho = 0.6$) for different values of m,n .

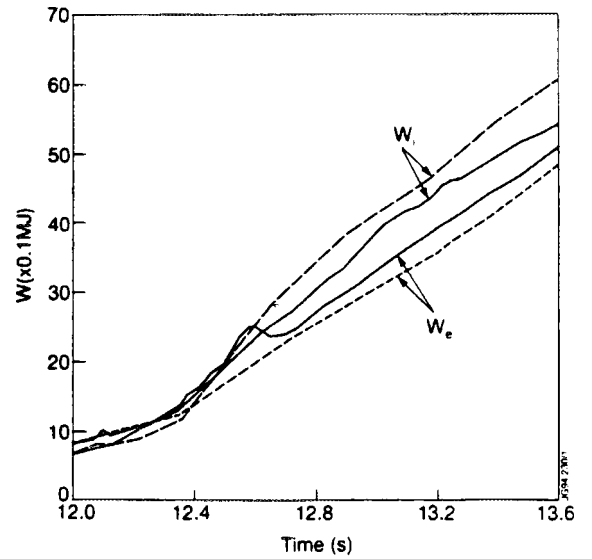


Fig. 4. Experimental (solid) and calculated (dashed) temporal evolution of electron and ion energy content for hot-ion H-mode

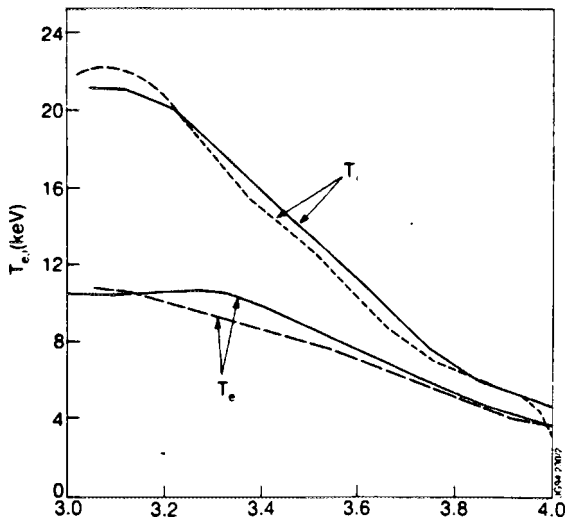


Fig. 5. Experimental (solid) and calculated (dashed) radial distribution of T_e and T_i in hot-ion H-mode.



FR9701766

A Numerical Study of Plasma Detachment Conditions in JET Divertor Plasmas

R Simonini, G Corrigan, G Radford, J Spence,
A Taroni, S Weber.

JET Joint Undertaking, Abingdon, Oxon, OX14 3EA.



Introduction

The problem of determining the conditions for plasma detachment and extinction in JET divertor plasmas, in order to reduce particle and energy loading onto the dump plates, has been studied by means of the EDGE2D/U chain of codes [1].

Detachment is characterised by a drop in particle, pressure and energy fluxes to the target. This phenomenon has been observed in several Tokamaks, including JET. A possible explanation for the pressure drop [2,3] is that if a region of low temperature (a few eV) and not too high density can be established in front of the targets, then in this region charge exchange dominates over ionisation and becomes an efficient means to remove "parallel" momentum from the plasma to the vessel. However, efficient power dissipation cannot be obtained at relevant values of SOL input power in a pure plasma, as found in predictions for the JET Mk I divertor [4], where the need was shown for a means of dissipating enough power to achieve extinction. Experiments show evidence [5] for the role of carbon in detachment in JET. The results reported here refer to two ('gas box') divertor configurations being considered for possible future upgrade of the JET divertor for extrapolations to ITER.

The modelling assumptions can be found in Refs. [6] and [7]. For boundary conditions, we have assumed that no energy is conducted to the vessel wall ($\nabla_{\perp} T=0$), but density has a prescribed radial decay length of $\lambda_n = 0.5$ and 0.2 cm at the outer mid plane and in the private region, respectively.

Dependence of Detachment on Density, Power, Geometry and Radiation

Table 1 summarises the results obtained for an equilibrium configuration ($I_p=4.5$ MA) in the gas box divertor with either flat (F) dump plates (cf. Fig. 2), or with the plasma hitting the side walls (V). By changing the particle inventory $2\pi N$ in the boundary region we have performed scans of the density at the separatrix mid-plane, n_s , for several values of the power input to the SOL. In the case of a pure plasma (impurity radiation $P_{RI}=0$) and input power $P_e=P_i=5$ MW, as n_s increases from about $2.3 \times 10^{19} \text{ m}^{-3}$ to $5.5 \times 10^{19} \text{ m}^{-3}$, the fraction $P_t/(P_e+P_i)$ of input power onto the targets drops from 47% to 14% in the F configuration.

The ratio f_p of the pressure at the mid-plane to the pressure at the targets, which depends on the efficiency of dissipating parallel momentum either by interaction with the neutrals or by radial transport to the vessel wall, rises from 2 to 12, and from 4 to 60, along the separatrix and along a field line approximately 1 cm outboard, respectively. An average of the pressure at the targets is taken, the in-out asymmetry being small, less than 20%.

Similar calculations performed for the JET Mk I divertor [4], where no power is allowed to flow to the wall ($\nabla_{\perp} n=0$) have shown that, although the volume power loss terms in a pure plasma are more efficient at higher densities, they do not seem sufficient to cause detachment at this power level. In the present case, however, an additional power dissipation mechanism is at work, namely wall loading P_w , which rises from 23% to 48% of the input power as n_s increases. The power loss P_{RH} (charge exchange + hydrogen radiation), instead, does not vary much.

Since a high flow of hot particles to the walls may not be desirable, and in order to achieve better detachment with a larger drop of the particle flow to targets, radiation induced by impurities (either sputtered from the walls or puffed in) could be exploited to reduce the energy content of the SOL. However, the additional power loss would be offset to a certain amount by a reduction in the power removed by hydrogenic atomic physics processes, owing to a reduction in recycled neutrals.

For this purpose, we carried out a series of simulations using a simple formula for the radiation efficiency proposed in [8] to simulate the radiation due to a mixture of carbon and oxygen in an otherwise pure plasma, rescaled in order to obtain a prescribed value of the total radiated power, P_{RI} . The main results obtained with this approach have also been reproduced by simulations with a consistent treatment of impurities, as discussed later.

It is found that if sufficient power is radiated such that $T < 5$ eV at the targets, namely when the ionisation rate starts to drop rapidly with respect to charge exchange, detachment can be obtained at large enough values of P_{RI} for a given input power P , and it improves as $P - P_{RI}$ decreases, as shown by f_p and the particle flux onto the targets, Γ_t .

The V configuration enters the regime of detachment more easily than the F configuration, since in the V configuration, the neutrals are recycled preferentially toward the separatrix, thus reducing the temperature there.

It is apparent that similar levels of detachment are obtained for similar values of $P - P_{RI}$, while P itself, the input power flowing into the SOL, is less important.

Effect of a Recycling Impurity and Gas Puffing.

A proper assessment of all the consequences of impurity radiation requires the simulation of the spatial impurity distribution by taking impurity transport into account. Several runs have been performed with the full multi-species EDGE2D/U code.

Since carbon or beryllium alone are unlikely [4] to produce the required amount of radiation by physical sputtering alone, we have considered the injection of neon, a recyclable impurity, into the SOL from all round the vessel. In the calculations reported here for the F configuration, the neon injected amounts to 0.3% of the hydrogen inventory, the input power is $P_i = P_e = 5$ MW. Since the injected impurity could contaminate the bulk plasma, we have also assessed whether an induced flow of plasma is able to keep the impurity in the divertor region.

To this end, gas is extracted from the bottom of the divertor chamber. The pumping efficiency has been estimated by Monte Carlo calculations [9]. The neutral albedoes are $A_1=92\%$ and $A_2=45\%$, at the bottom of the divertor box. The deuterium extracted is then fed back into the SOL, at the top in order to maximise the extension of the induced flow which by friction tends to carry the impurities toward the dump plates.

Fig. 1 shows the average impurity density in the plasma boundary, from the outer target to the inner target, for $N=10 \times 10^{19}$, without and with puffing. The enhanced entrenchment of neon due to the deuterium flow is clear. Better retention here implies that with deuterium puffing the neon radiation decreases from 3.5 MW to 2.5 MW. The pressure drop fits well with that computed from the simple formula for the same level of radiation.

We present in Fig. 2 contour plots for the impurity radiation, with neutral deuterium pumping. The induced flow makes the radiation pattern more in-out symmetric, and whereas without puffing the maximum radiation is near the X point, the enhanced impurity retention due to the puffing moves the maximum near the outer dump plate.

Conclusions

Results obtained so far confirm that for a given particle inventory in the SOL (including the divertor), the main parameter determining whether or not particle, momentum and energy detachment occurs is the residual power $P-P_{\text{lost}}$, where P is the total power entering the SOL and P_{lost} is the power lost by transport to walls and by volume losses in the SOL outside the region where detachment takes place.

For particle contents leading to reasonable values of the separatrix mid-plane density ($n_s < 4 \times 10^{19} \text{ m}^{-3}$ in JET), detachment is found if the residual power is low enough. Typically the residual power must be ≤ 3 MW for good detachment, with the exact value depending on the geometry of the divertor, the transport assumptions and the neutral recirculation scheme.

The results show that divertor plasma conditions relevant for the study of power exhaust and impurity control problems are possible in JET.

Acknowledgements: K Borrás, E Deksnis, P Harbour, L Horton, A Loarte, G Matthews and G Vlases are acknowledged for useful discussions.

References

- [1] R Simonini, G Corrigan, G Radford, J Spence, A Taroni, *Contrib. to Plasma Phys.* 34(1994)368
- [2] K Borrás, P Stangeby, 20th EPS Conf., Lisbon 1993
- [3] P Stangeby, *Nucl. Fus.* 33(1993)1695
- [4] A Taroni, G Corrigan, R Simonini, J Spence, S Weber, 11th PSI Conf. Mito, Japan (1994)
- [5] L D Horton et al., "Detached Plasmas in JET", this Conference.

- [6] A Loarte et al, 11th PSI Conference, Mito, Japan(1994)
 [7] A Taroni, G Corrigan, R Simonini, J Spence, G Vlases, Contrib. to Plasma Phys. 34(1994)448
 [8] R Schneider, B Braams, D Reiter et al., Contrib. to Plasma Phys. 33(1992)450
 [9] E Deksnis, private communication

Cf	N 10 ¹⁹	P _{e,i} MW	P _{RI} MW	n _s 10 ¹⁹ m ⁻³	P _t MW	P _w MW	f _p sep	f _p 1cm	P _{RH} MW	Γ _t 10 ²³ s ⁻¹
F	5	5	0	2.3	4.7	2.3	2	4	3.1	5.8
"	"	"	2	2.3	3.2	2.0	2	8	2.7	3.8
"	"	"	4	2.2	1.9	1.7	3	10	2.3	3.4
"	"	"	6	2.0	0.7	1.4	20	40	1.8	1.6
"	10	5	0	3.9	2.7	3.7	4	10	3.4	5.0
"	"	"	2	3.8	1.7	3.3	7	30	3.0	3.4
"	"	"	4	3.4	0.7	2.7	26	67	2.5	1.8
"	"	"	6	3.1	0.3	1.7	300	300	2.0	0.4
"	"	10	0	4.0	8.9	5.2	2	8	5.8	11.8
"	"	"	5	3.8	6.0	4.1	2	11	4.8	9.1
"	"	"	10	3.5	2.6	3.3	5	40	3.6	5.1
"	"	"	15	2.6	0.5	1.9	160	300	1.6	0.7
"	15	5	0	5.5	1.4	4.8	12	60	3.5	3.1
V	5	"	0	3.0	3.9	2.4	10	5	3.6	6.2
"	"	"	3	2.8	2.0	2.0	34	11	3.0	3.8
"	"	"	6	2.3	0.6	1.5	150	55	2.0	1.4
"	10	"	0	5.0	2.2	4.0	40	17	3.8	5.0

Table 1

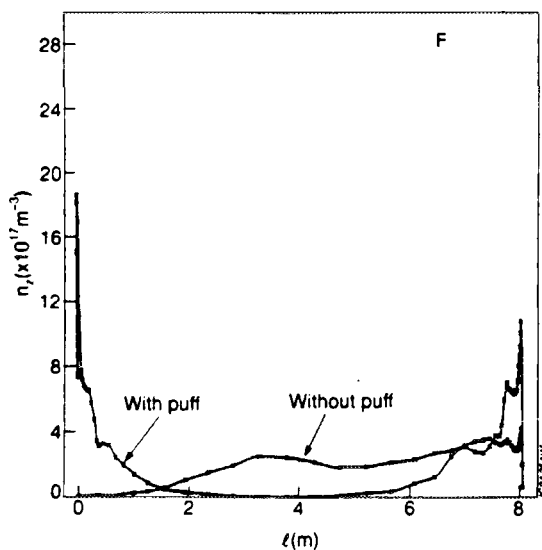


Fig.1 Average impurity density in SOL, F configuration, N=10x10¹⁹

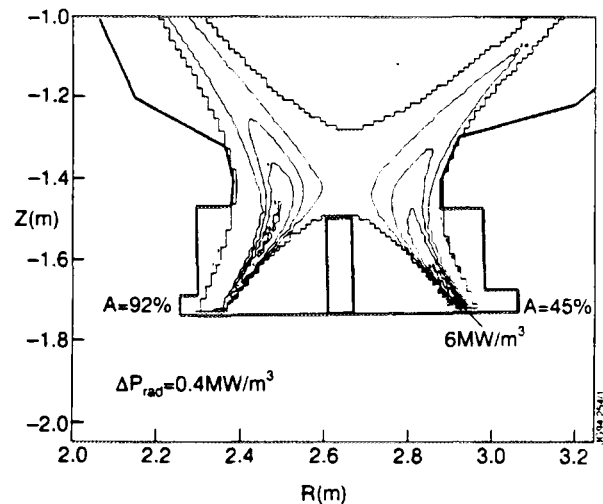


Fig 2 Contour plot of radiation with deuterium puffing. P_{RI}=2.5 MW



FR9701767

The SOL Width and the MHD Interchange Instability in Tokamaks

O Pogutse¹, W Kerner.

JET Joint Undertaking, Abingdon, Oxon, OX14 3EA.

¹ RRC Kurchatov Institute, Moscow, Russia.



1. INTRODUCTION

The hot core plasma in tokamaks is surrounded by the scrape-off-layer (SOL), a region of relatively cold plasma with open field lines intersecting the limiter or the divertor target plates. Previous theoretical work has revealed that instabilities in the SOL plasma can strongly influence the SOL plasma behaviour and, in particular, the SOL width, x_0 [1-4]. The SOL stability analysis (resembling that of open traps) shows that there exists a critical ratio of the thermal energy and the magnetic energy, β_{cr} . If the SOL beta is greater than this critical value, β_{cr} , the magnetic field cannot prevent the plasma displacement and a strong MHD instability in the SOL occurs. In the opposite case only slower resistive instabilities can develop. The resistive instabilities depend strongly on both the volume (Spitzer) conductivity and the sheath conductivity near the end plates. In this paper a theoretical investigation of the SOL plasma stability is presented for JET single-null and double-null divertor configurations. The dependence of the stability threshold on the SOL beta and on the sheath resistance is established. Applying a simple mixing length argument gives the scaling of the SOL width.

2. DISPERSION RELATION

The plasma is described by the macroscopic single-fluid MHD model. For the case of a strong magnetic field a simplified system of reduced equations can be applied [3]. The behaviour of linearised perturbations around an equilibrium state are studied by means of the Fourier Ansatz $e^{i\mathbf{k}\cdot\mathbf{r}}$ leading to the following dispersion relation for the growth rate γ .

$$\left[\gamma + k_{\perp}^2 \mu_{\perp} \right] - \frac{G(\ell)}{\left[\gamma + k_{\parallel}^2 \cdot \chi_{\parallel} + k_{\perp}^2 \cdot \chi_{\perp} \right]} + \frac{k_{\parallel}^2 \cdot C_A^2}{\left[\gamma + k_{\perp}^2 \cdot D_M \right]} = 0, \quad (1)$$

where
$$G(\ell) = \omega_g^2 \cdot \left(k_y^2 / k_{\perp}^2 \right), \quad \omega_g^2 = \frac{1}{R(\ell)M} \cdot \frac{dP_0}{n_0 dx} \equiv \frac{C_s^2}{x_0 R(\ell)},$$

$$\frac{1}{x_0} = - \frac{dP_0}{P_0 dx}, \quad C_A^2 = \frac{B_0^2}{4\pi M n_0}, \quad D_M = \frac{c^2}{4\pi \sigma_s}, \quad C_s = \left(P_0 / (M \cdot n_0) \right)^{1/2},$$

μ_{\perp} denotes the transverse viscosity, χ_{\parallel} (χ_{\perp}) the parallel (perpendicular) thermal conductivity and σ_s the Spitzer conductivity. A new coordinate system with ℓ the coordinate along the

$G(\ell)$ is adopted.

The eigenfunction in the unstable region I (see Fig. 2) is given by the ansatz

$$\phi_1(s) = C_1 \cdot [k \cdot \cos(k \cdot (1-s)) + \alpha \cdot \sin(k \cdot (1-s))], \quad k^2 = \beta^* \cdot (\bar{\gamma} + \delta) \cdot (1/\bar{\gamma} - \bar{\gamma}). \quad (4)$$

For the stable region II the eigenfunction has the following dependence

$$\phi_2(s) = C_2 \cdot [\kappa \cdot \text{ch}(\kappa \cdot (1-s)) + \alpha \cdot \text{sh}(\kappa \cdot (1-s))], \quad \kappa^2 = \beta^* \cdot (\bar{\gamma} + \delta) \cdot (1/\bar{\gamma} + \bar{\gamma}). \quad (5)$$

It is easily verified that these eigenfunctions satisfy the boundary conditions at both target plates. Using the matching conditions between the two regions

$\phi_1(0) = \phi_2(0)$, $\partial\phi_1(0)/\partial s = \partial\phi_2(0)/\partial s$ yields the dispersion relation

$$\frac{k + \alpha \cdot \tan(k)}{k \cdot (k \cdot \tan(k) - \alpha)} = \frac{k + \alpha \cdot \tanh(\kappa)}{\kappa \cdot (\kappa \cdot \tanh(\kappa) + \alpha)}, \quad (6)$$

The stability threshold is given by $\beta_{cr}^* = (2.365)^2 \approx 5.6$. The growth rate for arbitrary β^* is displayed in Fig. 2.

The corresponding diffusion coefficient obtained from the mixing length argument is in physical variables

$$\chi_{\perp} = D_{\perp} = c^2 / \omega_{pi}^2 \cdot (\beta^* / \beta_{cr}^*)^2 \cdot C_s / L_{\parallel}. \quad (7)$$

In comparison with the linear dependence on β^* for the double-null case a quadratic dependence occurs. Making use of the diffusion equation the SOL width for the single-null divertor is estimated as

$$x_0 = (\beta^* / \beta_{cr}^*) \cdot c / \omega_{pi} \quad \text{with the scaling } x_0 \sim L_{\parallel} \cdot R^{-1/2} \cdot n^{1/4} \cdot T^{1/2} \cdot B^{-1}. \quad (8)$$

The final result states that x_0 cannot exceed the value c / ω_{pi} .

DISCUSSION

The stability analysis concerning interchange modes in SOL plasmas has been carried out for single-null and double-null divertor geometry. Applying a mixing length argument scalings for the transport coefficients and the SOL width were derived in different regimes. The longitudinal loss mechanisms take into account the hydrodynamical regime ($\lambda_i < L_{\parallel}$) with $\tau_{\parallel} = L_{\parallel}^2 / \chi_{\parallel}$ and the kinetic regime ($\lambda_i > L_{\parallel}$) with $\tau_{\parallel} = L_{\parallel} / C_s$. The ideal MHD interchange instabilities define a stability limit for the SOL plasma beta, β_{cr}^* . At lower beta values ($\beta^* < \beta_{cr}^*$) resistive interchange instabilities occur and the resulting turbulence determines the SOL width. It is shown that for the volume (Spitzer) resistive being the dominant dissipation process the perpendicular transport $\chi_{\perp} \sim \chi_{\perp}^s \sim D_M \beta^* / \beta_{cr}^*$ is the same for single-null and double-null divertor configurations. For the sheath resistance the transport coefficient scales

as $\chi_{\perp}^{sh} \sim \frac{c^2}{\omega_{pi}^2} \left(\frac{\beta^*}{\beta_{cr}^*} \right)^2 \frac{C_s}{L_{\parallel}}$ for the single-null divertor and $\chi_{\perp}^{sh} \sim \frac{c^2}{\omega_{pi}^2} \left(\frac{\beta^*}{\beta_{cr}^*} \right) \frac{C_s}{L_{\parallel}}$ for the

magnetic field line and the local orthogonal coordinates (x, y) in the transverse (R, Z) plane is introduced. In this system all quantities have only weak dependence on ℓ and do not change sign except the quantity $R(\ell)$ which is defined by

$$\left(\bar{\mathbf{k}} \times \nabla(1/B) \right) \cdot \left[\bar{\mathbf{k}} \times \nabla P_0 \right] \cdot \mathbf{B}_0 / n_0 \equiv \frac{1}{R(\ell)} \cdot \frac{dP_0}{n_0 dx} \cdot k_y^2, \text{ and does change its sign}$$

along ℓ as indicated in Fig. 1. Since $R(\ell)$ is the most important term, the weak dependence of the other quantities on ℓ can be neglected. This ordering is suitable for taking into account small-scale transverse perturbations, where the transverse wave length is smaller than the SOL width. From Eq. (1) we can restore the differential equation. In particular, the component along the magnetic field line, i.e. along ℓ , is given by

$$\frac{\partial}{\partial \ell} \frac{C_A^2}{\left[\gamma + k_\perp^2 \cdot D_M \right]} \frac{\partial}{\partial \ell} \Phi' - \left[\gamma + k_y^2 \cdot \mu \right] \cdot \Phi' + \frac{G(\ell)}{\left[\gamma + 1/\tau_\parallel + k_\perp^2 \cdot \chi_\perp \right]} \Phi' = 0, \quad (2)$$

where Φ' is the perturbed electrostatic potential, $(\bar{\mathbf{b}} \nabla) \equiv \nabla_\parallel \equiv \partial / \partial \ell$, and the operator $k_\parallel^2 \cdot \chi_\parallel$ is replaced by the constant $1/\tau_\parallel$. This allows to reduce the order of the differential equation but still accounts for longitudinal losses. In the case of free-streaming losses onto the target plates at ion sound velocity, C_s, τ_\parallel is estimated as $\tau_\parallel = L_\parallel / C_s$, where $2L_\parallel$ is the distance between the target plates along $\bar{\mathbf{B}}$. The hydrodynamic region is characterised by $\tau_\parallel = L_\parallel^2 / \chi_\parallel$. The differential equation needs to be completed by an appropriate boundary condition as done in Ref. [5]. Neglecting small dissipative terms, i.e. μ_\perp, χ_\perp and $1/\tau_\parallel$, equation (2) and the boundary condition are rewritten in more convenient, dimensionless variables

$$\frac{\partial}{\partial s} \frac{1}{\beta^* \cdot \left[\bar{\gamma} + \delta \right]} \frac{\partial}{\partial s} \phi - \bar{\gamma} \cdot \phi + \frac{\bar{G}(\ell)}{\bar{\gamma}} \cdot \phi = 0, \quad \frac{\partial}{\partial s} \phi \Big|_{s=\pm 1} = (\mp 1) \cdot \alpha \cdot \phi. \quad (3)$$

Here $\phi = e \cdot \Phi' / T$, $s = \ell / L_\parallel$, $\bar{G}(\ell) = G(\ell) / G$, where G is a characteristic value such that $-1 < \bar{G}(\ell) < +1$, $\beta^* = L_\parallel^2 \cdot G / C_A^2 = L_\parallel^2 / (x_0 \cdot R) \cdot \beta$, where $\beta = 4\pi P / B_0^2$ is the usual beta for SOL parameters, $\bar{\gamma} = \gamma / (G)^{1/2}$, $\delta = k_\perp^2 \cdot D_M / (G)^{1/2}$, $\alpha = \alpha_1 \cdot (\bar{\gamma} + \delta)$ with

$\alpha_1 = \left(\frac{L_\parallel^2}{x_0 \cdot R} \right)^{1/2} \left(\frac{\omega_{pi}}{k_\perp \cdot c} \right)^2$. It is emphasised that in this dimensionless form β^* appears, which is of order unity, instead of the small β ($\approx 10^{-4}$).

The pumped divertor, which was recently installed at JET, is a single-null divertor. For this magnetic field line geometry the curvature term $G(\ell)$ in Eq. (2), plotted in Fig. 1, changes sign while the average part is approximately zero. Numerical evaluation shows that the closer the field is to the separatrix the more $G(\ell)$ assumes a step-function dependence. For analytical treatment we assume that $G(\ell) = \theta(\ell - \ell_\parallel)$ is a step function. However, the simplest situation with constant $G(\ell) \equiv 1$ can be regarded as a suitable model for a double-null divertor. For the **single-null divertor** the step-function model for the curvature term

double-null divertor. The dependence on beta is stronger for the single-null geometry due to the partial compensation of regimes with favourable and unfavourable curvature. The basic result is that with increasing SOL beta the difference between single-null and double-null disappears. Near the ideal MHD stability threshold the transport coefficient is

$$\chi_{\perp} \sim \frac{c^2}{\omega_{pi}^2} \frac{c_s}{L_{\parallel}}$$

values up to $x_0 \sim \frac{c}{\omega_{pi}}$.

REFERENCES

1. M. Endler, L. Giannone, N. Niedermeyer, A. Rudyj, G. Theimer and the ASDEX Team in proceedings of 20th EPS Conference, 4-8, Lisboa, 1993.
2. A.V. Nedospasov in Sov. J. of Plasma Physics 15 (1989) 10, 659-661.
3. O. Pogutse, W. Kerner, V. Gribkov, S. Bazdenkov, M. Osipenko, JET-P(93) 106.
4. H.L. Berk, D.D. Ryutov, Yu. A. Tsidulko, Physics of Fluids B3 (6) (1993), 1346-1354.
5. W. Kerner and O. Pogutse to be published.

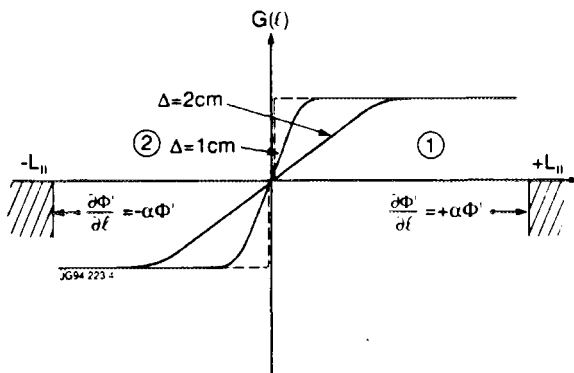


Fig. 1) The dependence of the driving curvature term along the field line for single-null divertor.

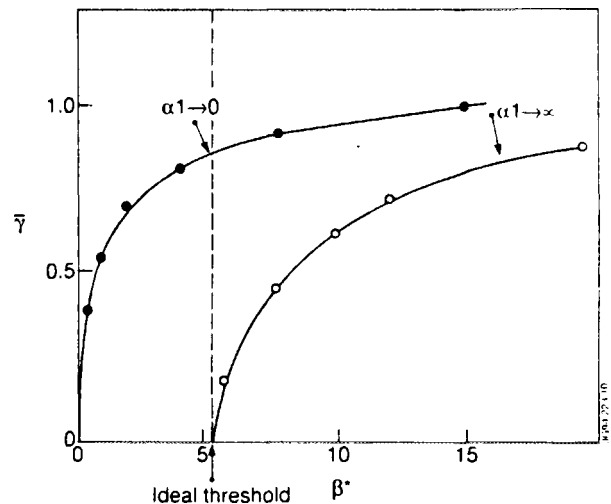


Fig. 2) The growth rate for single-null divertor



FR9701768

Nonlinear Magnetic Reconnection in Low Collisionality Plasmas

M Ottaviani, F Porcelli¹.

JET Joint Undertaking, Abingdon, Oxon, OX14 3EA.

¹ Politecnico di Torino, Torino, Italy.



INTRODUCTION. We discuss magnetic reconnection in collisionless regimes, where electron inertia is responsible for the decoupling of the plasma motion from that of the field lines. These regimes have become relevant in high temperature laboratory plasmas. For example, sawtooth relaxations at JET occur on a time scale shorter than the average collision time. The linear theory of $m=1$ modes has been recently extended to experimentally relevant regimes [1]. The conclusion from linear theory is that these modes can remain virulent at high temperature, with an initial growth rate, γ_L , which compares favourably with that observed in the experiments. Specifically, it was found that $\gamma_L \sim \omega_A d$ for $d > \rho$; $\gamma_L \sim \omega_A d^{1/3} \rho^{2/3}$ for $d < \rho$, where $d = d_e / r_s$, with $d_e = c / \omega_{pe}$ the inertial skin depth and r_s the $q=1$ radius; $\rho = \rho_i / r_s$, with ρ_i the ion (sound) Larmor radius; and $\omega_A = L_x / v_A$ is the Alfvén frequency.

Since the linear theory breaks down for very small magnetic island widths, a nonlinear analysis is called for. Recent nonlinear studies [2,3], which assumed that collisionless magnetic reconnection evolves according to a Sweet-Parker process, gave contradicting results.

In this paper, we analyze the behavior of a collisionless, 2-D fluid slab model in the limit $\rho / d \rightarrow 0$. Our main result is that, when the island size is larger than the linear layer but smaller than the equilibrium scale length, the reconnection rate exhibits a quasi-explosive time behaviour, during which a current density sub-layer narrower than the skin depth is formed [4].

THE MODEL. The equations we solve are

$$\partial_t U + [\varphi, U] = [J, \psi] \quad \text{vorticity equation} \quad (1)$$

$$\partial_t F + [\varphi, F] = 0 \quad \text{inertial Ohm's law} \quad (2)$$

where $[A, B] \equiv \mathbf{e}_z \cdot \nabla A \times \nabla B$, with \mathbf{e}_z the unit vector along the ignorable z direction ($\partial_z = 0$), φ is the stream function, $\mathbf{v} = \mathbf{e}_z \times \nabla \varphi$ is the fluid velocity, ψ is the magnetic flux function, $U = \nabla^2 \varphi$ is the *fluid vorticity*; $J = -\nabla^2 \psi$ is the *current density*; $F \equiv \psi + d^2 J$ is the *z -canonical momentum*. Eq. (2) implies $dF/dt = 0$: F is conserved on moving fluid elements. The **boundary conditions** are *periodic*. The co-ordinates x and y vary in the intervals $x \in [-L_x, L_x]$ and $y \in [-L_y, L_y]$, with the slab aspect ratio $\epsilon \equiv L_x / L_y < 1$. The magnetic field is $\mathbf{B} = B_0 \mathbf{e}_z + \nabla \psi \times \mathbf{e}_z$, $B_0 = \text{constant}$. All quantities are dimensionless, with $L_x = \pi$ and $\tau_A = (4\pi\rho_m)^{1/2} L_x / B_0$ determining the length and time scale normalisation. At **equilibrium**: $\varphi_0 = U_0 = 0$, $J_0 = \psi_0 = \cos x$, and $F_0 = (1 + d^2) \psi_0$. The **initial conditions** are the equilibrium plus a small tearing-parity perturbation of the form $(\varphi, \delta\psi) = \text{Real} \{ [\varphi_L(x), \delta\psi_L(x)] e^{\gamma t + ik y} \}$, with $k = m\epsilon$ and m an integer number. In the limit $d \ll L_x$, the solution of the linearized system can be obtained analytically using asymptotic matching techniques. For $0 < k^2 \leq 1$, the logarithmic jump of $\delta\psi_L$ across the reconnecting layers is

$$\Delta' = 2\kappa \tan(\kappa\pi/2), \quad \kappa \equiv (1 - k^2)^{1/2} \quad (3)$$

We are interested in the *large- Δ'* regime, defined by

$$\Delta' d \geq 1 \Rightarrow \text{macroscopic convection cells, } L_{\text{cell}} \sim L_x. \quad (4)$$

which can be obtained for low values of m and $\epsilon^2 \ll 1$ such that $\Delta' \sim (8/\pi k^2)$. In this regime, *the structure of the stream function is macroscopic*, with $\varphi_L \approx \varphi_\infty \text{sign } x$, $\varphi_\infty \equiv (\tau/k) \psi_\infty$, everywhere except in narrow layers near the reconnecting surfaces. The current channel in the linear stage has a width $\delta_L \sim d$. The linear growth rate is $\gamma_L \approx kd$.

NUMERICAL SOLUTION. The system of Eqs. (1,2) is solved numerically with a pseudospectral code truncated to 1024×64 (x, y) components. We concentrate on the *early nonlinear phase*, specified by the inequalities

$$d < w < 2L_x \quad (5)$$

where w is the magnetic island width. An important consequence of the inertial Ohm law is that the value of F at $x = 0$ is frozen to its initial value, i.e. $F(x = 0, y, t) = F_0(x = 0) = 1 + d^2$. The solution shown in Figs. 1-4 has been obtained for $\epsilon = 0.5$ and $d/(2L_x) = 0.04 \Rightarrow d\Delta' \approx 2.03$.

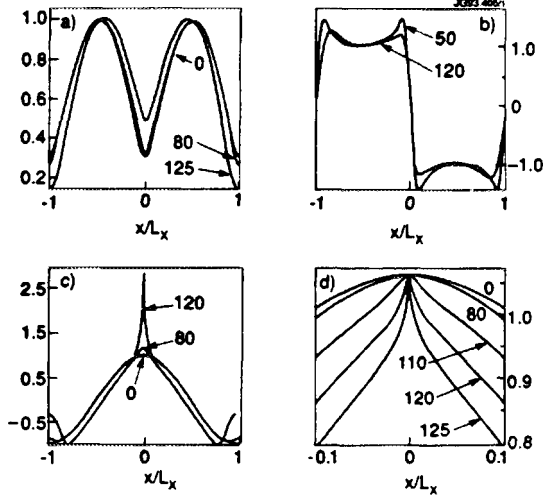


Fig. 1. Cross sections of a) normalized $\delta\psi$; b) normalized v_x ; c) J ; d) F versus x at $y=0$ and various times, indicated by arrows.

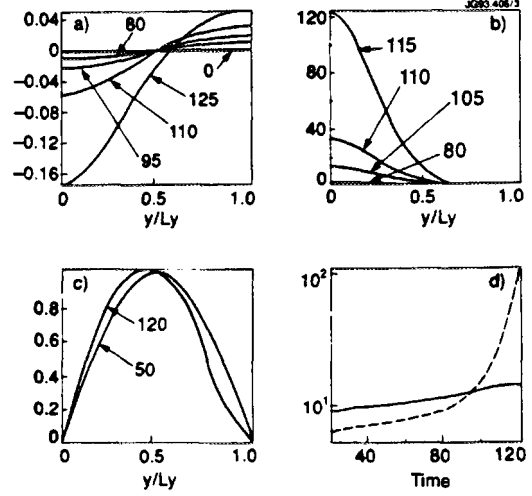


Fig. 2. Cross sections of a) $\delta\psi$; b) $\partial^2 F / \partial x^2$; c) normalized v_y versus y at $x=0$. Also, d) time dependence of the logarithm of the inverse scale lengths δ_ϕ^{-1} (solid line) and δ_J^{-1} (broken line).

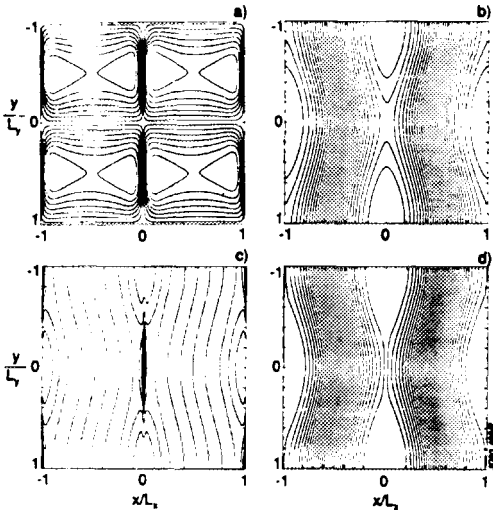


Fig. 3. Contour plots at $t=120$: a) ϕ ; b) ψ ; c) J ; d) F .

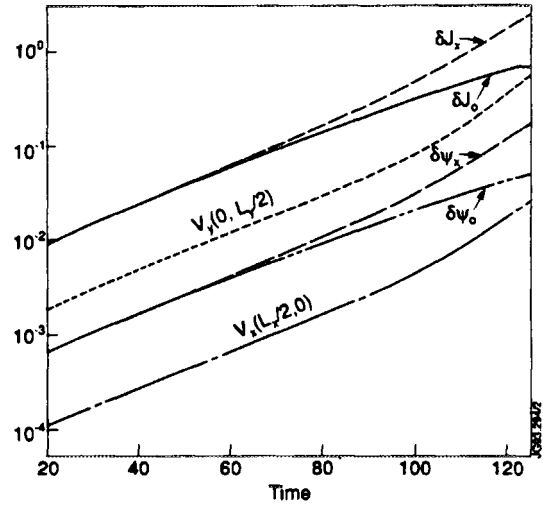


Fig. 4. Time dependence of $\delta\psi$ and δJ at the X- and O-points, of $v_x(-L_x/2, 0)$ and of $v_y(0, L_y/2)$.

RELEVANT PHENOMENOLOGY. The linear phase conventionally lasts until $t \sim 80$, when the magnetic island reaches a width of order d . For $t > 80$, the width of the profile of v_x , $\delta_\phi \equiv (v_x)_{x=L_x/2} / (\partial_x v_x)_{x=0}$, as well as that of $\delta\psi$, remain of the order of the skin depth (Fig. 1a,b and Fig. 2d). Therefore, the convection cells retain approximately their linear shape well into the nonlinear phase (Fig. 3a). By contrast, the current density profile (Fig. 1c) develops a sub-layer whose width around the X-point, $\delta_J \equiv (\partial_x^2 \delta J / \delta J)^{-1/2} < d$, keeps shrinking with time (see also Fig. 2d). This sub-layer is also visible in the profile of F across the X-point (Fig. 1d). The contraction of this sub-layer is extremely rapid in time, as shown by the graph of $\partial^2 F / \partial x^2$ versus y for $x=0$ and several times in Fig. 2b. Note the development of a current sheet around the reconnection line (Fig. 3c).

Also, note the preservation of the topology of the isolines of F (Fig. 3d). Finally (Fig. 4) the mode growth remains very rapid throughout the simulation. Indeed, the growth of φ , as well as that of $\delta\psi$ and δJ at the X-points, accelerate in the early nonlinear phase, which is symptomatic of an explosive behaviour (eventually, the mode growth slows down when w approaches L_x).

ANALYTIC TREATMENT. The numerical simulations suggest the following *ansatz*:

$$\varphi(x, y, t) = v_o(t)g(x)h(y) + u(x, y, t) \quad (6)$$

where $h(y) \sim k^{-1} \sin(ky)$, $g(x) \sim \varphi_L(x)/\varphi_\infty$ contains the linear scale length d and $u(x, y, t)$ develops the rapid scale length $\delta(t) \sim \delta_J$ observed in the numerical simulation. The relevant ordering is $u \ll v_o$ and $\partial_x u \sim v_o \partial_x g$. Integration of the collisionless Ohm's law gives $F = F_o(x_o)$, where $x_o(x, y, t) = x - \xi(x, y, t)$ is the initial position of a fluid element situated at (x, y) at time t and ξ is the displacement along the x direction defined by the equation $d\xi/dt = v_x$, $\xi(t = -\infty) = 0$. At $y = 0$,

$$-\int_{x_o}^x dx'/g(x') = \int_{-\infty}^t v_o(t') dt' \equiv \lambda(t). \quad (7)$$

The function $\lambda(t) > 0$ represents the amplitude of ξ outside the reconnection layer, where $g(x) \approx 1$. In the linear phase, $-\psi_\infty \approx \lambda < d$. When $\lambda > d$, the magnetic island width $w \sim 2\lambda$, so that the early nonlinear phase can also be characterised by the inequality $d < \lambda < L_x$, or alternatively $t_0 < t < t_D$, with $\lambda(t_0) \sim d$ and t_D the characteristic turnover time of the macroscopic eddies in Fig. 3a. Inverting equation (4) in the limit $d < \lambda < L_x$, we obtain $x_o = x_o(x, t)$, which depends on the time-dependent scale length

$$\delta(t) \equiv d \exp[-\lambda(t)/d]. \quad (8)$$

Thus we see that near the X-point along the x direction, $F(x_o)$ (and hence J) varies over a distance $\delta(t)$ which becomes exponentially small in the ratio λ/d . Conversely, F flattens over a distance $|x| \sim \lambda$ around the O-point. The formation of a sub-layer is the combined result of the conservation of F on each fluid element and the flow pattern around the X-point, which acts to increase the local curvature of the F profile (Fig. 1d). Integrating the equation $\psi + d^2 J = F$, where $J \approx -\partial_x^2 \psi$, we find that ψ has an integral structure such that any fine scale variation of F is smoothed out over a distance $\sim d$. Asymptotic evaluation of ψ at the X- and O-points in the early nonlinear phase gives

$$\psi_X \equiv \psi(0, 0, t) \sim 1 - \frac{1}{2} \lambda^2(t), \quad \psi_O \equiv \psi(0, \pm L_y, t) \sim 1 + \beta(d^2) \quad (9)$$

Now set $F = F_o(x) + \delta F$. Then, $\delta\psi + d^2 \delta J = \delta F$, and at $x = 0$, where $\delta F = 0$, we find $\delta J = -\delta\psi/d^2$. Thus, an asymmetry develops in the values of $\delta\psi$ and of J between the X- and O-points. The spike of the current density at the X-point has an amplitude $\delta J_X \sim 0.5(\lambda/d)^2$. Integrating the vorticity equation over the quadrant $S: [0 \leq x \leq L_x, 0 \leq y \leq L_y]$ gives

$$\partial_t \int_S U dx dy = \oint_C J d\psi. \quad (10)$$

where C is the boundary of S . With the *ansatz* (6), and neglecting corrections $\mathcal{O}(k^2 d^2)$ contributed by $\partial_y^2 \varphi$, we find

$$\partial_t \int_S (\partial_x^2 \varphi) dx dy \approx -(4c/k^2 d) d^2 \lambda/dt^2, \quad (11)$$

where $c > 0$ is a factor of order unity, which depends weakly on time (e.g. $1 \leq c \leq 1.4$ in Fig. 2d). The dominant contribution from the r.h.s. of Eq. (10) is

$$\oint_C J d\psi \approx \delta\psi_X - \delta\psi_O - (\delta\psi_X^2 - \delta\psi_O^2)/2d^2 \quad (12)$$

Finally, using an interpolation formula between the linear and early nonlinear limits of the r.h.s. of (12), we obtain an equation for the evolution of $\hat{\lambda}(t) \equiv \lambda(t)/d$:

$$d^2 \hat{\lambda}/d\hat{t}^2 \approx \hat{\lambda} + c_2 \hat{\lambda}^4 \quad (13)$$

where $\hat{t} \equiv \gamma_L t$ and $c_2 \approx 1/16c > 0$ can be taken constant. The solution is $\hat{\lambda}(\hat{t}) = \left[\frac{1-\alpha}{1-\alpha e^{3\hat{t}}} \right] e^{\hat{t}}$, where $\alpha = \beta - (\beta^2 - 1)^{1/2}$, $\beta = 1 + 5/c_2$, and we have chosen the time origin so that $\hat{\lambda}(0) \equiv 1$. Thus, once the early nonlinear regime is entered, $\lambda(t)$ accelerates and reaches a macroscopic size over a fraction $\sim \ln(\alpha^{-1})$ of the linear growth time. Eventually, we can expect this quasi-explosive growth to cease as λ approaches L_x .

DISCUSSION AND CONCLUSIONS. Collisionless reconnection in regimes where the instability parameter Δ' is large and global convection cells develop does not follow the standard Sweet-Parker scenario [5-7]. In

this context, we note a fundamental difference in the nonlinear flow pattern between the collisionless case (Fig. 3) and the resistive case (Fig. 5). The Sweet-Parker scenario applies to the regime $\eta^{1/2} \gg d$, where η is the normalized resistivity (inverse Reynolds' number). It is of interest to study the limit $\eta^{1/2} \ll d \ll \eta^{1/3}$. In this regime, the linear phase is dominated by exponential evolution with the resistive growth rate $\gamma_L \sim \eta^{1/3} \omega_A$. During an initial nonlinear phase, where $\eta^{1/3} < \lambda < \eta/d^2$, the displacement λ grows algebraically in time, $\lambda \sim \eta t^2$, while the width of the current channel shrinks from $\delta_L \sim \eta^{1/3}$ to $\delta \sim (\eta/\lambda)^{1/2}$. This initial nonlinear regime is consistent with Sweet-Parker. When $\lambda \sim \eta/d^2$, also $\delta \sim d$. Therefore, the initial nonlinear behavior must change for $\lambda > \eta/d^2$, as for these values of λ the current in the layer is distributed mostly over a distance $\sim d$, independently of λ . Assuming that the formation of the current spike (cf Eq. 10) is impeded (see below), we can expect a resumption of exponential growth in this later nonlinear phase, with $\lambda \propto \exp(d \cdot t)$.

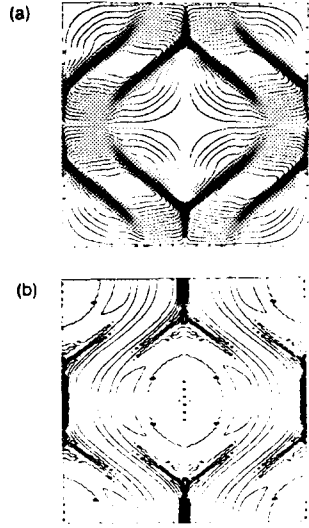


Fig. 5 Contour plots of a) the stream function φ and b) the current density J in the resistive case.

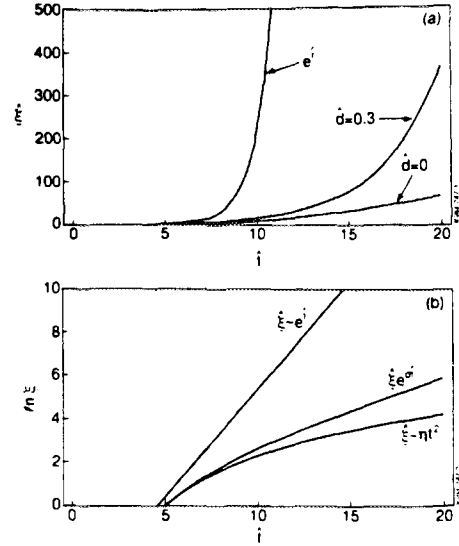


Fig. 6 Time evolution of the normalized displacement $\hat{\xi} = \lambda / \eta^{1/3}$ in the regime $\eta^{1/2} \ll d \ll \eta^{1/3}$: a) linear plot; b) semi-log plot.

This behavior can be summarized by the following phenomenological equation for $\hat{\xi} \equiv \lambda / \eta^{1/3}$:

$$d\hat{\xi}/d\hat{t} = \left[(1 + \hat{d}^2 \hat{\xi}) / (1 + \hat{\xi}) \right]^{1/2} \hat{\xi} \quad (14)$$

where $\hat{t} = \eta^{1/3} t$ and $\hat{d} = d / \eta^{1/3}$. The numerical solution of Eq. (14) is shown in Fig. 6. The growth eventually saturates when the displacement reaches a macroscopic size ($\lambda \sim L_{cell}$). One expects that the current spike will be limited by effects not taken into account by the present analysis. Such effects may include collisions (most notably, electron viscosity), velocity-space instability associated with the current density gradient, 3-D effects, etc. Further work needs to be done to determine the relevant effects for interesting applications. While the current spike is being formed, the reconnection rate exhibits a quasi-explosive time behavior. Physically, the flow rotation accelerates following the intensification of the electromagnetic torque $\oint_C \mathbf{J} \times \mathbf{B} \cdot d\mathbf{l} = \oint_C J d\psi$ in the early nonlinear regime. This torque is mainly contributed by the average $J_z B_x$ force between the X- and O-points within a magnetic island.

In conclusion, we believe that the inclusion of the electron inertial term in Ohm's law opens the possibility to understand the rapidity of relaxation processes observed in low collisionality plasmas.

- REFERENCES** [1] F.Porcelli, Phys. Rev. Lett. **66**, 425 (1991). [2] J.Wesson, Nuclear Fusion **30**, 2545 (1990). [3] J.F.Drake and R.G.Kleva, Phys. Rev. Lett. **66**, 1458 (1991). [4] M. Ottaviani and F. Porcelli, Phys. Rev. Lett. **71**, 3802 (1993). [5] P.A.Sweet, in *Electromagnetic Phenomena in Cosmic Physics*, ed. by B.Lehner (Cambridge University Press, 1958), p. 123. [6] E.N.Parker, J. Geophys. Research **62**, 509 (1957). [7] B.B.Kadomtsev, Fiz. Plasmy **1**, 710 (1975) [Sov. J. Plasma Phys. **1**, 389 (1975)].



FR9701769

Topology and Slowing Down of High Energy Ion Orbits

F Porcelli¹, L-G Eriksson, H L Berk².

JET Joint Undertaking, Abingdon, Oxon, OX14 3EA.

¹ Politecnico di Torino, Torino, Italy.

² Institute for Fusion Studies, University of Texas, Austin, USA.



INTRODUCTION. We consider the regime $\delta_p \geq r \Leftrightarrow \varepsilon \leq \Delta^{2/3} \equiv \delta_p / R$, where $\delta_p \sim \varepsilon^{-1/2} q \rho$ is the standard banana orbit width, $\varepsilon \equiv r/R$, $q_0 \equiv q(0)$ and $\Delta \equiv 2q_0 \rho / R$. In this regime, the banana-shaped orbit is distorted into a *potato*-shaped orbit with a characteristic width of the order of δ_p . For a 1 MeV Hydrogen ion and typical parameters of the JET Tokamak, $\delta_p \sim 0.3$ m is about one third of the plasma minor radius. A correct description of the high energy ion orbits is important to assess their effects on the energy balance and on MHD modes active in the central region of a Tokamak plasma (internal kinks, fishbones, TAE).

ORBIT EQUATION. The orbit equation for the particle guiding centres can be obtained from the invariance of the energy, $\mathcal{E} \equiv mv^2/2$, magnetic moment, $\mu \equiv mv_\perp^2/2B$, and toroidal canonical momentum in axisymmetric plasmas, $P_\varphi = (Ze/c)\psi - mRv_\parallel B_\varphi / B$, where $\psi \geq 0$ is the poloidal flux function. We consider a standard low- β Tokamak equilibrium where the departure from concentric flux surfaces is of order ε . Neglecting higher order corrections, let us set $v_\parallel = \pm v_{\perp 0}(\lambda + \varepsilon \cos \vartheta)^{1/2}$, where $v_{\perp 0} \equiv (2\mu B_0/m)^{1/2}$ and $\lambda \equiv (\mu/B_0)^{-1/2}$ are constants of the motion. We define $\psi_* \equiv cP_\varphi / Ze$. The orbit equation can be written as

$$v_\parallel / v_{\perp 0} = \pm (\lambda + \varepsilon \cos \vartheta)^{1/2} = (Ze/mcR_0 v_{\perp 0}) (\psi - \psi_*) \quad (1)$$

Let us introduce the dimensionless variables $\hat{r} \equiv r/\delta_p$, $\hat{\lambda} \equiv (R/\delta_p)\lambda$, $\hat{\psi} \equiv (2q_0/B\delta_p^2)\psi$, $\hat{\psi}_* \equiv (2q_0/B\delta_p^2)\psi_*$, where the characteristic potato width

$$\delta_p \equiv (2q_0 v_{\perp 0} / \Omega_0 R_0)^{2/3} R_0 \quad (2)$$

is defined here as a constant of the motion. For the sake of analytic progress, we shall assume that the fast ions are confined near the magnetic axis in a region of low magnetic shear, i.e. $(d \ln q / d \ln r) \ll 1$ for $r \leq \delta_p$. In this case, we can approximate $\hat{\psi} \approx \hat{r}^2$. Then, the orbit equation can be cast in the more compact form:

$$\pm (\hat{\lambda} + \hat{r} \cos \vartheta)^2 = \hat{r}^2 - \hat{\psi}_* \quad (3)$$

The potato range is defined by the inequalities

$$\hat{\psi}_* \leq 1, \quad \hat{\lambda} \leq 1. \quad (4)$$

ORBIT CLASSIFICATION. A classification of the orbit types can be obtained by studying the intersections of the orbits with the poloidal midplane. Squaring Eq. (9), we are led to consider the real non-negative roots of the quartic polynomial

$$F(\hat{r}) = \hat{\lambda} \pm \hat{r} - (\hat{r}^2 - \hat{\psi}_*)^2, \quad (5)$$

where the plus sign corresponds to intersections on the low field side ($\vartheta = 0$) and the minus sign corresponds to intersections on the high field side ($\vartheta = \pi$). The total number of intersections can be either 0, 2 or 4, corresponding to 0, 1 or 2 orbits. Limiting orbits correspond to the tangency of the straight lines $g_\pm(\hat{r}) = \hat{\lambda} \pm \hat{r}$ with the quartic $f(\hat{r}) = (\hat{r}^2 - \hat{\psi}_*)^2$. Thus, the loci of these orbits in the $(\hat{\lambda}, \hat{\psi}_*)$ plane are obtained from the solution of the system

$$\begin{cases} F = 0 \\ \partial F / \partial \hat{r} = 0 \end{cases} \Rightarrow \begin{cases} \hat{\lambda} = \mp \hat{r} + 1/16\hat{r}^2 \\ \hat{\psi}_* = \hat{r}^2 \mp 1/4\hat{r} \end{cases} \quad (6)$$

Eliminating \hat{r} , we obtain two curves in the $(\hat{\lambda}, \hat{\psi}_*)$ plane (Fig. 1). The curve obtained choosing the minus sign, $\lambda_-(\hat{\psi}_*)$, corresponds to the locus of the counter-passing stagnation orbits. No orbits exist below this curve. The curve obtained choosing the plus sign has a cusp at $\hat{r} = 1/2 \Rightarrow \hat{\lambda} = \hat{\psi}_* = 3/4$. Thus we can identify two branches: the lower branch, $\lambda_-(\hat{\psi}_*)$ which corresponds to the locus of the pinch orbits, and the upper branch, $\lambda_+(\hat{\psi}_*)$, which corresponds to the locus of the co-passing stagnation orbits. The cusp itself corresponds to a triple zero of F , i.e. to a pinch orbit where the inner loop degenerates to a point. The two branches together form the boundary between the one-orbit and the two-orbit regions of Fig. 1. Transitional orbits correspond to values of $\hat{\lambda}$ and $\hat{\psi}_*$ such that the

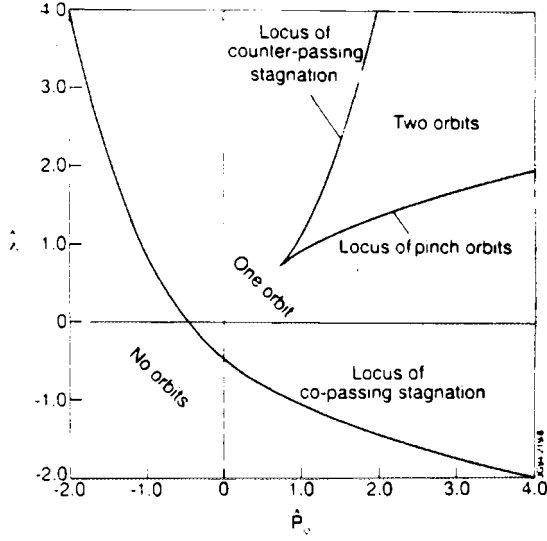


Figure 1

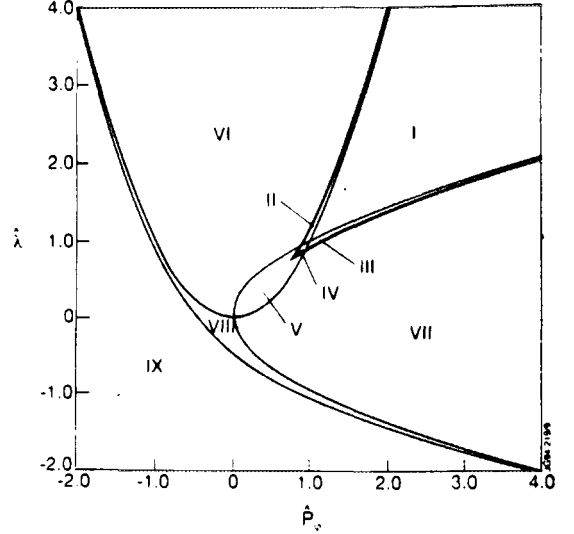


Figure 2

intersections between the curves $g_z(\hat{r})$ and $f(\hat{r})$ occur either at $\hat{r} = 0$ (orbits tangent to the axis) or at $\hat{r} = \hat{r}_*$ (marginally trapped orbits). Thus we are led to consider the two additional parabolic curves $\hat{\lambda} = \hat{\psi}_*^2$ (locus of the orbits that are tangent to the magnetic axis) and $\hat{\lambda} = (\hat{\psi}_*)^2$ for $\hat{\psi}_* \geq 0$ (locus of the marginally trapped orbits). These two parabolas, in addition to the two curves of Fig. 1, give rise to eight regions in the $(\hat{\lambda}, \hat{\psi}_*)$ plane, corresponding to as many distinct topological orbit types, plus a ninth region where no orbits exist, as shown in Fig. 2. Limiting and transitional orbits can be found on the boundaries and corners among these regions. A complete orbit classification and representative examples are given in Table 1 and Figure 3.

TABLE 1: ORBITS IN REGIONS I-IX.

REGION	ORBITS	ORBIT TYPE(S)
I: $\hat{r}_* < \hat{\lambda} < \hat{r}_*^2$	two	-co-passing, encircling the axis -counter-passing, encircling the axis
II: $\max\{\hat{r}_*, \hat{r}_*^2\} < \hat{\lambda} < \hat{\lambda}_{**}$	two	-co-passing, encircling the axis -counter-passing, high field side
III: $\hat{\lambda}_{**} < \hat{\lambda} < \min\{\hat{r}_*, \hat{r}_*^2\}$	two	-mirror-trapped, encircling the axis -counter-passing, encircling the axis
IV: $\max\{\hat{\lambda}_{**}, \hat{r}_*^2\} < \hat{\lambda} < \min\{\hat{r}_*, \hat{\lambda}_{**}\}$	two	-mirror-trapped, encircling the axis -counter-passing, high field side
V: $\hat{r}_*^2 < \hat{\lambda} < \hat{r}_* - \text{IV}$	one	-mirror-trapped, encircling the axis
VI: $\hat{\lambda} > \max\{\hat{\lambda}_{**}, \hat{r}_*, \hat{\psi}_*^2\}$	one	-co-passing, encircling the axis
VII: $-\hat{r}_* < \hat{\lambda} < \min\{\hat{r}_*^2, \hat{\lambda}_{**}\}$	one	-mirror-trapped, not encircling the axis
VIII: $\hat{\lambda}_{**} < \hat{\lambda} < \min\{\hat{\psi}_*^2, \hat{r}_*\}$	one	-co-passing, low field side
IX: $\hat{\lambda} < \hat{\lambda}_{**}$	no orbits	

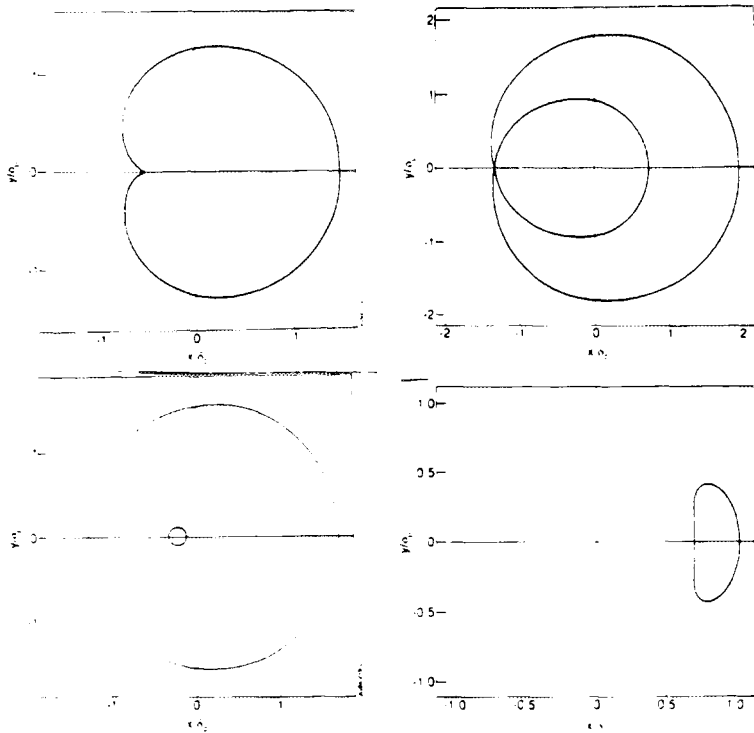


Fig. 3. Representative orbits: a) cusp orbit; b) pinch orbit; c) Pair of orbits in region II of Fig. 2, the inner orbit is close to the limiting counter-passing stagnation orbit; d) transitional orbit at the boundary between regions VII and VIII of Fig 2 (marginally trapped, not encircling the axis).

SLOWING-DOWN CHARACTERISTICS. In the high energy limit, only the collisional drag by the thermal electrons is important. The bounce-averaged Fokker-Planck equation for the fast ion distribution function, f_0 , has the form

$$\frac{\partial f_0}{\partial t} = \left\langle \frac{1}{\tau_s} \right\rangle \frac{1}{v^2} \frac{\partial}{\partial v} (v^3 f_0) + \left\langle \frac{P_s - Ze\psi/c}{\tau_s} \right\rangle \frac{\partial f_0}{\partial P_s} + \langle S \rangle, \quad (7)$$

where angle brackets denote bounce averaging, τ_s is the slowing-down time and S is the fast ion source term. Using the variables $\hat{\psi}_s, \hat{\lambda}$, assuming $\tau_s \approx \text{const}$, and introducing the normalized time $\hat{t} \equiv t / \tau_s$, we obtain

$$\frac{dF}{d\hat{t}} = \frac{\partial F}{\partial \hat{t}} + \frac{2}{3} \hat{\lambda} \frac{\partial F}{\partial \hat{\lambda}} + \left[g(\hat{\psi}_s, \hat{\lambda}; \sigma) + \frac{4}{3} \hat{\psi}_s \right] \frac{\partial F}{\partial \hat{\psi}_s} = \tau_s \langle S \rangle, \quad (8)$$

where $F \equiv v^3 f_0$ and the function $g(\hat{\psi}_s, \hat{\lambda}; \sigma) \equiv \langle \hat{\psi} - \hat{\psi}_s \rangle$, which is proportional to the fast ion toroidal

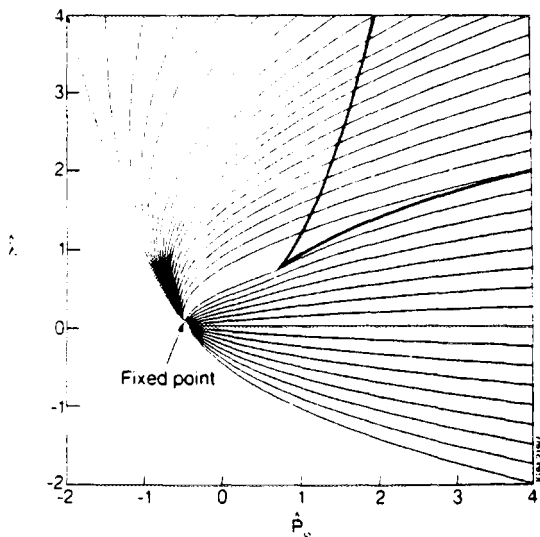


Figure 4

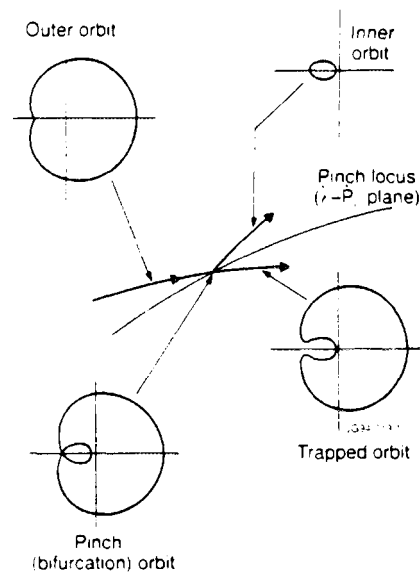


Figure 5

precession frequency, can be expressed in terms of elliptic integrals. The characteristic equations are

$$\frac{d\hat{\psi}_*}{dt} = g(\hat{\psi}_*, \hat{\lambda}; \sigma) + \frac{4\hat{\psi}_*}{3}, \quad \frac{d\hat{\lambda}}{dt} = \frac{2\hat{\lambda}}{3} \quad (9)$$

Analysis of this system reveals the existence of an unstable fixed point at

$$\hat{\lambda}_f = 0, \quad \hat{\psi}_* = -3(16)^{-2/3} \approx -0.47 \quad (10)$$

The characteristic curves in the $(\hat{\lambda}, \hat{\psi}_*)$ plane can be thought of as originating from this fixed point at $t \rightarrow -\infty$, as shown in Fig. 4. Some of these curves intersect the pinch locus. At this time, a bifurcation occurs, as represented by the diagram of Fig. 5. Part of the orbits will become trapped (region VII of Fig. 2), while the remaining orbits will become counter-passing (regions I-III). The characteristic curves of the latter orbits are shown in Fig. 6. In order to assign a probability of transition to either of the two branches of the bifurcation diagram, the basins of attraction need to be studied.

The loci of co- and counter-passing stagnation orbits are mapped onto themselves during the slowing-down evolution. A significant inward radial transport has been found for those high energy ions that initially do not encircle the axis. An example is shown in Fig. 7a. Note that, as the particle loses energy, its orbit must eventually become a standard one. Therefore, particles that initially do not encircle the axis, either move onto the axis and then become a passing orbit, as in the case of Fig. 7a, or move a finite distance toward the axis and then become a standard banana orbit, as in the example of Fig. 7b.

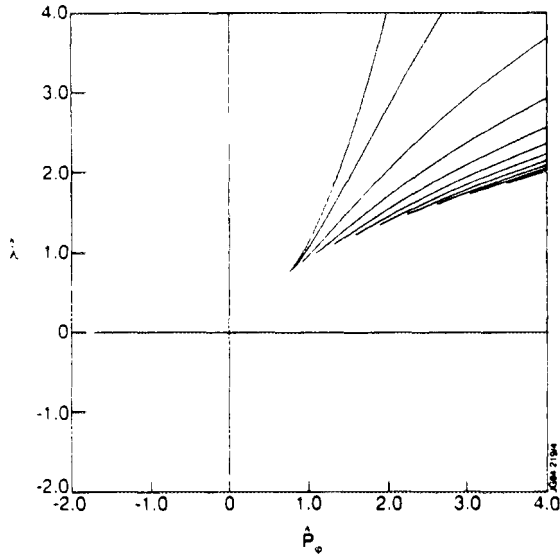


Figure 6

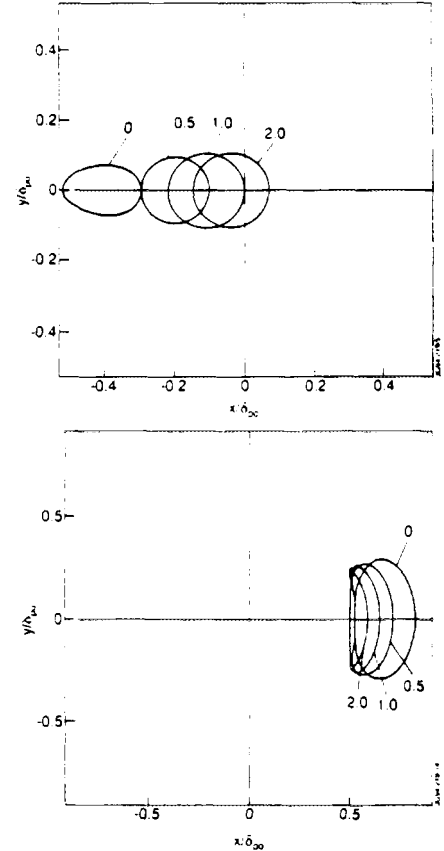


Figure 7

CONCLUSIONS. We have presented an analysis of nonstandard guiding centre orbits, which is relevant to MeV ions in a Tokamak. The orbit equation has been simplified from the start, so to enable us to present an analytic classification of the possible orbits. We have described the topological transitions of the orbits during collisional slowing down. In particular, the characteristic equations reveal the existence of a single fixed point in the relevant phase plane, and the presence of a bifurcation curve corresponding to the locus of the pinch orbits. A significant particle inward pinch has been discovered.



FR9701770

Sawtooth Crashes at High Beta on JET

B Alper, M F F Nave¹, G T A Huysmans, A C C Sips.

JET Joint Undertaking, Abingdon, Oxon, OX14 3EA.

¹ Associação EURATOM/IST, Instituto Superior Tecnico, Lisbon, Portugal.



INTRODUCTION

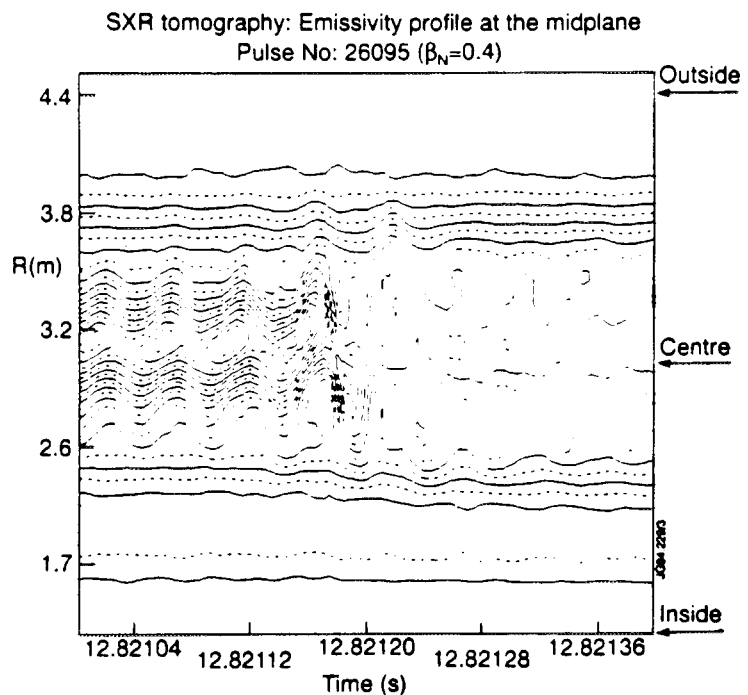
Sawteeth observed in high performance discharges on JET are observed to have features which extended well beyond the $q=1$ surface. Those sawteeth which occur at high beta often couple to a giant ELM typically within $50\mu\text{s}$ and, in all such cases, an irrecoverable fall in fusion yield results [1]. Similar phenomena have been observed in other high beta discharges on JET where an ELM is also observed to couple to the sawtooth collapse. In these discharges, with low values of toroidal magnetic field, a sequence of sawtooth/ELM events occurs which is associated with a saturation in beta [2,3].

COMPARISON OF SAWTOOTH CRASHES AT LOW AND MEDIUM BETA

Features which are clearly identified in sawtooth collapses at low beta such as mixing radii and heat pulses can become somewhat obscured as beta increases. Here we define low beta to correspond to values of $\beta_N < 0.35$ with β_N defined to be the toroidal beta, normalised to the Troyon limit: $\beta_T = 2.8 I(\text{MA})/a(\text{m})B_\phi(\text{T})$. The main cause of this is a fast perturbation associated with the final stages of the $(m,n)=(1,1)$ precursor mode of the sawtooth collapse which is observed to extend well beyond the inversion radius in medium and high beta

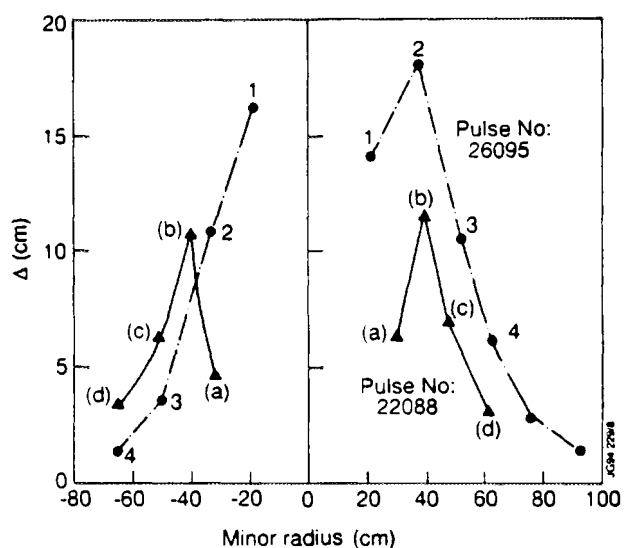
sawteeth. A noticeable ballooning effect is found with pronounced bulging of flux surfaces on the low field side in these cases. This is shown in **Figure 1**, a contour plot of soft X-ray (SXR) intensity vs time for a sawtooth crash at $\beta_N=0.4$.

Figure 1 Contour plot of SXR emissivities for an intermediate-beta sawtooth showing a bulge in the flux surfaces on the low field side, between $R=3.6\text{m}$ and 3.9m , at the time of the collapse.



We determined of the magnitude of the deviation (or excursion) of these flux surfaces from their mean value as a function of radius for discharges with different beta. The results of the maximum excursion of a flux surface during the sawtooth is plotted for a low and intermediate beta discharge in Figure 2. In the low beta discharge, (22088, $\beta_N=0.2$) the deviation is seen to be reasonably symmetric between the low and high field sides and to fall off rapidly beyond the inversion radius of ~ 40 cms. The intermediate beta discharge, 26095, shows a pronounced ballooning effect, with the field line excursion extending to large values of minor radius on the low field side just stopping short of the plasma edge at $a=120$ cms.

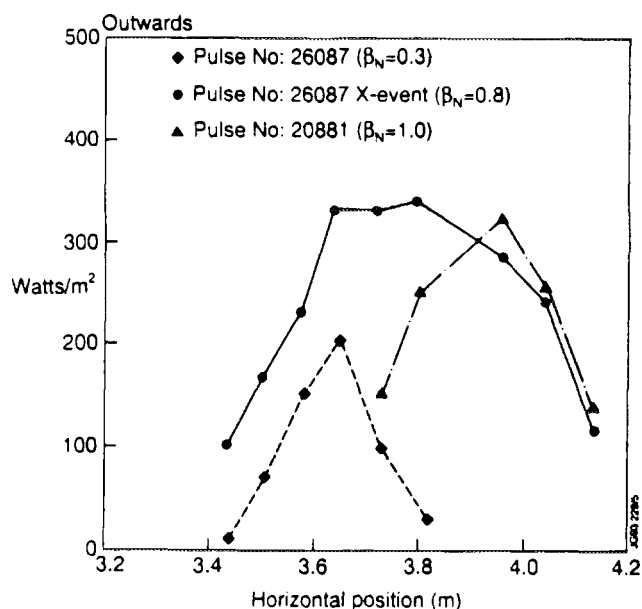
Figure 2. Comparison, between two discharges, of the maximum deviation of flux surfaces with minor radius, during a sawtooth collapse - one at low beta (22088), the other at intermediate beta (26095). Evidence of a ballooning effect on the low field side is apparent in shot 26095.



SAWTOOTH CRASHES AT HIGH BETA

The pronounced bulging of the flux surfaces - the sawtooth excursion as we have called it here - is observed to extend to larger radii as beta increases. This is illustrated in Figure 3. The figure shows how the magnitude of the perturbation of the line-integrated SXR signals varies with radius at different beta values. The high beta sawteeth ($\beta_N > 0.5$) clearly show the perturbation in SXR intensity extending right to the plasma edge especially in the outward (low field) direction. The perturbation is transient, lasting usually less than $30 \mu\text{s}$.

Figure 3. An illustration of how the sawtooth perturbation grows with beta. The magnitude of the perturbation in line integrated SXR emission is plotted as a function of radius. The perturbation, at high beta, can be seen to extend to the outside plasma edge.



COUPLING OF THE HIGH BETA SAWTEETH TO AN ELM

In most of the high beta discharges ($\beta_N > 0.5$) an ELM appears soon after the sawtooth crash i.e. within 25-60 μ s. This, we believe, is a direct consequence of the sawtooth perturbation extending to the edge on the low field side as discussed above. In the case of the hot-ion H-mode discharges, a giant ELM appears about 50 μ s after the sawtooth, initially localised close to the plasma X-point and is followed within a few milliseconds by an influx of carbon impurities which cool the plasma. This event can occur either at peak neutron yield or up to 300ms afterwards but in all cases the plasma fails to recover its high performance.

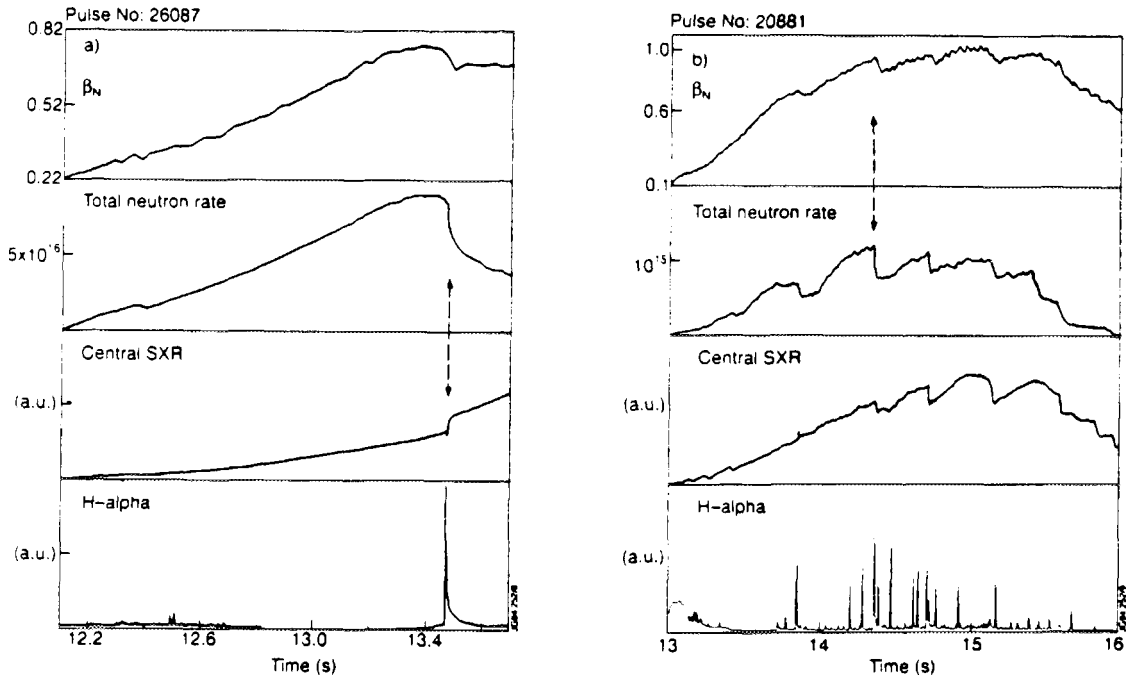


Figure 4. Traces of β_N , neutron yield, central soft X-rays and H-alpha for (a) the hot-ion H-mode discharge 26087 and (b) the low field high-beta discharge 20881. The dotted lines indicate the sawtooth events shown in figure 3 for these discharges.

In the high beta, low toroidal field, discharges, with lower power input to the plasma, an ELM occurs within 30 μ s of the sawtooth crash. Although the plasma can recover to similar values of beta afterwards, the process repeats itself and leads to a limitation in beta. Other ELMs and fishbone activity are present during this period which may also contribute to saturation in beta [4]. Figure 4 illustrates these effects.

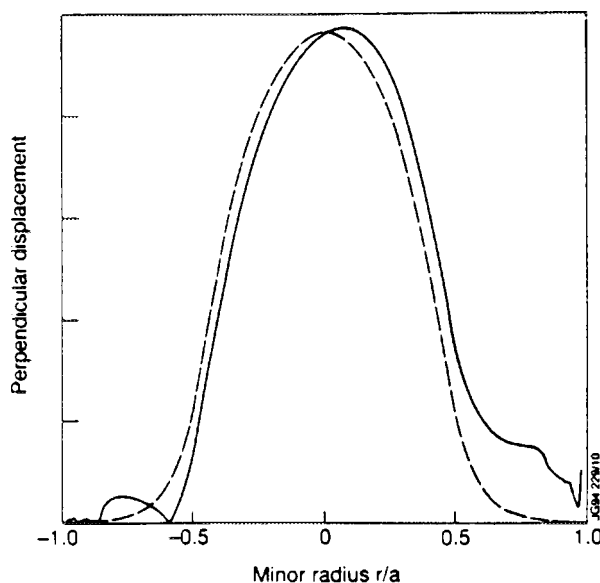
MODELLING

To compare the experimental results with theoretical mode structures, the eigenfunction of the internal kink mode has been calculated for different values of β , using the CASTOR toroidal stability code [5]. At low beta the displacement of the internal kink mode has a predominantly $m=1$ structure which does not extend far beyond the $q=1$ surface. The higher harmonics, which are due to toroidicity are relatively small. In contrast, Figure 5 shows the computed mode structure of the internal kink of a high performance discharge at high β

(#26087, $\beta_N = 0.8$). The amplitude falls off only slowly beyond the $q=1$ surface and is finite at the plasma boundary due to the coupling to the higher poloidal harmonics ($m \geq 2$). There is also a marked difference between the low and high field side. The poloidal harmonics generally add on the low field side whereas they tend to cancel each other on the high field side - a (low- n) manifestation of ballooning.

The amplitude of all the $m \geq 2$ harmonics relative to the $m=1$ harmonic increases linearly with β_p [6]. In the hot-ion H-mode discharges, this magnetic coupling is enhanced by the large radius of the $q=1$ surface [1]. Further, a finite edge current density can increase the mode amplitude locally at the plasma boundary.

Figure 5. The displacement perpendicular to the flux surfaces as a function of the minor radius for the high performance discharge 26087. The full line is the absolute value of total displacement along the horizontal axis, the dotted line is the $m=1$ harmonic.



CONCLUSIONS

The sawtooth crashes on JET display features which depend on β . The main observation is a transient bulging of flux surfaces (duration $< 30\mu\text{s}$), which is predominantly on the low field side and extends to larger radii as β increases. This phenomenon reaches the plasma boundary when β_N exceeds 0.5 and in these cases is followed by an ELM within $50\mu\text{s}$. These sawtooth/ELM events limit plasma performance. Modelling of mode coupling shows qualitative agreement between observations of the structure of the sawtooth precursor and the calculated internal kink mode at high β .

REFERENCES

- [1] M.F.F. Nave et al, MHD activity in JET hot ion H-mode discharges, submitted to Nuclear Fusion
- [2] The Jet Team, Proc. of 13th IAEA Conf. on Plasma Physics and Contr. Fus. Research, Washington, Vol.1(1990) 219
- [3] P. Smeulders et al, this conference
- [4] M.F.F. Nave et al., Nucl. Fus. 31(1991) 697
- [5] W. Kerner et al., Proc. 18th EPS Berlin (1991), part IV, p.89-93.
- [6] M.F.F. Nave et al., Proc. 20th EPS Lisbon (1993).



FR9701771

Fusion Performances and Alpha Heating in future JET D-T Plasmas

B Balet, J G Cordey, A Gibson, P Lomas,
P M Stubberfield, P Thomas.

JET Joint Undertaking, Abingdon, Oxon, OX14 3EA.



High fusion performance pulses have been obtained at JET in the hot ion H-mode regime during the 1991-1992 experimental campaign. The energy confinement time of these pulses is found to be enhanced by at least a factor 1.5 over the value predicted by H-mode scaling expressions [1]. However this enhanced phase (VH phase) is transient and is thought to be limited at high beta by an MHD instability. This results in a large heat flux to the X-point target tiles and is followed by a large carbon influx. The new pump divertor installed at JET should allow high performance pulses of a few seconds duration by both preventing the impurity influx and controlling the density evolution. The TRANSP code [2] has been used in a predictive mode to assess the possible fusion performance of such plasmas fuelled with a 50:50 mixture of D and T, and the effect of alpha particle heating on T_e and T_i . These predictions are based on the best D-D pulse # 26087 (single-null, 2.8T, 3.1MA) [1], [3], assuming: 1) The density and impurity profiles of pulse # 26087; 2) The profiles of the ion and electron thermal diffusivities χ_i and χ_e obtained from the reference TRANSP D-D run are used to predict the evolution of T_i and T_e ; 3) For the D-T case, half the beamlines inject tritium with the actual powers and energies used in pulse # 26087. Several cases are considered below.

CASE A : 50:50 D-T MIX This case corresponds to what would have been obtained in the actual experiment if one NBI box injected tritium into a 50:50 D-T target plasma. The total and central power transfers to the thermal plasma from NBI and alpha particles are compared in Table I for the two predictive TRANSP runs at the time of maximum neutron yield. Alpha particles mostly heat the plasma electrons because their energy is so much greater than the critical energy for slowing down. However, it is interesting to note that the total and central power transfers from NB and the equipartition term are lower in the D-T case than in the D-D case; this is due to the increased T_e in the D-T case. This latter effect therefore cancels out most of the alpha particle heating. The net result is a 1keV increase of the maximum $T_e(o)$ over the D-D case. There is no significant effect of the alpha particle heating on T_i . Such a plasma would transiently achieve $Q_{DT} \sim 1$, and release some 11MW of fusion power but would not permit unambiguous observation of alpha particle heating.

CASE B : 50:50 D-T MIX, NO C BLOOM Assuming that the carbon bloom can be avoided the previous TRANSP predictions are continued for a further 5s. The input data to the code are the same as previously up to the time of maximum neutron yield ($t = 13.35s$). For later times, the input data are kept constant at their 'pre-bloom' values except the electron

density which continues to increase linearly. The T_i and T_e profiles are therefore predicted up to 18s using χ_i and χ_e profiles obtained at 13.35s: For the whole continuation period, the full input power is maintained. Table I shows that, in the central region at the time of maximum D-T neutron yield ($t = 14.5s$), the transfer from alpha particles to the electrons at 128.3 kW/m^3 for the D-T case exceeds by \sim a factor 2 that from beams to electrons for the D-D case (62.3 kW/m^3). Consequently $T_e(o)$ in the DT case would exceed by some 2.7 keV its value in the D-D case (14.5 keV versus 11.8 keV). In this no bloom scenario, the D-T predictive TRANSP run shows that a maximum fusion power of 12.3 MW (with 8.5 MW from thermal-thermal reactions) would be reached at 14.5s. This corresponds to a total $Q_{DT} = 0.93$ with a thermal $Q_{DT} = 0.67$. However, steady state is not reached in such scenario.

CASE C : 50:50 D-T MIX, VH PHASE, DENSITY CONTROL The analysis of the energy transport of pulse # 26087 [1] shows that this discharge enters a regime of enhanced confinement (VH-mode). It is also shown that the enhanced confinement is lost at 13.2s prior to the roll-over of the neutron yield which occurs at 13.35s. In this scenario, the profiles of χ_e , χ_i and Z_{eff} are fixed at the lower values in the VH-phase and the density is controlled at the value just after the carbon bloom ($\bar{n}_e \sim 4 \cdot 10^{19} \text{ m}^{-3}$). By contrast to the previous case, this scenario results in a quasi-steady state for $t > 15s$ with β values such that $\beta/\beta_{TROYON} \lesssim 1$. The thermal energy saturates at $\sim 14.5 \text{ MJ}$ for the DT case and $\sim 13 \text{ MJ}$ for the DD case. The increase of the total central power transfer to the electrons in the DT case over the DD case (see Table I) leads to a significant effect of the alpha heating on $T_e(o)$ which is $\sim 24\%$ higher than in the DD case (see Fig.1). In this scenario, a $Q_{DT} = 1$ steady state is achieved and 14.3 MW of fusion power are obtained. Another way to detect unambiguous electron heating by alpha particles in such a scenario would be to switch off the neutral beam injection at 16s. The TRANSP predictions show that, after 1s without beam heating, $T_e(o)$ in the DT case would exceed by some 4 keV its value in the DD case (see Fig. 2).

CASE D : 50:50 D-T MIX; VH PHASE, DENSITY CONTROL, 6MA Increased plasma current should be able to support a much larger plasma energy content at the same β/β_{TROYON} , thus leading to higher fusion performance. The predictions now assume the same conditions as for case C extended up to 26s but at a higher plasma current of 6.3 MA. Note that $q_\psi(\rho = 0.9) = 2.4$ is lower than the normal range of JET operation for these high performance pulses. If the thermal diffusivities in the VH-mode scale as $1/I_p$ [4], such a DT discharge would reach steady state after 8s of full beam power heating, achieving a thermal energy of 28 MJ and a total fusion power of 37.3 MW (with 32 MW from thermal-thermal reactions, see Fig.3). This corresponds to a total $Q_{DT} = 2.6$ and a thermal $Q_{DT} = 2.25$; a total $Q_{DT} = 2$ is reached after 3s of full beam power heating. In this scenario, the alpha heating clearly dominates the electron power balance in the D-T case (see Table I) and leads to a 74% increase in T_e (see Fig.4).

CONCLUSION These predictions show that if the divertor is able to avoid the carbon bloom, just running existing JET discharges to longer times with a 50:50 D-T mix will lead to $Q_{DT} \sim 1$ and detectable electron heating by alpha particles. If the VH phase can be prolonged and providing the density is controlled, a $Q_{DT} = 1$ steady state plasma is achieved with significant alpha heating. If the bloom and MHD instabilities can be controlled at higher plasma currents using a higher toroidal field to keep a reasonable β value and if the confinement scales as $1/I_p$, then a higher fusion performance steady state plasma with $Q_{DT} > 2.5$ should be possible. The alpha heating power of 4.9 MW would lead to a 74% increase in T_e . Furthermore, if the energy confinement improves with atomic mass number, even better fusion performance might be expected.

REFERENCES :

- [1] Balet B., Stubberfield P.M., Borba D., et al., Nucl. Fusion 33 (1993) 1345.
- [2] Goldston R.J., McCune D.C., Towner H.H., et al., J. Comput. Phys. 43 (1981) 61.
- [3] JET Team, Nucl. Fusion 32 (1992) 187.
- [4] Christiansen, J.P., et al, Nucl. Fusion 32 (1992) 291.

Table I:	CASE A		CASE B		CASE C		CASE D	
time (s)	13.35		14.5		16.3		avg 21 -> 26	
	D-D	D-T	D-D	D-T	D-D	D-T	D-D	D-T
I (MA)	3.15		3.15		3.15		6.3	
B_t (T)	2.8		2.8		2.8		3.5	
$\beta/\beta_{\text{Troyon}}$	0.75	0.80	0.85	0.95	0.86	1.0	0.5	0.82
q_{cyl}	2.8		2.8		2.8		1.75	
q_ψ ($\rho = 0.9$)	3.9		4.1		4.2		2.4	
Total power transfers (MW):								
from α to e-	-	1.32	-	2.0	-	2.2	-	4.9
form α to ions	-	0.2	-	0.44	-	0.54	-	2.36
from NB to e-	2.16	1.73	2.53	2.02	2.01	1.51	1.54	0.87
from NB to ions	10.91	10.81	10.81	11.1	11.06	11.42	11.5	12.1
equipartition	2.42	1.96	2.6	1.93	2.09	1.24	2.58	0.92
Central power densities (volume averaged over the central 30 cm) (kW/m³):								
from α to e-	-	62.31	-	128.3	-	114.8	-	184.3
form α to ions	-	10.24	-	34.5	-	38.6	-	128.9
from NB to e-	76.45	44.6	61.12	40.7	59.5	37.4	28.14	9.83
from NB to ions	628.9	484.9	478.8	479.2	556.0	545.4	467.9	499.8
equipartition	81.7	55.7	67.1	33.8	93.3	44.1	97.2	35.7
D-T Fusion Parameters:								
P_{fusion} (MW)	-	10.97	-	12.3	-	14.3	-	37.3
$P_{\text{beam abs}}$ (MW)	-	14.3	-	14.3	-	14.3	-	14.3
Q_{total} (1)	-	1.1	-	0.93	-	1.0	-	2.6
dW/dt (MW)	-	6.0	-	1.5	-	0.0	-	0.0
Q_{thermal}	-	0.79	-	0.67	-	0.67	-	2.25
Maximum temperature (keV):								
T_e (0)	11.9	12.9	12.5	14.5	13.0	16.5	18.8	32.7
T_i (0)	19.0	18.5	19.0	19.0	21.0	21.0	30.3	43.0

- (1) Q_{total} is defined by $Q_{\text{total}} = Q_{\text{thermal}} + Q_{\text{beam}}$ with
 $Q_{\text{thermal}} = P_{\text{fusion, thermal}} / (P_{\text{beam abs}} - dW/dt)$
 $Q_{\text{beam}} = (P_{\text{fusion, beam-thermal}} + P_{\text{fusion, beam-beam}}) / P_{\text{beam.abs.}}$

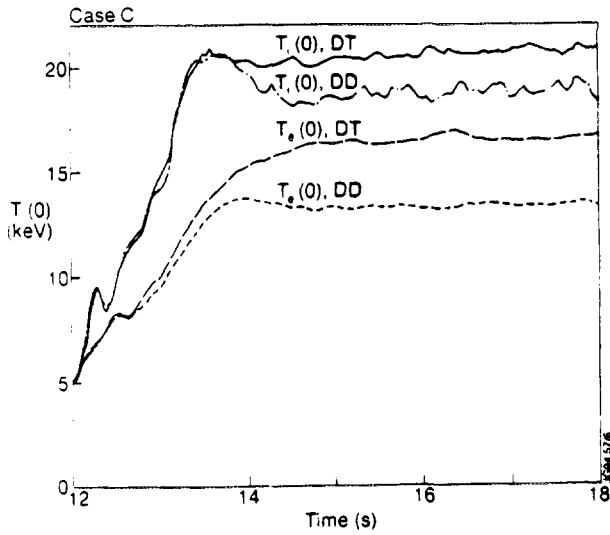


Fig. 1 The time evolution of $T_i(0)$ and $T_e(0)$ for the D-D and D-T plasmas in scenario C.

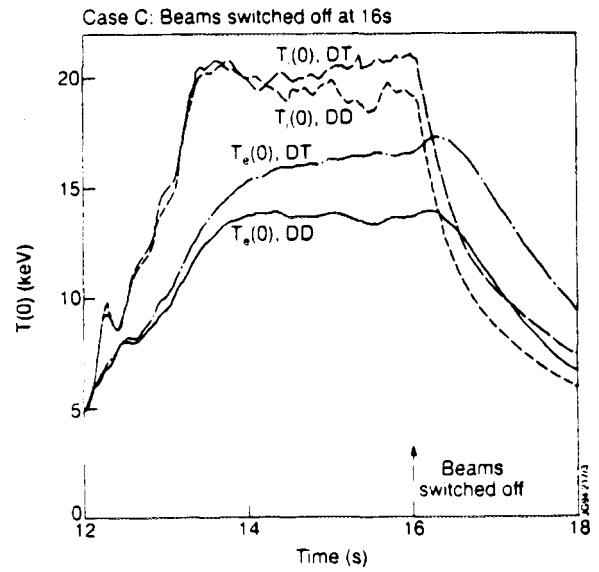


Fig. 2 The time evolution of $T_i(0)$ and $T_e(0)$ for the D-D and D-T plasmas in scenario C with NBI switched off at 16s.

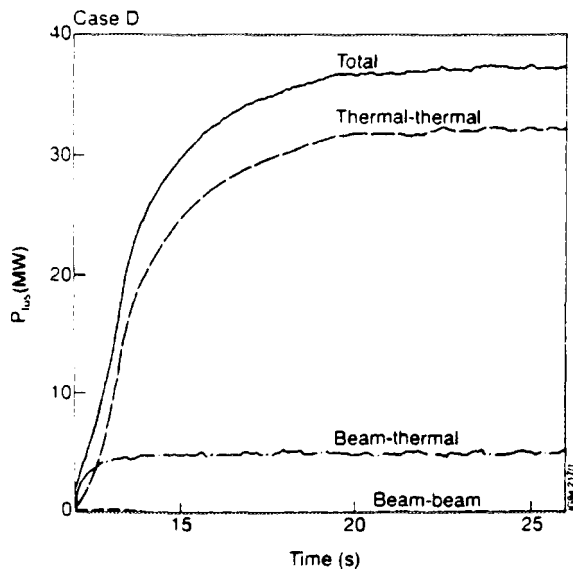


Fig. 3 The time evolution of the total fusion power and its components for a D-T plasma in scenario D.

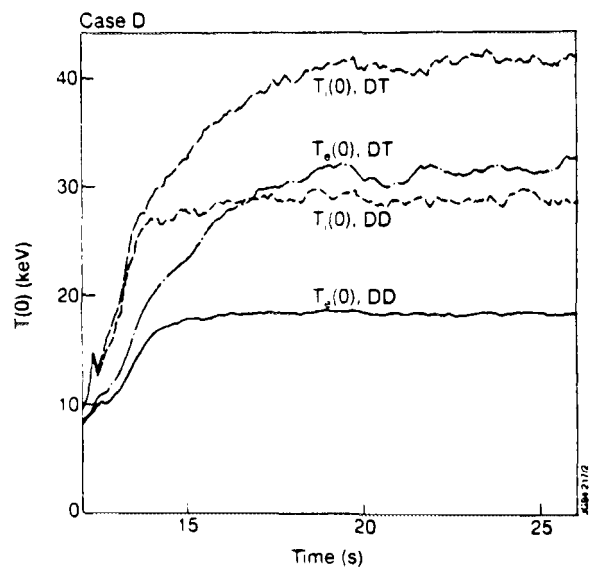


Fig. 4 The time evolution of $T_i(0)$ and $T_e(0)$ for the D-D and D-T plasmas in scenario D.



A Stable Route to High- β_p Plasmas with Non-Monotonic q-Profiles

F X Söldner, Y Baranov, V P Bhatnagar, A J Bickley,
C D Challis, J P Goedbloed¹, B Fischer, C Gormezano, H A Holties¹,
G T A Huysmans, W Kerner, V V Parail², G V Pereverzev²,
F Rimini, A C C Sips, E Springmann, A Taroni.

JET Joint Undertaking, Abingdon, Oxon, OX14 3EA.

¹ FOM Institute for Plasma Physics, Nieuwegein, The Netherlands.

² Kurchatov Institute of Atomic Energy, Moscow, Russia.



ABSTRACT

Steady-state operation of tokamak reactors seems feasible in so-called Advanced Scenarios with high bootstrap current in high- β_p operation. The stabilisation of such discharges with noninductive profile control will be attempted on JET in pursuit of previous high bootstrap current studies /1/. Results of modelling studies of full noninductive current drive scenarios in JET and ITER are presented in this paper. Fast Waves (FW), Lower Hybrid (LH) Waves and Neutral Beam Injection (NBI) are used for heating and current drive, alternatively or in combination. A stable route to nonmonotonic q-profiles has been found with a specific ramp-up scenario which combines LH-current drive (LHCD) and a fast Ohmic ramp-up. A hollow current profile with deep shear reversal over the whole central region is thereby formed in an early low- β phase and frozen in by additional heating.

MODEL DEVELOPMENT

Initially the different current drive and heating methods were treated in separate dedicated codes. The Monte Carlo code PENCIL is used for NBI, the ray tracing code BRAYCO for FW and a ray tracing code /2/ and a novel beam tracing code /3/ for LH. After validation on experimental data from previous experiments on JET, the codes for the bootstrap current and for NBI and the beam tracing code for LH were implemented as modules into the 1.5-D transport code JETTO. The energy transport in these calculations is described with a model developed on the basis of L- and H-modes in JET discharges /4/. The transport code results have been linked to the MHD stability code CASTOR which is used to study the behaviour of ballooning, kink and infernal modes. Several iterations of transport code and MHD analysis were made for each case for fully consistent parameter sets. Sensitive diagnostics signals available on JET for the measurement of current and power deposition profiles, as polarimeter signals, internal inductance and hard X-ray emission, are directly determined from the model calculations. These quantities are planned to be used in the experiment as input signals for a real time profile control system.

MHD STABILITY ANALYSIS

The feedback of MHD stability calculations is an essential part of the modelling of the profile control in reversed shear discharges with the transport/current code JETTO. The relevant MHD instabilities that can limit the operating window of these discharges are ballooning modes, external kink modes and specifically for plasmas with reversed shear, the so-called infernal modes [5]. With non-monotonic q-profiles, ballooning modes are stable in the region of negative shear without limit on the pressure gradient. Infernal modes, driven by the pressure gradient in a low shear region, can become unstable if the minimum in the q-profile is too close to a rational surface. The external kink mode is driven by a finite edge bootstrap current due to a large edge pressure gradient. Infernal modes appear to be the dominant limiting instability. In the worst case where the largest gradient occurs at the minimum q, a poloidal beta of 0.5 is still stable to infernal modes. At higher values of beta the shape of the pressure profile is essential; the largest gradient must be inside the negative shear region away from the q-minimum. On the outside of the minimum q the pressure gradient will be limited by ballooning mode stability, especially in the low positive shear region.

FULL CURRENT DRIVE SCENARIOS ON JET

A wide range of full noninductive current drive scenarios with LHCD, Fast Wave current drive (FWCD) and NBI-current drive together with the bootstrap current have been modelled. Phasing of the A2 FW antennae on JET and high energy coinjection NBI provide central current drive. LHCD is used for central and off-axis current drive. The deposition profile can be shifted through control of the $N_{||}$ spectrum. Full control of the current profile is achieved with the combination of these methods, as available on JET.

A stable route to high- β_p plasmas with nonmonotonic q-profiles has been identified for discharge scenarios on JET. With LH current drive (LHCD) applied during a fast plasma current ramp-up, a broad current distribution with negative shear in the central plasma region and $q_{\min} > 2$ can be generated already in an early low- β_p stage of the discharge. For JET, a current ramp-up rate of $dI_p/dt \geq 1.5$ MA/s is required for this purpose. Additional heating with FW and/or NBI is started at the end of the current ramp-up. The preconditioned hollow current profile is then frozen in and maintained into stationary conditions. MHD-unstable transitions from positive to negative shear in regions of high pressure during a discharge can be avoided by this scenario. Gradual variations between hollow and peaked current profiles for stability and confinement studies can be obtained by power adjustments among FWCD and NBI for central current drive and LHCD for off-axis current drive.

Two complementary cases are presented in this paper. Either hollow or peaked current profiles are generated on the same target plasma by using as dominant driver LHCD or FWCD, respectively. The basic discharge parameters are: $I_p = 3$ MA, $B_t = 3.4$ T, $n_{e0} = 3.5 \times 10^{19}$ m⁻³, $dI_p/dt = 1.5$ MA/s. A hollow current profile is formed by LHCD with $P_{LH} = 8$ MW during ramp-up and $P_{LH} = 7$ MW during flat-top. Additional ion cyclotron heating with $P_{ICRH} = 12$ MW is applied during flat-top. The waveforms of LH-driven current, bootstrap

current and the total plasma current are shown in Fig. 1. The LH-driven current increases during the high power heating phase due to the enhancement in current drive efficiency with higher electron temperature. The radial current profiles are shown in Fig. 2 for a late phase during current flat-top. The LH deposition profile has shifted from the central region during ramp-up to mid-radius. The resulting q-profiles at the end of the current ramp-up and late into flat-top are plotted in Fig. 3. The flat-top q-profile for a full current drive scenario with peaked current profiles is also given in Fig. 3. In this complementary case central current drive with FWCD at $P_{FWCD} = 8$ MW dominates. LHCD with $P_{LH} = 1.5$ MW is used for topping up to full current drive and additional off-axis profile control. Transitions between the two scenarios should allow to assess the stability and confinement characteristics of non-monotonic q-profiles. The result of the MHD analysis for the hollow current profile scenario, as presented in Fig. 1 is given in Fig. 4. The dependence of the growth rate of infernal modes ($n=1$ and $n=2$) on the q-minimum value shows that for the actual value of $q_{min} = 2.3$ in the late flat-top phase the modes are stable.

These noninductively driven plasmas with high bootstrap current and high β_p values will be studied on JET also in preparation of steady state scenarios on ITER.

STEADY-STATE SCENARIOS ON ITER

Profile control and steady-state operation in the presently proposed ITER device were modelled with the system of codes developed for the planned Advanced Tokamak Scenario experiments on JET. Burn instabilities can be encountered in scenarios with high bootstrap current fractions if the energy transport is linked to the current profile. Oscillations in the fusion power output are excited if the q-value in the center rises too much with dominant off-axis current drive. The time constant of these oscillations is roughly given by the geometric mean value of confinement time and resistive time for current profile changes. With a combination of LHCD and FWCD, central and off-axis current drive can be balanced to give constant fusion power output. A consistent scenario for steady state operation of ITER is then obtained. The full plasma current of 13.5 MA is driven by the combination of 10 MA bootstrap current, 2.8 MA LH-driven current and 0.7 MA FW-driven current. A wide region of shear reversal is created inside half of the plasma radius during the ramp-up phase and maintained into flat-top. The q-profile for this case is stable against ballooning and infernal modes. Constant fusion power output of 1.6 GW is obtained.

REFERENCES

- /1/ C.D. Challis, et al., Nuclear Fusion **33**, 1097 (1993).
- /2/ Y. Baranov, et al., 20th Europ. Conf. on Contr. Fusion and Plasma Physics, Lisbon, Vol. III, 881 (1993).
- /3/ G.V. Pereverzev, 20th Europ. Conf. on Contr. Fusion and Plasma Physics, Lisbon, Vol. III, 885 (1993).
- /4/ V.V. Parail, et al., internal report JET-P(93)87 (1993), to be published.
- /5/ T. Ozeki, et al., Nuclear Fusion **33**, 1025 (1993).

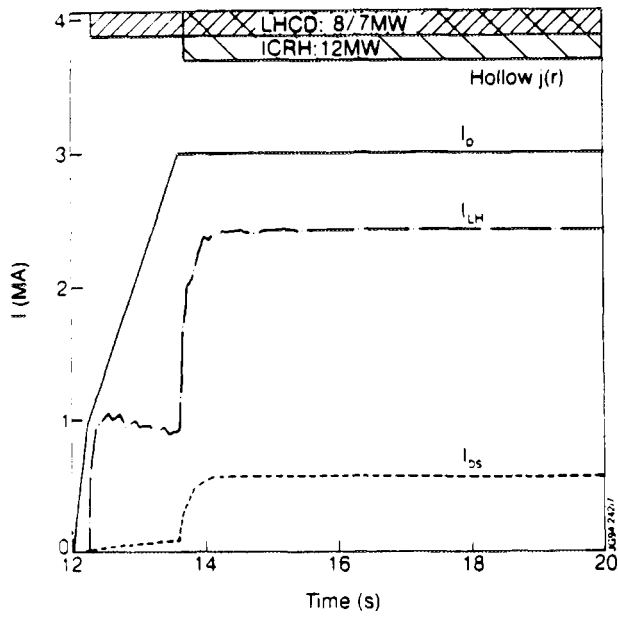


FIG.1: Waveforms of bootstrap current, LH-driven current and total plasma current in a hollow current ramp-up scenario.

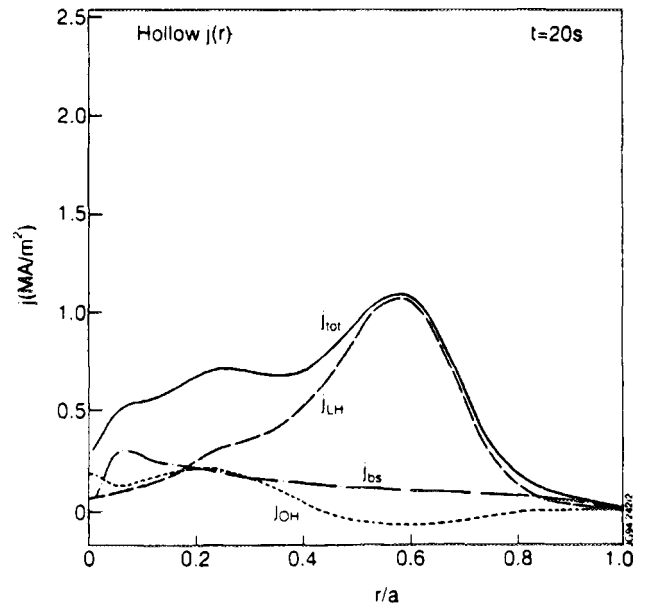


FIG.2: Radial profiles of LH-driven, bootstrap, OH-driven and total current profile late in current flat-top.

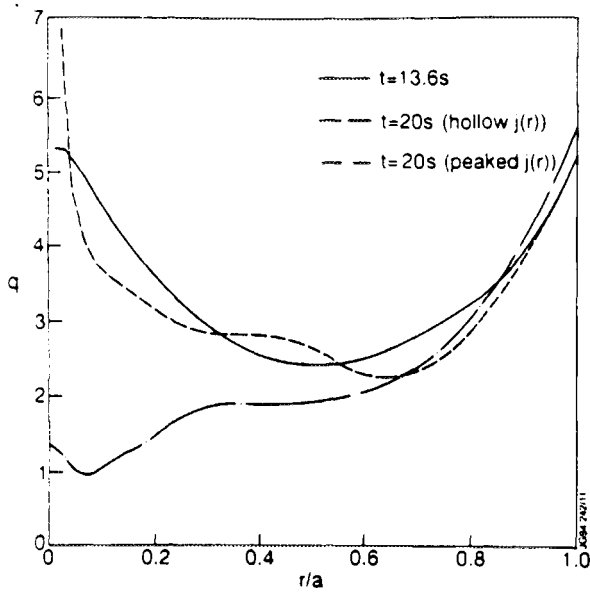


FIG.3: The q -profile at the end of current ramp-up and late in the flat-top phase for hollow and peaked current scenarios.

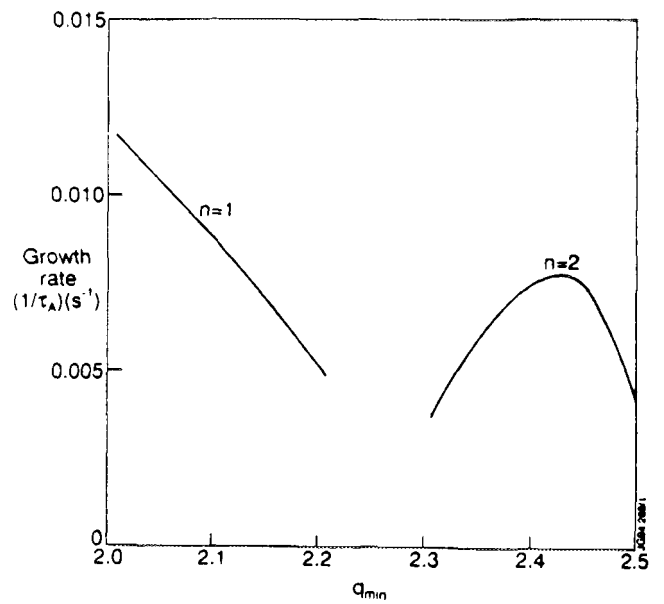


Fig.4: Growth rate of $n=1$ and $n=2$ infernal modes versus the minimum q value for the flat-top hollow current profile conditions.



FR9701773

A Theory for the Propagation of Changes to Confinement

J P Christiansen.

JET Joint Undertaking, Abingdon, Oxon, OX14 3EA.



1. INTRODUCTION

A heat pulse triggered by a sawtooth near $q_\psi = 1$ surface propagates on a msec. timescale towards the edge in TFTR [1, 4] and JET [2, 3]. A cold pulse triggered by impurity injection propagates towards the $q_\psi = 1$ surface on a msec. timescale towards the $q_\psi = 1$ surface in TFTR [5]. The transitions from L to H and H to L-mode confinement propagate inwards on a msec. timescale in JET [6]. If a diffusive process is invoked to explain these phenomena then it requires a heat diffusivity χ which initially, in the ballistic phase [4], is one order of magnitude larger than the steady state value inferred from a power balance calculation. In the case of the rapid L to H transition [6] this implies that the relative change $\Delta\chi / \chi$ initially is of order + 10 and then has to relax towards $- 1/2$.

The omnipresence of "some global mode" could be invoked to explain these rapid changes; such "a global mode" would switch on-off during the L to H transitions; however, heat pulses produced by sawteeth propagate at similar speeds in ohmic, L-mode and H-mode plasmas. At present no conventional theory can explain the rapid changes to confinement; conventional theory means in this context a theory which assumes that the rapid changes occur via diffusive processes. A recent study on TFTR [4] concludes that the initial phases of the heat pulse propagation is non-diffusive.

A physics model is being developed in an attempt to describe rapid changes to confinement. The work is divided into three parts: i) the derivation of a fluid model based on kinetic drifts; ii) a study of the linearized response from these drift-kinetic fluid equations to a perturbation; iii) the evaluation of the characteristic propagation speed of a finite amplitude perturbation through a toroidally confined plasma with varying shear and collisionality. This paper will summarise Part I and outline a simplified approach to Part III. The initial simplification made is to employ a spectral representation of a temperature perturbation \tilde{T} ; i.e. \tilde{T} varies as $e^{i\mathbf{k}\cdot\mathbf{r}}$, and then to apply standard approximations of weak turbulence theory. Work in progress replaces the spectral representation by a statistics based description.

2. FLUID EQUATIONS FOR TEMPERATURE ANISOTROPY BASED ON KINETIC DRIFTS

The Boltzmann equation is used to derive equations for velocity moments M of the distribution function $f(\underline{v})$ for plasma particles of mass m , velocity \underline{v} , and charge Ze in a magnetic field \underline{B} and electric field \underline{E} . Four moment equations are derived with $M = 1, m\underline{v}, m\underline{v}\underline{v}, m\underline{v}\underline{v}\underline{v}$ for respectively density n , momentum $m\underline{u}$, pressure tensor \underline{P} and heat flow tensor \underline{Q} . The fifth moment enters the equation for \underline{Q} and formal closure of the four equations is obtained by reducing the moment $m\underline{v}\underline{v}\underline{v}\underline{v}$ into products $(m\underline{v}\underline{v})(\underline{v}\underline{v})$ of dyadics. The four moment equations include on the RHS terms describing collisions between ions and electrons (ei) and between ions, electrons and an external source. The former leads via the collision operator C_{ei} to respectively for the four moments; $0, \underline{R}^c, \underline{P}^c, \underline{Q}^c$. The external source leads to respectively: a source rate S , directional momentum $S m \underline{U}$, power transfer $S \underline{E}$, collisional heat flow tensor $\underline{\Theta}$. The external source can represent: i) low energy Frank-Condon neutral atoms undergoing charge-exchange in the edge, ii) neutrals being ionized, iii) neutral beam injection, iv) ICRF accelerated minority ions residing in the plasma. For any such source a separate calculation of $S, \underline{U}, \underline{E}, \underline{\Theta}$ must be made. This is done in computer codes like TRANSP.

The derived equations for the anisotropic temperatures T_{\parallel} and T_{\perp} and density n are

$$\partial_t n + \underline{u}_F \cdot \nabla n + n \left(\frac{\underline{u}_\kappa}{T_{\parallel}} \cdot \nabla T_{\parallel} + \left(\frac{\underline{u}_B}{T_{\perp}} - \frac{\underline{u}_\kappa}{T_{\parallel}} \right) \cdot \nabla T_{\perp} \right) + n \left(1 - \frac{T_{\perp}}{T_{\parallel}} \right) \Omega_{\parallel} + \Omega_E = C \quad (1)$$

$$\partial_t \frac{1}{2} T_{\parallel} + (\underline{u}_F + \underline{u}^{(||)}) \cdot \nabla \frac{1}{2} T_{\parallel} + T_{\parallel} \underline{u}_\kappa \cdot \frac{\nabla n}{n} + (T_{\parallel} - T_{\perp}) \Omega_{\parallel} + T_{\parallel} \omega = \frac{1}{2} C_{\parallel} \quad (2)$$

$$\partial_t T_{\perp} + (\underline{u}_F + \underline{u}^{(\perp)}) \cdot \nabla T_{\perp} + T_{\perp} \left(\underline{u}_B - \frac{T_{\perp}}{T_{\parallel}} \underline{u}_\kappa \right) \cdot \frac{\nabla n}{n} + T_{\perp} (\Omega_{\parallel} + \Omega_E + \omega) = C_{\perp}. \quad (3)$$

The advective fluid velocities, $\underline{u}_F, \underline{u}^{(||)}, \underline{u}^{(\perp)}$ contain $\underline{E} \times \underline{B}$ drift, curvature drift \underline{u}_κ , ∇B drift \underline{u}_B , but not diamagnetic and collisional drifts. The inverse time scales $\Omega_{\parallel}, \Omega_E, \omega$ in (1 - 3) do not contain $\nabla n, \nabla T_{\parallel}, \nabla T_{\perp}$ and the RHS terms denote the collisional effects. Eqs. (1 - 3) are coupled non-linear hyperbolic equations and they show that diamagnetic drifts do not transport plasma or energy. In this drift kinetic formulation magnetic curvature $\underline{\kappa}, \nabla \times \hat{b}$ and ∇B can maintain anisotropy.

3. SIMPLIFIED TURBULENT TRANSPORT

In a toroidal configuration the stochastic nature of drift motion continuously generates fluctuations \tilde{T}_\perp , \tilde{T}_\parallel , \tilde{n} on each magnetic surface. The advection of \tilde{n} etc. and collisions will attempt to isothermalize ($\partial_t \tilde{n} \rightarrow 0$) each surface as described by Eqs. (1 - 3). The isothermalization rates $\partial_t \tilde{T}_\parallel$ etc. arise from drifts in three directions labelled β (along \hat{b}) μ (diamagnetic direction) and x (normal to a surface); the rate in the parallel directions is faster than in the other directions. $\partial_t \tilde{T}_\parallel$ therefore depends strongly on the mode rationality numbers ($q_\psi = m/n$) of a surface. In a tokamak these numbers have a rapid x variation. In the (x, μ) plane a disturbance \tilde{T}_j induced on a field line j will propagate faster in the μ direction (via parallel flows and \perp drifts) than in the x direction (via \perp drifts). The displacement of a field line μ_2 after one toroidal turn is

$$\mu_2 \approx \frac{1}{m} \int_0^{2\pi} \frac{d\ell}{b\phi} \quad (4)$$

while the maximum displacement of a particle from a magnetic surface $\Delta x \sim \epsilon \rho_\theta$ (Larmor radius in poloidal field). Since $\mu_2(x)$ differs strongly from $\mu_2(x + \Delta x)$ the flow pattern associated with the disturbance \tilde{T}_j at x becomes decorrelated from that at $x + \Delta x$ after one toroidal transit time. The linear contributions to $\partial_t \tilde{T}$, $\underline{u}_F \cdot \nabla \tilde{T} + \underline{u}_F \cdot \nabla \tilde{T}$, will average out quickly and transport in the model presented will arise from the non-linear term $\underline{u}_F \cdot \nabla \tilde{T}$. An assessment of the random spatial displacements $\underline{\Delta}$ of energy (or \tilde{T}) are described by the evolution of the velocity correlation tensor

$$\underline{\underline{C}} = \langle \underline{u}_F(t) \underline{u}_F(t + \tau) \rangle = \underline{\alpha} \underline{\alpha} \langle \tilde{T}(t) \tilde{T}(t + \tau) \rangle \quad (5)$$

where $\underline{\alpha}$ contains the magnetic curvature $\underline{\kappa}$ and ∇B vectors. The non-linear solution for the temperature correlation function C_T is obtained from Eqs. (1 - 3) with the following simplifications: $\tilde{n} = 0$, $\tilde{T}_\perp = \tilde{T}_\parallel = \tilde{T}$, $C = C_\parallel = C_\perp = \Omega_\parallel = \Omega_E = \omega = 0$, and it involves calculating the evolution of harmonics in an assumed spectral representation

$$\tilde{T} = \sum_{\mathbf{k}} \tilde{T}_{\mathbf{k}} e^{i\mathbf{k} \cdot \mathbf{r}}, \quad \tilde{T}_{\mathbf{k}}(t + \tau) = \tilde{T}_{\mathbf{k}}(t) e^{P_{\mathbf{k}} \tau}, \quad P_{\mathbf{k}} = i\underline{\alpha} \cdot \mathbf{k} \int_t^{t+\tau} \tilde{T}(t') dt' \quad (6)$$

The propagator $P_{\mathbf{k}}$ describes the probability that the entire history $\tilde{T}(t) \rightarrow \tilde{T}(t + \tau)$ takes place. From stochastic theory the expectation value of $P_{\mathbf{k}}$ is the following variance

$$E\{P_k\} = [(i\alpha \cdot k)^2 2Q_T]^{1/2}, \quad Q_T = \frac{1}{2} \int_0^{\tau} \int_0^{\tau} C_T dt_1 dt_2.$$

The resulting equation for Q_T has the first integral

$$\frac{1}{2} \left(\frac{dQ_T}{d\tau} \right)^2 = \iiint S_k \left(1 - e^{-(\alpha \cdot k)^2 Q_T} \right) \frac{d\mathbf{k}}{\alpha \cdot \mathbf{k}} \quad (7)$$

where $S_k = \langle \tilde{T}_k^2(t_0) \rangle$ represents a stationary fluctuation spectrum. The immediate response to a disturbance (small τ) shows advective or wavelike transport with a propagation speed obtained from expanding (7) $2 \left(\frac{d}{dt} \langle \Delta \Delta \rangle^{1/2} \right)^2 = \alpha \alpha \iiint S_k d\mathbf{k}$ or $v_{prop} = \alpha \langle S_k \rangle^{1/2} = \alpha_F \langle \tilde{T}_k^2 / T^2 \rangle^{1/2}$. This means that the disturbance in this simplified model propagates with the fluid drift velocity (appropriately scaled) independent of the nature or origin of the fluctuations. In a more complex model the propagation speed derived from Eqs. (1-3) will depend on $\langle \tilde{n}_k^2 / n^2 \rangle$, $\langle \tilde{T}_{\perp k}^2 / T_{\perp}^2 \rangle$, $\langle \tilde{T}_{\parallel k}^2 / T_{\parallel}^2 \rangle$. Experimental observations show fluctuation levels to be largest at the edge while the drift velocities themselves are largest at the centre.

4. SUMMARY

A drift kinetic fluid model has been developed. It shows that diamagnetic drifts do not contribute to transport of plasma and energy (no entropy generation). Application of the model to a simplified description of plasma turbulence shows that disturbances, such as heat-cold pulses, L to H transitions, all can propagate with the fluid advective drift velocity irrespective of the nature of these disturbances.

REFERENCES

- [1] E.D. Frederickson, J.D. Callen, K. McGuire et al., Nucl. Fusion, 26, 849 (1986).
- [2] B.J.D. Tubbing, et al. Nucl. Fusion, 27, 1843 (1987).
- [3] A. Griguoli, A.C.C. Sips, Application of Dynamic Response to Analysis to JET Heat Pulse Data, JET Report, JET-R(93)04).
- [4] E.D. Frederickson, A.C. Janos, K.M. McGuire, S.D. Scott, G. Taylor, Nucl. Fusion 33, 1759 (1993).
- [5] M.W. Kissick, E.D. Frederickson, J.D. Callen, Nucl. Fusion 34, 349 (1994).
- [6] S.V. Neudatchin, D.G. Muir, J.G. Cordey, The Time Behaviour of the L-H and H-L Transitions in JET, JET preprint JET-P(93)58, to appear in Nucl. Fusion.4



FR9701774

Spatial Distribution of γ Emissivity and Fast Ions during (^3He)D ICRF Heating Experiments on JET

E Righi¹, D F H Start, C Warrick².

JET Joint Undertaking, Abingdon, Oxon, OX14 3EA.

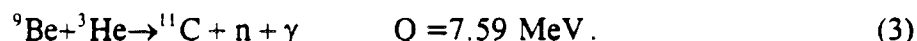
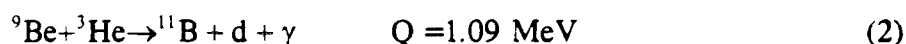
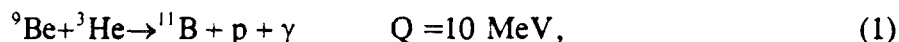
¹ Imperial College of Science, Technology and Medicine, London, UK.

² AEA Technology, Culham, Oxfordshire, OX14 3DB, UK.



Introduction. During the 1991-92 JET experimental campaign the neutron profile monitors measured along both the horizontal and vertical lines of sight the γ emissivity produced by nuclear reactions of ^3He ions accelerated by ICRF heating with ^9Be impurities during ICRF heating experiments in a (^3He)D plasma [1]. In the present paper a numerical technique is presented that simulates such measurements by merging information obtained from the fast ion distribution and from nuclear reactions producing the observed γ emissivity. This technique is full of potentialities to be developed, and it can play an important role in the identification of plasma instabilities that affect the redistribution of the fast ions in the plasma, like the TAE modes and the ripple in the tokamak magnetic field.

Production of γ photons during ^3He - ^9Be reactions. High energy ^3He ions accelerated by ICRF heating can undergo exothermic nuclear reactions with ^9Be impurities present in the plasma, namely,



The γ photons are produced when the residual nucleus is formed in an excited state, and subsequently decays to one of the lower excited states, or the ground state. In the present analysis Eq.(1) is considered, because the reaction energy of Eq.(2) is one order of magnitude lower, and can therefore be neglected, while Eq.(3) is the isobaric equivalent of Eq.(1). Extensive studies of the $^9\text{Be}(^3\text{He},\text{p})^{11}\text{B}$ reaction exist [2,3,4,5,6], from which information can be obtained about the differential cross-sections at 90° in the laboratory frame of reference and in the energy range between 1 and 3 MeV for protons leaving ^{11}B in its excited states. Since the γ detectors used have no energy resolution, a "total" cross-section $(d\sigma / d\omega)_{\text{tot}}$ has been derived, sum of all the excitation curves for the energy levels from first to ninth, which gives an estimate of the relative probability that a γ photon is emitted from any excited state in the energy interval of interest (see Fig.1).

Simulation of γ -ray emission. In order to describe correctly the interaction of ^3He ions with ^9Be impurities it is also necessary to know the distribution of ^3He ions in $(v_{\parallel}, v_{\perp}, r, \theta)$ space and the orbit paths of the fast ^3He ions. The distribution of ^9Be ions is here assumed to be uniform and with a concentration equal to 1% of the electron density,

consistent with the measurements of Z_{eff} for the discharges considered. The ^3He distribution has been calculated by means of a 2D numerical code that solves the bounce-averaged steady-state Fokker-Planck equation in cylindrical coordinates [7]. This code does not include the effects of finite orbit width of high energy fast ions, which therefore have to be included *a posteriori*. To this end the orbit following code ORBIT [8] has been used that estimates the time $(\Delta t / T)_{T \rightarrow \infty}$ spent by the ^3He ions at each point in the configuration

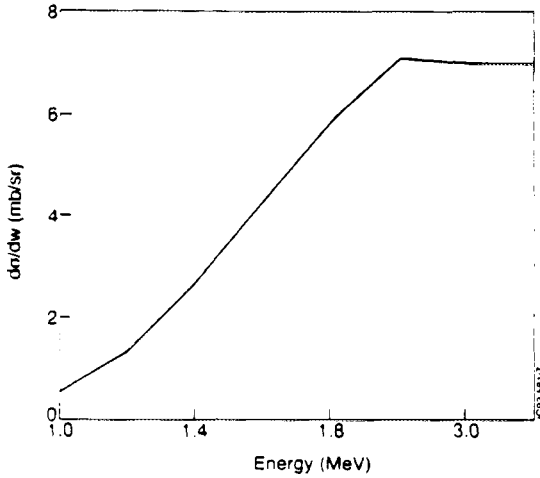


Fig.1. "Total" differential cross-section for ^{11}B .

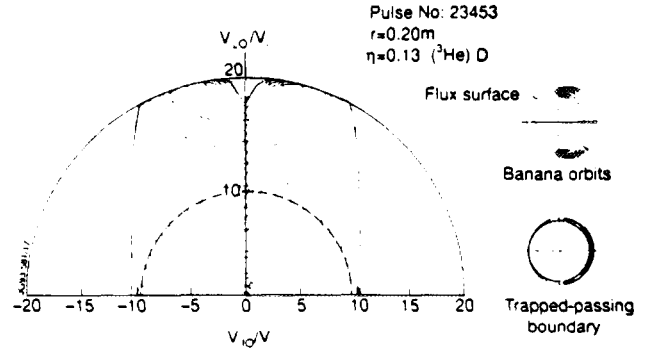


Fig.2. Minority ion distribution function in $(v_{||}, v_{\perp})$ space.

space. A plot of the intensity of γ emissivity,

$$I_{\gamma} \propto \int d^3r \int dE \sqrt{E} f(E, r, \theta) \left(\frac{d\sigma}{d\omega} \right)_{tot} \left(\frac{\Delta t}{T} \right)_{T \rightarrow \infty}, \quad (4)$$

can then be generated for each energy considered and a number of test particles, once the weight function,

$$w(E, r, \theta) = \sqrt{E} f(E, r, \theta) \left(\frac{d\sigma}{d\omega} \right)_{tot} \left(\frac{\Delta t}{T} \right)_{T \rightarrow \infty}, \quad (5)$$

is known. Information about the ^3He distribution in energy, pitch angle and minor radius and the excitation curves of ^{11}B have therefore been combined in the weight function Eq.(5) as input for the ORBIT code to calculate the γ -ray emission of monoenergetic test particles launched at the midplane. The results of simulations at different energies have been subsequently integrated to give the total γ emissivity.

Results and comparison with the experiment. The JET shots for which experimental measurements of the γ emissivity exist are those of Table I, where their main plasma parameters are listed. Measurements of γ emissivity can be plotted either as a 3D

reconstruction of γ intensity in the poloidal plane, or as line integrated data of γ emission along a vertical and horizontal line of sight [1]. Both cases have been simulated numerically. In Fig.3 the intensity of γ emission in the (r,z) plane is reported for the off-axis discharge JPN 23450. Analysis of these simulations show that different types of orbits contribute to determine the two γ distributions when on-axis and off-axis ICRF are considered, which leads also to a different localization of the emissivity peak (the "hot spot"). In particular, the off-axis ICRF discharge (JPN 23450) is dominated by passing particles in the plasma

centre, while trapped particles are localised either on the RF resonance or nearby. On the contrary, in the case of on-axis ICRF heating (JPN 23453) trapped particles dominate near the plasma centre (on the RF resonance), with a clear contribution of high energy D-shaped orbits. If the numerical γ emissivity in the (r,z) plane is line integrated into γ intensity along the horizontal and vertical lines of sight [1], then the γ -ray calculations can be compared with the experimental curves. The results, shown in Fig.4 for JPN 23450, clearly indicate that experiment and simulation agree qualitatively, meaning that the main elements

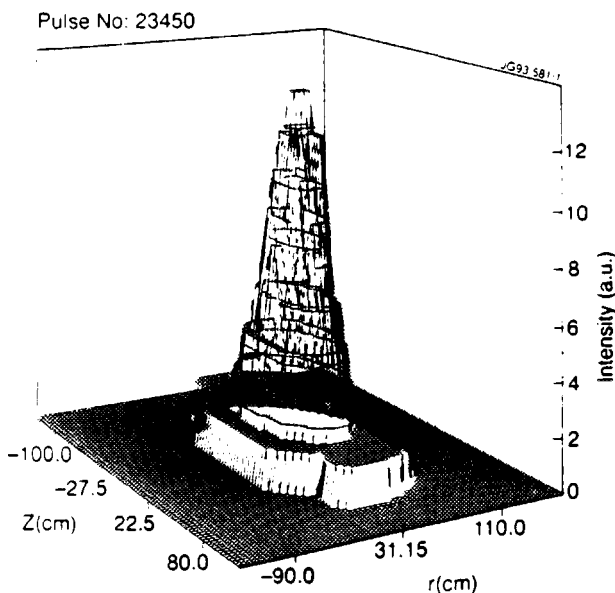


Fig.3. Numerical reconstruction of γ -ray emissivity in the poloidal plane for the off-axis ICRF heated discharge JPN 23450.

Table I - Plasma parameters

	JPN 23450	JPN 23453
time slice (s)	49.0	49.0
plasma current (MA)	3.5	3.5
B, on-axis (T)	3	3
T_{e0} (keV)	7.3	7.4
n_{e0} (10^{19} m^{-3})	2.8	3.0
P_{RF} (MW)	7.9	11.7
magnetic axis R_0 (m)	3.10	3.12
resonance off-set (m)	0.29	0.06
fast ion energy (MJ)*	0.2	1
Z_{eff}	1.5	1.6
n_{He}/n_{e0} *	0.045	0.13

*estimated with the orbit code PHANTOM [9] and cross-checked with experimental data

responsible for the distribution of γ emissivity (and fast ions) are all present in the model. However the picture also shows that while along the horizontal line of sight the measured and calculated intensities have the same profiles, along the vertical line of sight the intensity peaks are displaced of one channel. This means that the simulated "hot spot" is displaced horizontally with respect to the measurement. This difference could find an explanation in the approximations used. In particular, the Fokker-Planck code calculates $f(E,r,\theta)$ in cylindrical coordinates, while the actual discharges have substantial elongation and triangulation. Also orbit

effects are not introduced self-consistently, but *a posteriori*. It is also not excluded that other nuclear reactions (of ^{12}C with ^3He , for instance) should be included in the analysis.

Conclusions and future work. In this paper a model has been presented that can simulate the γ emissivity in the poloidal cross-section during (^3He)D ICRF heated discharges in JET plasmas. Calculations show reasonable agreement with the experiment, indicating that all the main elements that produce the distribution are present. However the model is still only a first order description of the γ production. Future work will therefore be oriented especially to improve the calculation of the

fast ion distribution function by including self-consistently effects of toroidal geometry and finite orbit widths of ^3He ions (through already available Monte-Carlo codes). This technique can be useful to analyse JET discharges in all those scenarios where the ^3He distribution plays a major role, like in the presence of Toroidal Alfvén Eigenmode (TAE) modes or ripple in the tokamak magnetic field. In the former case the distribution is expected to lose its peakedness due to the redistribution of the passing fast ions into high energy D-shaped orbits.

Acknowledgements. The authors would like to acknowledge the cooperation with the JET RF Team and the Neutron Group, in particular P. van Belle, G. Sadler, P.J.A. Howarth and O.N. Jarvis. Special thanks go to Dr. E. Jelley, of the Nuclear Physics Laboratory in Oxford, for his precious help to dig out the references on ^{11}B cross-sections.

References

1. P.J.A. Howarth et al., these Proceedings.
2. H.D. Holmgren, M.L. Bullock and W.E. Kunz, *Phys. Rev.* **104** (1956), 1446.
3. S. Hinds and R. Middleton, *Proc. Phys. Soc.* **A74** (1959), 196.
4. E.A. Wolicki et al., *Phys. Rev.* **116** (1959), 1585.
5. S. Hinds and R. Middleton, *Proc. Phys. Soc.* **A75** (1960), 754.
6. W.R. Coker et al., *Nucl. Physics* **A91** (1967), 97.
7. M.R. O'Brien, M. Cox and D.F.H. Start, *Nucl. Fusion* **26** (1986), 1625.
8. P. van Belle, private communication.
9. E. Righi, Ph.D. thesis, Imperial College of Science, technology and Medicine (1994).

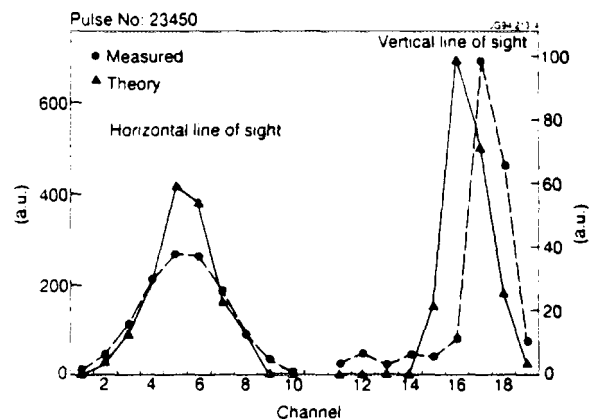


Fig. 4. Comparison between experimental and theoretical line integrated intensity of γ emissivity along the horizontal and vertical lines of sight of the γ detectors for JPN 23450 (courtesy of P.J.A. Howarth).



The JET Multi-Camera Soft X-Ray Diagnostic

B Alper, K Blackler, S F Dillon, A W Edwards, R D Gill,
E Lyadina, W Mulligan, S A B Staunton-Lambert,
D G Thompson, D J Wilson.

JET Joint Undertaking, Abingdon, Oxon, OX14 3EA.

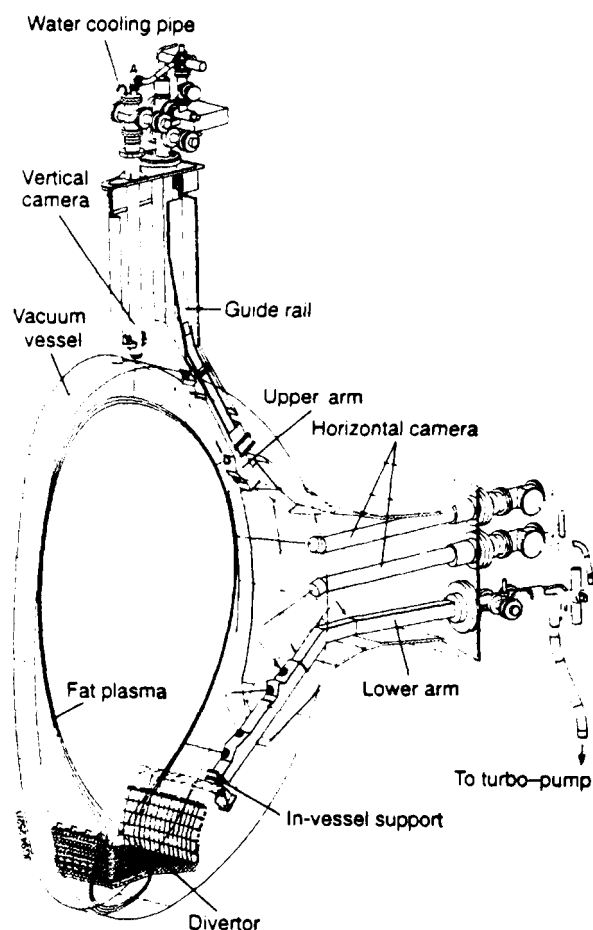


INTRODUCTION

A new soft X-ray detector system has been constructed for the pumped divertor phase of JET which incorporates a number of enhancements over the previous system in both hardware and data acquisition. The hardware improvements include: six independent views of the plasma at one toroidal location (as opposed to two in the old system), spatial resolution improved from 7cm to 3cm, frequency response increased from 30kHz to 100kHz and improved toroidal mode resolution. These enhancements will allow the study of MHD activity in finer detail. The tomographic reconstruction of soft X-ray emissivities will be improved to include Fourier terms up to $\cos(5\theta)$ compared with only $\cos(2\theta)$ before. Also through the implementation of a fast central acquisition and trigger system, data from a range of diagnostics will be available at high bandwidth to allow processing of plasma phenomena of far greater complexity than was possible before.

GENERAL LAYOUT OF NEW SXR SYSTEM Figure 1 shows the general layout of the new SXR diagnostic at octant 2 of the JET torus. Five separate assemblies have been constructed to house the detectors - 35 channel PIN diode arrays. A sixth assembly (not shown), identical to the vertical camera, has been installed at octant 7 for the purpose of toroidal mode number identification.

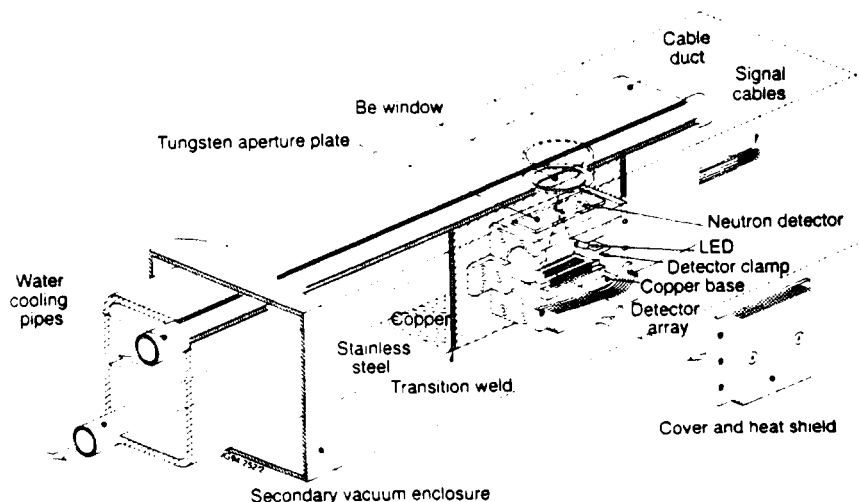
Figure 1. General view of 5 new SXR diagnostic system assemblies. The central viewing lines of each camera (11 in all) are shown in the figure.



FEATURES OF THE SXR CAMERA ASSEMBLIES

To obtain views of the plasma from a number of directions at one toroidal location requires the installation of cameras around the vessel wall away from access ports. As JET operates with the vessel at elevated temperatures (up to $\sim 300^{\circ}\text{C}$), this has required various novel features to be incorporated into the system design, see Figure 2. These include: the use of 35-channel PIN diode arrays mounted in pairs to provide six independent views of the JET plasma; (each compact camera pair has a $\sim 90^{\circ}$ viewing angle), up to four arrays enclosed in a single water-cooled secondary vacuum assembly and a dedicated turbo-pumping system to reduce convective heat losses. Each camera views the plasma through a $250\mu\text{m}$ thick Be window which provides SXR energy filtering and isolation of the primary and secondary vacua. An enclosed single element version of the diode is included to allow subtraction of neutron and gamma ray backgrounds during high performance discharges together with a pair of infra-red emitting diodes for calibration. A 1mm thick tungsten contoured aperture plate enables precise viewing definition of both low and high energy X-rays and the copper content (required for conductive cooling of diodes) has been minimised to reduce possible forces on assemblies from eddy currents during plasma disruptions. Removal of single-camera assemblies whilst maintaining the torus under vacuum will be possible.

Figure 2. Schematic of camera assembly in one of the multi-camera arms



DETECTOR PERFORMANCE

The detectors used are Centronic LD35-5 PIN photodiode arrays. Normally designed to operate in the visible, these type of detectors have been found to work well in the SXR region[1]. Each array consists of 35 elements with anodes 4.5mm by 0.96mm at 1mm spacing with common cathodes. In this application we use only every other channel in each array, i.e. 18 channels per array, (except in the vertical and toroidal cameras where every element is used). The unused channels have their anodes shorted to the common cathode as floating channels were found to affect the gain of neighbouring elements by up to 20%. The

detectors are operated in **photoamperic mode**; that is with zero bias into low impedance amplifiers. This has the advantage of minimising noise and dark current and removing the possibility of cross-talk through a common power supply for the bias voltage. Tests were carried out (using LEDs) which showed that the gain was stable against small variations in bias voltage around 0V and that the frequency of response was adequate for the 100kHz bandwidth, originally specified.

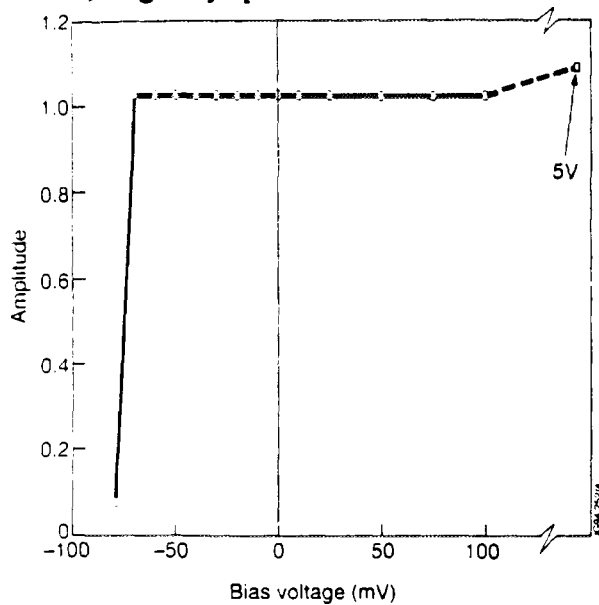


Figure 3. The amplitude of a 10kHz signal is seen to be independent of bias, both forward and reverse, over a wide voltage range.

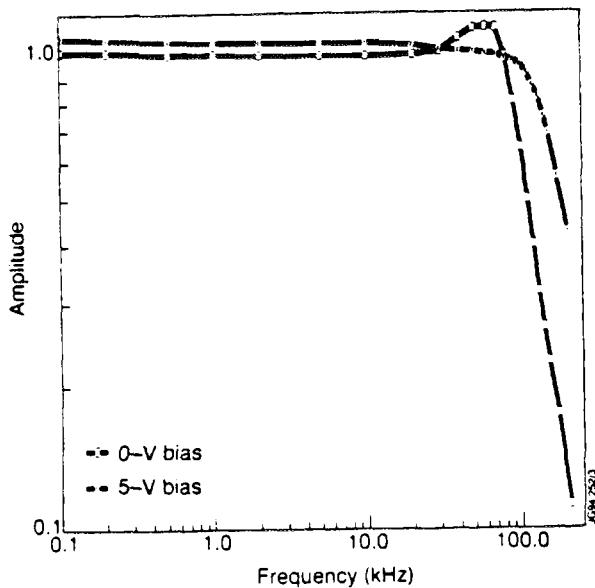


Figure 4. With no bias voltage, the bandwidth is adequate up to 100kHz as required. With 5V bias, the response improves above 100kHz.

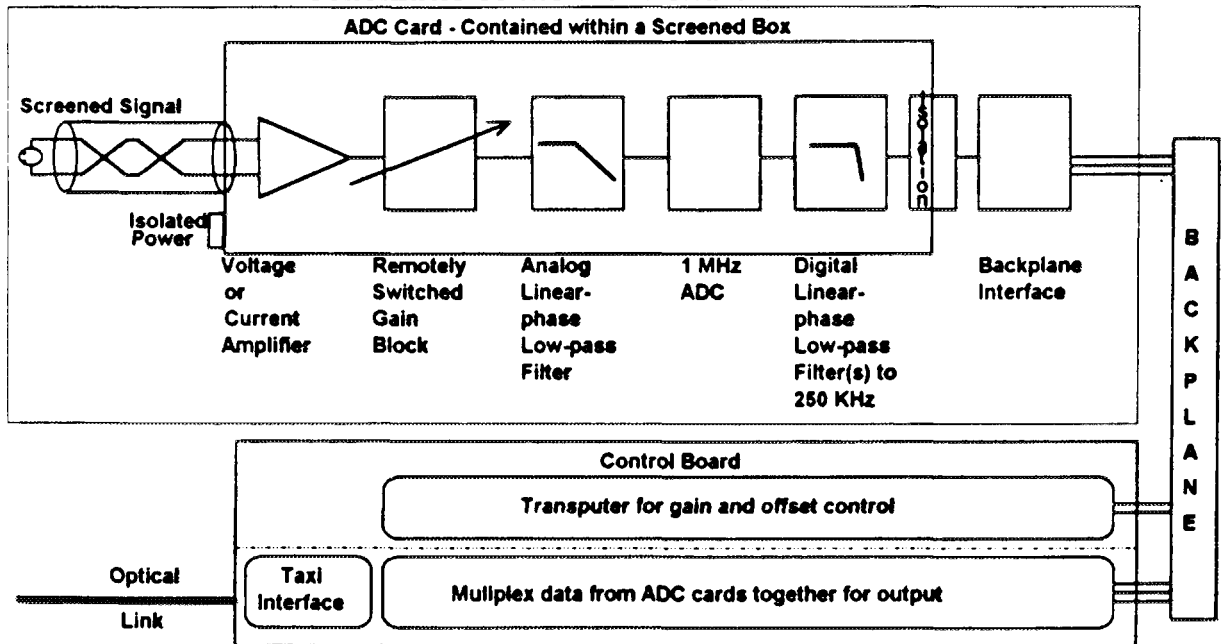
Calibration with 8 keV X-rays: Operating with zero bias means that the diodes are not operating in a fully depleted mode. Studies by Cho[2] indicate that electron-hole pairs created in a diffusion region of 50-120 μm depth can diffuse into the depletion region ($\sim 10\mu\text{m}$ with zero bias) and contribute towards signal current. For 8 keV X-rays this would lead to a collection efficiency in the range 55% to 85%. The relative calibration of all diode elements for 8 keV X-rays was carried out at MIT. A variation in efficiency comparable to that mentioned above was found between the best and worst detectors. In practice, a selection was made of the 12 best arrays out of a total of 28 tested, leading to a variation of only $\pm 3\%$ for all central channels and $\pm 4\%$ for all edge channels.

Radiation Effects: With the small volume of each detector, and through the use of zero-bias operation, large dark (or leakage) currents are not expected. Possible problems may occur if the neutron fluence through a diode exceeds 10^{13} cm^{-2} . This corresponds to a total yield of $\sim 5 \cdot 10^{19}$ neutrons from JET plasmas. Under these conditions effective doping concentrations can change with n-type inverting to p-type. However, self-annealing of the detectors should occur due to the pulsed nature of the neutron source which should extend their life.

ELECTRONICS

The front-end electronics for each camera is contained in a single rack-schematically illustrated below. Each ADC card is powered from an isolated linear power supply in order to reduce noise. The single ended current-source to voltage input amplifier has gain and DC offset adjustment. An 8-pole analogue filter is included to prevent aliasing from out of band signals or noise. Output from the ADC, a 12-bit device sampling at 1 MHz, is fed through two digital filters which lower the sampling frequency to 250kHz at 16 bits, for a pass band to 100kHz and stop band of 125 kHz. Each ADC card is optically isolated with data passed via the backplane to the Control card. Each Control card contains a Transputer to provide a programmable facility for setting gains / DC offsets and driving the calibration LEDs. The control card multiplexes the data from up to 19 ADC cards and transmits the data via a single TAXI / fibre-optic interface to the diagnostic area. The back-end data collection and trigger system uses Texas Instruments TMS320C40 (C40) microprocessors to provide a fast storage and central trigger system for the SXR data. Other JET diagnostics including magnetics, ECE, reflectrometry and H-alpha, are to be incorporated into the C40 central trigger system to enable simultaneous collection of data at 250 kHz from these diagnostics.

Schematic of the front-end electronics



STATUS The diagnostic hardware has been completely installed onto JET together with water cooling and vacuum systems. The ADC cards have been fabricated and tested. The Control card is currently undergoing prototype testing with complete testing of the data acquisition system expected in the next few weeks.

REFERENCES [1] Camacho JF and Granetz RS, Rev. Sci. Instr. 57 (3), 1986, p417
 [2] Cho T et al, Phys. Rev. A, 46(6), 199



Radiation Phenomena and Particle Fluxes in the X-Event in JET

H J Jäckel, D V Bartlett, H Falter, J Lingertat, R Reichle.

JET Joint Undertaking, Abingdon, Oxon, OX14 3EA.



Introduction

The highest fusion yield of $\Gamma_n \approx 4 \times 10^{16}$ n/s has been observed in JET in hot ion H-mode discharges at a heating power of $P_{\text{heat}} \approx 15$ MW with average electron densities of $\bar{n}_e \leq 4 \times 10^{19} \text{ m}^{-3}$ [1,2,3]. The energy confinement during the H-mode was typically 3 times better than in the L-mode. The final termination of the high confinement regime can take place within milli-seconds. The sudden loss of stored energy then causes an intense heat-flash on the divertor dump plates, accompanied by a dramatic increase of divertor particle fluxes (X-event).

Several typical patterns of the H-mode termination have been observed, showing different dynamic and radial range of the confinement deterioration, as reflected in the response of stored energy, W_p , the total neutron rate, Γ_n , and the electron and ion temperature profiles:

The diffusive decay: Γ_n and W_p degrade gradually on a time scale of up to several hundred milli-seconds. The plasma temperature starts to decrease from the edge. A 'cold wave' appears to travel towards the plasma centre.

The fast edge, diffusive core decay: The core ($r \leq a/2$) confinement degradation takes place on a diffusive time scale, while the outer half is deteriorating fast.

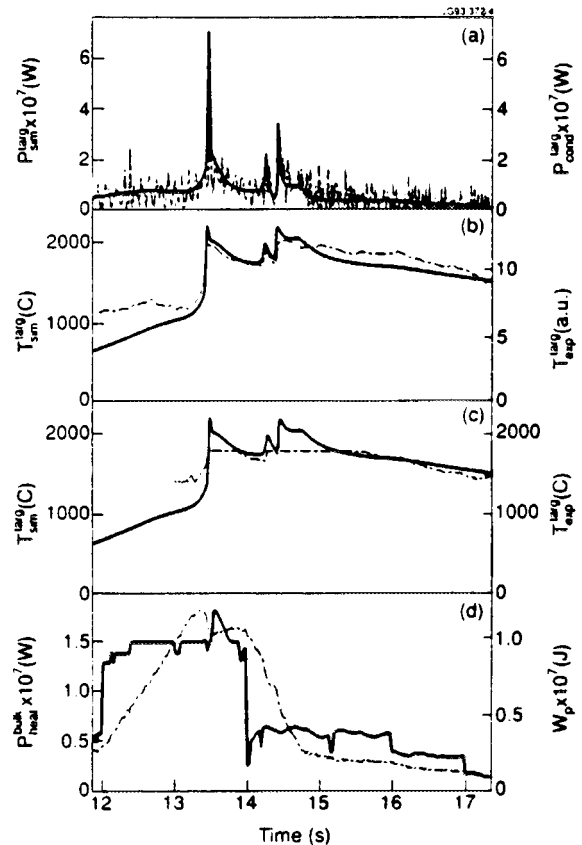
The sudden decay: Core and edge confinement decay simultaneously on a sub milli-second time scale.

A final power flash, dumped on the divertor target plates, resulting from the final fall-back into L-mode, can reach more than 100 MW and is observed in all three types.

Experimental:

The radiation build-up and the particle fluxes in the phase, immediately preceding the X-event, has been studied with bolometry and spectroscopy. Only the D_α data have a time resolution (≈ 2 ms), which comes close to the dynamic of the X-event itself. Bolometry, spectroscopy and the infrared diagnostic have resolution in the 20 to 100 ms range.

Fig. 1: a: Total heating power (solid) and stored energy; b+c: Fitted temperature (solid) and measured one; d: Fitted (solid) and measured target power.



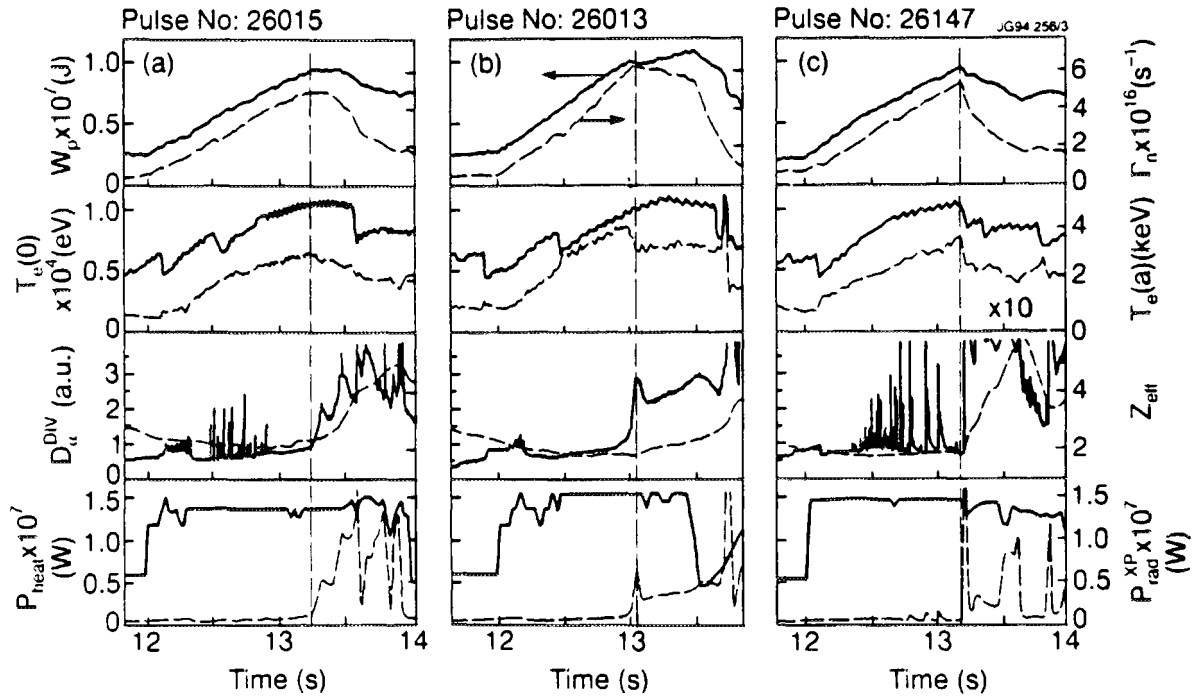


Fig. 2: Three HMI discharges with differing X-event pre-phase. The curves depict (bottom to top, solid refers to left scale): Total heating power and total divertor radiation, divertor D_α -emission and Z_{eff} , central and edge electron temperature, stored energy and total neutron rate, respectively.

The measurement of the target temperature, T_{targ} , was fraught with difficulties. The measuring range of the CCD and infrared cameras did not cover the fast rise of T_{targ} and the temperature pattern was complicated by mechanical alignment errors of the target tiles. For the graphite divertor an attempt had been made [4] to fit the target temperature, calculated from the conductive power into the divertor to experimental data. Figure 1 shows, for a HIM discharge with X-event, the development of the measured and calculated target temperature.

Results and Discussion:

Figure 2 depicts relevant plasma parameters during the H-mode of representative hot-ion mode (HIM) discharges for the above classification. The discharges of figure 2a (pulse 26015) and 2b (pulse 26013) show a gradual degradation of the confinement before the actual X-event, which is marked by the sharp drop of the central electron

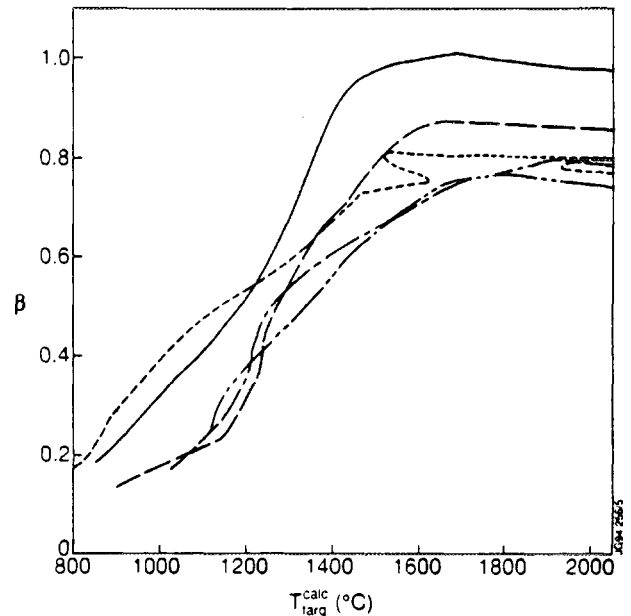


Fig. 3: development of β as a function of the calculated target temperature during the course of the high performance regime of 5 HIM discharges.

temperature. The edge electron temperature decays well before the central one. Figure 2c (pulse 26147) demonstrates the simultaneous and sudden decay of the electron temperature in the centre and the edge and, not shown, of the ion temperature and, accordingly, the sudden drop of stored energy and total neutron rate.

Although MHD-activities are often coinciding with the termination, there is no clear correlation to a critical β . Figure 3 shows the relation between β and the calculated target temperature during the course of the H-mode for 5 HIM-discharges with similar heating power, $P_{\text{heat}} \approx 15$ MW, and electron density, $\bar{n}_e \leq 4 \cdot 10^{19} \text{ m}^{-3}$. The run-away target temperature of about 1400 °C is reached at different β -values. The temperature is too low, to contribute through sublimation to the divertor carbon flux. However, any further confinement deterioration increases the power load on the target and can, at this temperature level, lead to run-away conditions:

MHD-activities: A fast loss of stored energy leads to high target surface temperatures, even if ΔW_p is small. If a sawtooth is coupling to an ELM, as in discharge 26147, \dot{W}_p can easily reach 50 to 100 MW.

Recycling losses: High target bulk temperature can cause a significant release of deuterium, trapped in the graphite and, due to the enhanced recycling, can lead to an effective edge cooling.

Thermally decoupled carbon: Recent NBI test-bed experiments on graphite tiles [5] have demonstrated the existence of a partial coverage of particles without or with reduced thermal contact to the bulk. This carbon can be vapourised and/or ejected into the plasma on a ms time scale, even with relatively small heat pulses, similar to a laser blow-off. The particle coverage can not be removed completely, even at intensive pulsing. Redeposited carbon might also contribute in the same way.

The development of the calculated target temperature T_{targ} and the time-integrated target power

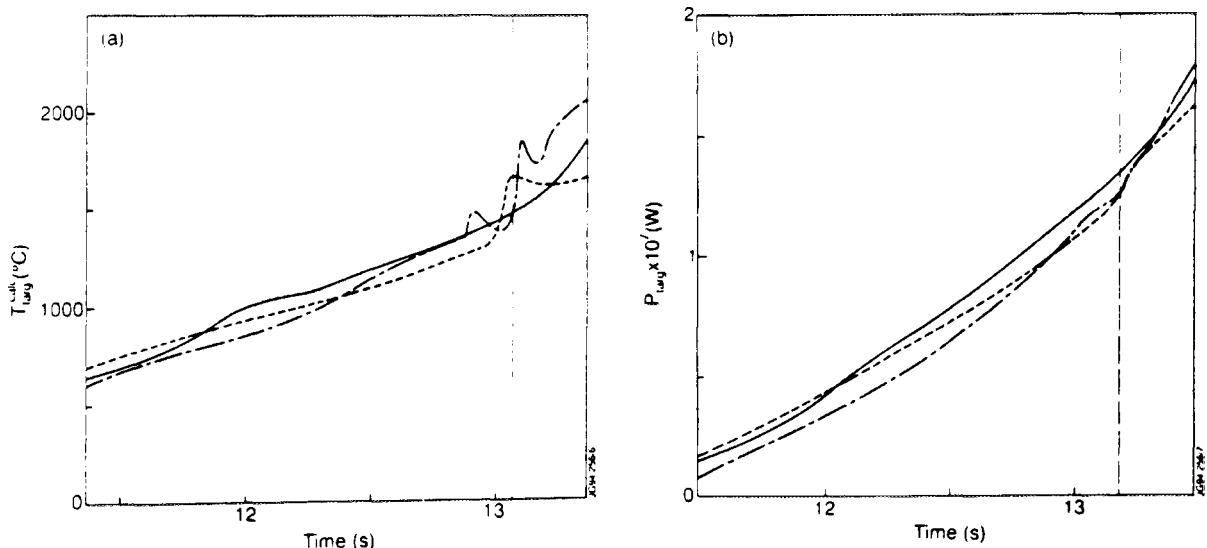


Fig. 4: The development of target temperature (left) and integrated target load (right) during the high performance regime for the 3 discharges of picture 2. The vertical dotted line marks the onset of the X-event, the start of the decline of the total neutron rate.

$E_{t, \text{arg}} = \int_{t_{\text{xp-s}}}^{t_0} P_{t, \text{arg}} dt$ are depicted in figure 4 ($t_{\text{xp-s}}$ = start of the X-point configuration). At the time of the X-event, marked by the vertical dotted line, typical values are $T_{t, \text{arg}} \approx 1400 \text{ }^\circ\text{C}$ and $E_{t, \text{arg}} \approx 13 \text{ MJ}$.

Summary:

- The H-mode phase in high performance discharges tends to collapse irreversibly. The (calculated) target temperature just before the X-event amounts to about $1400 \text{ }^\circ\text{C}$. Any deterioration of confinement at this temperature leads to run-away conditions of the target temperature and a final fall-back into L-mode. However, there is no clear of a correlation between a critical β and the H-mode termination.
- Possible causes of the confinement deterioration are:
 1. MHD activities can cause a fast plasma loss and, hence, a power flash, dumped on the divertor target, leading to a temperature jump of up to $1000 \text{ }^\circ\text{C}$. At a bulk temperature $T \geq 1400 \text{ }^\circ\text{C}$ this leads to run-away conditions of confinement and target surface temperature.
 2. Enhanced recycling, due to thermal release of trapped deuterium from the graphite target plates causes an effective plasma edge cooling.
 3. Loose graphite on the target tiles with virtually no thermal coupling to the target bulk can be sublimated and ejected into the main plasma with even small power levels.
- Apart from major instabilities, the bulk temperature of the divertor dump plates appears to play an important role. Increasing temperature reduces the equilibrium pressure of trapped deuterium in the graphite and leads to higher recycling fluxes and hence, stronger edge cooling, making the discharge vulnerable to any further confinement deterioration. An active cooling, keeping the bulk target at ambient temperature could make the discharge more resilient against even medium MHD instabilities, as e.g. giant ELMs.

References:

- [1] E. Thompson, D. Stork, H.P.L. de Esch and the JET Team, *Phys. Fluids B* 5 (1993) 2468
- [2] The JET Team, *Nucl. Fus.* 32 (1992) 187
- [3] J.G. Cordey, R. Reichle, D. Stork and the JET Team, "The enhanced Confinement Regime in JET", submitted for publication in *Plasma Phys. and Contr. Fus.*
- [4] H.J. Jäckel et al., *Proc. 20th EPS Conf. Contr. Fus. & Plasma Phys., Vol. I* (1993) 287
- [5] D. Ciric et al., to be published in *Proc. 18th Symp. on Fus. Techn.*



FR9701777

Local Measurement of Transport Parameters for Laser Injected Trace Impurities

R Giannella, L Lauro-Taroni.

JET Joint Undertaking, Abingdon, Oxon, OX14 3EA.



1. INTRODUCTION

The local measurement of transport parameters of a particle population essentially amounts to the analysis of the relationship between the fluxes Γ of that population and the spatial gradients ∇n of its density. In the study of transient radial propagation in a tokamak, this analysis depends exclusively on the possibility to measure, with adequate space resolution, n as a function of time.

Earlier attempts, however, to make use of time resolved tomographic soft X-ray diagnostics to infer directly the diffusivity D and convection speed V of injected trace impurities [1] were frustrated by the inconsistency between reproduced and measured data, when the profiles of D and V so inferred were used in the simulations of the injection experiments [2]. The obtained values of D , in particular, appear too high by a factor of 2 to 3 [3]. So far, therefore, the best method of transport analysis for these experiments has been the check of consistency of simulations of the impurity transport with the relevant diagnostic data.

Our analysis shows that the main source of error in Ref. [1] lies with the assumption that the density n_I of the injected impurity I can be deduced from the perturbation $\Delta\epsilon$ induced by those impurities on the soft X-ray emissivity by the simple expression $n_I = \Delta\epsilon / (Q_I \cdot n_e)$. Here n_e is the electron density and the radiation coefficient Q_I is assumed to be a function of the electron temperature T_e alone. Values of $Q_I = Q_{ICE}$ appropriate for the coronal equilibrium (CE) [4] were used in that work. It appears, however, that Q_I is not equal to Q_{ICE} . It is also not only a function of T_e , but of the time as well, depending on the state of motion of the injected impurity, that is in turn dependent on the transport parameters determining its propagation.

2. ITERATIVE PROCEDURE FOR DETERMINATION OF IMPURITY TRANSPORT

Based on the above observation an iterative procedure has been developed.

0 Using an initial guess (D^0 and V^0) for the profiles of D and V , a simulation of the entire phenomenon is performed producing a first tentative simulation of the impurity density $n_{ISim}^1(r, t)$, as well as of the perturbation to the soft X-ray emissivity $\Delta\epsilon_{Sim}^1(r, t)$.

1 From that simulation a first estimate of the radiation coefficient Q_I^1 is worked out as

$$Q_I^1(T_e(r, t)) = \Delta\epsilon_{Sim}^1(r, t) / (n_{ISim}^1(r, t) \cdot n_e(r, t)).$$

2 Using $Q_I^1(T_e, t)$, the first approximation n_I^1 to the measure of n_I , is produced as

$$n_I^1 = \Delta\epsilon / (Q_I^1 \cdot n_e).$$

- 3 Following Ref. [1] the first approximation to the flux $\Gamma_I^1(r)$ across the flux surface $S(r)$ is worked out as

$$\Gamma_I^1(r, t) = -\frac{1}{S(r)} \int_0^r \frac{\partial n_I^1}{\partial t} dV$$

and consequently the first approximations to $D(r)$ and $V(r)$, $D^1(r)$ and $V^1(r)$ are deduced by fitting, at every radial position r , a straight line to the plot of $\Gamma_I^1(r, t) / n_I^1(r, t)$ versus $\nabla n_I^1(r, t) / n_I^1(r, t)$:

$$\frac{\Gamma_I^1(r, t)}{n_I^1(r, t)} = -D^1(r) \frac{\nabla n_I^1(r, t)}{n_I^1(r, t)} + V^1(r). \quad (1)$$

- 4 A new simulation is then run, using profiles for the transport parameters $\hat{D}^1(r)$ and $\hat{V}^1(r)$ that are derived (as explained below) from D^1 and V^1 , that leads to the second simulations of the impurity density, $n_{ISim}^2(r, t)$, and of the perturbation to the soft X-ray emissivity, $\Delta \varepsilon_{Sim}^2$, as in the preparatory step 0 above.

- ◆ Repeating then steps 1 to 4 new approximations are found for Q_I , n_I , D and V .

In a few iterations (say N) the procedure is seen to converge (see fig. 1) supplying the measured profiles of the transport parameters D^N and V^N (only extending up to a certain radial position as explained below) as well as the best estimate of the extended profiles \hat{D}^N and \hat{V}^N .

This procedure intrinsically assures consistency of the obtained transport parameters with the experimental emissivities. In fact, if the ansatz expressed by equation (1) is compatible with the data, close agreement is also found between the limit determinations of n_I and their simulations n_{ISim} , as well as between the simulated emissivities $\Delta \varepsilon_{Sim}$ and the measured values $\Delta \varepsilon$ (see fig. 2).

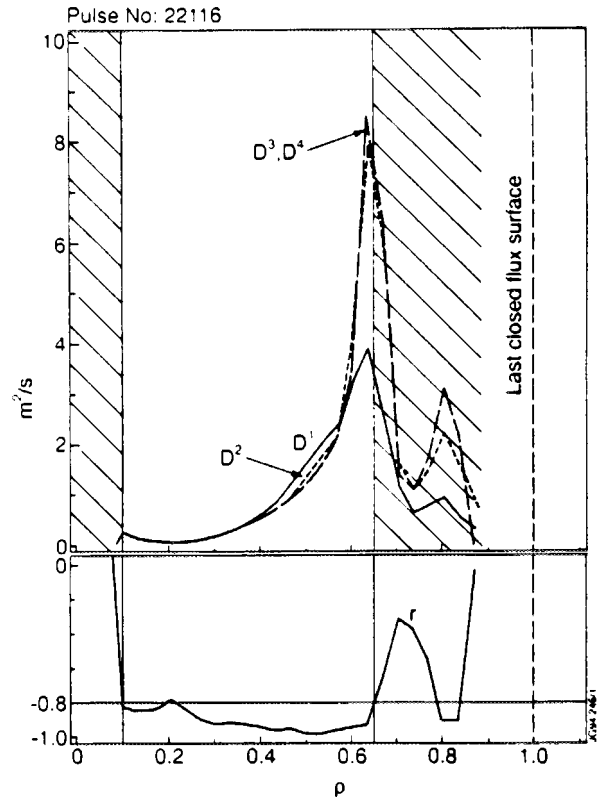


Fig. 1 Successive determinations D^n of the impurity diffusion coefficient. The correlation coefficient r of the linear regression (step 3 in the iterative procedure) for the determination of D and V , as obtained at the last iteration, is also shown. The shaded area represents the radial region where, due to the emissivity $\Delta \varepsilon$ being too low, correlation is poor and the deduced values of D , are unreliable.

3. CONSTRAINTS ON THE SIMULATIONS AND ERROR ANALYSIS

Due to the relatively thick (250 μm) Be filters used in the JET soft X-ray tomographic diagnostic, the detected emissivity profiles are very weak outside a certain radius leading to increasing uncertainties outside that position. Because of this, the measure of transport parameters by means of the regression fit (fig. 3) is only reliable in a certain core region ($\rho < 0.6 - 0.8$).

The estimate of $Q_I(T_e, t)$ however depends on the whole time history of the impurities from their ingress in main plasma. The simulation therefore needs D and V profiles up to the plasma edge. In order to complete the radial description of impurity transport, the soft X-ray

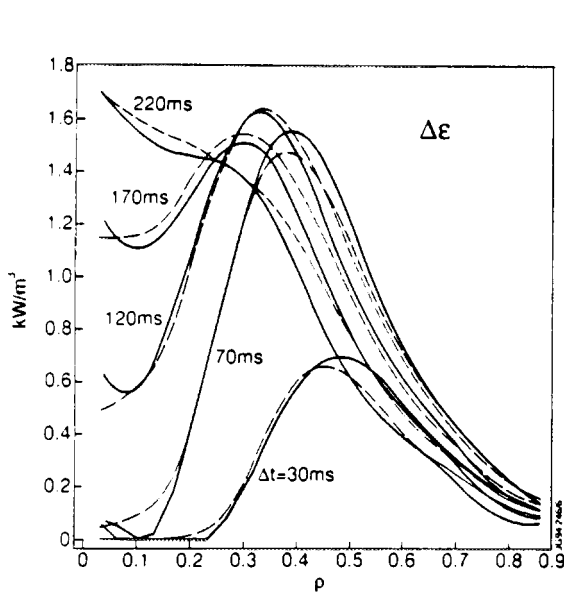


Fig. 2 Experimental (solid lines) soft X-ray line emissivities at different times Δt following injection of Ni into the plasma. The broken lines represent the simulation of the emissivity as obtained at the end of the iterative analysis procedure.

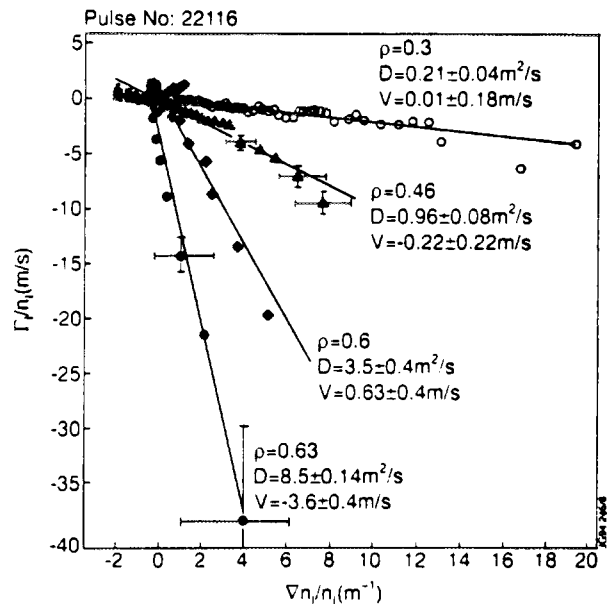


Fig. 3 Normalised fluxes Γ_I/n_I and density gradients $\nabla n_I/n_I$ at four radial positions as obtained at the last iteration in the iterative analysis procedure. The best fitting straight lines, the deduced local values of the transport parameters and their uncertainties are also indicated.

data need to be supplemented by the brightnesses of lines from individual ion states emitted in the VUV domain.

To this end step no 4 in the above mentioned iterative procedure really consists of a search for a most suitable extension in the outer region to the transport parameters, obtained by optimizing the simulation of a number of VUV and soft X-ray line brightnesses.

This is the most CPU-time consuming step in the whole procedure. In fact the optimization is performed by minimizing the time integral of the squared differences between the experimental and simulated brightness signals. The minimizing routine calls typically 100 times the simulation program equivalent to about 40 minutes of CPU with the IBM

3090/300-J mainframe computer at JET. The whole iterative procedure requires, until convergence, ~ 120 minutes of CPU-time

The error analysis, performed on a statistical basis, attributes to the different time slices and space points different weights according to the calculated uncertainties on Γ_I and ∇n_I . It shows that the most useful phase typically extends from 20 - 40 ms to 100 - 200 ms after the injection, depending on the particular space point. In fact during the first few tens of milliseconds the perturbative signals are too low and the limited space resolution of the diagnostics introduces large systematic errors on ∇n_I . After the first few tenths of a second, on the other side, the reliability of the signal is impaired by the growing uncertainty on the background radiation.

4. TREATMENT OF SAWTOOTH CRASHES

For pulses where sawtooth activity is present, the simulation has to reproduce the rearrangement in the impurity density profile that occurs at the sawtooth crashes. This rearrangement is simulated by interrupting the one-dimensional diffusive-convective transport at a time t_1 , 1 or 2 ms before the crash, and restarting it at a time t_2 , 3 or 4 ms later, with a new initial condition for the density n_{zSim} of each ionization state z of the injected impurity:

$$n_{zSim}(r, t_2) = R \frac{n_{zSim}(r, t_1)}{n_{ISim}(r, t_1)} n_I^*(r, t_2)$$

where $n_I^*(r, t_2) = \Delta\varepsilon(r, t_2) / (\hat{Q}_I(r, t_2) \cdot n_e(r, t_2))$, $R = \int n_{ISim}(r, t_1) dV / \int n_I^*(r, t_1) dV$,

$$\hat{Q}_I(r, t_2) = \frac{\sum n_{zSim}(r, t_1) q_z(T_e(r, t_2))}{n_{ISim}(r, t_1)}$$

and $q_z(T_e)$ is the radiation coefficient for the z ion state.

5. CONCLUSIONS

A procedure has been developed that determines local measurements of transport parameters' profiles for injected impurities. The measured profiles extend from the plasma centre up to a certain radial position (usually $\rho = 0.6 - 0.7$).

In the outer region of the plasma the procedure supplies "most suitable extensions" up to the plasma edge of the measured transport profiles.

The procedure intrinsically assures consistency and excellent agreement between the simulated and experimental data of local broad band soft X-ray emissivity and intensities of individual emission lines from different ion states of the injected impurities.

REFERENCES

- 1 *The JET Team*, in Plasma Physics and Controlled Nuclear Fusion Research 1990 (Proc. 13th Int. Conf. Washington, DC, 1990) Vol. 1, IAEA, Vienna (1991) 27.
- 2 R.Giannella, L.Lauro-Taroni, M.Mattioli et al., submitted to Nucl. Fus. (1993).
- 3 M. Mattioli, Private communication.
- 4 H.Weisen, D.Pasini, A.Weller A., A.W.Edwards, Rev. Sci. Instrum. **62** (1991)1531.



FR9701778

Impurity Transport of High Performance Discharges in JET

L Lauro-Taroni, B Alper, R Giannella, K Lawson¹,
F Marcus, M Mattioli², P Smeulders, M von Hellermann.

JET Joint Undertaking, Abingdon, Oxon, OX14 3EA.

¹ Culham Laboratory, Abingdon, Oxfordshire, OX14 3DB, UK.

² Association Euratom-CEA sur la Fusion, Cadarache, France.



Long sawtooth-free periods are typical of high performance discharges in the JET tokamak (e.g. Hot-Ion (HI) and Pellet Enhanced Performance (PEP) H-mode discharges).^[1,2,3]

Depending upon the time duration of these quiescent phases, the degree of peaking of density and temperature profiles and the level of collisionality, as well as the shape of the q-profile, the light impurities' behaviour assumes different characteristics: either they accumulate towards the plasma centre, leading to various levels of depletion of the main plasma ions or, on the contrary, hollow profiles are measured, without any significant dilution effects on the fuel reactants. In general, medium and high-Z impurities play only a minor role.

The total radiation loss in the centre (up to $\sim 50 \text{ kW/m}^3$) is in all cases much smaller than the local heating power. Also, the large excursion observed sometimes in the effective ion charge on axis (e.g. from $Z_{\text{eff}} \sim 1$ to $Z_{\text{eff}} > 4$ in some PEP discharges) does not lead to an important decrease of electric conductivity, because of a compensating effect due to the concomitant electron temperature rise. So the impurity behaviour appears not to be the cause of the abrupt MHD events ^[4,5] that normally terminate PEP or HI discharges, with the possible exception of cases close to marginal stability.

1. PELLET ENHANCED PERFORMANCE (PEP) H-MODE DISCHARGES

a. Analysis of Experimental Data

The clearest evidence of strong central impurity accumulation is supplied by the time evolution of the broad band soft X-ray and neutron emissivity profiles: when the neutron emission profiles decline and broaden, the SXR radiation from the central region increases.^[2]

The VUV spectroscopic data indicate that the plasma main contaminants are C and Be and that Ni and Cl are also present. The absolutely calibrated line-of-sight measurements of the NiXXVII resonance line from the crystal spectroscopy indicates that the amount of Ni during the high performance phase is small: $n_{\text{Ni}} < 3 \cdot 10^{-5} n_e$.

Both the VUV and the crystal spectroscopic data indicate that the Cl

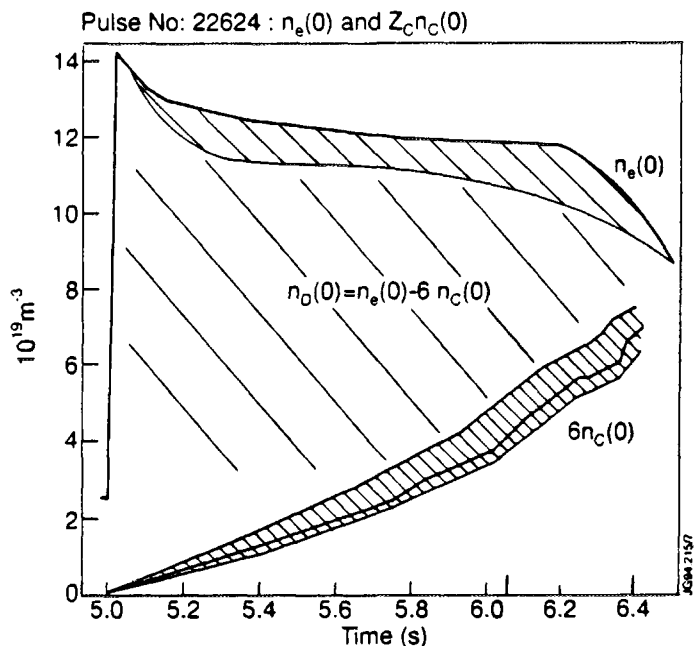


Fig. 1: 22624. Time evolution of the central electron density and of the central density of electrons carried by carbon ions as estimated from $\epsilon_{\text{SXR}}(0)$. Their difference is an estimate of the central deuterium density.

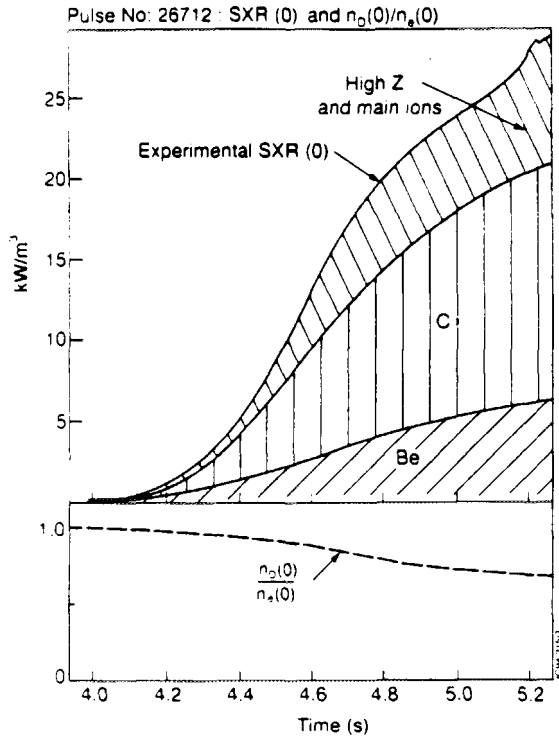


Fig 2. Above: time evolution of the experimental $\epsilon_{SXR}(0)$ with its simulated components from Be and C for 26712. Below: simulated central fuel dilution.

ions in the central zone of the discharge can be severe for some PEP pulses, with $n_D(0)$ falling as low as $\leq 0.3 n_e(0)$.

b. Impurity Transport Simulations

For PEP's, the impurity transport is anomalous in the outer region ($\rho \geq 0.5$, ρ being the normalised minor radius), and is dominated by convection (1-2 m/s) with a reduced diffusivity ($D \sim 0.1$ m²/s) in the plasma core ($\rho \leq 0.4$)

Ni simulations, reproducing the absolute values and time evolution of the intensities of the available line brightnesses, confirm that its contribution (even if it varies from case to case) to the total $\epsilon_{SXR}(0)$ is $\sim 10\%$ or less. So, allowing for the bremsstrahlung radiation emitted by the main plasma ions, we conclude that 70-80% of $\epsilon_{SXR}(0)$ is due to low-Z impurities. Its simulation, assuming that C and Be are present in approximately equal amounts, requires high concentrations $n_Z/n_e \sim 3-7\%$ in the centre, implying a depletion of deuterium in the same region.

content (usually varying in anticorrelation with Ni) does not seem to be significant in the high performance phase. So, the soft X-ray radiation from the central region is mostly due to light impurities (C and Be).

The soft X-ray emissivity from the plasma centre (where transport can be neglected) is

$$\epsilon_{SXR}(0) = n_e \sum_Z n_Z(0) Q_Z(T_e(0), \text{filter}) \quad (1)$$

where $n_e(0)$ and $n_Z(0)$ are the electron and impurity central densities and the radiation coefficient Q_Z depends solely the impurity element, the central electron temperature $T_e(0)$ and the SXR Be filter [6].

To evaluate an upper limit for the central deuterium density $n_D(0)$, one can assume that a considerable fraction (70-80%) of the central emissivity is emitted by C alone. Thus eq.(1) yields a reasonable estimate of the central carbon density $n_C(0)$. The central deuterium density $n_D(0)$ is then readily given by the quasi-neutrality condition, as shown in fig.1. It follows that the depletion of the main plasma

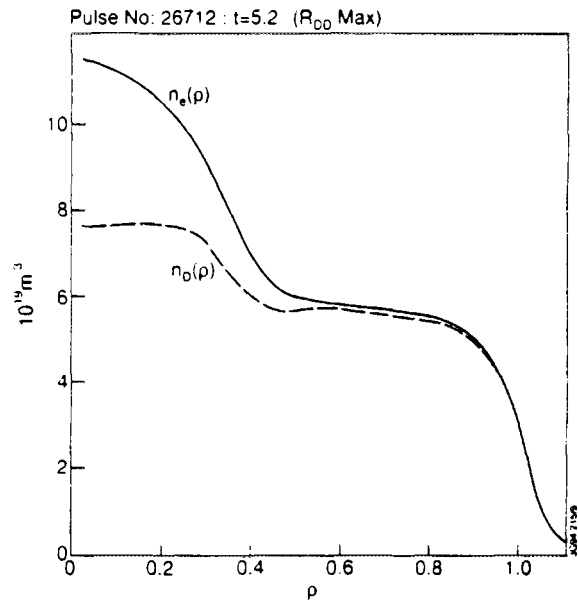


Fig.3: electron and deuterium (simulated) density profiles at $t=5.2$ s (max RDD).

For the pulse 26712 the depletion is mild (figs 2 and 3). In this case, neutron emissivity profiles were available. The simulated n_D profile at the time of the maximum neutron rate (fig.3) accounts for $\approx 55\%$ of the experimental neutron emissivity profile.

As the beam-thermal contribution is estimated to amount to $\approx 35\%$, the n_D profile is consistent with neutron data.

In the case of the discharge 22624, the simulation confirms the analysis shown in fig.1. For that shot, unfortunately neutron data were not available, but carbon profiles from Charge Exchange Recombination Spectroscopy (CX) were, and they were well reproduced by the simulation.

Fig.4 shows the electron and deuterium (simulated) density profiles for pulse 22624 at the time of maximum neutron production ($t=6.0$ s) and their evolution at the later time $t=6.4$ s, when the central SXR emission reaches its maximum.

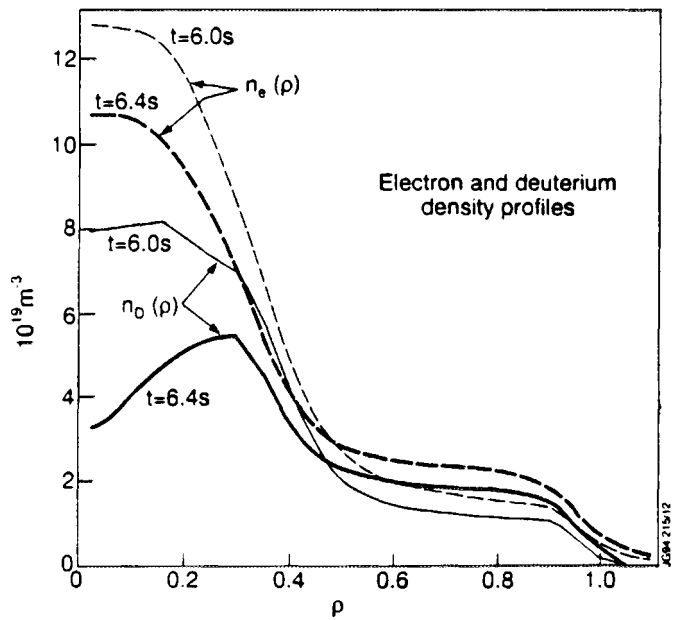


Fig.4.22624: $n_e(\rho)$ and $n_D(\rho)$ (simulated) at the times of max RDD ($t=6.0$ s) and max fuel dilution ($t=6.4$ s)

2.HOT-ION (HI) DISCHARGES

HI discharges have a low impurity content in the high performance phase. Heavy impurities are present only as traces ($n_{Ni}/n_e \sim 10^{-6}-10^{-5}$) and among low-Z impurities, C is dominant.

These pulses do not show C central accumulation, but the profiles observed by CX are rather hollow (fig.5). C concentration in the plasma core ($\rho \leq 0.4$) is about $n_C/n_e \sim 1\%$, with no major effects on the fuel dilution.

The SXR emissivity from the centre is an order of magnitude lower than in the PEP's (few kW/m^3 for HI's against few tens of kW/m^3 for PEP's): it can be accounted for mainly by bremsstrahlung radiation from the main plasma ions.

The C transport in the central region is characterised for this case again by a reduced diffusion ($D \sim 0.1 \text{ m}^2/\text{s}$), but the convective term is smaller (0.1 m/s) and directed outwards.

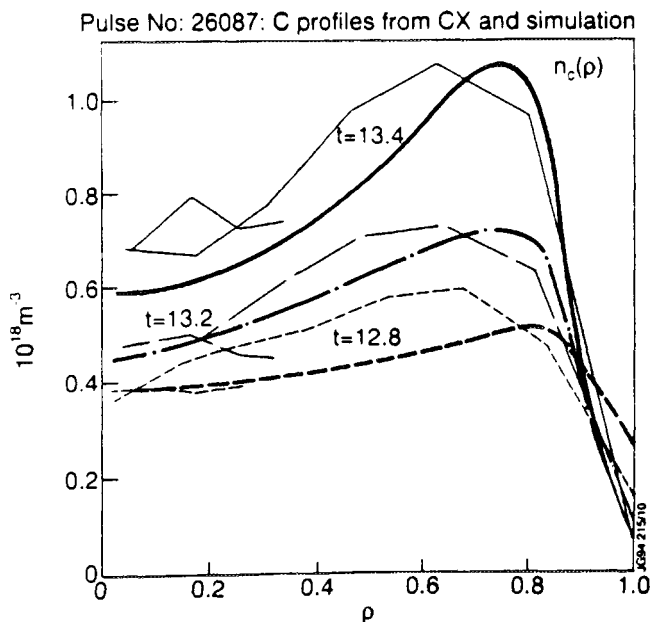


Fig 5: 26087 (HI). C profiles measured by CX at three times, plotted together with their corresponding simulated profiles (thicker lines)

3. COMPARISON OF CARBON TRANSPORT IN THE PLASMA CORE: PEP vs HI.

Due to the different plasma parameters in the two cases, during the PEP shots C is well in the plateau collisionality regime, while it is in the banana regime during the HI pulses. In both cases the neoclassical diffusivity is low, of the same order as the heuristic values, but the dependence of the convection on the driving forces is different in the two cases (fig.6).

In PEP's C is usually in the plateau regime and the neoclassical convection specialised for these conditions is:

$$v_C^{nc} \propto \left(\frac{\nabla n_D}{n_D} + 1.13 \frac{\nabla T}{T} \right),$$

where T is the ion temperature.

In this case, the strong inward-directed term $\propto (\nabla T / T)$ can allow the accumulation towards the centre to continue even if ∇n_D changes sign.

In HI pulses C is usually in the banana regime and:

$$v_C^{nc} \propto \left(\frac{\nabla n_D}{n_D} - 0.3 \frac{\nabla T}{T} \right)$$

In this case, we can see a slight screening effect of the $(\nabla T / T)$ term: the accumulation is inhibited for peaked T-profiles when ∇n_D is small (which is the case for hot ion pulses in the plasma core)

CONCLUSIONS

The experimental data show that in the PEP-H discharges the light impurities are dominant and accumulate. Furthermore, strong fuel depletion may occur in the plasma centre with n_D/n_e falling to ~ 0.3 in some cases.

On the other hand, in Hot-Ion discharges hollow profiles are measured for C: it is present in lower concentrations and has little effect on fuel dilution.

The different behaviour of carbon in the two cases is in agreement with neoclassical predictions for the convection in the plasma core.

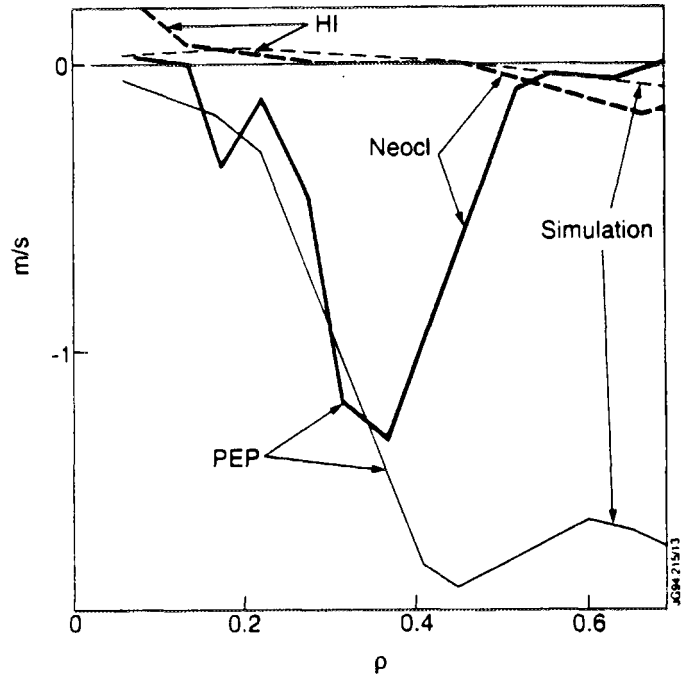


Fig. 6: Comparison of the heuristic C convections used in the simulations for PEP (solid line) and HI (dashed line) and their corresponding neoclassical evaluations (thick solid line for PEP and thick dashed line for HI)

¹D. Stork and the JET Team, Proc 4th IAEA TCM on H-mode Physics, 1994

²P. Smeulders et al, Survey of Pellet Enhanced Performance in JET Discharges, accepted in Nucl. Fus., 1994

³B. Balet et al, Energy Transport during the Pellet Enhanced Performance (PEP) Discharges in JET, Proc. Varenna Workshop on 'Local Transport Studies in Fusion Plasmas', Sept. 1993

⁴G. Schmidt et al, (1987) Proc 11th International conf. on Plasma Physics and Contr. Nucl. Fus. Research, Kyoto Vol1, p.33

⁵R. Reichle et al, Termination of High Performance Discharges at JET, to be submitted to Nucl. Fus.

⁶H. P. Summers, Atomic Data and Analysis Structure, User Manual, JET Report, to be published, 1994



Negative Snakes in JET: Evidence for Negative Shear?

R D Gill, B Alper, A W Edwards, D Pearson¹.

JET Joint Undertaking, Abingdon, Oxon, OX14 3EA.

¹ Present address: University of Reading, UK.



INTRODUCTION

Snakes have been observed in many tokamaks as a novel form of MHD activity which consists of a long lived small region of high electron pressure on the $q = 1$ magnetic surface. They have a $m = n = 1$ topology and are often formed during the injection of solid pellets of D_2 [1] which reach in to the $q = 1$ surface. Snakes have also been observed [2], at the onset of sawtoothing, after neutral beam heating of the plasma centre, and in discharges with rather flat central profiles of electron density and pressure. The name "snake" arises from their characteristic appearance when observed by a soft X-ray camera.

A detailed analysis of the soft X-ray data together with the electron density (n_e) and temperature (T_e) information from the interferometer and ECE systems respectively has shown that the pellet induced snakes typically have perturbed parameters relative to their surroundings of $\delta n_e / n_e \sim 25$ to 140% and $\delta T_e \sim 0$ to 200eV. Generally, pellet induced snakes have no visible temperature perturbations at times greater than 100ms after their creation. In discussing the properties of the snakes it is useful to write simplified expressions for the plasma radiated X-ray power (P_x) and the plasma resistivity (R)

$$P_x = A n_e^2 \zeta f(T_e) \quad \text{and} \quad R = B \frac{Z_e}{T_e^{3/2}}$$

where ζ is the X-ray anomaly factor and $f(T_e)$ is a function of temperature which, for the particular filters placed between the plasma and the detectors, is proportional to T_e^α with $\alpha \approx 1$. The plasma effective charge Z_e is approximately proportional to ζ , and A and B are constants. Small perturbations within the snake may therefore be written as

$$\frac{\delta P_x}{P_x} = 2 \frac{\delta n_e}{n_e} + \frac{\delta \zeta}{\zeta} + \frac{\delta T_e}{T_e} \quad \text{and} \quad \frac{\delta R}{R} = \frac{\delta Z_e}{Z_e} - \frac{3}{2} \frac{\delta T_e}{T_e} \approx \frac{\delta \zeta}{\zeta} - \frac{3}{2} \frac{\delta T_e}{T_e}.$$

The perturbed impurity concentration within the snake is generally not known. However, $\delta R/R$ may be obtained by eliminating $\delta \zeta/\zeta$. A detailed analysis [2] has shown that at early times in the pellet snake's lifetime $\delta R/R$ is positive because of the reduced T_e , whereas on longer timescales $\delta T_e/T_e \sim 0$ but $\delta \zeta/\zeta > 0$ which also leads to an enhanced resistivity in the snake. The association of the snake with a reduced temperature or enhanced impurity concentration leads to the idea that it is formed by a magnetic island with the locally changed parameters producing a region of increased resistivity and decreased current density. This is particularly plausible for pellet injection as the stagnation of the cold particles on the $q = 1$ surface would produce, on a short timescale, a region of very much reduced T_e .

NEGATIVE SNAKES Occasional observations have been made in JET of so-called negative snakes. A typical example is shown in Fig. 1 where data from the 38 channel vertical soft X-ray camera is displayed. The signature of these from the soft X-ray cameras is very similar to the more usual snakes except that the localised region of the snake has, compared with its surroundings, decreased rather than increased emission. Negative snakes have been seen under the following circumstances. (i) Between sawteeth in low-q discharges with $I_p = 3.3 - 7\text{MA}$. (ii) As successor oscillations following a sawtooth crash. (iii) Immediately after pellet injection. The first type of negative snake is shown in Fig. 1 for a discharge with $I_p = 7\text{MA}$.

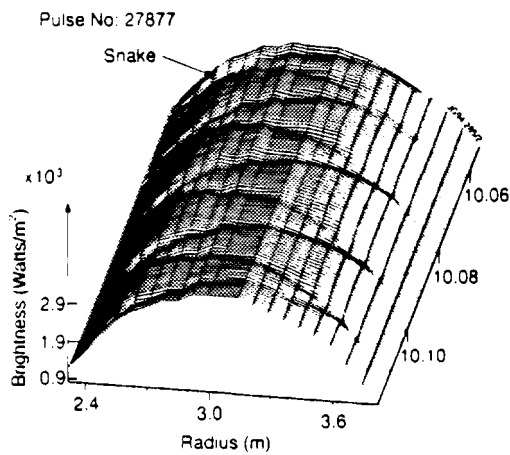


Fig. 1: Line integrated soft X-ray emission observed by the vertical soft X-ray camera showing the negative snake.

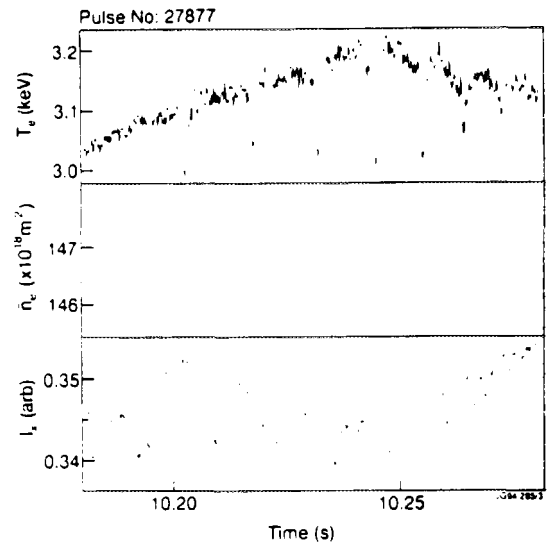
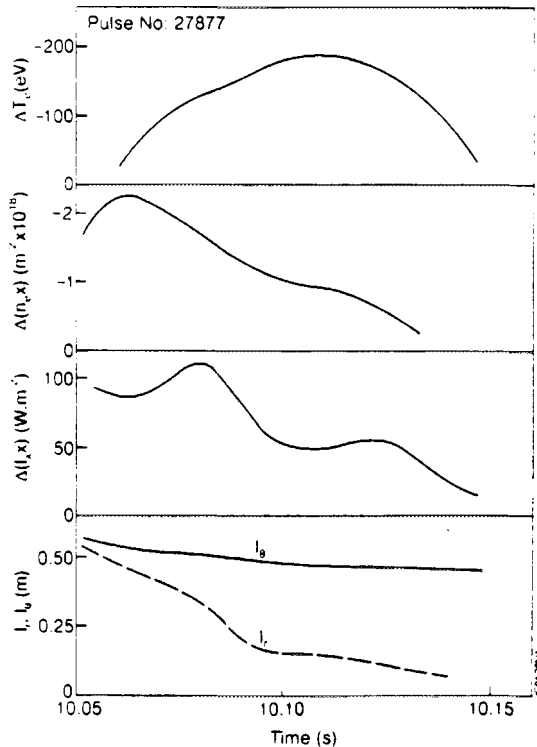


Fig. 2: The traces shown are T_e at $R = 3.67\text{m}$, the electron density line integrated along a central vertical chord and a line integrated soft X-ray signal.



The interpretation of these negative snakes has always been difficult due to the lack of detailed measurements of n_e and T_e profiles. It had always been assumed that the negative snakes had a very similar structure to the normal snakes. However the detailed n_e and T_e measurements (Fig. 2) show a different picture. The variation of various parameters for the negative snake are collected in Fig. 3 and in Table 1 the negative snakes are

Fig. 3: The time variation is shown for various negative snake parameters. The variations of T_e , the line integrated n_e and line integrated X-ray intensity are shown in the upper part of the figure. The radial and poloidal dimension are also shown.

Table 1

$\frac{\delta P_x}{P_x} (\%)$	$\frac{\delta n_e}{n_e} (\%)$	$\frac{\delta T_e}{T_e} (\%)$	ℓ_r (m)	ℓ_θ (m)
-8	-10	-3.3	0.41	0.52 } - ve snake early
-15	-13	-5.4	0.11	0.47 } - ve snake late
+150	+140	-22	0.14	0.25 } Pellet snake early
+100	+40	< 5	0.20	0.25 } Pellet snake late

contrasted with pellet induced snakes. The radial and poloidal dimensions of the snake are ℓ_r and ℓ_θ . From the figure it may be seen that the shape of the negative snake varies from nearly circular to a shape with only a small radial extent. The figures in the table can be used to show that $\delta R/R \sim 20 - 25\%$ i.e. that the negative snake is a region of increased resistance and, as $\delta \zeta/\zeta = 13 - 16\%$, also a region of increased impurity density. In these respects the negative snakes are similar to normal snakes. However, contour plots of the ECE data show quite a different picture. In these measurements T_e is determined along a minor radius in the outer half of the median plane. The rotation of the plasma makes it possible to produce a pseudo-contour plot over the entire structure of the snake. These plots (Fig. 4) clearly show that the negative snake sits at the X-point of the island structure. If the temperature is plotted normalised to the average temperature at a particular radius then the more familiar localised picture of the snake appears (Fig. 5). The other prominent feature of the temperature profile is its hollowness. The negative snakes are in fact sitting on the rim of a volcano shaped structure.

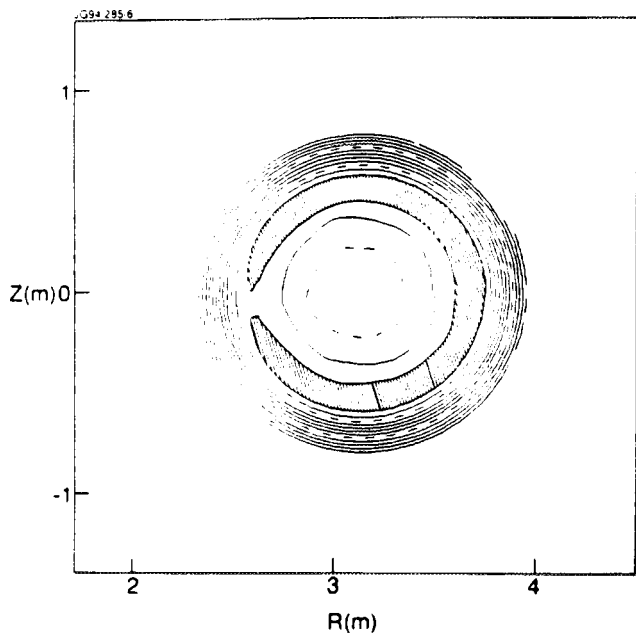


Fig. 4: Contour plot of T_e .

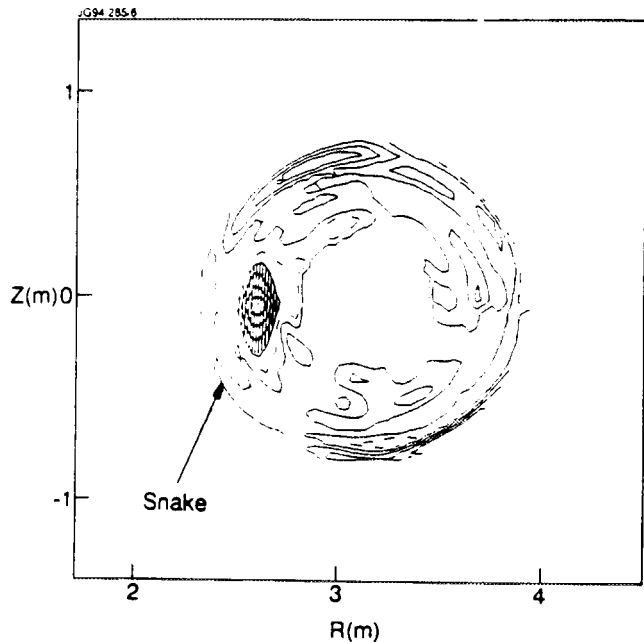


Fig 5: Contour plot of T_e normalised to the average temperature $\langle T_e \rangle$ at a particular minor radius.

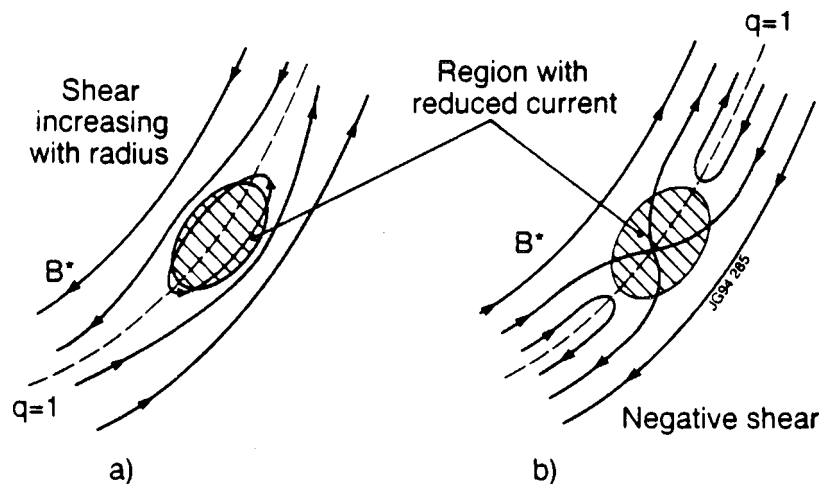


Fig. 6: Magnetic field structure with (a) positive shear and (b) negative shear.

EFFECTS OF SHEAR In the case of normal snakes, the effect of substantial plasma cooling by the pellet injection was convincingly argued to be a cause of magnetic island formation which then became identified with the snake. These calculations assumed a "normal" q -profile that increased with minor radius. Further theoretical work [3] showed that the bootstrap current could explain several of the observed features of the snake. The relationship between the shear and the current perturbation is shown schematically in fig. 6 where the magnetic poloidal field, $B^* = B_\theta (1-q)$, in helical coordinates is shown in the region of the $q=1$ surface. If q increases with radius then B^* is in the same direction as B_θ within the $q=1$ surface and reversed outside it. A locally reduced current density will form an island as shown in fig. 6a. However, as the negative snakes have a locally reduced current density and sit at the X-point of the island structure it seems to be an inescapable conclusion that the magnetic shear is reversed at the point of the snake, i.e. that q is decreasing with radius, as shown in fig. 6b. This could be possible in these particular discharges as the electron temperature profiles are generally hollow except just for the time before the sawtooth collapse where the snakes in any case disappear. It would therefore appear that the q -profile in these low q -discharges is different from what might have been expected, but other instances of unusual q -profile have been observed in JET in PEP discharges [4], hot ion H-modes [5], and counter-injection [6] heated discharges.

REFERENCES.

- [1] A. Weller et al., Phys. Rev. Lett., **59** (1987) 2303.
- [2] R.D. Gill et al., Nuclear Fusion, **32** (1992) 723.
- [3] A. Thyagaraja and F.A. Haas, Phys. Fluids., **B5** (1993) 3252.
- [4] M. Hugon et al., Nuclear Fusion, **32** (1992) 33.
- [5] M.F.F. Nave et al., submitted to Nuclear Fusion.
- [6] A. Edwards et al., 1992 Int. Conf. on Plas. Phys. (Innsbruck) **16C**, Part 1, 379.



FR9701780

Prospects of Real-Time Ion Temperature and Rotation Profiles based on Neural-Network Charge Exchange Analysis.

R W T König, J Svensson¹, M von Hellermann.

JET Joint Undertaking, Abingdon, Oxon, OX14 3EA.

¹ KTH, Stockholm.



INTRODUCTION. A neural network technique used at JET to extract plasma parameters like ion temperature, rotation velocities or spectral line intensities from charge exchange (CX) spectra is described. Based on earlier proof-of-principle results /1/ on the application of neural nets for the analysis of complex spectra such as the HeII ($n=4$ to $n=3$) spectrum, the options for a real-time analysis of complete radial profiles using the simpler C VI CX-spectrum with fewer components are addressed. A similar attempt has recently been undertaken at DIII-D /2/. Usually spectra are analysed by fitting Gaussian line shapes to all observed spectral components using a least squares algorithm. The least-squares technique is a well advanced and established procedure providing high accuracy and error estimates. It is, however, extremely time consuming (>200 ms/spectrum) and human interaction is often required to provide appropriate initial guesses. In this paper it is shown that in the case of the C VI CX spectra, neural networks can give a good estimation (better than $\pm 20\%$ accuracy) for the main plasma parameters (T_i , v_{rot}). Since the neural networks approach involves no iterations or initial guesses the speed with which a spectrum is processed is so high (0.2 ms/spectrum) that real time analysis will be achieved in the near future.

THE C VI SPECTRUM. Fig. 1 shows a typical example of a C VI CX spectrum that a

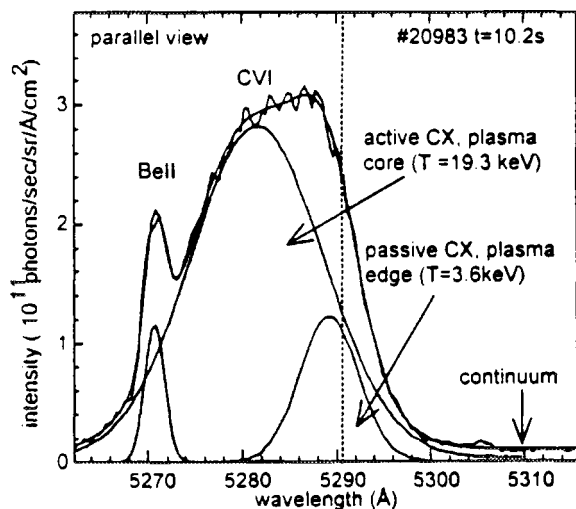


Fig. 1 C VI charge exchange spectrum showing all its individual components

neural network has been trained to analyse. The spectrum consists of three different spectral lines. The Be II line is excited by electron collisions and originates from areas just outside the separatrix. The active C VI charge exchange line is emitted from the intersection volume of the neutral beam and the viewing line, while the passive C VI charge exchange emission line is produced just inside the separatrix by reactions with

recycling neutral hydrogen. Due to the toroidal rotation of the plasma, the active as well as the passive CX lines are shifted relative to their nominal wavelength position. This means, if one disregards the continuum level (since it can be determined separately from a line free part of the spectrum), 9 fit-parameters are required to describe such a spectrum by 3 Gaussians. The ion temperature is derived from the width of the spectral lines. Since experiments have shown that the Be II ions do not rotate with the plasma, the toroidal rotation velocity is derived from the shift of the active CX line relative to the Be II line.

THE CHARGE EXCHANGE SPECTROSCOPY NEURAL NETWORK. A back-propagation neural network simulation program has been developed on an IBM-PC in C++ which runs under Windows. For the back-propagation algorithms a commercial library /3/ was used which could be used together with a Digital Signal Processor (DSP) board for the PC. The DSP board reduced the training time by a factor 12; a significant gain considering that training often takes several hours. The PC program automatically produces a FORTRAN subroutine for the forward code, which can easily be transferred to the IBM mainframe and implemented in the standard analysis codes. In order not to produce a look-up table, but to make a neural network with a good generalisation ability, two data sets have always been used, a training set and a test data set, which had a size of about 10% of that of the training set. Moreover the training was always stopped whenever the error of the test set started to increase, which is the point when the network starts to memorise insignificant features of the training set. This status is usually achieved after a few hundred epochs or 1 to 3 hours. However, good accuracy is already reached after about 1/3 of this time (fig. 2). To achieve a

good generalisation ability a neural network should always have as few neurons in the hidden layers as possible. As a rule of thumb it was assumed that the number of hidden neurons should be approximately equal to the number of fit-parameters needed to describe a spectrum. Practical tests revealed that 7 hidden neurons were sufficient for the C VI spectrum. All networks trained had 298 input neurons, one for each pixel in the

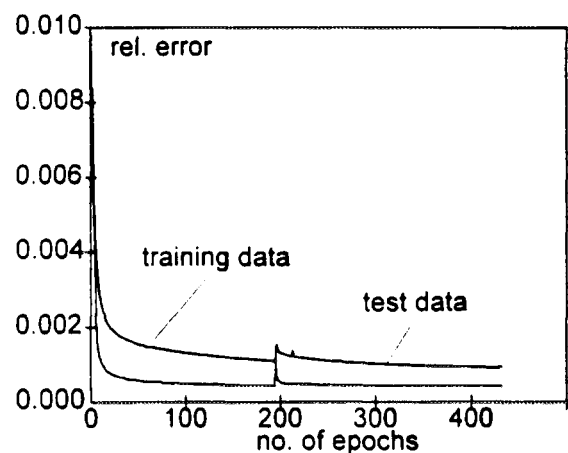


Fig. 2: Error of the training (13315 spectra) and test data set (1492 spectra) of the ion temperature network.

spectrum, and only one output neuron representing ion temperature, rotation velocity or line intensity respectively (fig. 3). It appeared that having only one output neuron made it considerably easier (reduced convergence time) for the network to learn, compared to a network with 3 or more parameters as output. It also simplified the decision of when the network had the best generalisation ability for the different parameters.

CONCLUSIONS AND FUTURE PROSPECTS. The neural network was tested on 30000

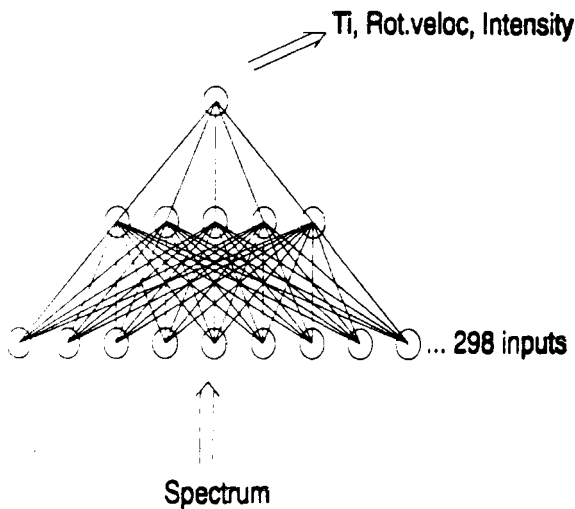


Fig. 3 Basic structure of the neural net used. The number of hidden layer neurons varied

spectra, selected from a widely changing range of core and edge plasma conditions (i.e. $1 \text{ keV} < T_i < 25 \text{ keV}$, $10^{17} \text{ m}^{-3} < n_C < 2 \cdot 10^{18} \text{ m}^{-3}$). Over 80 % of the neural network results are within 20 % of the more accurate least-square results (fig. 4) showing that the feed forward neural network can be an efficient tool with a wide range of applications. However, a substantial number of training spectra is required to train a network. A set of 13000 training spectra and

1500 test spectra has been used. Presently the neural network is used to provide reliable initial estimates for the least square fitting routine and for immediate analysis in-between shots.

In fig. 5-8 some examples are given which show the typical quality of neural network based ion temperature analysis. It is expected that it will also be possible to provide real-time ion temperature and plasma rotation profiles in the control room, which in the near future can for example be used as input for plasma stability control (rotation frequency) or as feed back signal (ion temperature) enabling burn-control studies for applications in Next-Step machines. In order to improve the training

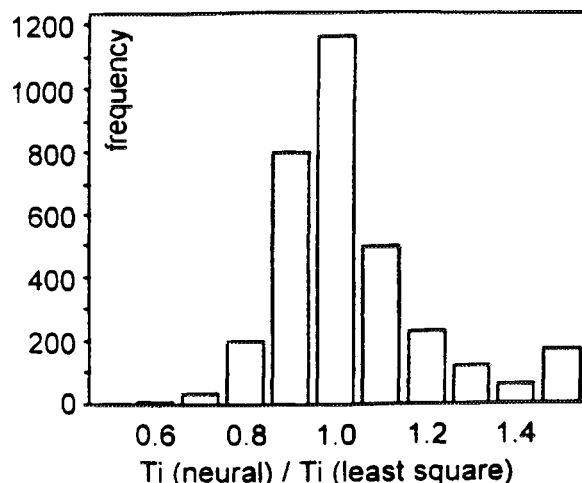


Fig. 4 Ratio of neural network and least-square solutions for the ion temperature of 3000 test spectra taken at $R=3.4 \text{ m}$. The values at 0.5 and 1.5 are the sum of all values further out on each side.

algorithm it is planned to introduce, in a next step, a method to dynamically change the momentum and learning coefficient and also to implement the conjugate gradient method, which is believed to be an order of magnitude faster than the ordinary back-propagation method. On the input side the pre-processing of the data will be improved. Moreover an attempt will be made to use Bayesian methods, which have only recently been developed for back-propagation networks /4/, to choose network parameters (such as the number of hidden neurons) and to determine the errors of neural network estimations.

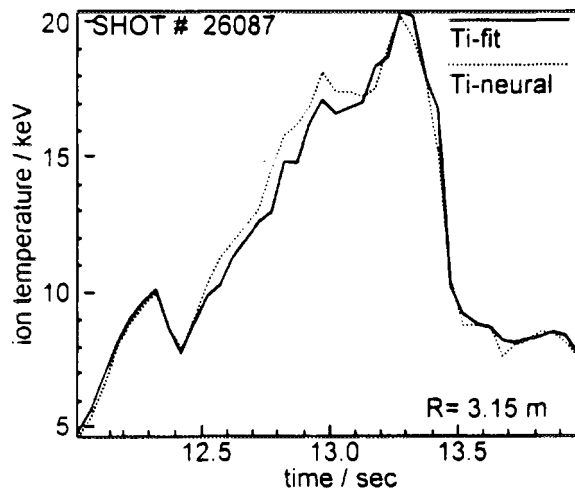


Fig. 5: Ion temperature time trace for a case where the temperatures reach the extremes of the training set.

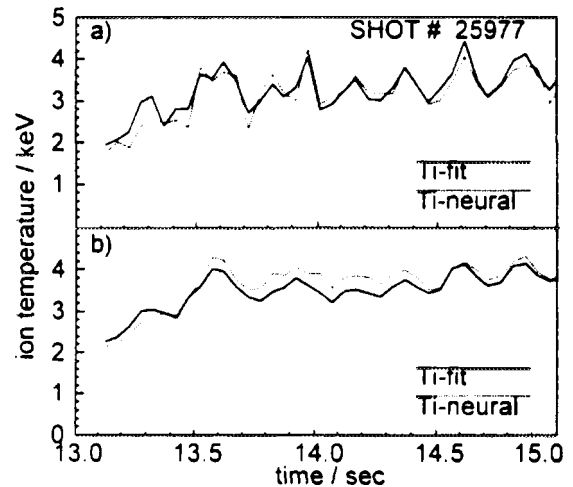


Fig. 6: Ion temperature sawteeth resolved by the neural net. In a) the spectra were analysed without averaging, while in b) the spectra were averaged over 3 frames prior to analysis.

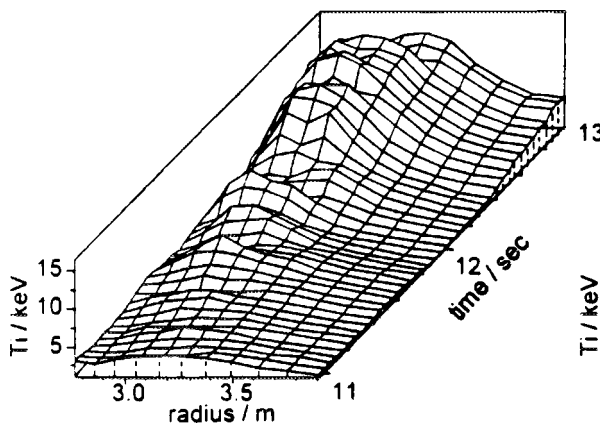


Fig. 7: Least-square fit ion temperature profile.

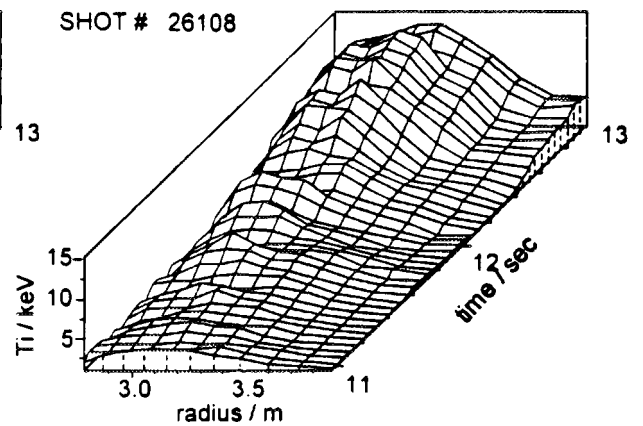


Fig. 8: Neural network ion temperature profile.

/1/ C Bishop et al., Plasma Phys. Contr. Fusion **35**, 765 (1993)

/2/ D R Baker, R J Groebner and K H Burrell, GA-Report, GA-A21260, 1993

/3/ Neural Net Inc.

/4/ D J C MacKay, PhD thesis, California Institute of Technology, 1992



FR9701781

Ion Temperature Anisotropy in High Power Helium Neutral Beam Fuelling Experiments in JET

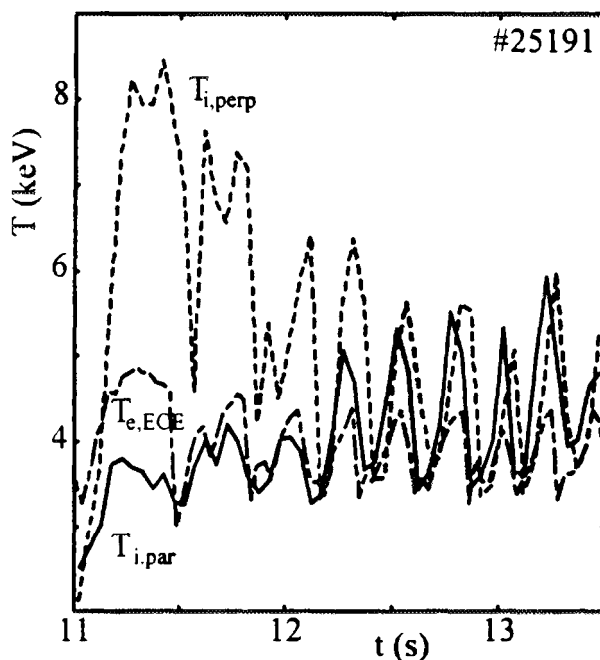
A C Maas, W G F Core, U C Gerstel, M G von Hellermann,
R W T König, F B Marcus.

JET Joint Undertaking, Abingdon, Oxon, OX14 3EA.



Introduction. During helium beam fuelling experiments in JET, distinctive anisotropic features have been observed in the velocity distribution function describing both fast and thermal alpha particle populations [1]. During the initial fuelling phase the central helium ion temperature observed perpendicular to the magnetic field is higher than the central electron temperature, while the central helium ion temperature observed parallel to the magnetic field is lower than or equal to the central electron temperature (fig.1).

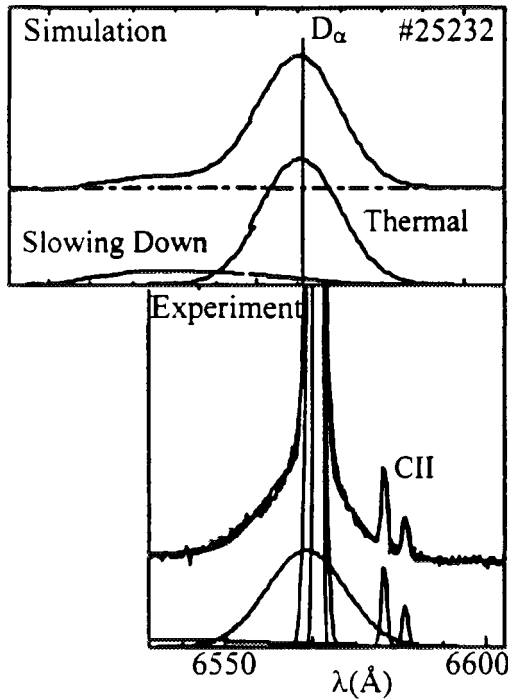
Theory. The trajectories of fast injected ions are initially sharply peaked around the line of injection. As they slow down through Coulomb scattering on the plasma electron and ion species, they scatter in pitch angle, making the fast ion distribution function increasingly more isotropic. This scattering, which is preferentially on the cold electrons and hot plasma ions, gives rise to distorted background distribution functions and in particular to the development of a non-Maxwellian anisotropic high energy tail. The effect of fast ions slowing down on the distortion of the background ion distribution



1. Example of helium ion temperature anisotropy

function has been investigated and Fokker-Planck studies of the JET injection configuration considered are in close agreement with the measured bulk ion temperature and perpendicular to parallel temperature anisotropy ratio [2].

Deuterium Ion Temperature. To verify temperature measurements of both perpendicular and parallel lines of sight other independent methods of deducing the ion temperature were investigated. The carbon content of the plasma, around 1 %, is too low to give reliable data on C-VI ion temperatures, especially in combination with the reduced C-VI emission for a



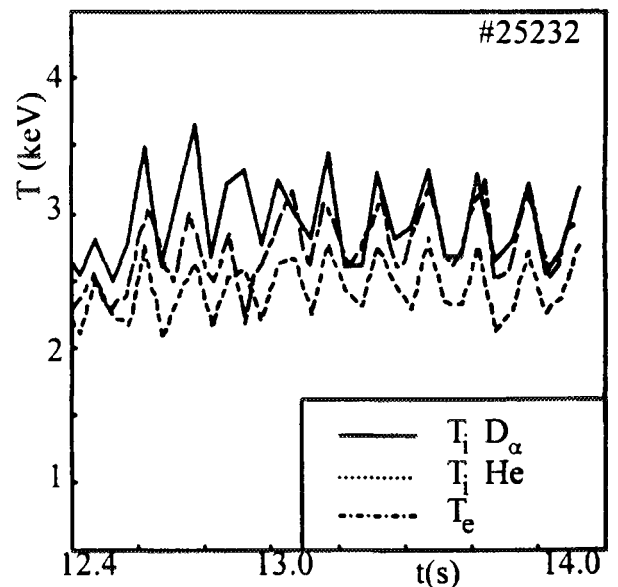
2. Simulated and experimentally observed slowing down deuterium population

other spectral components small. More experimental data are needed to further study the slowing down deuterium population.

The parallel deuterium ion temperature found is in agreement with electron and parallel helium ion temperatures (fig.3). Since helium beams were used for both fuelling and diagnostic purposes, the D_α spectrum is free of beam emission spectral components, and beam-halo effects [3] seem to have far less influence than in the case of deuterium beams. The beam-halo can extend up to 0.5 m around the beam, making localisation of the T_i measurement difficult.

An absolute assessment of the influence of the beam-halo on the deduced temperature can at this stage not be made since no data are available for the effective emission rate of the D_α line with helium as a donor. The relative contribution of the halo to the spectrum compared to the charge exchange contribution is however thought to be much

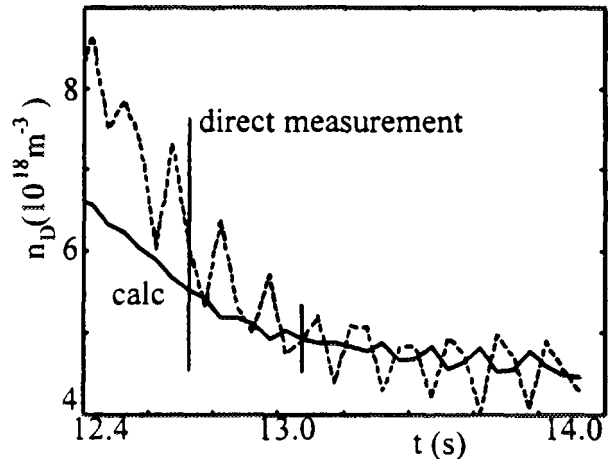
helium beam as donor. Data, however, do exist for the central deuterium ion temperature for a few discharges, deduced from the Balmer Alpha (D_α) charge exchange spectrum observed parallel to the magnetic field [3]. Limited experimental results confirmed by simulation calculations, indicate the existence of an anisotropic fast particle population of deuterons, which are injected by neutral beams opposite the charge exchange spectroscopy (CXS) diagnostic. The slowing-down features, similar to those in the HeII spectrum [1], can be observed in the D_α spectrum (fig.2), but the amplitude is significantly lower, making the influence on



3. Ion temperatures measured parallel to magnetic field and electron temperature

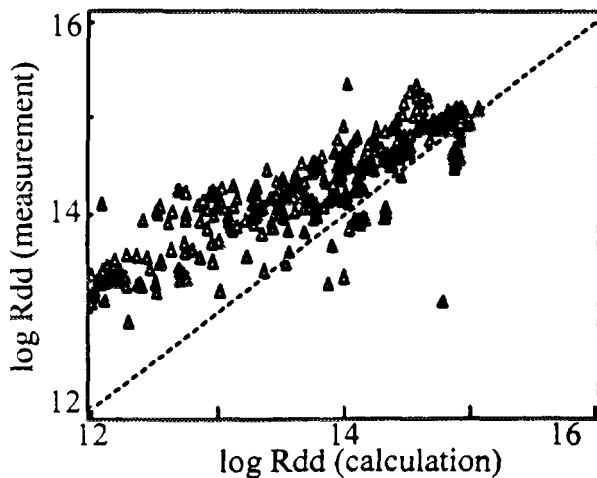
smaller in these cases, since the spectral contribution of the halo scales roughly with n_D^2 while the charge exchange contribution scales with n_D . In helium beam fuelling experiments the majority of electrons in the deuterium target plasma is provided by helium, making n_D up to a factor 10 lower than in normal deuterium discharges, where the beam-halo effect is needed to explain data from the D_α spectrum.

Deuterium Density. In the deduction of the deuterium density from the D_α charge exchange spectrum an absolute assessment of the beam-halo effect is difficult as well and also cross-section data are not available. The deuterium density can therefore only be calculated using the electron and major impurity densities: $n_D = n_e - 2n_{He} - 4n_{Be} - 6n_C$. The densities of helium, beryllium and carbon are provided by the CXS diagnostic. The result is shown (fig.4) as well as a curve deduced from the D_α spectrum, using the effective emission rate as a fitting parameter. An effective emission rate of $1.5 \cdot 10^{-9} \text{ cm}^3 \text{ s}^{-1}$ is found to give good agreement between the two techniques.



4. Measured deuterium density and calculation from charge neutrality

Neutron Rates and Profiles. Another check on data consistency is the comparison of neutron rates from neutron diagnostics with those obtained from calculations using CXS data. In the cases considered helium neutral beams were used for fuelling, so neutrons arise from thermal plasma-plasma reactions only. The deuterium ion temperature needed for the calculation is



5. Overview of calculated total neutron rate as function of measured total neutron rate

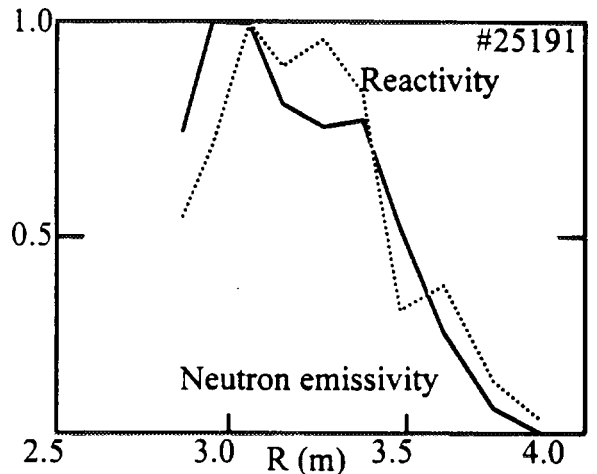
assumed to be equal to the helium ion temperature, while the deuterium density is calculated from the electron and impurity densities as described above. The calculated neutron rates are found to be always smaller than the measured neutron rates (fig.5). To investigate the cause of this discrepancy the shape of the reactivity profile, deduced from the ion temperature, is compared with the shape of the neutron emissivity profile, obtained from a tomographic deconvolution

of data from the neutron profile monitor [4]. Since all density profiles are reasonably flat, the ion temperature will have the biggest influence on the neutron emission profile shape. The shapes of the reactivity and the neutron emission are in good agreement (fig.6), leaving the deuterium density as parameter to adjust the total neutron rate.

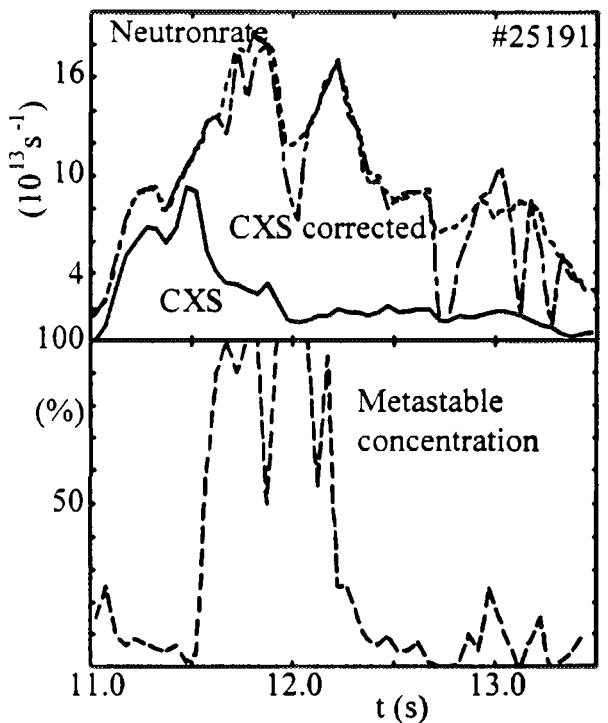
Metastable Helium. One of the reasons the absolute deuterium density is not deduced correctly is the possible existence of a

metastable population of helium in the fuelling beam. The effective emission rate for helium with a metastable donor is thought to be approximately five times higher than with a normal donor [5]. This leads to an over-estimation of the helium density and therefore the deuterium

density is found to be lower than in reality. The metastable concentration required in the helium beam to change the deuterium density sufficient to get agreement between the calculated and measured total neutron rates was simulated (fig.7). At some points a metastable concentration of more than 50 % is required to get agreement, while estimates for JET indicate that metastable beam fractions certainly do not exceed 7 % when entering the plasma [6]. Other mechanisms to explain the discrepancy in the neutron rate measurements, such as plume-effects and helium beam-halo effects are under investigation.



6. Normalised reactivity and neutron emissivity profiles



7. Metastable concentration needed to obtain consistency in neutron rates

- 1 M von Hellermann et al., 20th EPS Conf. on Contr.Fusion and Plasma Phys., Lisbon, vol 17C, p.1071, 1993
- 2 W G F Core to be published
- 3 W Mandl et al., Plasma Phys. Contr. Fusion, 35, 1373, 1993
- 4 J M Adams et al., 16th EPS Conf. On Contr.Fusion and Plasma Phys., Venice, vol 13B, p.63, 1989
- 5 R Hoekstra, 9th APS Atomic Processes in Plasmas, San Antonio USA, September 1993, JET-P(94)16
- 6 H P Summers et al., 7th APS Atomic Processes in Plasmas, Portland Maine USA, August 1991, JET-P(91)48



FR9701782

Impurity Line Emission due to Thermal Charge Exchange in JET Edge Plasmas

C F Maggi, L D Horton, R König, M Stamp, H P Summers¹.

JET Joint Undertaking, Abingdon, Oxon, OX14 3EA.

¹ Dept. of Physics and Applied Physics, University of Strathclyde, Glasgow, UK.



Introduction

High n -shell emission from hydrogen-like carbon (C VI, $n=8-7$) has been routinely observed from the plasma edge of JET. The C VI observation is along an absolutely calibrated visible chord traversing the plasma cross section vertically from top to bottom of the vessel, just outside the outer strike point during upper X-point configurations (fig.1).

Supplementary observations of D I, C II and C III spectral line signals have been made along an identical chord and at nearby chords directed at the divertor strike zones. By

comparing the measured spectral line intensities with the signals predicted by advanced atomic physics modelling of carbon and hydrogen radiation, integrated with modelling of the divertor and edge plasma, it is concluded that charge transfer from excited state hydrogen donors into fully stripped carbon ions can account for the observed spectral emission, but that the hydrogen distribution and to a lesser extent the carbon distribution away from the strike zone predicted by the transport model are too low. The data presented here are those of three upper X-point discharges - performed during the 1991/92 JET experimental campaign - where the target material was carbon.

Thermal Charge Exchange and Excited Neutral Hydrogen

The calculated C VI ($n=8-7$) emission due to electron impact excitation is estimated to be a factor 2 to 15 lower than that due to charge exchange. This estimate depends strongly on

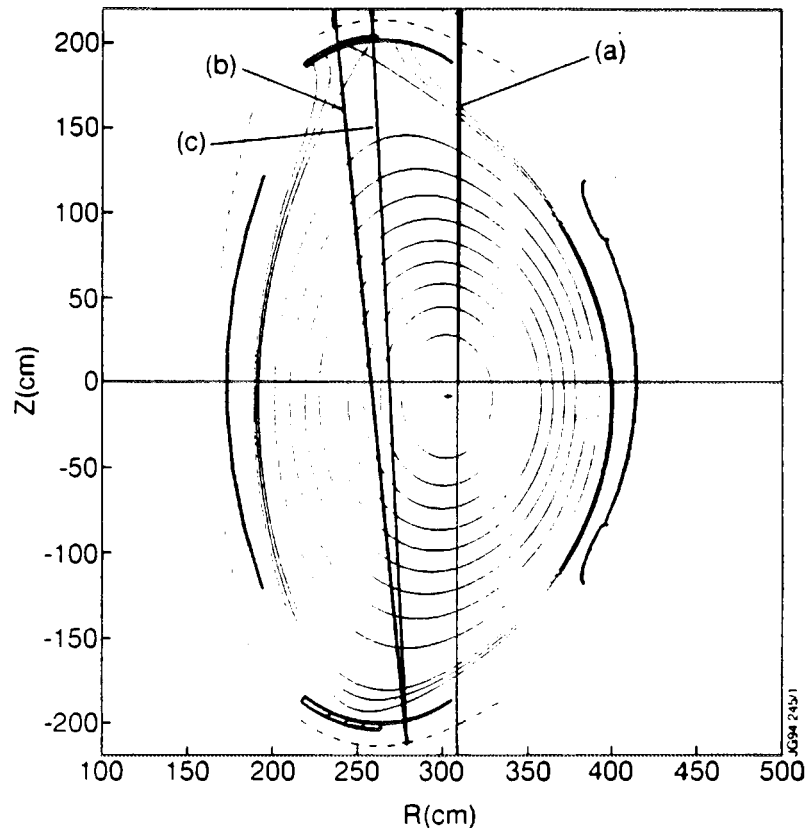


Figure 1. Plasma equilibrium for JET pulse #24174 with superimposed geometries for the visible chord at 3.1 m (a) and two supplementary visible viewing lines at the inner (b) and outer (c) strike point.

the mixing of the l-states in the C VI (n=8) level. More detailed calculations are in progress. In this paper the charge exchange origin of the line is assumed. In the edge region, rich with recycling neutral hydrogen, thermal charge exchange processes with fully stripped carbon impurity ions represent a suitable candidate. Due to the highly excited emitting state of the receiver species, however, charge transfer from ground state hydrogen is a negligible populating mechanism. On the contrary, charge exchange from excited states of hydrogen populates levels of the carbon ions high enough to contribute to the observed emission. Of hydrogen excited states, n=2 has the largest population density and its partial charge transfer cross section peaks at C VI (n=8). Therefore direct charge transfer from D I (n=2) into C VI (n=8), followed by radiative decay into C VI (n=7), is the mechanism considered.

Modelling

The characteristic spectral emission is well localised in the region of overlap of the spatial profiles of the neutral hydrogen donor and the fully stripped carbon ions. Thus the modelling of these spectral line intensities strongly depends upon an accurate transport picture of the reacting species at the edge. A steady state background plasma has been analytically constructed, defining the electron temperature and density profiles at the divertor target plates and, using classical transport, mapped around the scrape-off layer (SOL) [1]. This procedure draws upon experimental measurements from an array of Langmuir probes imbedded in the target tiles. The 2-D Monte Carlo code DIVIMP [2] is then used to model the production and transport of the carbon impurities. It is linked to the 2-D Monte Carlo code NIMBUS [3], which models the neutral hydrogen transport and recycling at the edge. A full collisional-radiative atomic model [4] relates the hydrogen excited state population densities to that of the ground state, whose spatial distribution is given by the transport codes. The atomic model also provides the modifications to the carbon ionization balance, resulting from charge exchange with neutral hydrogen [5] and the effective emission rate coefficients, necessary for the interpretation of the line intensity spectroscopic measurements.

Discussion

Three discharges have been selected for comparison with the model. The main plasma parameters are listed in Table 1. Comparison of the model to the observed spectral emission is extended by including additional spectroscopic signals directly related to the presence of carbon and hydrogen in the emission region. An additional absolutely calibrated visible observation, along an identical viewing line as the one measuring the C VI emission (see fig.1), measures the line intensity of the C III multiplet ($\lambda = 4647 \text{ \AA}$) and the H_α radiation. A visible viewing line to the outer strike point (for #24174 and #24175) or to the inner strike point (#26291) on the divertor target tiles (see fig.1) monitors the H_α , H_γ and the C II ($\lambda = 6579.7 \text{ \AA}$) line intensities. Table 2 shows the observed and predicted line-of-sight integrated emission from H and C for #24174, #24175 and #26291 at the time of the probe

measurements. Table 3 shows the comparison between the observed C VI ($n=8-7$) spectral line intensities, integrated along the vertical line of sight through the plasma, and the model predictions.

Table 1. Main plasma parameters of the selected discharges.

Discharge	time(s)	$B_T(T)$	$I_p(MA)$	$P_{in}(MW)$	$T_e(0)(keV)$	$n_e(0)(m^{-3})$
#24174	12.18	2.1	3.1	13.0	4.0	1.8×10^{19}
#24175	13.59	2.1	3.1	5.6	3.5	1.6×10^{19}
#26291	13.90	2.8	3.1	3.1	3.0	2.1×10^{19}

Table 2. Comparison between observed and predicted line-of-sight integrated spectral emission from H and C (photons/cm²/s/sr), using the viewing lines at 3.1 m and at the outer strike point, for JET pulse #24174 and #24175, and at the inner strike point for #26291.

	#24174		#24175		#26291	
	Exp.	Model	Exp.	Model	Exp.	Model
$I(H_\alpha) @ 3.1 m$ $\times 10^{14}$	1.50 ± 0.35	0.48	1.40 ± 0.35	0.40	0.75 ± 0.19	0.43
$I(CIII,4647\text{\AA})$ $@ 3.1 m$ $\times 10^{13}$	2.50 ± 0.62	1.99	2.60 ± 0.65	1.67	1.35 ± 0.34	0.93
$I(H_\alpha)$ $@ strike point$ $\times 10^{15}$	1.30 ± 0.32	1.55	1.09 ± 0.27	1.34	3.20 ± 0.80	3.70
$I(H_\gamma)$ $@ strike point$ $\times 10^{13}$	1.75 ± 0.87	3.97	1.50 ± 0.75	3.48	6.00 ± 3.00	7.20
$I(CII,6580 \text{\AA})$ $@ strike point$ $\times 10^{13}$	0.91 ± 0.23	2.30	0.91 ± 0.23	1.77	12.0 ± 3.0	31.0

Table 3. C VI ($n=8-7$) LOS integrated (see fig.1) spectral line intensities (photons/cm²/s/sr). Comparison between observations and model predictions. The time of the measurements coincides with that of the Langmuir probe data.

JET Discharge	I(experiment)	I(model)	I(model, normalized)
#24174	$(2.0 \pm 0.4) \times 10^{11}$	2.2×10^{10}	8.6×10^{10}
#24175	$(1.6 \pm 0.4) \times 10^{11}$	2.3×10^{10}	1.2×10^{11}
#26291	$(1.2 \pm 0.6) \times 10^{11}$	6.2×10^{10}	1.6×10^{11}

The relatively large error bars on the experimental values are due to the weakness of the C VI edge charge exchange signal in these discharges. The simulated values are lower than the experimental measurements, particularly for #24174 and #24175. These discrepancies originate from the fact that for these discharges the model fails to give an adequate description of the neutral and impurity transport in the SOL. For both #24174 and #24175, in fact, the H_{α} signal at the outer strike point matches quite well with the observed one. At 3.1 m, on the other hand, the H_{α} signal is underestimated by a factor 3 to 4 (see Table 2) with respect to the observed emission. Since the intensity of the H_{α} signal marks the neutral hydrogen abundance in the emission region, this leads to a corresponding underestimation of the predicted neutral hydrogen density at 3.1 m. Similarly, the C III density in the same region is underestimated by the model, in spite of the C II line intensity being about a factor two higher than the observed one at the outer strike point. Such trends suggest that the hydrogen and the carbon impurities do not spread as far away from the strike point as appears experimentally. By scaling the modelled C VI emission using the ratio of measured to modelled H_{α} emission and the ratio of measured to modelled C III emission, one obtains much better agreement with experiment (see Table 3).

Conclusions

Thermal charge exchange from excited state hydrogen ($n=2$) to C^{+6} ions can account for the measured spectral line emission from hydrogen-like carbon (C VI, $n=8-7$) in JET edge plasmas. The emission due to electron impact excitation is estimated to be a factor 4 to 50 lower than the normalized charge exchange emission, this variation strongly depending on the mixing of the l-states in the C VI ($n=8$) level. The analysis is complicated by the failure of the simulations to describe correctly the leakage of hydrogenic and impurity particles from the divertor. However, if the experimental values of H_{α} and C III signals are used to normalise the model results, the predicted C VI line emission agrees within a factor 2 of the measurements. The observation and modelling of impurity line emission due to thermal charge exchange constitutes a promising diagnostic for the derivation of neutral hydrogen density spatial profiles in the edge region of JET. In fact, these studies have demonstrated a deficiency in the transport model for neutral deuterium and/or impurities, which is being investigated. These studies will also be extended to the very low temperature, high density divertor regimes planned for the 1994 experimental campaign.

References

- [1] G.F. Matthews et al., J. Nucl. Mater. **196-198** (1992) 374.
- [2] P.C. Stangeby, J.D. Elder, J. Nucl. Mater. **196-198** (1992) 258.
- [3] E. Cupini, A. De Matteis, R. Simonini, NET Report EUR XII (1984) 324.
- [4] H.P. Summers, ADAS, JET Report, in progress.
- [5] C.F. Maggi, Laurea Thesis, (1992).



FR9701783

The Control of Convection by Fuelling and Pumping in the JET Pumped Divertor

P J Harbour, P Andrew, D Campbell, S Clement, S Davies,
J Ehrenberg, S K Erents, A Gondhalekar, M Gadeberg, N Gottardi,
M von Hellermann, L Horton, A Loarte, C Lowry, C Maggi,
K McCormick, D O'Brien, R Reichle, G Saibene, R Simonini,
J Spence, M Stamp, D Stork, A Taroni, G Vlases.

JET Joint Undertaking, Abingdon, Oxon, OX14 3EA.



1 INTRODUCTION

Convection from the scrape-off layer (SOL) to the divertor will control core impurities, if it retains them in a cold, dense, divertor plasma. This implies a high impurity concentration in the divertor, low at its entrance. Particle flux into the divertor entrance, Γ_d , can be varied systematically in JET, using the new fuelling and pumping systems. We estimate the **convection ratio**, Γ_d/Γ_t , where Γ_t is the particle flux to the divertor target, for various conditions of operation. Particle convection into the divertor should increase thermal convection, decreasing thermal conduction, and temperature and density gradients along the magnetic field, hence increasing the frictional force and decreasing the thermal force on impurities.

The **convection ratio**, Γ_d/Γ_t , is estimated as follows ($n_s \approx 2 \times 10^{19} \text{ m}^{-3}$), based on EDGE2D [1].

Open configuration (horizontal target)	0.15	0.35
Closed configuration (vertical target)	0.03	0.19
Typical conditions	Low pumping/wall pumping and/or fuelling in divertor	High pumping/wall pumping & fuelling in torus

The limited range is due to ionisation in the divertor. The configuration is more "open" at low density and with hydrogen, giving higher Mach number at the divertor entrance.

The control of convection is important, so is studied in JET, using the new fuelling system. We discuss a limited study, using the Mk I Divertor, with horizontal target, and no pumping. It is expected that the control of impurities may be sensitive to small changes in Mach number, $-0.1 \leq M \leq 0.1$, say. The study of fuelling is supported by modelling with EDGE2D, as described in Sections 5,6.

2 THE EXPERIMENT IN JET AND THE MODEL PLASMA FOR EDGE2D

Fuelling ("puff" in Figures) is now provided at three poloidal locations in JET (Fig 1a), top (thick SOL), outer midplane, OMP (thin SOL, hence deeper penetration), and in the divertor, just below the X-point. The divertor system has 24 toroidally distributed inlet pipes, controllable in quadrants (six pipes each), via four independent fast gas valves. Pumping will be via a cryopump, stronger in the outer divertor, but not yet available, so we use wall-pumping in this study. Wall-pumping is assumed to occur mainly in the divertor and is found to decrease in strength throughout the day, from $\sim 4 \times 10^{21} \text{ s}^{-1}$ to $\sim 2 \times 10^{21} \text{ s}^{-1}$ in high density Ohmic discharges. The plasma configuration studied is shown in Fig 1a and the model geometry in Fig 1b. Fuelling in EDGE2D is simulated by introducing D atoms ($T \approx 0.1 \text{ eV}$) at the walls where indicated, while pumping is simulated by absorbing 10% of the flux of neutrals onto the divertor walls. Steady state is achieved by matching the fuelling rate to the wall pumping rate found in experiment and model respectively.

3 EXPERIMENTAL PROCEDURE

An Ohmic density scan was made in a series of discharges (2.8T, 2MA), with deuterium fuelling in the divertor (1,2 or 4 quadrants). Several discharges had top or OMP fuelling for comparison. The total electron content, N , increased until fairly constant. The pumping rate, ϕ_{pump} , is given by

$$\phi_{pump} = \phi_{fuel} - dN/dt \quad (1),$$

and in every discharge $|dN/dt| \ll \phi_{pump}, \phi_{fuel}$ during the \approx constant density phase. On the first day, with purely Ohmic discharges (#29756-66), data were taken at $t_{data} = 14 - 16 \text{ s}$. On the second day (#29810-23), $t_{data} = 13.5 \text{ s}$, avoiding the NBI commissioning time ($t_{NBI} \geq 16 \text{ s}; P_{NBI} \leq 12 \text{ MW}$).

4 EXPERIMENTAL RESULTS

Figure 2 shows the density scan. The specific pumping rate, ϕ_{pump}/N (Fig 2a), lies mostly between 1 s^{-1} and 3.3 s^{-1} . Considering the pumping observations sequentially, there was first a density limit pulse

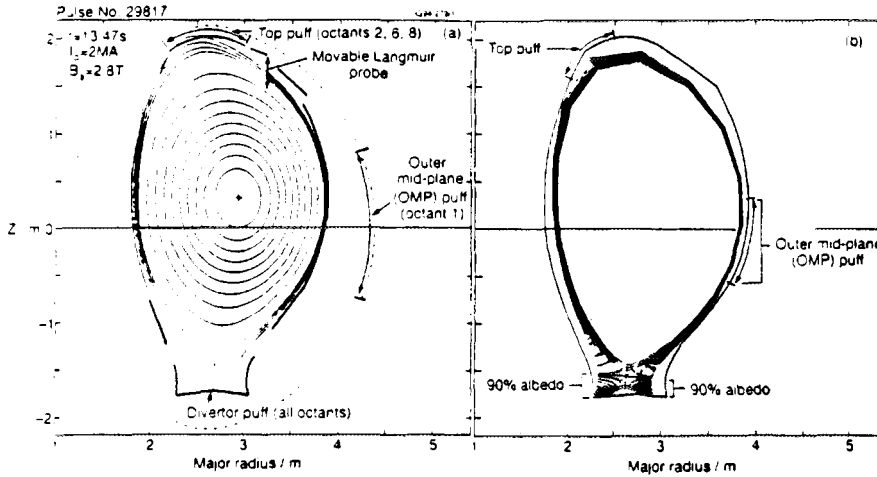


Figure 1: The geometric configuration, with fuelling locations of a) the experiment in JET, and b) the model plasma used in EDGE2D.

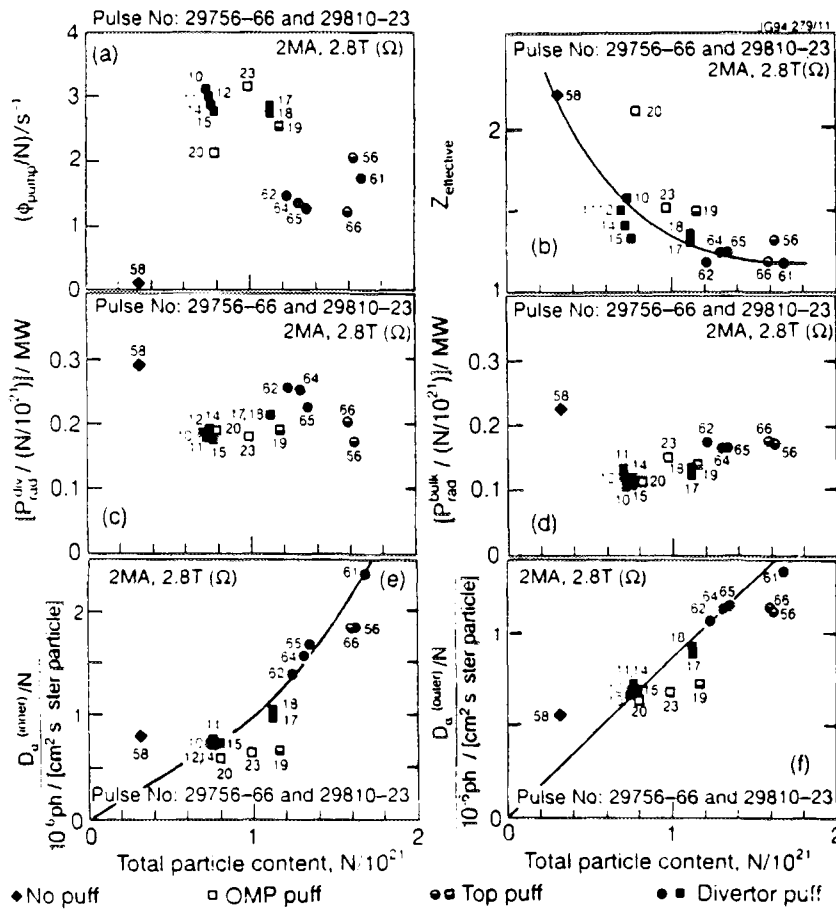


Figure 2: The density (total electron content, N) scaling of a) the specific wall-pumping rate, Φ_{pump} / N (see Equ. 1), b) the global $Z_{effective}$, c,d) radiation power in divertor and bulk plasma (power/particle is plotted), and e,f) D_{α} intensity in inner and outer divertors (radiation intensity per particle is plotted). Solid symbols represent fuelling in the divertor; open/half-solid symbols represent SOL fuelling. With SOL fuelling we see higher $Z_{effective}$ and lower divertor radiation (total and D_{α}) but no change in bulk plasma radiation or in wall pumping.

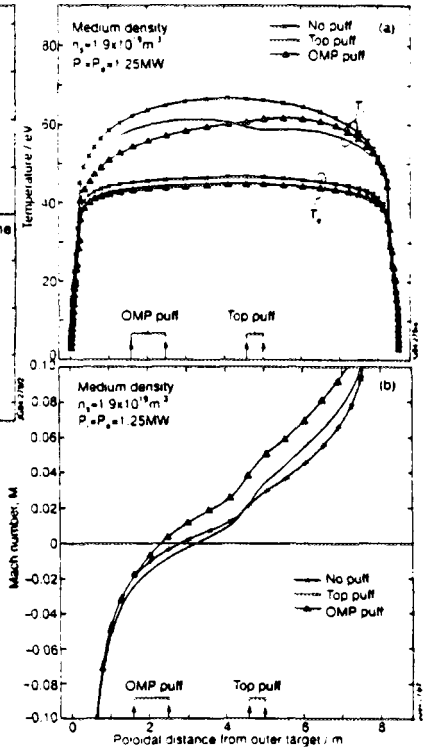


Figure 3: Poloidal profiles on the separatrix, fuelling as shown: a) T_i, T_e , b) Mach number along the separatrix.

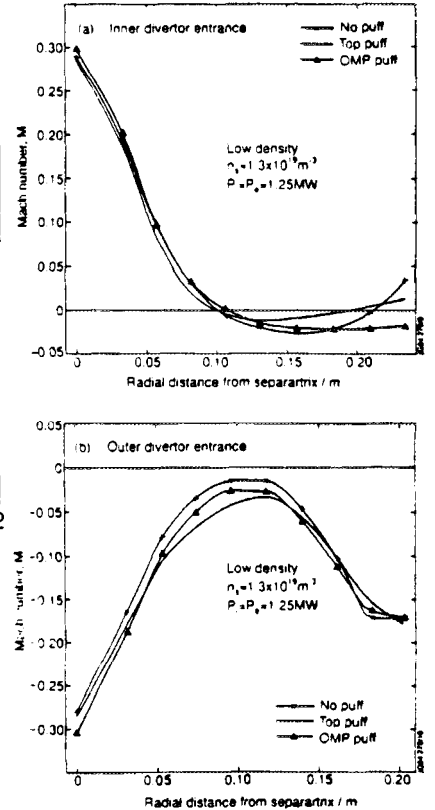


Figure 4: Mach number of the plasma outside the divertor entrance, against radial distance from the separatrix, a) inner divertor entrance, b) outer entrance.

(29756) with top fuelling, then a low density pulse (fuelling off), where ϕ_{pump}/N was much lower. Divertor fuelling was used in 61, which showed 20% less pumping than 56, and the specific pumping rate continued to fall throughout the sequence 62-65, with divertor fuelling, and 66, with top fuelling. There seems little to distinguish the pumping in these Ohmic discharges, with top or divertor fuelling. On the second day, ϕ_{pump}/N was almost twice as large (only partly due to the timing of the observation, 1.5 s earlier). Again the specific pumping rate fell, the sequence 29810-15 showing this clearly. The trend was resumed during 17,18 & 19, the latter with top fuelling, and if we allow for the density variation there is nothing to suggest that 19 (top fuelling) or 20 (OMP fuelling) lie outside the sequence. In contrast, 23 (OMP fuelling) has at least 50% more pumping than expected. The specific pumping rate falls by 3% to 10% per discharge, increasing with plasma density as expected under high recycling conditions. A regression fit to the data in Fig.2a shows that ϕ_{pump} varies approximately as $N^{1.3}$ and that it increased by a factor greater than two on the second day. All measured values of ϕ_{pump} lay within about 10% of the regression line (apart from #29823) and, for those observations with fuelling in the main SOL, the deviations from the regression fit were random in sign as well as being of similar magnitude to those with divertor fuelling. This confirms the analysis of data given above.

The global $Z_{effective}$ varies with density as usual, but is higher for four of the five plasmas with SOL fuelling (Fig2b). This implies greater carbon content, due either to sputtering at the fuelling location or increased sputtering and escape of carbon from the divertor. In contrast, the bulk radiation is not affected fuelling location (Fig2d): either it is dominated by high Z species (e.g. Cl), little affected by changes at the edge, or we have an inconsistency. However the trends do appear to be significant.

Radiation in the divertor shows consistent trends in line with expectations. With divertor fuelling, the D_{α} intensity at both targets increases rapidly with N, D_{α}/N increasing linearly with N up to $N=10^{21}$, with about 10% greater intensity in the inner divertor. Above $N=10^{21}$ the increase, still linear in the outer diveretor, is faster than linear in the inner, indicating a cold plasma. The D_{α} intensity is up to 25% lower with fuelling in the SOL (Fig.2e,f). There is a similar trend in the total divertor radiation obtained bolometrically (Fig 2c).

Overall, there is clear evidence (D_{α} /bolometry) that particle fluxes in the divertor increase with density ($D_{\alpha} \sim N^2$ or more) as well as with divertor fuelling. Also the specific pumping rate increases with density ($\phi_{pump} \sim N^{1.3}$), but at a lower rate than the increase in particle fluxes in the divertor. It is surprising that the specific pumping rate is not increased by fuelling in the divertor, when fluxes are higher. Can it be that pumping occurs near the fuel inlet, possibly due to charge exchange?

SOL profiles, measured with a movable Langmuir probe in discharges 29810-20, showed a fairly constant narrow layer. In 29819 (top fuelling) the scrape-off thickness increased substantially compared to 29818 with divertor fuelling, (λ_n , 13.7→21mm; λ_r , 8.8→14mm; λ_T , 23→27mm). We expect broadening with fuelling in the SOL, especially at the top of the vessel, which would exaggerate differences between torus and divertor fuelling. No significant difference is apparent in Fig.2 for discharge 29819. Plasma profiles at the target were unavailable in these discharges.

5 MODELING WITH EDGE2D: PROCEDURE

Nine steady state runs with EDGE2D and NIMBUS were performed ($P_i^{SOL}=P_e^{SOL}=125MW$; $D_{\perp}=0.2 \text{ m}^2\text{s}^{-1}$, $\chi_{\perp}=1.5 \text{ m}^2\text{s}^{-1}$; L-mode values), with three densities and three fuelling assumptions: top or outer mid-plane (OMP) fuelling and no fuelling (\approx divertor fuelling). The plasma geometry is similar to that used experimentally (Fig 1). The interaction between plasma and walls in the torus was minimised, so that changes due to changing fuelling point would be detectable. To this end, a diffusive flux boundary condition with shallow gradient ($\lambda_n=3\text{cm}$) was set at the outer surface of the plasma region used in EDGE2D (Fig.1b). Plasma crossing this outer surface was recycled at the divertor target. About half of the recycling was of this type, the other half flowing to the target via the model plasma

region (Fig.1b). This outer boundary condition produced relatively flat radial density profiles in the SOL, so, although the average density simulates experimental results, details of density profiles do not. The temperature profiles are consistent with typical observations, however.

6 MODELLING WITH EDGE2D: RESULTS AND DISCUSSION

Total plasma flow to the targets, Γ_t , is tabulated below, with other flows of interest. The prescribed wall pumping removes up to 8% of the target flow, which is then re-injected as fuel. Pumping and fuelling has a predictably small effect on parameters in the SOL and divertor channel. At all three

	No fuelling			Top fuelling			OMP fuelling		
Albedo in divertor	100%			90%			90%		
Edge density/ 10^{19}m^{-3}	2.45	1.84	1.31	2.50	1.91	1.32	2.67	2.04	1.41
Flow to target, $\Gamma_t/10^{21}\text{s}^{-1}$	202	202	197	210	210	201	208	210	200
Fuel/pump flow/ 10^{21}s^{-1}	0	0	0	16.2	13.2	10.1	16.3	12.7	9.6
Flow into divertor/ 10^{21}s^{-1}	54.9	47.3	36.8	58.8	48.4	38.8	60.2	50.7	38.2

Edge plasma densities and global flows obtained in simulations of fuelling and pumping with EDGE2D/NIMBUS. densities, T_i is reduced (more so at the fuelling point) by $\sim 5\text{eV}$ at the separatrix, and T_e fell by 1 to 2eV (Fig.3a). Although impurities were not studied, the dip in T_i implies the thermal force on impurity ions is directed from the fuelling point towards the divertor. Frictional forces increase due to reduced T_i and to flow induced by fuelling. Mach number profiles (Fig.3b) show SOL fuelling moves the stagnation point in the SOL towards the fuelling point from its location with no fuel, and increases the gradient of M.

SOL fuelling had little influence on *separatrix* Mach number at the divertor entrance, radial profiles (Fig.4) showing strong flow ($M \approx 0.3$) into each divertor. The outer part of the profile shows a tendency to flow reversal, reduced by SOL fuelling. Detailed study shows flow reversal at/or near each divertor entrance, only in the outer part of the profile. SOL fuelling diminishes the flow reversal zone and increases plasma density away from the separatrix. Fuelled neutrals are attenuated within a few mm. Those surviving, having charge-exchanged, penetrate easily, especially at the outer mid-plane.

7. SUMMARY AND CONCLUSIONS

Changes in convection in the SOL, caused by gaseous fuelling, have been studied, both experimentally in the JET Mk I divertor, and with EDGE2D/NIMBUS. In Ohmic plasmas (2MA, 2.8T), divertor fuelling gave low $Z_{\text{effective}}$ with increased radiation intensity (D_α /bolometry) in the divertor. Fuelling in the main SOL gave higher $Z_{\text{effective}}$ but not bulk radiation, and decreased radiation in the divertor. The wall-pumping speed varied day by day by at least a factor of two. On a given day, $\phi_{\text{pump}} \sim N^{1.3}$, and $D_\alpha \sim N^2$ (or more). Despite extra fluxes with divertor fuelling, there was no increase in wall-pumping speed, suggesting that pumping may occur at the fuelling point. Preliminary measurements with a movable Langmuir probe show a thicker SOL with top fuelling, in qualitative agreement with EDGE2D. One aim of the experiment was to investigate the need for toroidally uniform fuelling. Preliminary results, though unclear, help to define a future investigation. The experiment described was part of a larger study, to include controlled pumping with a cryo-pump. When commissioned, it will be possible to test whether wall-pumping occurs at the fuelling point. With EDGE2D, a 90% albedo on the divertor side-plates pumped $\leq 8\%$ of the target plasma flow. Fuelling in the main SOL reduced T_i , with a minimum near the fuelling point. This suggests fuelling in the SOL might control impurities, via frictional and thermal forces. In contrast, increased impurity content was found in JET, using the Bremsstrahlung measurements, but not the bolometry. Impurities generated at the fuelling point might be implicated here, further work being needed. EDGE2D showed that fuelling alters profiles at the divertor throat, flow reversal regions being diminished if not removed. Although details may be model dependent, the sensitivity to fuelling procedure implies that a versatile fuelling system such as now installed in JET, is needed to optimise performance.

[1] R Simonini, G Corrigan, J Spence, A Taroni and G Vlases, 20th EPS, Lisbon, 26-30 July 1993.



FR9701784

VH Mode Accessibility and Global H-Mode Properties in Previous and Present JET Configurations

T T C Jones, S Ali-Arshad, M Bures, J P Christiansen,
H P L de Esch, G Fishpool, O N Jarvis, R König, K D Lawson,
P J Lomas, F B Marcus, R Sartori, B Schunke, P Smeulders,
D Stork, A Taroni, P R Thomas, K Thomsen.

JET Joint Undertaking, Abingdon, Oxon, OX14 3EA.



1. INTRODUCTION AND OVERVIEW

JET H-modes exhibit a considerable range of confinement enhancement. About 50 ELM free H-modes obtained in JET during 1991-2 were designated as VH modes, defined by the condition $\tau_E/\tau_{ITER-93HP} > 1.4$ where the ITER-93HP scaling is given by [1]. In JET VH modes, there is a distinct confinement transition following the cessation of ELMs [2], observed in a wide variety of tokamak operating conditions, using both NBI and ICRF heating methods. Important factors which influence VH mode accessibility such as magnetic configuration and vessel conditions have been identified. The new JET pumped divertor configuration has much improved plasma shaping control and power and particle exhaust capability and should permit exploitation of plasmas with VH confinement properties over an even wider range of operating regimes, particularly at high plasma current; first H-modes have been obtained in the 1994 JET operating period and initial results are reported.

2. GLOBAL CONFINEMENT

Fig.1 plots diamagnetic energy versus loss power for all VH modes in the old JET configuration up to 1992 at different I_p values. For comparison, H-mode data for $I_p \geq 3\text{MA}$ from the 1991-2 operating period are given in Fig.2. VH modes have not been obtained for $I_p > 3\text{MA}$; the best H-mode confinement above 3MA scales more weakly than linearly with I_p , and whilst the record stored energy of 12.7MJ is obtained in an ELM-free H-mode at 4MA with 22MW combined NBI+ICRF heating, the high-current H-modes do not qualify as VH due to the approximately linear I_p dependence of the ITER93-HP benchmark. A characteristic of the hot-ion VH-mode is near constant dW_{DIA}/dt maintained until the termination phase; the maximum attainable stored energy corresponds to a common limiting value of normalised toroidal β which is less than the Troyon limit [3]. At low B_T the VH termination therefore occurs sooner after the VH transition at a lower value of W_{DIA} and is a more gradual process than the more violent collapse from very high stored energies ($W_{DIA} > 12\text{MJ}$) observed at high B_T ('X-event' phenomenon).

3. OPERATION AND HEATING REGIMES FOR VH MODE ACCESS

I_p - B_T parameter space. The VH mode has been accessed in the range of plasma current $1 < I_p < 3\text{MA}$ and $1.9 < B_T < 3.3\text{T}$, corresponding to a wide range of safety factors in single and double null X-point plasmas in the old JET configuration. In the JET pumped divertor configuration the value of q_{cyl} at 4.5MA/3.4T would correspond approximately to the present low q limit for JET VH mode existence (3MA/1.9T).

Heating mix. VH confinement is observed under both NBI and ICRH heating, individually and in combination. The predominant ion versus electron heating effects of NBI and ICRH are evident in the VH dataset, demonstrating VH access over a wide range of T_i/T_e . A large variation in T_i in VH modes with NB heating is partly attributable to the range of electron densities in the dataset; for $P_{NBI}/\langle n_e \rangle > \approx 2.5 \times 10^{-19} \text{ MWm}^3$ the hot-ion regime is readily accessed; at the VH transition thermal transport in the ion channel is everywhere strongly reduced such that neither the

stored energy nor $T_i(0)$ saturate within the duration of the VH phase, but increase continuously at approximately constant plasma loss power [2].

4. FACTORS INFLUENCING H-MODE QUALITY AND VH MODE FORMATION

Vessel conditioning. Whilst the causal role of high edge bootstrap current density and ballooning mode stability on VH formation is not absolutely established, there does appear to be a link between factors influencing the former and VH mode access, e.g. low edge density and collisionality and high plasma purity. The historically earliest JET VH mode occurred in the 1988 operating period prior to the introduction of beryllium following a series of helium conditioning tokamak plasmas; the particular discharge (#15894) was one of a number of similar 3MA/2.8T H-modes at moderate NBI power (≈ 8 MW) but was distinguished from the others by lower Z_{eff} of the target plasma and lower edge n_e throughout the heating. These and other results, obtained particularly during an assessment of the reproducibility of the hot-ion scenario selected for the preliminary tritium experiment (PTE) [4], point to the primary importance of clean vessel conditions and low particle recycling for VH mode formation. Following a repetitive series of high power pulses of identical configuration in preparation for the PTE, one discharge with predominant ICRH formed a 'hot-electron' VH mode of long duration; low Z_{eff} of the target plasma and slow rate of n_e rise are particular features of this discharge whose time evolution is shown in Fig 3.

Magnetic configuration. During 1991 the top single-null X-pt (SNX) was established as the best high-performance plasma configuration to take most advantage of the CFC upper X-pt target tiles which were of an optimised power handling geometry. The toroidal field direction was usually chosen such that the ion ∇B drift was away from the target tiles in order to help equalise the in/out tile power loading. VH modes were also obtained in the up-down symmetric double-null X-pt (DNX) configuration which allowed better matching of the plasma shape to the RF antenna geometry. In particular, the VH confinement enhancement using ICRH alone at $I_p = 1$ MA led to high values of poloidal β with large bootstrap current fraction [5]. Large separation of the X-pt null from the tiles resulted in easier VH mode access and generally lower values of Z_{eff} during the heating (Fig.4) Difficult VH access in marginal X-pt configurations, including all experiments with $I_p > 3.0$ MA, is attributed to lack of screening of impurities generated at the X-pt target plates and increased penetration of recycled neutrals beyond the separatrix resulting in higher edge n_e .

5. FIRST H-MODE RESULTS IN THE JET PUMPED DIVERTOR CONFIGURATION

To date during 1994 up to 16 MW of NB heating has been applied at plasma currents in the range 1.5-4 MA in divertor configurations giving good clearance (> 5 cm) of the separatrix from all surfaces. ELMing H-modes of long duration (> 3.5 s) have been readily obtained, with confinement enhancement (so-called 'H-factor') relative to e.g. Goldston L-mode up to $H=2$. ELM-free periods occur at heating power sufficiently above a threshold level (which exhibits the usual B_T dependence [6]), but at the time of writing the duration of the ELM-free phase is limited to about 1.3 s. Time traces for a 2.5 MA/2.8 T, 16 MW H-mode discharge are given in Fig.5; in this case the target plasma density was pumped out by inner-wall limiter contact prior to heating in order to create a moderately peaked density profile and the hot-ion regime was established during the 0.5 s ELM-free phase. From their global confinement these transient hot-ion plasmas have not been classed as VH modes but more detailed confinement analysis is still required. The rate of density increase during the ELM free phase corresponds to 2-3 x beam fuelling, to be compared with near-correspondence to the beam fuelling observed in the best hot-ion VH modes previously. The ELM free phase is terminated by a sudden very large onset of H_α radiation, indicating the generation of a large amount of gas originating in the divertor but also seen at other remote locations, e.g. on Penning gauges in the NB ducts. These results suggest more intensive conditioning may be required in order to deplete the CFC target plates of bound gas in order to prolong the ELM-free phase. Data for a

4MA/3.4T, 12MW discharge are also shown (Fig.6); in this case the power margin above the threshold is smaller, but following a burst of ELMs an ELM-free period does then develop and lasts until the power is stepped down. Apart from a short duration burst of divertor CIII radiation which coincides with the spike observed on bolometers, there is no evidence of large impurity influxes to the bulk plasma during ELM-free or ELMy phases; measured target tile temperatures remained $< 1200^{\circ}\text{C}$ (no sweeping, 40MJ NBI input) and $< 850^{\circ}\text{C}$ (with sweeping, 90MJ NBI input).

6. CONCLUSIONS

The VH mode has been accessed over a wide range of previous JET operation and heating regimes, spanning a range of I_p and B_T which includes low q values corresponding to high plasma current operation up to $\approx 4.5\text{MA}$ in the JET pumped divertor configuration. There is evidence that maximum attained stored energy is dictated by a limiting value of normalised toroidal β . Therefore, opening up VH access at high plasma current ($I_p=5\text{MA}$, $B_T=3.4\text{T}$) should allow a factor ≈ 2 -fold increase in maximum attainable stored energy over existing best values proportional to $I_p B_T$, in both high density $T_i=T_e$ and hot-ion regimes, provided that favourable VH confinement current scaling is recovered above 3MA. See also [7]. This represents a major experimental goal and has important implications for future DT and α -particle heating experiments. Improved control of impurities and more favourable magnetic configurations with the pumped divertor are expected to overcome the limitations to VH access identified in the present work. Preliminary H-mode results have already been obtained.

References

- [1] D P Schissel *et al.*, Proc. 20th EPS Conf. on Controlled Fusion and Plasma Physics, (Lisbon, 1993) ECA 17c, p.103
- [2] V Parail *et al.*, this conference
- [3] P Smeulders *et al.*, this conference.
- [4] The JET Team, Nuclear Fusion, 32 (1992) p.187
- [5] C D Challis *et al.*, Nuclear Fusion, 33 (1993) p.1097
- [6] D F H Start *et al.*, this conference.
- [7] B Balet *et al.*, this conference

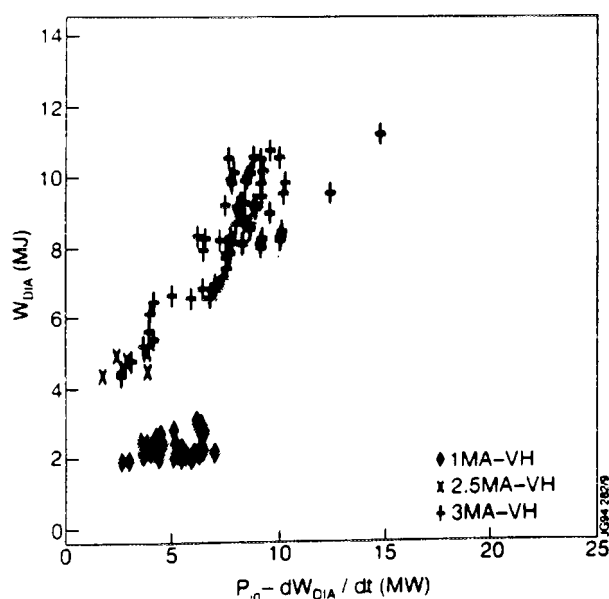


Fig. 1 Diamagnetic energy W_{DIA} versus $P_{in} - dW_{DIA}/dt$ for JET VH modes

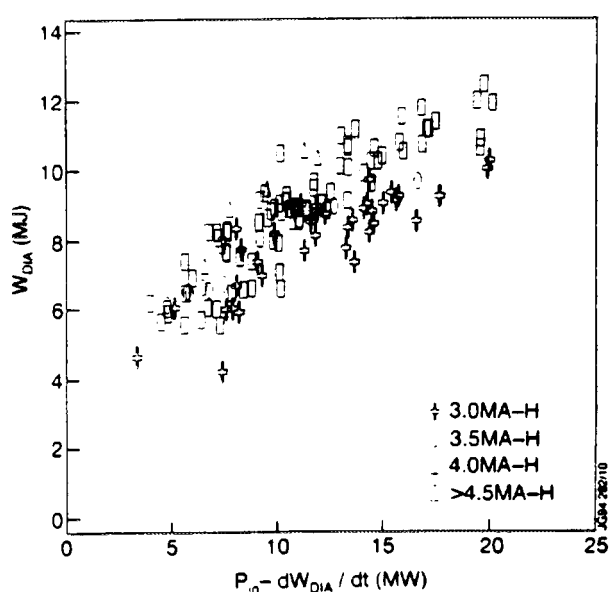


Fig. 2 Diamagnetic energy W_{DIA} versus $P_{in} - dW_{DIA}/dt$ for JET H modes in 1991-92

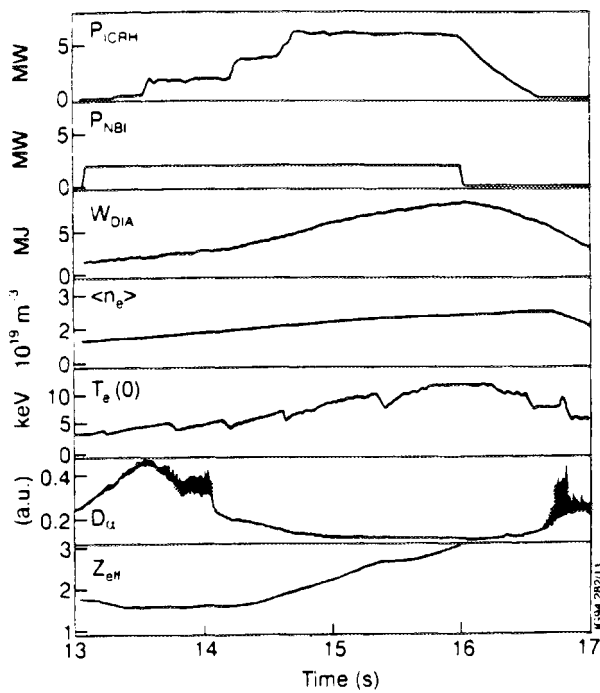


Fig.3 Plasma parameters for 'hot-electron' VH mode (#25990) with predominantly H-minority ICRH in a DNX configuration ($I_p = 3\text{MA}$, $B_T = 2.8\text{T}$) in a well-conditioned vessel following a long series of high-power NBI pulses in preparation for the JET PTE.

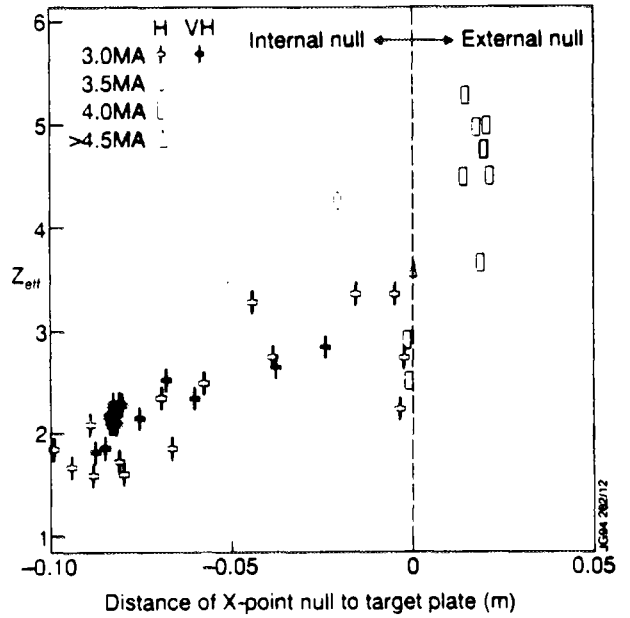


Fig.4 Z_{eff} values and X-pt to target distance different plasma currents for during ELM-free phase at the restricted range $3 < P_{\text{loss}}/n_e < 4$ (10^{-19} MWm^3)

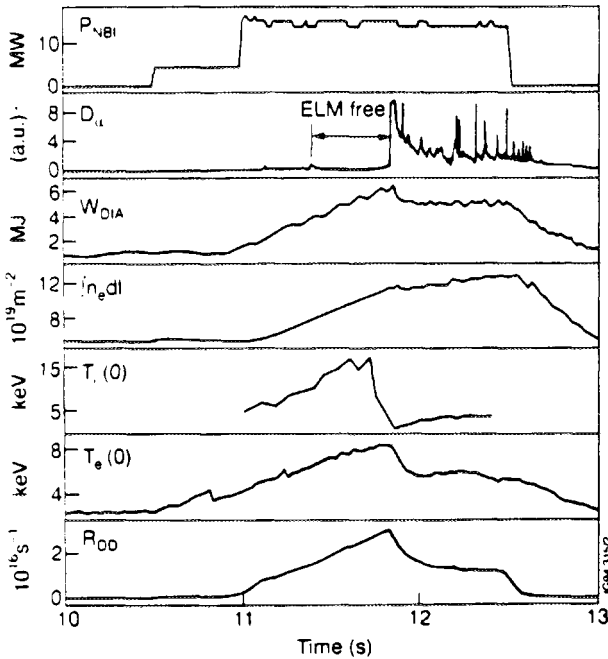


Fig.5 Time traces of measurements for hot-ion H-mode, pulse #30260 (2.5MA/2.8T) in the JET divertor configuration, with 0.5s ELM-free phase

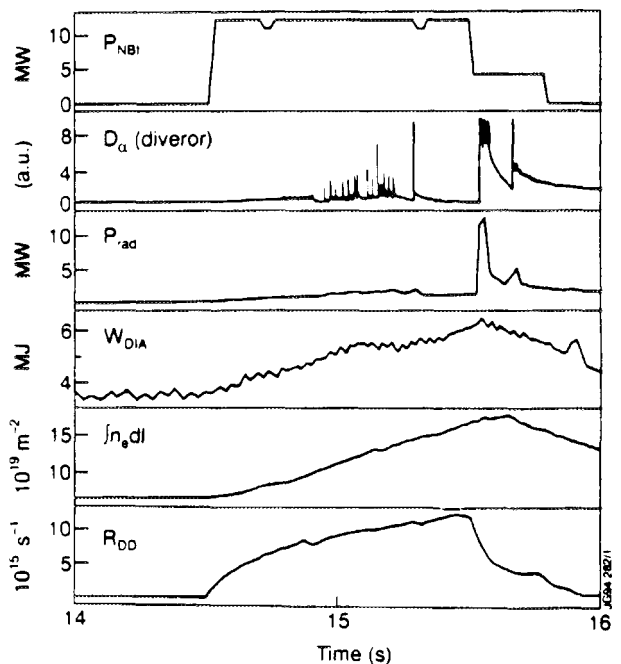


Fig.6 Time traces of measurements for H-mode pulse #30166 (4MA/3.4T) in the JET divertor configuration



FR9701785

Ion Cyclotron Emission by Spontaneous Emission

O Da Costa, D Grésillon¹.

JET Joint Undertaking, Abingdon, Oxon, OX14 3EA.

¹ Ecole Polytechnique, Lab PMI, Cedex, France.



1 introduction

Ion Cyclotron Emission (ICE) in the frequency range 10-350 MHz has been measured in different tokamaks for the last 10 years. It is detected using an ICRH antenna in reception mode or a probe. It is a good candidate for a fast ion, especially fusion α -particle, diagnostic similar to the Electron Cyclotron Emission (ECE). A common feature of the experimental ICE spectra in this frequency range is the narrow regularly spaced peaks. They are at the majority ions cyclotron frequency harmonics at the plasma outer edge. This last point represents a challenge to interpretative theories. These results were confirmed during JET's 1991 Preliminary Tritium Experiment (PTE)¹.

2 hypothesis and method

The goal of this study is to see whether the spontaneous emission can account for ICE experimental results, or part of them. We chose a straightforward approach to plasma emission, by investigating the near equilibrium wave radiation by gyrating ions, and thus building from the majority and fast fusion ions the plasma fluctuations and emission on the fast magnetoacoustic or compressional Alfvén wave mode in the IC frequency range. The plasma is assumed infinite and homogeneous.

The calculation proceeds from the electric current created by one gyrating test particle, a Fourier analysis from (\vec{r}, t) space to (\vec{k}, ω) space, the hot plasma dielectric tensor in a plane perpendicular to \vec{B} to express the electric field radiated in the fast magnetoacoustic mode by one particle, a statistic summation over all the ions using their specific distributions (Maxwellian distribution for the bulk deuterium and slowing-down distribution for the α -particles at the plasma centre) and a numerical resolution of the dispersion relation to find the frequencies solution for each wave number in the range where the mode is coupled with the Bernstein modes, and therefore the fast ions, through a finite Larmor radius effect.

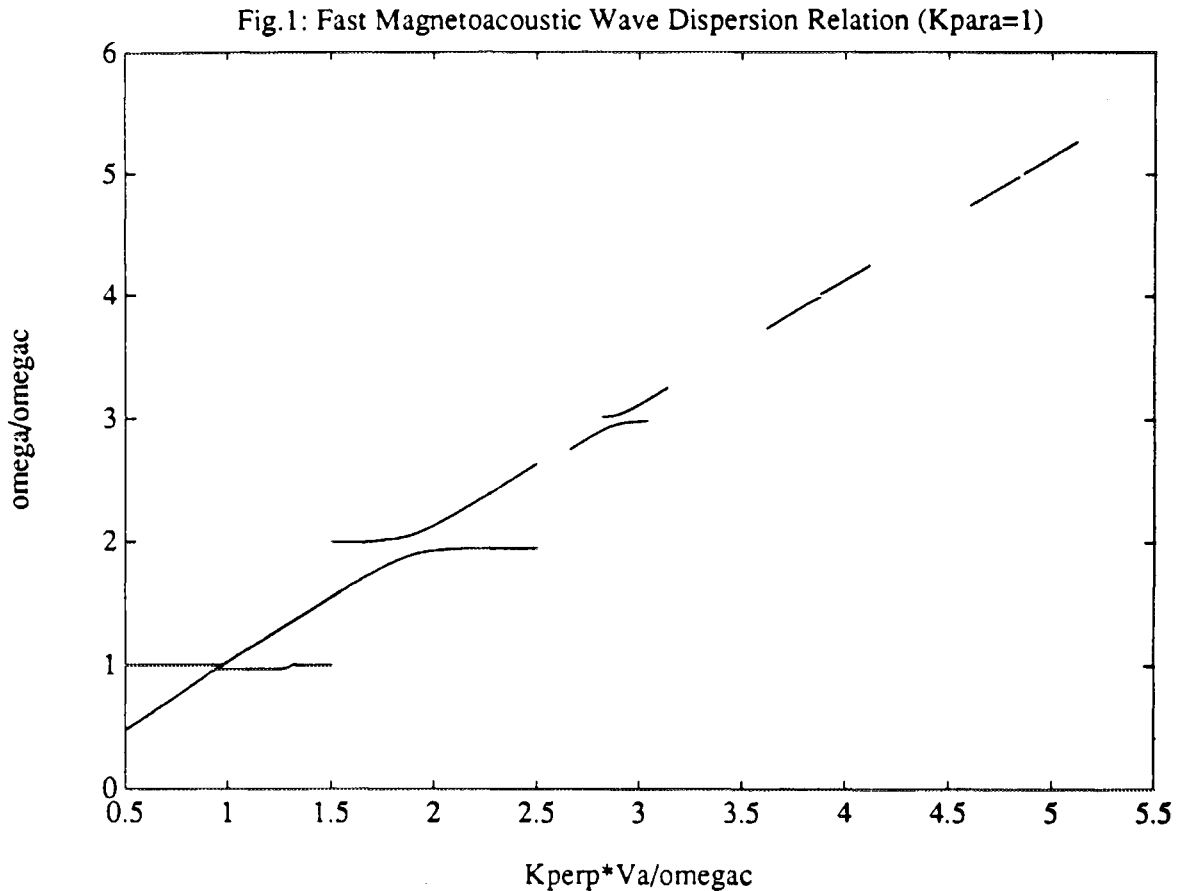
For each k_{\perp} and k_{\parallel} we calculate the solution ω of the dispersion relation and the temporal damping rate (imaginary part of ω for \vec{k} real), the wave electric and magnetic field, the plasma electromagnetic energy density for these modes, the power flux (Poynting vector) in each direction, the group velocity obtained from the dispersion relation slope and the spatial damping rate or damping length (imaginary part of \vec{k} for ω

real) obtained from the temporal damping rate and the group velocity. We integrate the electromagnetic energy density and the power flux for $\omega(k_{\perp})$ solution of the dispersion relation.

3 modelling results

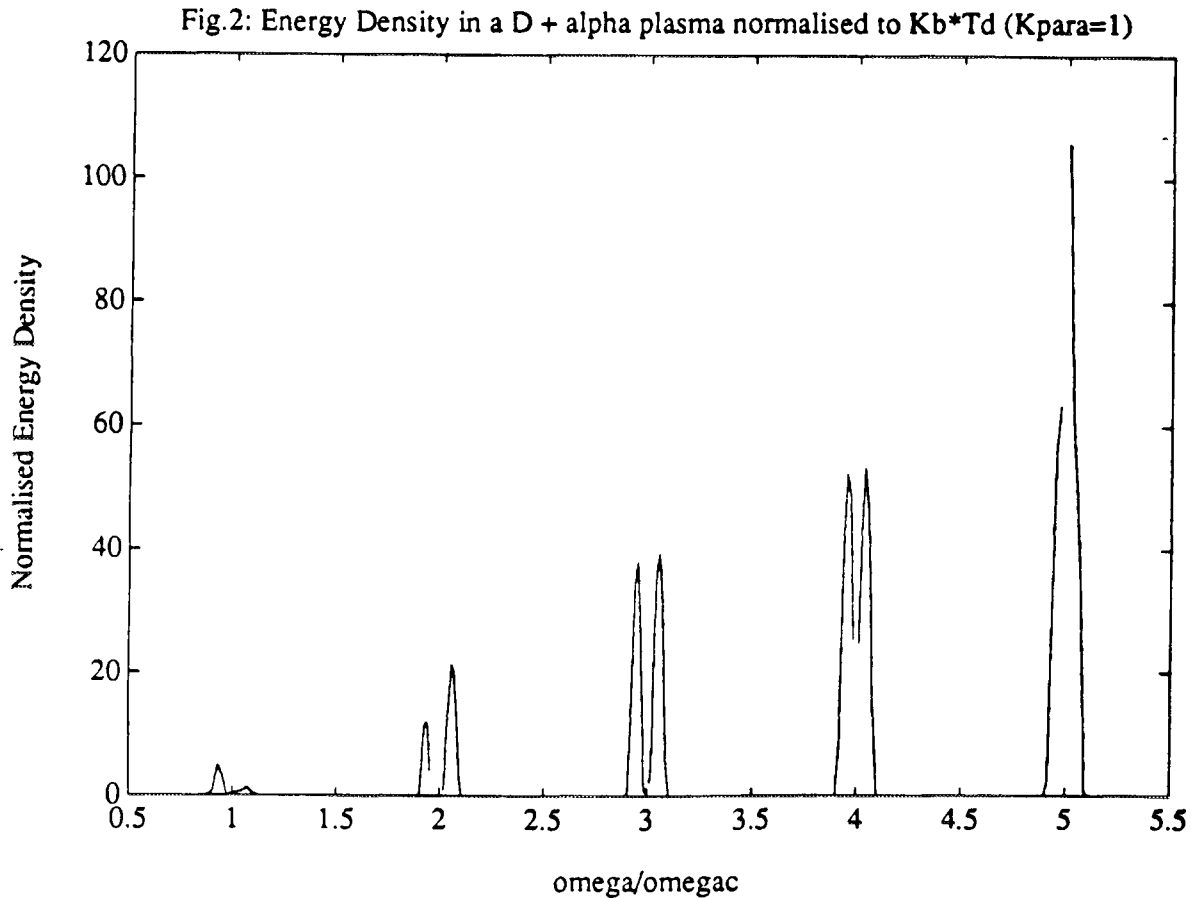
The numerical simulations are done with the plasma parameters at the plasma centre of JET's PTE discharge #26148². In particular the relative α -particle concentration to deuterium is $1.3 \cdot 10^{-3}$. The value of 1 m^{-1} for k_{\parallel} is taken for illustration.

Figure 1 displays the fast magnetoacoustic mode dispersion relation for the first five ion cyclotron harmonics. Between two harmonics, the mode is well approximated by the cold plasma mode, whose phase and group velocities are equal to the Alfvén velocity. At each harmonic it separates into two different branches, one below the harmonic frequency and one above. This represents the coupling with the ion Bernstein modes.



The emission spectra shape is similar to the energy density spectra shape. Figure 2 shows for illustration spectra of integrated energy density (integrated in respect to k_{\perp}) versus the normalised frequency in a deuterium + alpha plasma. The energy density is normalised to K_B (Boltzman constant) * T_D (deuterium temperature). These computed

spectra have a shape similar to the experimental emission spectra. The emission being created by the resonance between the fast ion $v_{//}$ and the wave parallel phase velocity, the splitting of the dispersion relation into two branches near each harmonic explains why the computed emission peaks are split into doublets. This double-line shape of the emission peaks is a well-known experimental feature¹.



In the presence of α -particles, the electromagnetic energy density level is much larger than $K_B * T_D$ and increases strongly with the harmonic. On the contrary in the case of a pure deuterium plasma, the electromagnetic energy density level of the dispersion relation two branches is close to the classical energy level in a thermal plasma ($K_B * T_D$) and stays constant with the harmonic. This is due to the larger α -particle Larmor radius.

The damping length or spatial decay is a very meaningful quantity. It represents physically the minimum spatial depth the plasma should have if it was to emit as a black body. In a pure deuterium plasma it is found to be very large compared to the emission layer width and to decrease with the harmonic. In a D + alpha plasma it is about 20 times smaller and decreases also with the harmonic.

Although the whole modelling is done for an infinite and homogenous plasma, we can apply some of the results to a tokamak plasma in the following simplified way. The

frequency width of the power flux peaks in a D + alpha plasma for $k_{//} = 1$ and $V_{\alpha\text{birth}} = 3.6 \text{ MeV}$ is $\Delta\omega = 0.04\omega_c$ (Fig.2), what is equivalent to a spatial width of the emission layer: $\frac{\Delta R}{R} = \frac{\Delta\omega_c}{\omega_c} = \frac{\Delta\omega}{\omega} \approx \frac{\Delta\omega}{n\omega_c} \approx \frac{0.04}{n}$, n harmonic number. As $R(\text{centre}) = 3\text{m}$. in JET, $\Delta R \approx \frac{0.12}{n} \text{m}$.. The emission of a ΔR width layer with a damping length D, $P_{\Delta R}$, is deduced from the black body level, P_B , in a ratio obtained from the Kirchhoff radiation law: $P_{\Delta R} = \left(1 - e^{-\frac{2\Delta R}{D}}\right) P_B$.

A pure deuterium plasma is therefore white in the IC frequency range, whereas a D + alpha plasma is white at the first harmonic and grey from the second to the fifth. We explain consequently why the ICE of a plasma without fast particles is very difficult to detect and why the fast ion emission increases strongly with the harmonic¹. The strong emission increase with the harmonic was also observed in a pure D plasma because of the H fusion fast ions. This explains also why the even-harmonic peaks are more intense¹ in both cases: H cyclotron frequency is twice as large as the D cyclotron frequency.

4 conclusion

The investigation of the fast magnetoacoustic mode spontaneous emission in fusion plasma shows significant similarities with the ICE experimental observations: the emission peaks at each ion cyclotron frequency harmonic, the large radiation temperature in the presence, even in a very small amount ($n \approx 10^{-3}$), of fast ions, the strong fast ion emission increase with the harmonic, the fine double-line splitting of each peak, the linear but not proportional increase of the peak width with the harmonic.

Further developments will include non-homogeneity effects, an estimation of the total power radiated in a tokamak and the consequence of the non-monotonic and anisotropic α -particle distribution at the edge.

5 references

- 1 G.A. Cottrell, O. Da Costa et al., 19th EPS Conference, Innsbruck, 1992; G.A. Cottrell, O. Da Costa et al., Nuclear Fusion, vol.33, n.9, 1993.
- 2 JET-Team, Nuclear Fusion, vol.32, n.2, 1992.
- 3 D.B. Melrose: 'Plasma Astrophysics', vol.1: 'The Emission, Absorption and Transfer of Waves in Plasmas', chap. 4, Gordon & Breach, 1980, presents a similar approach to ICE but for astrophysics plasma.

We acknowledge the help of P. Lamalle and D. Start in the preparation of this paper.



FR9701786

Analysis of JET LCHD/ICRH Synergy Experiments in Terms of Relativistic Current Drive Theory

D F H Start, Y Baranov, M Brusati, M Cox¹, A Di Vita²,
A Ekedahl, P Froissard, C Gardner¹, C Gormezano, J Jacquinet,
M R O'Brien¹, L Paquin, F G Rimini.

JET Joint Undertaking, Abingdon, Oxon, OX14 3EA.

¹ UKAEA Fusion, Culham, Abingdon, Oxfordshire, OX14 3DB, UK.

² Ansaldo Recherche, Ansaldo Spa, Genova, Italy.



INTRODUCTION. Synergetic effects between lower hybrid current drive (LHCD) and ion cyclotron resonance heating (ICRH) have led to substantially improved current drive efficiencies. Values of the usual figure of merit ($\gamma = IP^{-1}Rn_e$) as high as $0.4 \times 10^{20} \text{AW}^{-1} \text{m}^{-2}$ have been achieved in JET experiments [1]. So far the mechanism underlying the synergy has not been ascertained. Experimentally, it is clear from fast electron bremsstrahlung (FEB) data that the improved efficiency in full current drive cases (zero remanent electric field) is due to acceleration of the electron tail to MeV energies, well beyond the 200keV achieved by the LHCD alone. The tail temperature increases rapidly as γ increases and reaches 0.8MeV for $\gamma = 0.4 \times 10^{20} \text{AW}^{-1} \text{m}^{-2}$. In the light of these observations, a question which arises naturally is whether the improved figure of merit agrees quantitatively with the relativistic efficiencies derived from classical theory by Karney and Fisch [2]. In the present paper we give an analysis which demonstrates that this is indeed the case, regardless of the nature of the mechanism responsible for the synergy.

METHOD OF ANALYSIS. The radial profile of the photon temperature obtained from Abel inversion of the FEB data is shown in fig. 1 for pulse 24966 into which was injected 2.4MW of LHCD power and 3.2MW of ICRH power. At the position of the ICRH resonance the photon temperature reaches 120keV. The photon distribution is modelled assuming a fast electron distribution of the form:

$$f_{\text{fast}} = C(r) \cdot \exp(-p_{\parallel}^2 / 2T_{\parallel} - p_{\perp}^2 / 2T_{\perp}) \text{ for } p_{\parallel} > 0.$$

This fit gives combinations of T_{\parallel} and T_{\perp} but is most sensitive to T_{\parallel} [3]. The average value of the perpendicular temperature is obtained by fitting the non-thermal, downshifted second harmonic peak in the electron cyclotron emission (ECE) spectrum [3]. In the case of shot 24966, $\langle T_{\perp} \rangle$ was found to be 80keV and T_{\parallel} varied from a peak value of 1.3MeV to 600keV near the plasma boundary. The above distribution is used to calculate the current density profile, $J(r)$, which, when normalised to the experimental $J(r)$ profile yields the function $C(r)$. In this way the radial profile of the distribution function of the current carrying fast electrons is determined and is used in conjunction with the narrow spectrum current drive efficiencies of Karney and Fisch to calculate the absorbed power density profile. This profile is integrated to give the total power absorbed and hence a value γ for comparison with experiment. In addition, by integrating over the electron distribution above the LHCD maximum energy the power required of the fast wave to produce the synergy is estimated. A flow chart of the analysis is given in fig.2.

RESULTS. Comparison with experiment is made using the figure of merit γ , the predicted value of which is obtained from the ratio of the plasma current (full current drive) and the calculated total power absorbed. The comparison is shown in fig.3 where experimental and calculated values of γ are plotted against $\langle T_{//} \rangle$. The efficiencies are normalised to $Z_{\text{eff}}=1$ using the factor $(Z+5)/6$. Two theoretical curves are presented, one with no fast electrons flowing in the backward direction and the other with a distribution having $T_{//B}=20\text{keV}$ and a normalisation constant $C(r)$ equal to that of the forward flowing distribution. This latter effect reduces the predicted efficiency by about 10%. The experimental values are all taken from shots which have full current drive, so that electric field acceleration can be neglected, and are in good agreement with classical collision theory.

The power absorbed by all electrons above a specified minimum energy has also been obtained and is shown in fig.4 for pulse 24966. The calculated total power absorption of 2.7MW by the fast electrons agrees well with that derived from modulation experiments, namely 1.9MW of LHCD power (80% of the input of 2.4MW, see ref 4) plus 0.6MW directly damped on the high energy electrons from the fast wave. With $T_{//B}=20\text{keV}$ the predicted power increases to 2.9MW. Taking account of an approximate estimate of the bootstrap current for shot 24966 reduces the calculated power to 2.5MW. The power required to sustain the tail beyond the maximum energy ($\sim 230\text{keV}$, ref.4) created by LHCD alone is found to be 0.83MW which is 30% higher than the measured 0.6MW absorbed directly from the fast wave.

The efficiency tends to saturate (fig.3) at a value of γ around $0.5 \times 10^{20}\text{AW}^{-1}\text{m}^{-2}$ as the electron mass increases. This is less than the limit of the narrow spectrum efficiency which reaches $\gamma=1 \times 10^{20}\text{AW}^{-1}\text{m}^{-2}$ at 700keV energy. The difference arises from the fact that most of the power is absorbed by electrons with energy below the tail temperature due to their greater numbers and higher collision frequency. Experimentally an improvement in γ requires either higher T_e or a flatter electron distribution function, akin to that developed by LHCD, which might be attained with a narrower spectrum and more power coupled from the ICRF.

Note also that the fast wave power with $N_{//}$ between 1 and 1.5 (resonant with electrons above 200 keV) is only 6% of the total power. This is much less than the predicted 0.8 MW absorbed by electrons above the LHCD maximum energy which constitutes 26% of the ICRH power. A resolution of this difficulty might lie in the poloidal field effect on $N_{//}$. A change in the field angle of only 3° can give rise to $\Delta N_{//} = \pm 1$ and within this range there is 23% of the fast wave power.

PROFILE CONTROL WITH SYNERGY. The JET experiments have shown that the minority resonance, or the ion-ion hybrid resonance, needs to be close to the source of fast electrons. If the fast electrons diffuse significantly whilst slowing down, it might be possible to move the current density profile away from the LH power deposition by employing more than one minority resonance. To show this effect we have used a 3D Fokker-Planck code (BANDIT) with two velocity variables a radial space coordinate. The lower hybrid power deposition was obtained using a model operator resonating with electrons between 50 keV and 250keV. The fast wave absorption was modelled using a Landau damping operator accelerating electrons between 100keV and 400keV. The fast wave operator was located at the cyclotron resonance layer with a radial width of 0.1m. The value of the RF diffusion coefficient was chosen to give typical synergy parameters, namely a γ of $0.4\text{AW}^{-1}\text{m}^{-2}$ and

about equal LHCD and fast wave power absorption as shown in fig.5. The fast electrons with energies above twice the thermal velocity v_e were assumed to spatially diffuse with a coefficient varying as $D(\text{m}^2/\text{s}) = 0.5v_{||}/v_e$. For a single ICRF resonance close to the LHCD absorption peak, the current density peaks at the power density maximum and the fast electron diffusion creates $0.2\text{MA}/\text{m}^2$ central current density (fig.5). Adding two additional ICRF resonances on the inside, to accelerate the diffused electron tail, produces a two fold increase of the central current density relative to the maximum (fig.6). Thus depending on the degree of fast electron diffusion there is some scope for changing the current density profile, and especially the central current density, using multiple minority resonances.

SUMMARY. The present analysis shows that the observed efficiency of current drive with synergy between LHCD and ICRH is in good agreement with the relativistic theory of Karney and Fisch for Landau damped waves. The predicted power absorption from the fast wave by the electron tail is within 30% of the measured value. In the presence of significant fast electron diffusion within a slowing down time it would be possible to produce central current drive using multiple ICRF resonances even when the LHCD deposition is at half radius, as in an ITER type device.

REFERENCES

1. C Gormezano et al. Proc. of 10th Topical Conf. on Radio Frequency Power in Plasmas, Boston 1993.
2. C F F Karney and N J Fisch, Physics of Fluids, 28 (1985) 120.
3. M Brusati et al. Nuclear Fusion 34 (1994) 23.
4. Y Baranov et al, 20th EPS Conf. on Contr. Fusion and Plasma Physics, Lisbon, 881 (1993).

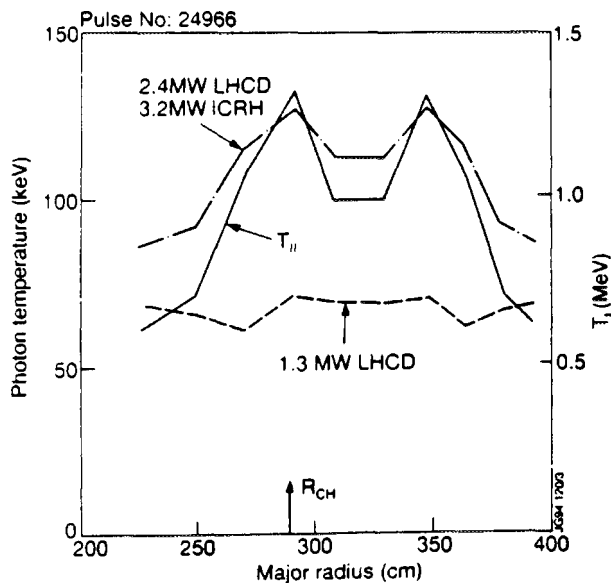


Fig. 1: Photon and fast electron temperatures.

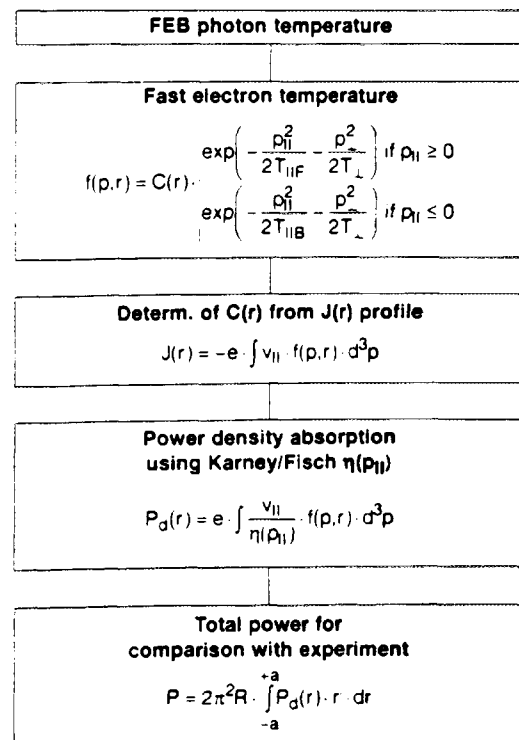


Fig.2: Analysis flow chart

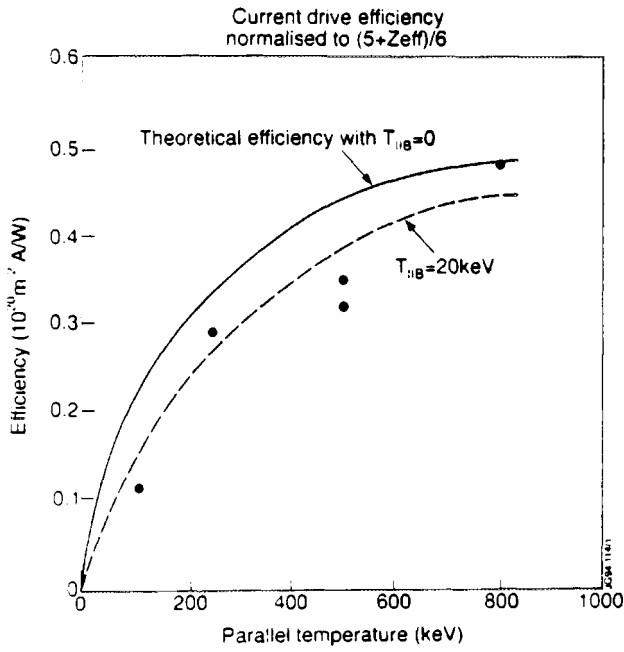


Fig.3: Comparison of experimental and predicted efficiencies for given full current drive experiments and for average tail temperatures up to 800 keV.

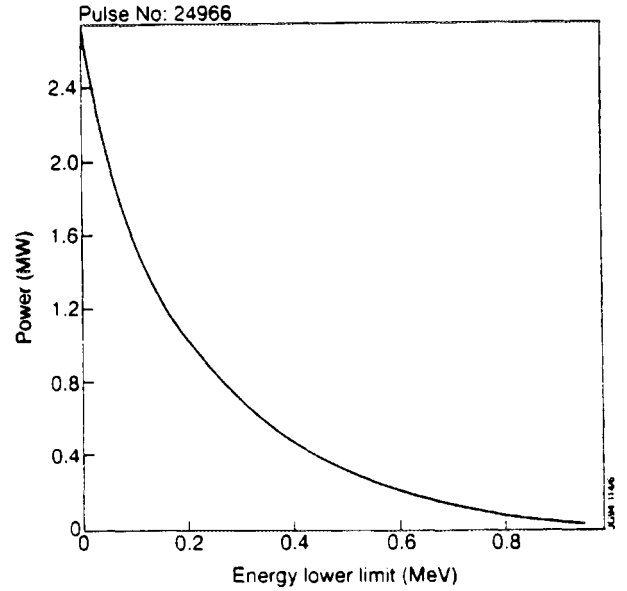


Fig.4: Power damped on electrons above a minimum energy

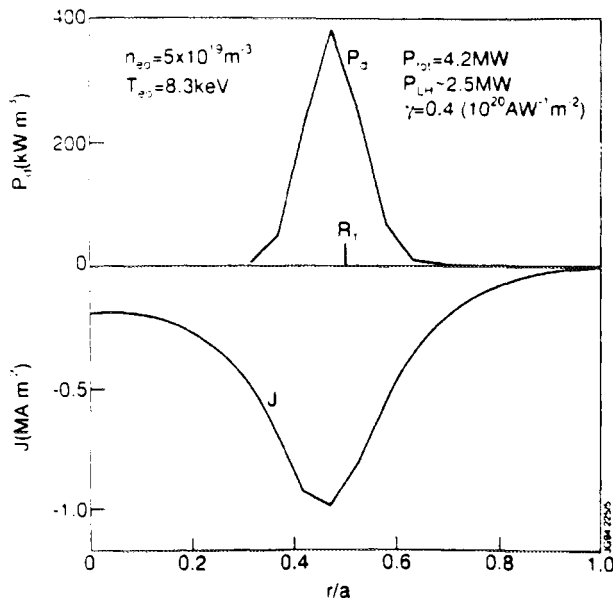


Fig.5: Simulations of synergism with electron diffusion present

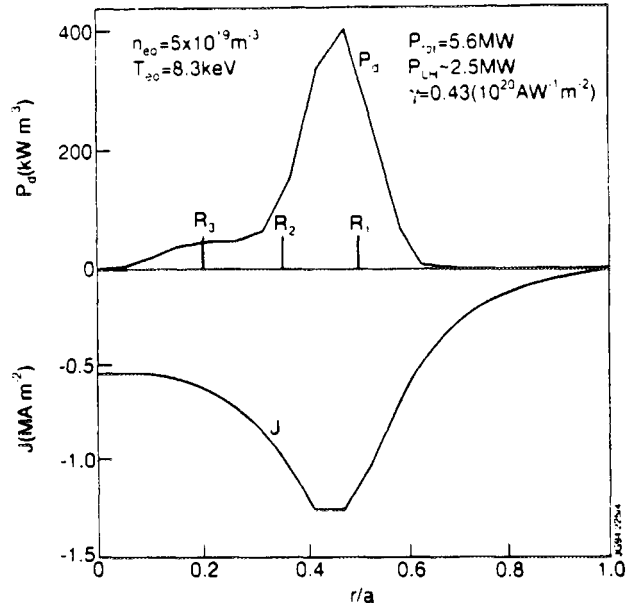


Fig.6: Enhancement of the central current density using three minority resonances.



Correlations between Locked Modes and Impurity Influxes

K D Lawson¹, G M Fishpool.

JET Joint Undertaking, Abingdon, Oxon, OX14 3EA.

¹ Culham Laboratory, UKAEA/Euratom Fusion Association,
Abingdon, Oxfordshire, OX14 3DB, UK.



Abstract

An analysis of pulses that were disturbed by medium Z impurity influxes (Cl, Cr, Fe and Ni) recorded during the 1991/92 JET operations has demonstrated that such influxes can result in MHD modes which subsequently 'lock'. A correlation is found between the power radiated by the influx and the time difference between the start of the influx and the beginning of the locked mode. The growth in the amplitude of the locked mode itself can lead to further impurity influxes. A correlation is noted between intense influxes ($P_{\text{rad}} \geq 10\text{MW}$) and the mode 'unlocking' and beginning to rotate more rapidly.

1. Introduction

During past JET operations a correlation has been noted between impurity influxes and poor plasma performance. In the worst cases the plasma terminates in a disruption, this usually being a consequence of a rotating MHD mode which has slowed and 'locked' (Snipes *et al.*, 1988). The high performance operation of JET in the 1994 campaign and the consequent need for disruption avoidance makes a study of the connection between impurity influxes and MHD activity topical. The metallic influxes observed during the 1991/92 JET operations enable such an investigation to be carried out. In this study, the emphasis has been on influxes of medium Z impurities, such as Cl and the metals Cr, Fe and Ni. A comparison is also made with those due to the low Z impurities Be and C. Preliminary results of this analysis are presented.

2. Experimental measurements

The diagnostic technique which most directly enables the magnitude of the influx to be quantified is the bolometric measurement of the total radiated power. This is determined from an array of bolometers with 14 vertical lines-of-sight (Mast and Krause, 1985). The system has a time resolution of 20ms. The impurity responsible for the influx is found from VUV and XUV spectroscopic signals, the respective instruments being described by Fonck *et al.* (1982) and by Schwob *et al.* (1987). The temporal resolution varies between 30 and 200ms.

The magnetic diagnostics include arrays of tangential, B_{θ} field pickup coils, which are situated inside the vessel, and normal field saddle loops. Combinations of signals from different coils give measures of the rate of change of the $n=1, 2$ and 3 tangential field and the amplitude and phase of a locked mode is derived from the external saddle coils. The magnetic

data used in the study are processed data in which the rms of the raw signal is taken. Although the frequency response of the tangential field coils is typically 10kHz, the time interval between the processed data points is 6 to 8ms and 8 to 24ms for the locked mode signal.

3. Results

a) Impurity influxes causing locked modes. Examples have been found where there is a clear correlation between an influx and a locked mode. It is observed that 90-400ms after the beginning of the influx there is an increase in MHD activity. After a further 10-70ms the locked mode indicator external to the vessel responds. This is illustrated in figure 1, which uses pulse 25730 as an example. A 2.7MW influx of Ni and Cr, whose original source is most likely the inconel of the vessel walls, occurs at 3.34s, during the current ramp. MHD activity begins 90ms later and the rotating mode locks within a further 10ms, before further influxes occur. In this case the plasma disrupts 0.4s later.

Both the excess energy radiated between the start of the influx and the beginning of the locked mode and the peak radiated power have been used to measure the magnitude of the influx. The larger the influx, the greater the perturbation is expected to be and the quicker the onset of the locked mode. The peak radiated power, shown in figure 2 as a function of the time interval between the influx and the beginning of the locked mode, shows this behaviour and is therefore taken as the measure of the influx size. This emphasizes the importance of the influx duration, a short influx causing a greater perturbation than a smaller, longer influx of a comparable energy. The existence of a correlation between peak power and delay time confirms that the influxes cause the locked modes.

A possible Z dependence is suggested by figure 3. Pulses exhibiting the longest delay times have influxes which are predominately due to Cl. Further evidence comes from a comparison of similar pulses such as pulses 25675 and 25676. The former has a 6.5MW influx due to the low Z elements Be and C, the latter a smaller, 4.7MW influx due to Ni and Cl. Of the two, it is the latter that subsequently develops a locked mode. No dependence on plasma current, safety factor or T_e is evident from this limited database, although a dependence on n_e would be consistent with the data. Those pulses with a higher n_e tend to have longer delay times.

b) Correlation between influxes and mode 'unlocking'. In the pulses studied, it is often seen that further influxes coincide with the growth of the locked mode amplitude. They can give rise to high radiated powers, ~tens of MW, and are usually short-lived, ≤ 40 ms. This correlation can be clearly seen in pulse 25695, figure 3. A series of 7 influxes, radiating ~4 to 15MW of power and due to Ni, Fe and Cl, result from the repetitive growth of the locked mode.

In some cases, a correlation is observed between the impurity influx and the mode 'unlocking' and rotating more rapidly. The signal indicating the locked mode amplitude falls and the tangential field indicator of rotating $n=1, 2$ and 3 MHD activity rises sharply. This correlation

is evident in the repetitive locking and unlocking observed in pulse 25695 and can be seen in figure 4, pulse 25666. In the latter, a sharp rise in the locked mode amplitude precedes its reduction. Despite the rapid sequence of events, there is evidence, in a few cases, that the influx begins before the mode unlocks or the tangential field indicator of $n=1$ activity responds.

4. Discussion

The influx preceding any observable MHD activity and the relationship found between the magnitude of the influx and the time before the onset of the locked mode suggests that the growth of the mode is a result of the influx. It is of interest that the magnitude is best represented by the peak radiated power rather than by the radiated energy. Its use emphasises the importance of the short timescale of the influx that most readily causes a sustained MHD perturbation. The number of medium Z particles involved in influxes which radiate $\leq 5\text{MW}$ of power is comparatively small, typically $\leq 10^{-5}$ to 5×10^{-4} of n_e . Consequently, it is not expected that such influxes would have a significant effect on the plasma Z_{eff} . Rather, the changes are more likely to involve increases in the plasma resistivity due to cooling by the intense radiation. The disturbance created by the influx will have most effect, if it occurs on a timescale faster than that of a heat pulse into the disturbed region, $\sim 10\text{ms}$, any flow of heat tending to ameliorate the disturbance. A further consequence of this short timescale is that the disturbance which causes the locked mode must occur chiefly in the edge region of the plasma, since an influx of particles requires from 100 to 200ms to penetrate to the plasma core. If it is confirmed that the intense impurity influx does precede the mode unlocking, a possible explanation is that the influx results in a minor disruption, following which the mode amplitude is reduced, leading to the unlocking of the mode. The observed rise in the plasma current would be consistent with this interpretation.

5. Conclusions

A study has been made of the relationship between medium Z impurity influxes and MHD activity in JET, which demonstrates that influxes can cause locked modes. It is found that the magnitude of the influx is best described by its peak radiated power, rather than by its radiated energy, the higher the peak radiated power, the sooner the onset of the locked mode. A growth in the locked mode amplitude can itself result in further impurity influxes. Intense influxes are seen to correlate with the 'unlocking' of the mode.

References

- Fonck R J *et al.*, 1982, *Appl. Opt.* **21**, 2115
- Mast K F and Krause H, 1985, *Rev. Sci. Instrum.* **56**, 969
- Schwob J L *et al.*, 1987, *Rev. Sci. Instrum.*, **58**, 1601
- Snipes J A *et al.*, 1988, *Nucl. Fusion*, **28**, 1085

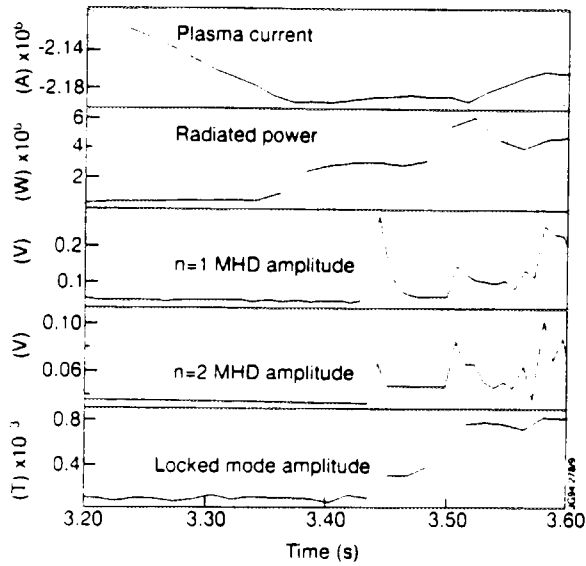


Figure 1. The typical effect of an impurity influx on MHD activity as seen in pulse 25730

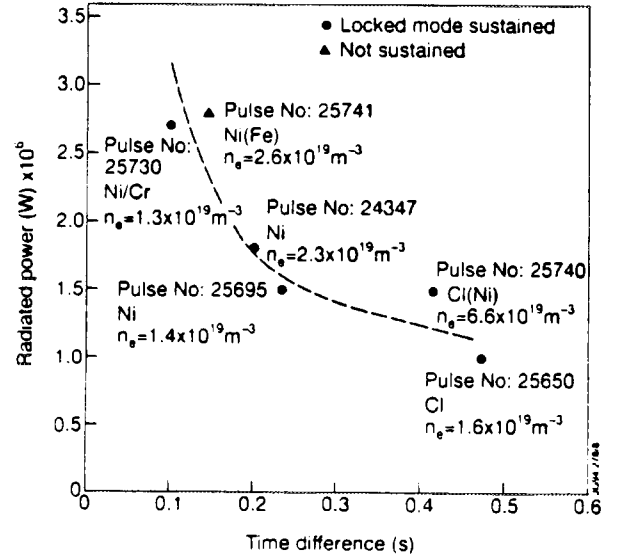


Figure 2. Power radiated by an impurity influx against the time difference between the start of the influx and the beginning of the locked mode

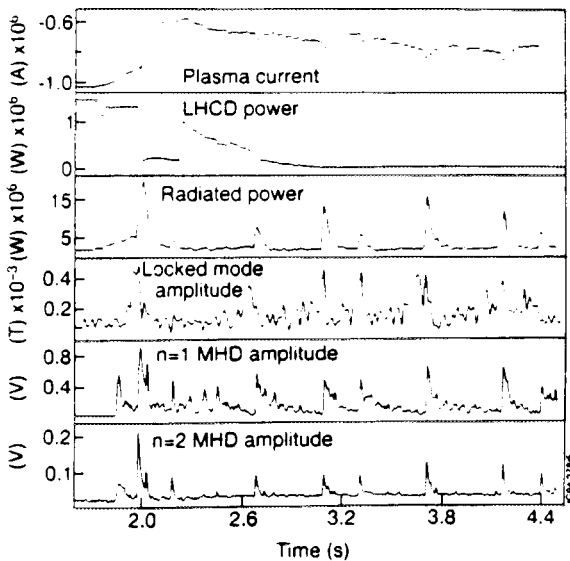


Figure 3. The correlation between the growth in the locked mode amplitude and impurity influxes seen in pulse 25695

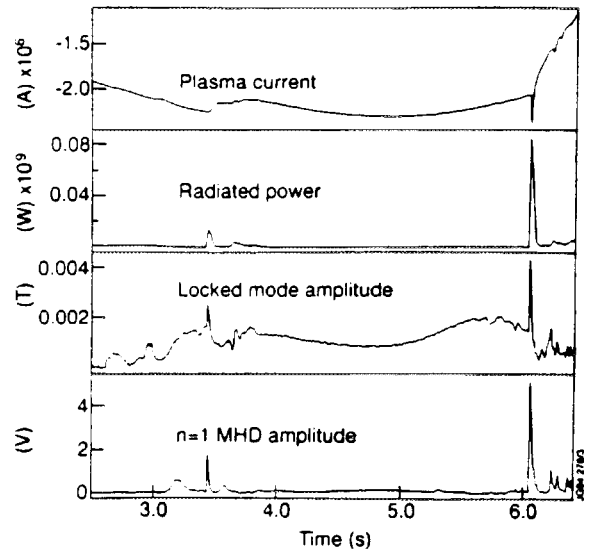


Figure 4. Correlation between impurity influxes and the reduction in the locked mode amplitude in pulse 25666



FR9701788

An Analysis of JET Fast-Wave Heating and Current Drive Experiments Directly Related to ITER

V P Bhatnagar, L Eriksson, C Gormezano, J Jacquinet,
A Kaye, D F H Start.

JET Joint Undertaking, Abingdon, Oxon, OX14 3EA.



1. INTRODUCTION. The ITER fast-wave system is required to serve a variety of purposes, in particular, plasma heating to ignition, current profile and burn control and eventually, in conjunction with other schemes, a central non-inductive current drive (CD) for the steady-state operation of ITER. We analyse, in terms of dimensionless parameters, the ICRF heating and current drive data that has been obtained in JET with a view to ascertaining its direct relevance to key ITER requirements. The analysis is then used to identify areas both in physics and technological aspects of ion-cyclotron resonance heating (ICRH) and CD that require further experimentation in ITER-relevant devices such as JET to establish the required data base.

2. PLASMA HEATING. Heating to ignition is a direct extrapolation from the JET high power (22 MW) minority ICRF heating [1] including that of the high minority ($n_H/n_{He3} \leq 1$) heating [2] experiments reported earlier. Also, a 2 MA (magnetically) steady-state discharge lasting 60 s and heated by ICRH at a level of 3 MW for the entire duration of the discharge has been produced [3]. Deuterium fundamental and tritium second harmonic heating scenarios, proposed for ITER, are also scheduled to be carried out later in the D-T phase of JET.

3. MINORITY-ION CURRENT DRIVE AND BURN CONTROL. With a view to burn control, the stabilization or destabilization of sawteeth due to magnetic shear control at the $q=1$ surface has been obtained by minority ion current drive [4,5] in JET. This behaviour results in a change in the DD reactivity of up to 60% in JET. A model calculation predicts that by changing the sawtooth period from 3 s to 0.2 s in ITER-EDA like plasmas, the D-T reactivity could be reduced by a factor of 0.75 [6]. In this preliminary calculation, the dynamic behaviour of burn control (delayed response-time due to current diffusion) has not yet been evaluated.

4. ELECTRON-TTMP CURRENT DRIVE. The scenario predicted to be the most effective for electron transit-time magnetic pumping (e-TTMP) current drive by fast waves in ITER is at a frequency (22 MHz) that lies below all ion resonances [1] so as to avoid strong ion damping. In this domain, the experimental data base is scant principally due to low β_e (ratio of kinetic to magnetic pressure) and relatively small plasma size and hence weak damping in present day devices. We note that for good current drive efficiency ($\bar{\eta}$), one should operate at normalized speed $\xi \equiv v_p/v_e \geq 2$ to avoid deleterious effects of electron trapping [7] (see Fig. 1), but optimum damping occurs at $\xi = 1/\sqrt{2}$ (see Fig. 2). This eventually reflects in lower CD efficiency. The electron damping of the fast wave can be represented as [8],

$$\frac{k_{i\perp}}{|k_{\perp}|} = \frac{\sqrt{\pi}}{4} \beta_e \xi e^{-\xi^2}$$

where k_{\perp} is the wave vector perpendicular to the magnetic field, $k_{i\perp}$ is the imaginary part of k_{\perp} and $\beta_e \equiv 2\mu_0 n_e T_e / B^2$ where μ_0 is the vacuum permeability. A contour plot of the right hand side of the above equation in a (β_e, ξ) -plane is plotted in Fig. 2. It is clear that the absorption increases linearly with β_e and it is optimum at $\xi = 1/\sqrt{2}$. Using ray tracing [9], we calculate single pass absorption (SPA) of fast waves by electrons launched from an antenna located on the low-field side in which the tokamak geometry, profiles and the effect of poloidal field

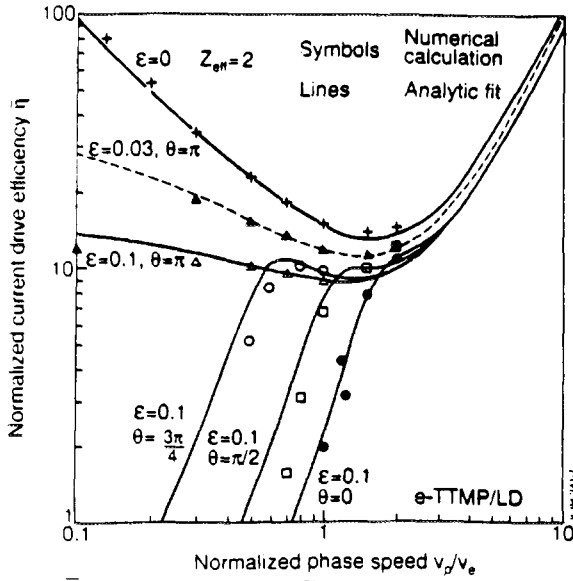


FIG. 1. $\bar{\eta}$ vs v_p/v_e for several poloidal angles (θ) and inverse aspect ratio (ϵ). v_e is the electron thermal speed and $v_p = \omega/k_{||}$. Courtesy Ref. 7.

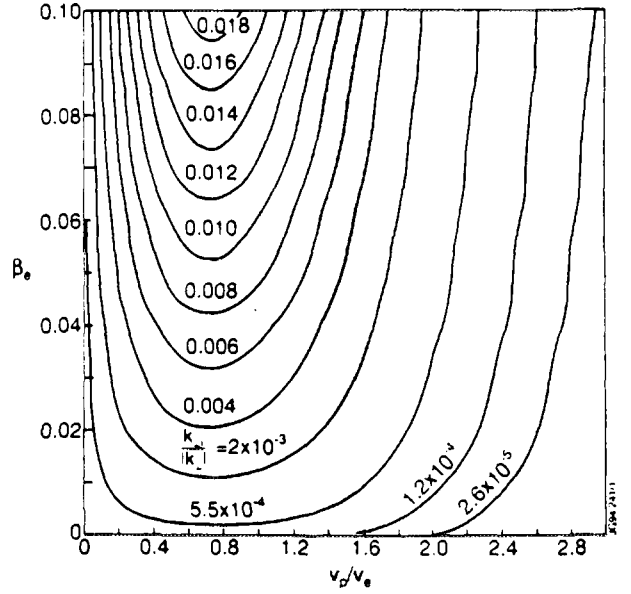


FIG. 2. Contours representing fast-wave e-TTMP/e-Landau dampings ($k_{\perp||}/|k_{\perp}|$) in $(\beta_e, v_p/v_e)$ -plane.

are fully taken into account. An aspect ratio of 3.2 in the present divertor phase of JET allows us to exclude H and D ion resonances from the plasma (33 MHz at 3 T without introducing He3) for an operation of ITER-relevant e-TTMP current drive scheme in JET in deuterium plasmas. In Fig. 3, we plot the e-SPA as a function of the toroidal field (B_t) for two values of central electron temperature (T_{e0}). To exclude the ion resonances, the ratio of frequency to B_t is maintained constant. As expected, the e-SPA decreases as B_t^2 . The same data is plotted as a function β_e in Fig. 4 and shows a linear dependence on β_e . A minimum value of SPA of about 10% appears to be necessary from other experiments (Tore Supra and DIII-D) for significant electron heating. These calculations show that at 3 T in JET, the e-SPA is poor. An operation at 2.55 T (28.3 MHz) and $T_{e0} = 10\text{keV}$ would lead to an e-SPA of about 12%. Operation at a still lower B_t would be better but then the frequency goes out of the band of the JET ICRF plant which was initially designed for heating rather than the electron current drive scheme.

We now present the e-SPA results in Fig. 5 for ITER where the operating frequency ($f = 22$ MHz) for electron current drive at a given $B_t = 6\text{T}$ is chosen to exclude all ion resonances from the device. These results are an average of three rays (at $\theta = -20, 0, 20^\circ$; covering the poloidal extent of the antenna) launched from the low-field side of the tokamak. This permits us to take account of the variation of $k_{||}$ due to poloidal field in single pass calculations more correctly. The single pass damping decreases as v_p/v_e increases in the range of v_p/v_e shown. Finally, we note that e-SPA depends on β_e , v_p/v_e and plasma diameter.

In Fig. 6, we present results of normalised current drive efficiency factor ($\gamma_{CD} = \langle n_e \rangle RI/P \propto T_e \bar{\eta}$) for e-TTMP current drive in JET and ITER. These results are calculated using multiple-bounce multi-ray trajectories and using CD efficiencies from Fig. 1 for ITER-EDA and JET parameters. Here, I is the current driven, P the RF power, R the major radius and $\langle n_e \rangle$ the average electron density. The higher γ_{CD} values in ITER as compared to JET are principally due to higher T_{e0} and higher antenna directivity in ITER. The model assumes no loss of power on a ray reflection on the cutoff at the plasma edge which may be questionable for very weak SPA cases.

5. ICRF FAST-WAVE TECHNOLOGY. We note that on the technology side, the basic ITER ICRF system (20-60 MHz) does not need to be very different from that of the present JET system ($f = 23\text{-}57$ MHz and $P_{\text{GEN}} = 32$ MW). To take advantage of the different

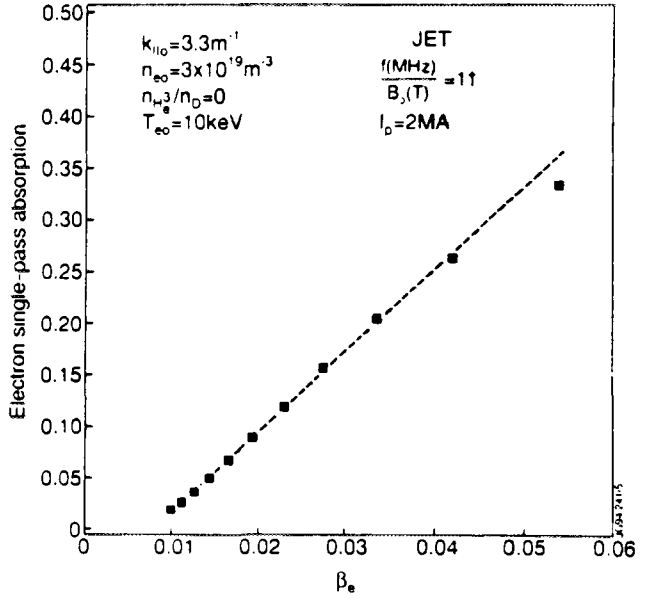
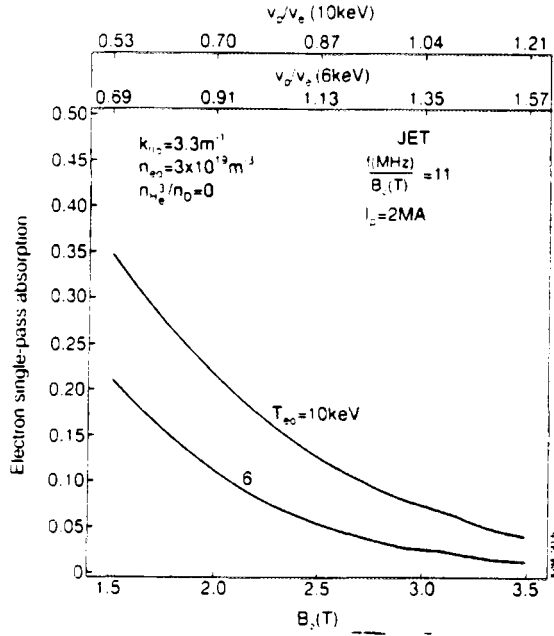


FIG. 3. e -SPA vs B_0 in JET when frequency is varied to exclude H and D resonances from the plasma. FIG. 4. Single-pass electron absorption vs β_e for the case of Fig. 3 at $T_{e0} = 10$ keV.

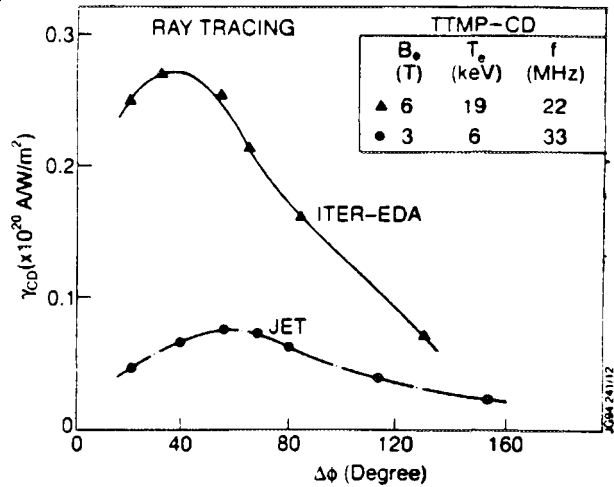
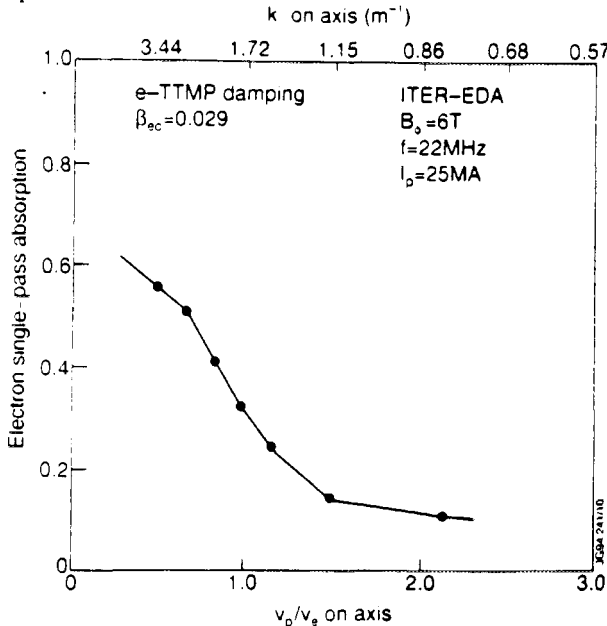


FIG. 5. Single-pass electron absorption vs v_p/v_e for ITER-EDA parameters: D-T, straps. ITER-EDA: 6-straps ($L_z = 0.74$ m). $T_{e0} = 19$ keV, $n_{e0} = 1.4 \times 10^{20} \text{ m}^{-3}$. FIG. 6. Current drive efficiency factor γ_{CD} as a function of $\Delta\phi$ between successive antenna straps. ITER-EDA: 6-straps ($L_z = 0.74$ m). JET-A2: 4-straps ($L_z = 0.4$ m).

fast-wave scenarios spread over a large frequency range, a "violin" [10] antenna (a multiple resonance, asymmetrically excited antenna) has been proposed (see Fig. 7) in which a long strap is connected in parallel with a very short section. The latter acts as a matching element located within the antenna and improves the power coupling property especially at low frequencies. It has high coupling resistance capability at a number of desired frequencies in a wide band [10]. The proposed violin antenna for ITER features a remote ceramic as the antenna is supported at its two short-circuited ends. The remote ceramic aspect of the ITER violin antenna is being simulated [11] with the successful operation of JET A2-antennas with 9 MW coupled up to now to a 2 MW single-null divertor plasma [12]. The antennas have also been tested up to 35 kV in vacuum without arcing. A simplified drawing of the JET

A2-antenna together with the vacuum transmission line and the remote ceramic window (also a support) is shown in Fig. 8.

6. CONCLUSIONS. The fast-wave ICRF system is well suited for heating to ignition of next-step devices such as ITER. The minority ion current drive can be used to control sawteeth. In conjunction with other methods, the fast wave central non-inductive current drive can also be used for steady-state operation of ITER. However, the demonstration of latter is in its infancy due to low β_e in present day devices. The fast wave ICRF technology does not need major developments for the next step and a successful integration of an ICRH antenna with screen into first wall of ITER constitutes the main task. The very recent operation of JET antennas with remote ceramic provides additional design flexibility.

ACKNOWLEDGEMENTS. Contribution of the JET team in this work is greatly acknowledged.

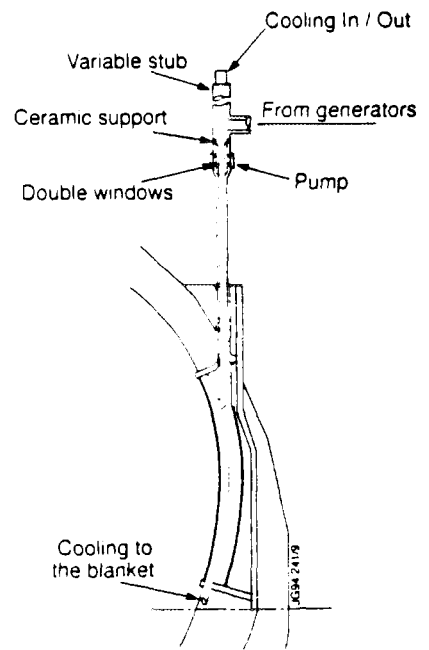


FIG. 7. A poloidal view of a proposed "violin" antenna for ITER with a short and a long section both short circuited at their far ends.

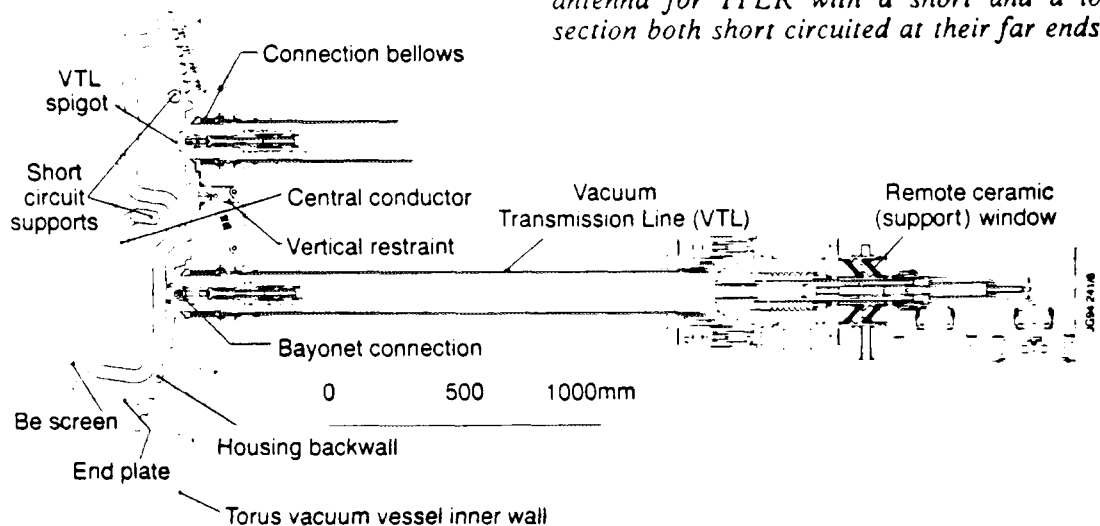


FIG. 8. A simplified drawing of a poloidal view of a strap of a JET-A2 antenna. Also shown is the connection to VTL with a remote ceramic (support) window.

REFERENCES.

- [1] JACQUINOT J. et al, Plasma Phys and Contr Fusion, 35 (1993) A35.
- [2] BHATNAGAR, V.P. et al., Nuclear Fusion, 33 (1993) 83.
- [3] BRUSATI, M. et al., AIP Topical Conf. Proc. 244, Charleston, SC (1991) 115.
- [4] START, D.F.H., et al., Proc. IAEA TCM on Fast Wave Current Drive in Reactor Scale Tokamaks, Arles, France (1991) 260.
- [5] BHATNAGAR, V.P. et al., submitted to Nuclear Fusion.
- [6]. START, D.F.H., ERIKSSON, L., (1993) private communication.
- [7] EHST, D. et al., Nuclear Fusion, 31 (1991) 1933.
- [8] START, D.F.H. et al., Nucl. Fusion 30 (1990) 2171.
- [9] BHATNAGAR, V.P. et al., Nucl. Fusion 24 (1984) 995.
- [10] BHATNAGAR, V.P., JACQUINOT, J., to be published in Nucl Fusion,
- [11] JACQUINOT, J. et al., Proc. IAEA TCM on RF Launchers, Naka, Japan (1993).
- [12] BURES, M. et al., these proceedings.



FR9701789

The H-Mode Power Threshold in JET

D F H Start, V P Bhatnagar, D J Campbell, J G Cordey,
H P L de Esch, C Gormezano, N Hawkes, L Horton, T T C Jones,
P J Lomas, C Lowry, E Righi, F G Rimini, G Saibene, R Sartori,
G Sips, D Stork, P Thomas, K Thomsen, B J D Tubbing,
M von Hellermann, D J Ward.

JET Joint Undertaking, Abingdon, Oxon, OX14 3EA.



1. INTRODUCTION

The JET tokamak is presently equipped with new divertor coils which allow single null configurations to be produced over a wide range in plasma current and with a large flexibility in shape and X-point position. Already H-modes have been produced for plasma currents between 1.5MA and 4MA, for toroidal field values in the range 1.0T to 3.4T and with the ion ∇B drift directed towards the target plates. ELM-free H-modes lasting more than one second are presently being achieved. The power thresholds (P_{th}) for production of H-modes in this new configuration has been analysed and scalings with both toroidal field and the product of density and toroidal field, $n_e B_t$ have been obtained. These results are compared with the data from 1991 and 1992 which show almost exactly the same $n_e B_t$ scaling for carbon X-point tiles and the same ion drift direction. The assembly of the JET 1991/92 H-mode threshold data is almost complete and part of it has been incorporated into the international power threshold database. The important features of the JET database are presented in this paper. It incorporates both double null (DN) and single null (SN) configurations with the ion ∇B drift either towards or away from the X-point in the SN cases. There is evidence for increasing P_{th} with increasing density at constant toroidal field. A unique feature to JET is that the threshold can be studied for different types of heating, namely neutral beam injection (NBI), ion cyclotron resonance (ICRH), combined heating and a few shots with LHCD. The effect of the target tile material (carbon or beryllium) has been investigated as well as the sensitivity of the threshold to plasma current, X-point height and plasma-to-limiter separation.

2. RESULTS OF THE NEW CAMPAIGN.

The longest ELM-free H-mode obtained in the present experimental period lasted for 1.3 sec and is shown in fig.1. The plasma current (I_p) was 2MA, the toroidal field was 2.1T. The H-mode was produced by 6MW of NBI and the energy content increased to almost 5MJ before the first series of ELMs terminated the rise. Thereafter the energy content diminished as the frequency of the ELMs increased. The lowest H-mode threshold achieved so far is with 3MW of NBI in pulse 30071 which was a discharge with $I_p = 1.5MA$ and $B_t = 1T$. The initial 0.5 second pulse at 3MW was sufficient to trigger the H-mode which was sustained by only 1.8MW for a further two seconds. At this stage the power was raised to 7MW giving an energy content of 2.1MJ and a poloidal beta (β_p) of 0.8.

In figure 2 the total input power, which was predominately NBI, is plotted against the product of average density and toroidal field. For these cases the most widely varied quantity was the toroidal field with values in the range 1T to 3.4T. The density was also substantially varied by a factor of 2.7 and the plasma current was either 1.5MA, 2MA or 2.5MA. All the relevant parameters for figure 2 and for all the other scaling studies shown in this paper were measured just prior to the H-mode formation. Clearly the power threshold shows a linear dependence on $n_e B_t$. The threshold is similar to that for the 1991/2 data (fig.2) for similar conditions, namely single null configurations, carbon target tiles and ions drifting towards the target. When 1994 data are plotted against B_t only there is a linear dependence of P_{th} with B_t but the threshold is about a factor of two higher than for the corresponding 1991/92 data and is comparable with that obtained by Ward et al [1] for just 1991 data.

3. THE JET 1991/92 H-MODE DATABASE.

The data are from extensive studies with $1 < I_p(\text{MA}) < 5$, $1 < B_t(\text{T}) < 3.2$, $1 < n_e(10^{19}\text{m}^{-3}) < 6$, forward and reversed toroidal fields, NBI, ICRH and LHCD auxiliary power input, X-point heights varying from 0.02m outside the target plates to 0.17m inside the plates, carbon or beryllium target tiles, and up to 0.25m distance (ΔX) between the last closed flux surface and the limiter. In this section the dependencies of P_{th} on B_t , n_e , heating type, ion ∇B drift direction, I_p , ΔX and the target material are discussed.

3.1 Scaling with n_e , B_t and I_p

A plot of power versus the produce $n_e B_t$ for the whole database including an ohmic heating H-mode is shown in fig.3. There is a marked linear dependence of the threshold power on $n_e B_t$. This is in good agreement with the ASDEX result [2], $P_{\text{th}}/S = 4.4 \times 10^{-3} n_e B_t$ where S is the surface area and varies between 150m^2 and 180m^2 for the JET discharges. The band corresponding to this range of S is shown in fig.3. This scaling gives $P_{\text{th}} \sim 300\text{MW}$ for ITER at a density of 10^{20}m^{-3} . A large fraction of these data was taken at $B_t = 2.8\text{T}$ which provides an opportunity to check for dependence P_{th} on density. All the data for 2.8T are plotted as P_{tot} versus average density in fig.4. Again a linear relationship appears for the threshold power in agreement with results from other tokamaks [3]. However, some caution should be applied to our present findings. It should be noted that the ICRH data alone show a much weaker scaling with density, NBI shows a much stronger scaling, and combined heating contributes strongly to the linear relationship apparent in fig.4.

The scaling with toroidal field alone was obtained for a density range $1 < n_e(10^{20}\text{m}^{-3}) < 2$. The power threshold increases with increasing B_T but at a rate which is a factor of two less than for the 1994 data (fig.2).

The dependence of P_{th} on plasma current was studied at a constant toroidal field of 2.8T and a window in density between $n_e = 1.5 \times 10^{19}\text{m}^{-3}$ and $n_e = 2.5 \times 10^{19}\text{m}^{-3}$. The threshold power is almost constant over the five-fold range in I_p except for a few shots at 3MA which have P_{th} as low as 3-4MW. This "optimum" I_p corresponds to a $q_{95} = 3$. A similar effect has been found in ASDEX [2].

3.2 Dependence on ion ∇B drift direction.

Single null discharges were produced with the null either at the top of the vessel where the target plates were made of carbon or with the X-point at the bottom of the machine where there were beryllium target tiles. The toroidal field was reversed so that the effect of the ion ∇B drift direction (either towards or away from the tiles) could be explored. A plot of P_{tot} versus $n_e |B| \text{sig}$ is shown in fig.5 where the value of sig is +1 for ion ∇B drift towards the target and $\text{sig} = -1$ for drift away from the target. The points are identified according to whether the null was at the top or the bottom of the machine. For completeness the new 1994 data are also included. For the shots with the single null at the top, SN(T), the threshold is greater by about a factor of two if the ∇B drift is away from the target as was found by Ward et al [1] for the scaling with B_t only. For the shots with the single null at the bottom of the vessel, SN(B), and the ion drift away from the target, (negative $n_e |B_t| \text{sig}$), the threshold is about a factor of two less than that with the null at the top for the same drift direction. It is in fact slightly less than the threshold for the SN(B) discharges with the ions drifting towards the target. This result could be due to the effect of the Be tiles or it could be a result of the different heating systems used. Plasmas with the single null at the bottom and the ion drift away from the target were predominantly heated by ICRH or by combined heating. Perhaps fast ion anisotropy or the combination of a non-fuelling heating system combined with the pumping properties of Be tiles is beneficial for reducing the power threshold.

3.3 Effect of X-point height and plasma position.

The influence of the X-point height above the target plates was studied in 3MA 2.2T single null configurations with reversed toroidal field. The results are shown in fig.6. The X-point position was varied from 0.17m inside the target plates to 0.02m behind the target surface. There is clearly only a very weak dependence of P_{th} on ΔX with a small reduction in the threshold level as the X-point is moved further inside the tokamak. The variation of P_{th} with the distance between the limiter and the last closed flux surface is also weak for distances greater than 2cm but increases rapidly as the separation is reduced below 2cm.

4. SUMMARY.

New H-mode threshold data over a range of toroidal field and density values have been obtained from the present campaign. The scaling with $n_e B_t$ is almost identical with that of the 1991/92 period for the same discharge conditions. The scaling with toroidal field alone gives somewhat higher thresholds than the older data. The 1991/2 database shows a scaling of P_{th} with $n_e B_t$ which is approximately linear and agrees well with that observed on other tokamaks.

For NBI and carbon target tiles the threshold power is a factor of two higher with the ion ∇B drift away from the target compared with the value found with the drift towards the target. The combination of ICRH and beryllium tiles appears to be beneficial for reducing P_{th} . The power threshold is largely insensitive to plasma current, X-point height and distance between the last closed flux surface and the limiter, at least for values greater than 2cm.

ACKNOWLEDGEMENTS.

We wish to thank everyone in the JET Team who have contributed to the present campaign and to the 1991/92 H-mode database.

REFERENCES

1. D J Ward et al, Proc. of 18th EPS Conf., Berlin 1991, Part 1, p353
2. F Ryter and the H-mode Database Working Group. Proc. of 19th EPS Conf, Lisbon 1992, Vol. 17c, part 1, p.23.
3. F Ryter et al, Ibid, Vol.17c, part 1, p.15.

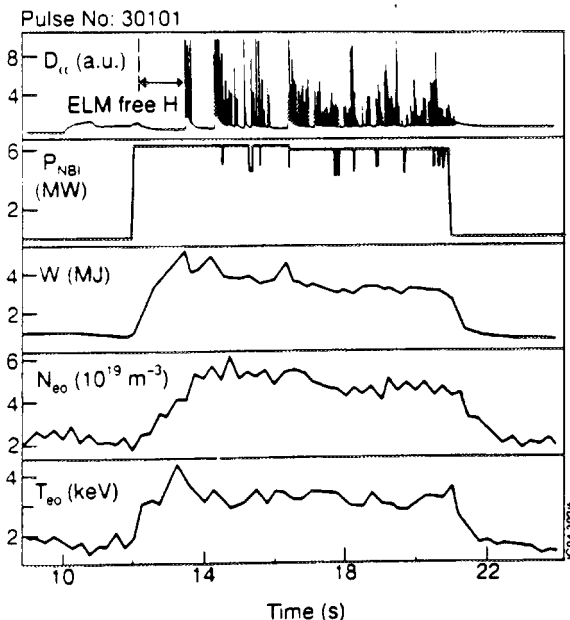


Fig.1 Pulse 30101 with the longest ELM-free period.

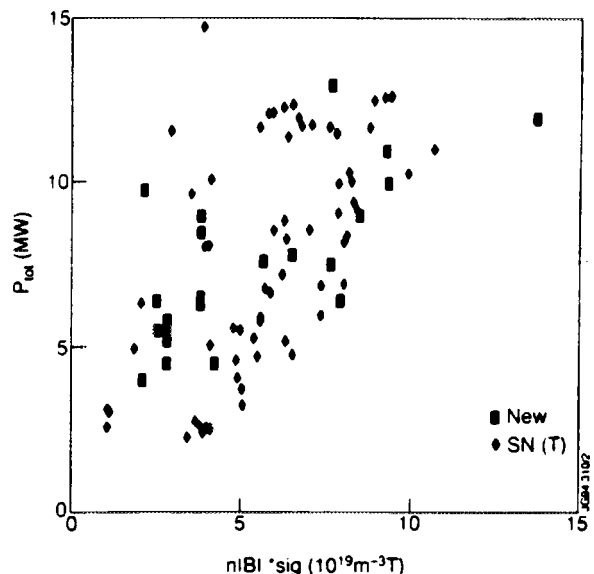


Fig.2: Comparison of 1994 and 1991/2 JET data

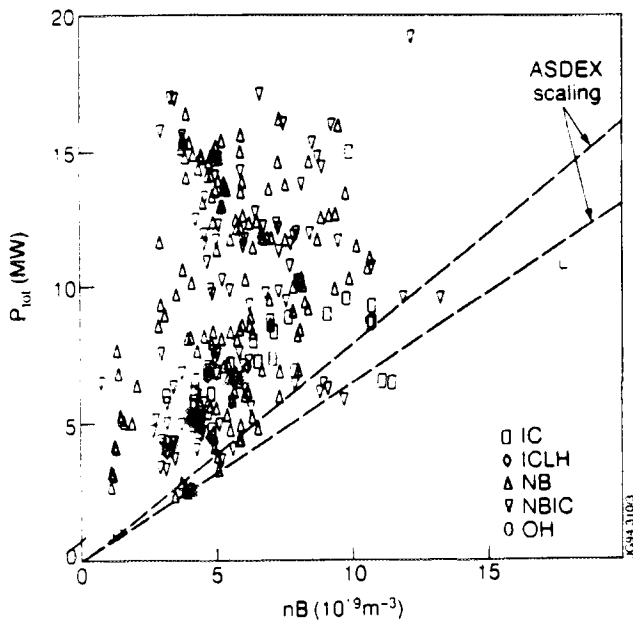


Fig.3: P_{th} versus $n_e B_t$ for the complete 1991/2 database

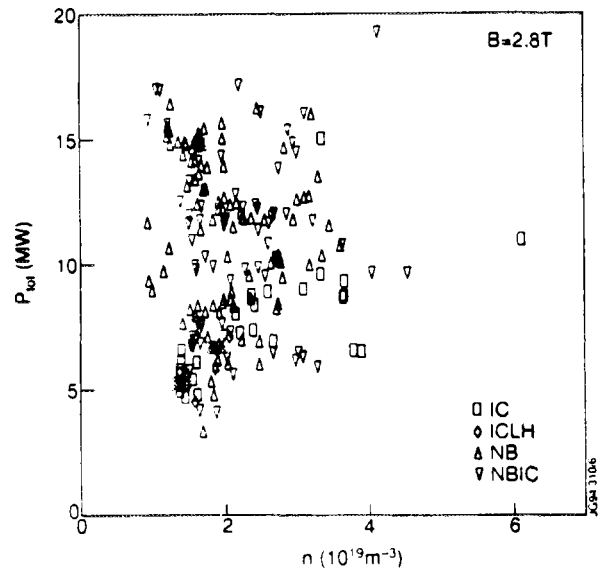


Fig.4: P_{th} versus n_e for $B_T = 2.8T$

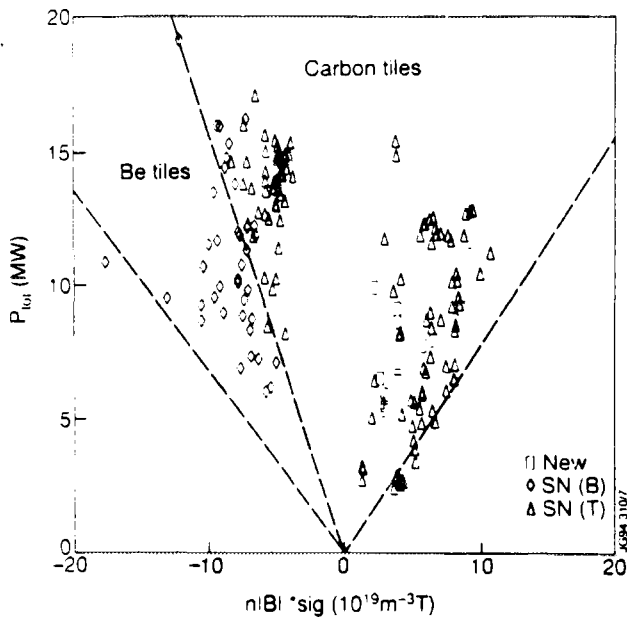


Fig.5: Scaling of P_{th} with $n_e B_t$ for different ion ∇B drift directions in Sn discharges

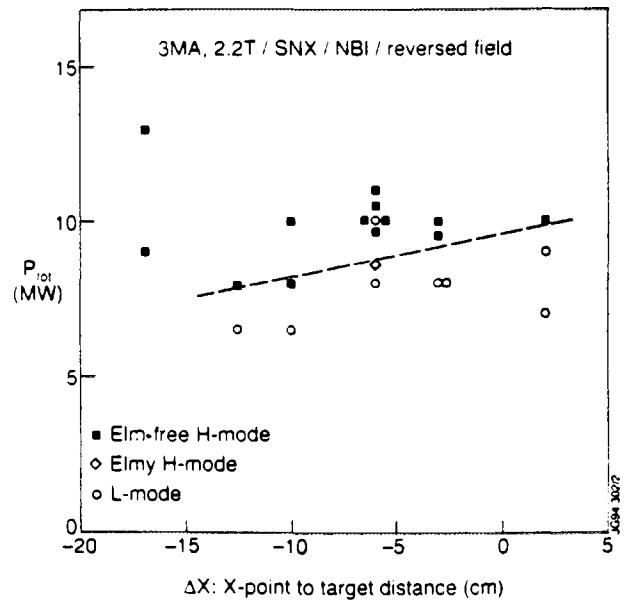


Fig.6: Effect of X-point height on P_{th}



The Density Limit in JET Diverted Plasmas

D J Campbell, S Clement, N Gottardi, C Gowers, P Harbour,
A Loarte, L Horton, J Lingertat, C G Lowry, R Monk¹,
G Saibene, M Stamp, D Stork.

JET Joint Undertaking, Abingdon, Oxon, OX14 3EA.

¹ Dept. of Physics, Royal Holloway College, University of London,
Surrey, TW20 0EX, UK.



1. Introduction

In JET limiter plasmas the density limit is associated with radiated power fractions of 100% and, in plasmas with carbon limiters, it is invariably disruptive. However, in discharges with solid beryllium limiters the limit is identified with the formation of a MARFE and disruptions are less frequent. In addition, the improved conditioning of the vessel arising from the use of beryllium has significantly improved the density limit scaling, so that the maximum density rises with the square root of the input power [1,2]. In diverted plasmas several confinement regimes exist, making the characterization of the density limit more complex. While the density limit in L-mode plasmas is generally disruptive, the limit in ELMy and ELM-free H-modes generally prompts a return to the L-mode and a disruption is not inevitable. The density limit does rise with increasing power, but the L-to-H transition complicates the analysis. Nevertheless, at low plasma currents (<2MA), densities significantly above the Greenwald limit [3] can be achieved, while at higher currents power handling limitations have constrained the range of density which can be achieved.

2. Phenomena at the Density Limit

In L-mode plasmas, the density could be raised until the radiated power fraction was ~60%, at which point the temperature in the divertor had fallen to ~10eV [4]. Subsequently a MARFE entered the main plasma from the divertor, the radiated power fraction rose to 100%, and mhd activity grew, leading to a disruption. In ELM-free H-modes, which were normal in the old JET configuration, the density rose monotonically, impurities built up in the plasma edge and the radiated power rose until it was approximately equal to the input power, with the major fraction arising from the bulk plasma. At this point, a transition back to the L-mode occurred, leading to a rapid fall in density and radiated power. In the majority of cases the fall in radiated power was sufficient to permit a return to a stable L-mode plasma and, if the input power was maintained, the H-mode could re-occur. In other cases, for example in the presence of strong gas-puffing or if the input power fell too rapidly, an L-mode density limit disruption occurred. This general behaviour was independent of whether CFC or beryllium targets were used.

ELMy H-modes, which could be established under limited conditions in the old JET

configuration [5,6], were sustained in steady-state conditions on the CFC targets at radiated power fractions of up to 70%. In addition, a series of steady-state plasmas with radiated power fractions of $\sim 100\%$ were established using the beryllium targets [7], but in these confinement fell to L-mode levels. In high density steady-state H-modes, such as that in figure 1, small fluctuations in input power or radiation could lead to a transition in which the total radiated power fraction rose to 100% and the plasma returned to the L-mode, causing the density to decay as particle confinement fell. This is, therefore, interpreted as representing the density limit for steady-state H-modes.

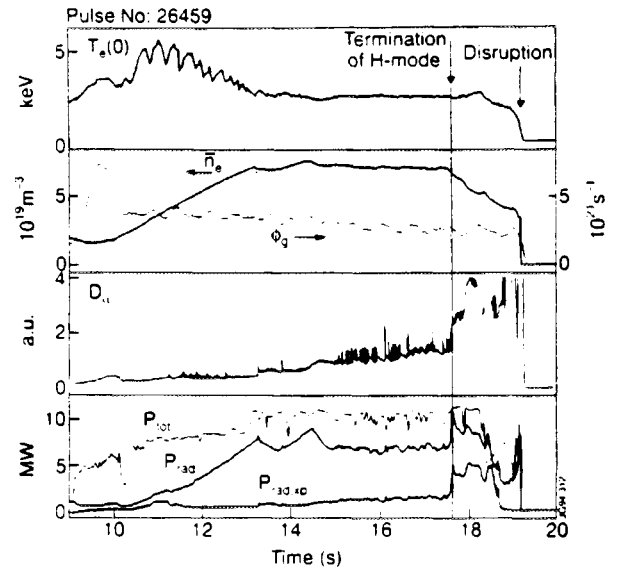


Figure 1: Overview of ELMy steady-state H-mode, terminating in a density limit disruption.

During the H-mode, the radiation was emitted predominantly from a region of $\sim 20\text{cm}$ at the plasma edge. When the radiation rose to 100%, the additional radiation came mainly from the X-point region, but after a period of several 100ms, a MARFE entered the main plasma, the plasma detached fully from the divertor and evolved towards a disruption. The final disruption was not inevitable, but depended on the rate at which the plasma density and input power fell. In these plasmas the plasma density and level of radiation could be adjusted by variation of the gas-puff rate. The density limit appears, therefore, to be associated with a power imbalance, with the limiting density being determined by the input power level and radiation losses.

3. Density Limit Scaling

Following the introduction of beryllium into JET, the density limit was found to rise as $P_{\text{tot}}^{0.5}$ [1,2]. However, in some devices, the density limit is not found to scale with input power, but follows the 'Greenwald' scaling [3]. Comparison of JET data with the predictions of this scaling (figure 2) shows that at low currents ($< 2\text{MA}$) the JET limit exceeds the Greenwald limit, but at high currents ($> 3\text{MA}$) it falls below this. It is likely that the behaviour at high currents was caused by limitations in the power handling of the divertor targets, which restricted the duration of high power heating experiments.

For a device in which the density limit is determined by a power imbalance, such as JET, the power required to exceed the Greenwald limit increases quadratically with current, so that it is

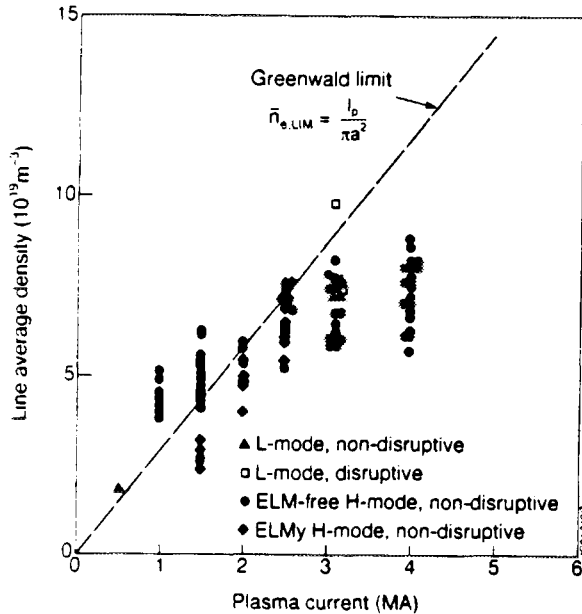


Figure 2: Comparison of densities achieved in JET diverted discharges with Greenwald scaling.

At high currents the 'limit' in diverted plasmas falls some 30% below that achieved in equivalent limiter plasmas, essentially because the heating experiments in diverted plasmas were of shorter duration.

4. Initial Experiments with the Pumped Divertor

Initial experiments in X-point plasmas following the recent upgrade have shown that the ohmic density limit is comparable with that observed previously, with helium plasmas reaching densities $\sim 30\%$ higher than comparable deuterium discharges. Figure 3 shows a 2MA plasma in which the density limit occurred with $\bar{n}_e \approx 3 \times 10^{19} \text{ m}^{-3}$. It can be seen that the major disruption is preceded by a rise in the radiated power fraction to 100%, the occurrence of a MARFE and the growth of an $n=1$ mode, all typical of disruptive density limit phenomena in previous experiments.

Figure 4 illustrates the observations made in the divertor during the approach to the limit. The central panels show measurements of the ion saturation current in the inner and outer strike regions. The modulation of the currents correspond to sweeping of the strike points at 4Hz, essentially to reduce the time averaged power deposition. This modulation, therefore, represents a sequence of time resolved profiles of ion saturation current at the inner and outer strike points during the approach to the limit. Also shown are the D_α and C-III signals for the two strike points. It can be seen that at $\sim 12\text{s}$ there is a sudden reduction in the peak value of

easiest to exceed the Greenwald limit at low currents. Moreover, in experiments prior to the recent upgrade, the majority of high power heating experiments were constrained to be of short duration by the occurrence of the carbon bloom. This limited the period over which the density could be raised, thereby limiting the final density which could be achieved. It is noticeable that the majority of points plotted in figure 2 were non-disruptive. This indicates that, in many cases, the density 'limit' was the highest density which could be achieved during the heating phase, rather than that at which density limit phenomena occurred. A similar pattern is found in comparing diverted plasmas with limiter plasmas: at low currents (and, therefore, moderate power), the achievable densities are similar; at high

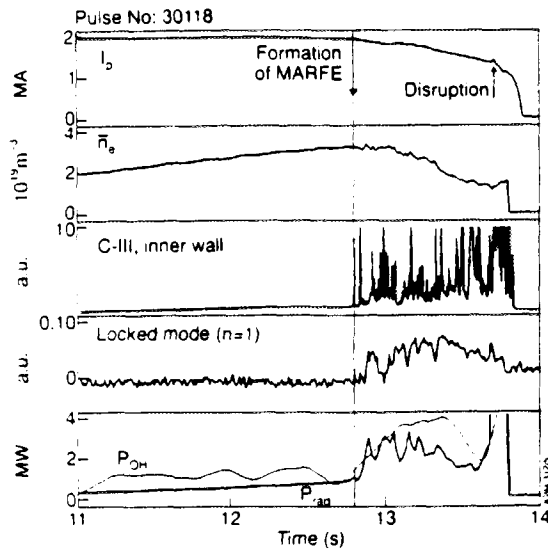


Figure 3: Overview of 2MA ohmic density limit shot in the Pumped Divertor configuration.

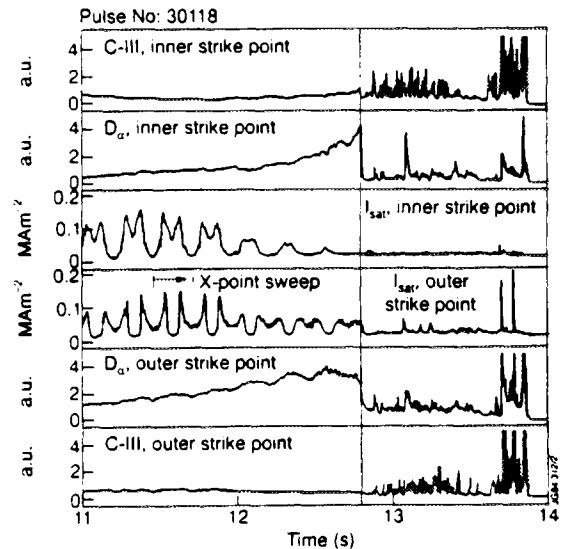


Figure 4: Divertor measurements during the approach to the density limit of figure 3.

ion saturation current which persists until 12.8s, at which time the modulation disappears and the D_α and C-III signals fall precipitately. This corresponds to the final detachment from the divertor and the entry of a MARFE into the main plasma, which is responsible for the subsequent large fluctuations on the D_α and C-III signals. However, the period between 12s and 12.8s appears to correspond to a stable period of detachment during which the X-point configuration is maintained but very little power flows to the target. These results suggest that, as in previous JET experiments [7], there may be a stable window of operation below the density limit in which the exhaust power is dissipated by radiation and charge exchange. The focus of future JET experiments will be to explore and expand this regime at high levels of auxiliary power.

References

- [1] C G Lowry et al, Proc 17th EPS Conf, Amsterdam, 1990, 1 339.
- [2] K Borrass, Nucl Fusion **33** 63 (1993).
- [3] M Greenwald et al, Nucl Fusion **28** 2199 (1988).
- [4] S Clement et al, Proc 33rd APS Meeting, Tampa, 1991.
- [5] P R Thomas et al, Proc 19th EPS Conf, Innsbruck, 1992, 1 239.
- [6] D J Campbell et al, JET Preprint JET-P(94)01 (to be publ in Plasma Phys and Contr Fus).
- [7] S Clement et al, Proc 19th EPS Conf, Innsbruck, 1992, 2 723.